



TECHNISCHE UNIVERSITÄT
MÜNCHEN



Fakultät für Chemie

Investigation and Application of Multinuclear Coinage Metal Organometallic Complexes

Shengyang Guan

Vollständiger Abdruck der von der Fakultät für Chemie der Technischen Universität München zur Erlangung des akademischen Grades eines Doktors der Naturwissenschaften (Dr. rer. nat.) genehmigten Dissertation.

Vorsitzender: Prof. Dr. Klaus Köhler

Prüfende der Dissertation: 1. Priv.-Doz. Dr. Alexander Pöthig

2. Prof. Dr. Angela Casini

Die Dissertation wurde am 01.07.2021 bei der Technischen Universität München eingereicht und durch die Fakultät für Chemie am 21.09.2021 angenommen.

Anhang I

Eidesstattliche Erklärung

Ich erkläre an Eides statt, dass ich die bei der Fakultät für Chemie der TUM zur Promotionsprüfung vorgelegte Arbeit mit dem Titel:

Investigation and Application of Multinuclear Coinage Metal Organometallic Complexes

in der Fakultät für Chemie, Lehrstuhl für Anorganische und Metallorganische Chemie

unter der Anleitung und Betreuung durch Priv.-Doz. Dr. Alexander Pöthig ohne sonstige Hilfe erstellt und bei der Abfassung nur die gemäß § 6 Ab. 6 und 7 Satz 2 angebotenen Hilfsmittel benutzt habe.

× Ich habe keine Organisation eingeschaltet, die gegen Entgelt Betreuerinnen und Betreuer für die Anfertigung von Dissertationen sucht, oder die mir obliegenden Pflichten hinsichtlich der Prüfungsleistungen für mich ganz oder teilweise erledigt.

× Ich habe die Dissertation in dieser oder ähnlicher Form in keinem anderen Prüfungsverfahren als Prüfungsleistung vorgelegt.

× Ich habe den angestrebten Doktorgrad noch nicht erworben und bin nicht in einem früheren Promotionsverfahren für den angestrebten Doktorgrad endgültig gescheitert.

Die öffentlich zugängliche Promotionsordnung der TUM ist mir bekannt, insbesondere habe ich die Bedeutung von § 28 (Nichtigkeit der Promotion) und § 29 (Entzug des Doktorgrades) zur Kenntnis genommen. Ich bin mir der Konsequenzen einer falschen Eidesstattlichen Erklärung bewusst.

Mit der Aufnahme meiner personenbezogenen Daten in die Alumni-Datei bei der TUM bin ich einverstanden,

Shengyang Guan

Garching, 26.06.2021

Abstract

For several years now, the research on supramolecular organometallic complexes based on N-heterocyclic carbenes (NHCs) has been flourishing. Given the advantage of easy preparation and structural and electronic versatility of NHC ligands, the derived supramolecular organometallic complexes (SOCs) allow for a facile functionalization towards desired supramolecular properties. The recently introduced coinage-metal “pillarplexes” represent a family of NHC-based SOC, obtained by a macrocyclic templation strategy. The characteristic M_8L_2 motif of pillarplexes leads to the formation of tubular-shaped structures with a cylinder-shaped cavity. Owing to this pore, the shape-persistent complexes were found to be able to encapsulate linear guest substrates. To explore the potential of pillarplexes in medicinal applications, such as drug delivery systems, the pillarplex compounds were tested for their stability and biological activity. Pyrazolate-based silver pillarplexes $[Ag_8L^{Me_2}](PF_6)_4$ and $[Ag_8L^{Me_2}](OAc)_4$ share the behavior of $AgNO_3$ in that they showed antimicrobial and antifungal activity as well as moderate toxicity towards human HepG2 cells. The corresponding gold pillarplexes $[Au_8L^{Me_2}](PF_6)_4$ and $[Au_8L^{Me_2}](OAc)_4$ were inactive against most bacterial strains and fungi while showing lower HepG2 toxicity. The observed effects are attributed to the increased stability of the gold pillarplexes compared to the silver pillarplexes, as supported by 1H NMR spectroscopic studies and UV-vis titration experiments.

Subsequently, in order to expand the pillarplex family, the synthesis of derived SOC following the macrocyclic templation strategy was investigated. Macrocyclic ligand platforms bearing different functional entities were prepared and their SOC formations were explored. Out of three prepared ligand systems, sterically and electronically modified macrocyclic NHC ligand $H_6L^t(OTf)_4$,

featuring triazolate moieties, was found to yield a new subclass of pillarplex SOCs. The solid-state structure of the resulting gold(I) hexafluorophosphate complex $[\text{Au}_8\text{L}'_2](\text{PF}_6)_4$ revealed unprecedented structural flexibility of this pillarplex, possibly caused by the lower steric demand of the introduced nitrogen atom at the rim. This is supported by DFT calculations, showing a significantly higher energetic penalty for a similar deformation of the previously reported pyrazolate-based $[\text{Au}_8\text{L}^{\text{Me}_2}]$ pillarplex fragment. Additionally, the triazolate nitrogen atom at the rim was shown to act as a hydrogen bond acceptor, enabling the self-recognition between the cationic complexes in the solid state.

The second major focus of this thesis was the study of cyclic trinuclear gold(I) complexes (CTCs) based on an imidazole ligand. The structural and photophysical properties of $\text{Au}_3(1\text{-methylimidazolate})_3$ were investigated. A new solvatomorph was identified and structurally characterized. The new compound was obtained by a cryogenic crystallization protocol and features strong intermolecular Au–Au interactions through the dimeric $[\text{Au}_3]$ cores. The intermolecular metallophilic interactions were further investigated by DFT calculations: Strong interactions between the individual complexes in the dimer were observed, rather than weak metallophilic interactions within a single $[\text{Au}_3]^{3+}$ core. The photophysical properties of a solvent-free polymorph of $\text{Au}_3(1\text{-methylimidazolate})_3$ were studied, which showed thermochromism with unexpectedly high quantum yields at very low temperatures.

Zusammenfassung

Seit einigen Jahren floriert die Forschung rund um supramolekulare organometallische Komplexe basierend auf *N*-heterocyclischen Carbenen (NHCs). Angesichts ihrer einfachen Synthese und der strukturellen wie elektronischen Vielseitigkeit der NHC-Liganden können die davon abgeleiteten supramolekularen organometallischen Komplexe (SOCs) einfach funktionalisiert werden, um gewünschte supramolekulare Eigenschaften zu erlangen. Die kürzlich vorgestellten Münzmetall-basierten "Pillarplexe" stellen eine Familie von NHC-basierten SOCs dar, die durch eine makrozyklische Templationsstrategie erhalten werden können. Das charakteristische M_8L_2 -Motiv der Pillarplexe führt zur Bildung von röhrenförmigen Strukturen mit einem zylinderförmigen Hohlraum. Dank dieser Pore sind die formstabilen Komplexe in der Lage, lineare Gastsubstrate zu insertieren. Um das Potenzial von Pillarplexen in medizinischen Anwendungen zu erforschen, wurden die Pillarplex-Verbindungen auf ihre Stabilität und biologische Aktivität getestet. Pyrazolat-basierte Silber-Pillarplexe $[Ag_8L^{Me_2}](PF_6)_4$ und $[Ag_8L^{Me_2}](OAc)_4$ zeigen analog zu $AgNO_3$ eine antimikrobielle und antimykotische Aktivität, sowie eine moderate Toxizität gegenüber menschlichen HepG2-Zellen. Die entsprechenden Gold-Pillarplexe $[Au_8L^{Me_2}](PF_6)_4$ und $[Au_8L^{Me_2}](OAc)_4$ waren gegen die meisten Bakterienstämme und Pilze inaktiv und zeigten gleichzeitig eine geringere HepG2-Toxizität. Die beobachteten Effekte werden auf die erhöhte Stabilität der Gold-Pillarplexe im Vergleich zu den Silber-Pillarplexen zurückgeführt, was durch 1H NMR-spektroskopische Untersuchungen und UV-vis-Titrationsexperimente untermauert wird.

Um die Pillarplex-Familie zu erweitern, wurde anschließend die Synthese von davon abgeleiteten SOCs, dargestellt über eine makrozyklische Templationsstrategie, untersucht. Makrozyklische Ligandenplattformen, die

verschiedene funktionelle Einheiten tragen, wurden synthetisiert und ihre SOC-Bildung wurde untersucht. Unter den drei vorbereiteten Ligandensystemen, die sich sterisch und elektronisch von der Pyrazolat-Stammverbindung unterscheiden, zeigte sich vor allem das Derivat mit Triazolot im makrozyklischen NHC-Liganden, $\text{H}_6\text{L}^t(\text{OTf})_4$, als erfolgreich in der Pillarplex-SOCs-Bildung. Die Festkörperstruktur des Gold(I)-Hexafluorphosphat-Komplexes $[\text{Au}_8\text{L}^t_2](\text{PF}_6)_4$ zeigte eine strukturelle Flexibilität der Pillarplexe, potentiell verursacht durch die geringeren sterischen Anforderungen des eingeführten Stickstoffatoms am Rand des Supermoleküls. Dies wird durch DFT-Berechnungen unterstützt, die eine signifikant höhere energetische Barriere für die Deformation eines ähnlichen zuvor eingeführten Pyrazolat-basierten $[\text{Au}_8\text{L}^{\text{Me}_2}]$ Pillarplex-Fragments zeigen. Zusätzlich konnte gezeigt werden, dass das Triazolot-Stickstoffatom am Rand als Akzeptor für Wasserstoffbrückenbindungen fungiert, wodurch eine Selbsterkennung zwischen den kationischen Komplexen im festen Zustand ermöglicht wird.

Der zweite Schwerpunkt dieser Doktorarbeit war die Untersuchung von zyklischen dreikernigen Gold(I)-Komplexen (CTCs), die auf einem Imidazole-Liganden basieren. Die Struktur und die photophysikalischen Eigenschaften von $\text{Au}_3(1\text{-Methylimidazolot})_3$ wurden untersucht. Ein bisher unbekanntes Solvatomorph wurde identifiziert und strukturell charakterisiert. Die neue Verbindung wurde durch ein kryogenes Kristallisationsprotokoll erhalten und weist starke intermolekulare Au–Au-Wechselwirkungen zwischen je einem Au_3 -Zentrum zweier Komplexe auf. Die intermolekularen metallophilen Wechselwirkungen wurden durch DFT-Rechnungen weiter untersucht: Es wurden stärkere Wechselwirkungen zwischen den einzelnen Komplexen im Dimer beobachtet, als schwache metallophile Wechselwirkungen innerhalb eines einzelnen $[\text{Au}_3]^{3+}$ -Kerns. Die photophysikalischen Eigenschaften eines lösungsmittelfreien Polymorphs von $\text{Au}_3(1\text{-Methylimidazolot})_3$ wurden untersucht, welches Thermochromie mit unerwartet hohen Quantenausbeuten

bei sehr niedrigen Temperaturen zeigte.

Acknowledgment

It is an unforgettable experience to achieve a doctorate degree in Germany. During the time, I encountered numerous challenges, which frustrated me a lot, especially at the beginning. With help from my colleagues and family, I reached the finals. Without their help, the experience would have been very difficult.

First of all, I would like to address my special thanks and appreciation to my Ph.D. supervisor, **Priv.-Doz. Dr. Alexander Pöthig**, for hosting me in the Supramolecular Organometallics group in the Chair of Inorganic and Metal-Organic Chemistry (AMC) to work on this interesting topic. I am very grateful for his continuous instruction, suggestion and encouragement during my Ph.D. study, as well as for his numerous effort put into my work. His invaluable guidance has always been a great source of inspiration, helping me to enrich my knowledge and improve my scientific skills.

Secondly, I would like to thank my mentor **Prof. Dr. Roland Fischer**, for hosting me in the Chair of Inorganic and Metal-Organic Chemistry (AMC) group and for the comfortable working environment in Catalysis Research Center.

My deep gratitude also goes to **Prof. Dr. Angela Casini**, who guided and financially supported me in the last year of my Ph.D. studies. Special thanks to her for her support during the difficult period of the COVID-19 outbreak last year.

I acknowledge to China Scholarship Council (CSC) for providing the full scholarship to support my living and studying in Germany. I am grateful for the financial support to an international tour to China by the Graduate School of the Technical University of Munich.

I would like to address my special thanks to **Prof. Dr. Klaus Köhler** for accepting to be the chairperson of my doctoral dissertation defense. I would

like to express my special thanks and appreciation to **Priv.-Doz. Dr. Alexander Pöthig** and **Prof. Dr. Angela Casini** for accepting to be the examiners of my doctoral dissertation defense.

Special thanks to **Dr. Christian Jandl** for his help in lab and XRDs, fruitful discussions with him always help me from different aspects. Also, thanks to **Dr. Wei-Jin Li**, **Dr. Juan Liu** for their warm welcome and when I come to Munich for the first time. Hope they will enjoy their research life in Japan soon.

I would also like to thank **Dr. Eliza Gemel** for the instruction in ACII teaching course, **Jürgen Kudermann** for training the operation of UV-Vis, **Maria Matthews** for the NMR measurements. Special thanks to my colleagues **Thomas Pickl**, **Fabian Schmidt**, **Lena Staiger**, **Stefan Burger**, **Joao Carvalho**, **David Mayer**, **Patricia Weishäupl (née Heiß)**, **Sebastian Weishäupl**, **Dr. Markus Anneser Maximilian Muhr**, **Margit Aust**, **Karina Hemmer**, **Kathrin Kollmannsberger**, **Alexandra Heidecker**, **Dr. Suttipong Wannapaiboon**, **Dr. Konstantin Epp**, **Dr. Stefano Dissegna**, **Dr. Christian Schneider**, **Werner Heinz**, **Michael Ehrenreich**, **Rodica Dumitrescu** and **Maria Matthews** for their help and support in my work.

I am grateful to **Martin Schellerer** and **Dr. Dana Weiss** for their help with administrative work. And special thanks to **Dr. Julien Warnan**, **Dr. Christian Gemel**, **Dr. Gregor Kieslich**, **Dr. Markus Drees** and **Prof. Dr. Richard Fischer** for their suggestions, supports and help in my project.

Also, I am very grateful to all members of AMC for such a good working atmosphere. Particularly, I want to thank **Thomas Pickl**, **Ruirui Zhang**, **Zhenyu Zhou**, **Shujin Hou**, **Zhiying Fan** and **Xiaoxin Ma** for numerous suggestions, supports and helps. Special thanks to **Zhiying Fan** and **Xiaoxin Ma**, it is a pleasure to be with you in Munich.

Last but not least, I would like to address my deepest appreciation to my beloved family for their encouragement.

大鹏一日同风起, 扶摇直上九万里

Abbreviations

% Vbur	percent buried volume
Å	Ångström (10^{-10} m)
Ac	acetyl
Ad	adamantyl
ADP	adenosine diphosphate
ATP	adenosine triphosphate
BNAH	1-benzyl-1,4-dihydronicotinamide
Boc	tertiary butyloxycarbonyl
BF ₄	tetrafluoroborate
Bz	benzyl
COD	1,5-cyclooctadiene
Cy	cyclohexyl
dba	dibenzylideneacetone
DCM	dichloromethane
DFT	density functional theory
Dipp	2,6-diisopropylphenyl
DMF	N,N-dimethylformamide
DMSO	dimethyl sulfoxide
DNA	deoxyribonucleic acid
DIPA	diisopropylethylamine
Dipp	2,6-diisopropylphenyl
em	emission
equiv.	equivalent
ESI	electrospray ionization
Et	ethyl
ex	excitation
G2/M	Mitotic G2 (gap 2) phase

HSP60	heat shock protein 60
IC50	half maximal inhibitory concentration
KHMDS	potassium bis(trimethylsilyl)amide
LEP	Lever electronic parameter
LUMO	lowest unoccupied molecular orbital
M	variable metal
<i>m</i>	<i>meta</i>
m/z	mass-to-charge-ratio
Me	methyl
Mes	mesityl, 2,4,6-trimethylphenyl
MOF	metal-organic framework
MS	mass spectrometry
NEt ₃	triethylamine
<i>n</i> Bu	normal butyl, butyl
NHC	N-heterocyclic carbene
NMR	nuclear magnetic resonance
ORTEP	Oak Ridge Thermal Ellipsoid Plot
<i>p</i>	<i>para</i>
PCy ₃	tricyclohexylphosphine
PF ₆	hexafluorophosphate
Ph	phenyl
ppm	parts per million
py	pyridyl
R	variable substituent
r.t.	room temperature
SC-XRD	single crystal X-ray diffraction
triflate	trifluoromethanesulfonate
<i>t</i> Bu	tertiary butyl
TEP	Tolman electronic parameter

THT

tetrahydrothiophene

YB-1

Y box binding protein 1

Table of Content

Abstract	III
Zusammenfassung	V
Acknowledgement	VIII
Abbreviations	XII
Table of Content.....	XV
1. Introduction to N-heterocyclic Carbenes.....	18
1.1 N-heterocyclic Carbenes - an Overview.....	18
1.2 Structure of N-heterocyclic Carbenes.....	20
1.3 Synthesis of N-heterocyclic Carbenes.....	23
1.3.1 Synthetic Approaches towards N-heterocyclic Carbene Ligand Precursors	23
1.3.2 Synthetic Approaches towards Metal N-heterocyclic Carbene Complexes.....	32
1.4 Properties of N-heterocyclic Carbenes.....	42
1.4.1 Electronic Stabilization.....	42
1.4.2 pKa values of Ligand Precursors	43
1.4.3 σ -Donation Properties of NHCs	45
1.4.4 Steric Properties of NHCs.....	47
1.5 Conclusion of Chapter 1	49
1.6 References of Chapter 1.....	49
2. Applications of N-heterocyclic Carbenes Complexes	63
2.1 Applications of NHCs in Catalysis	63
2.2 Medicinal Applications of NHCs	67
2.3 Supramolecular Chemistry Based on NHC Complexes	74
2.4 Conclusion of Chapter 2	86

2.5 References of Chapter 2.....	86
3. Objective.....	96
4. Result and Discussion	98
4.1 Biological Activity & Stability Studies of Pillarplex*	98
4.1.1 Abstract.....	98
4.1.2 Introduction.....	98
4.1.3 Results and Discussion.....	103
4.1.4 Conclusion	107
4.1.5 References of Section 4.1.....	108
4.2 Rim-Modified Pillarplexes	112
4.2.1 Abstract.....	113
4.2.2 Introduction.....	114
4.2.3 Results and Discussion	118
4.2.4 Conclusions	144
4.2.5 References of Section 4.2.....	145
4.3 Cyclic trinuclear Au₃(1-Methylimidazolate)₃	149
4.3.1 Abstract.....	150
4.3.2 Introduction.....	151
4.3.3 Results and Discussion	153
4.3.4 Conclusion.....	163
4.3.5 References of Section 4.3	164
5 Conclusion and Outlook	167
6 Experimental Method.....	170
6.1 General Remarks	170
6.2 Single-Crystal X-Ray Diffraction.....	170
6.3 Experimental Details of Section 4.1	172
6.4 Experimental Details of Section 4.2	172
6.5 Experimental Details of Section 4.3	177

6.6 References of Chapter 6.....	178
7 Appendix	180
7.1 NMR Spectroscopy	180
7.2 ESI-MS Spectra	192
7.3 Job-Plot Titrations	195
7.4 Solid-State Emission Spectra	196
7.5 Crystallographic Data.....	198
7.6 Hirshfeld Surface Analysis Fingerprint Plots	212

1. Introduction to N-heterocyclic Carbenes

1.1 N-heterocyclic Carbenes – an Overview

A carbene is a neutral molecule featuring a divalent carbon atom and two unshared valence electrons. Prior to 1960s, following the pioneering contributions of Doering and Fischer in synthesizing carbene and carbene complexes,^{1,2} there was a school of thought that carbenes were too reactive to be isolated, this thought thwarted extensive efforts to study carbene chemistry. This hypothesis might be true for the majority of the carbene species, but has proven to be inaccurate for the N-heterocyclic carbenes, which are singlet carbenes incorporated in nitrogen-containing heterocycles (NHCs). In 1962, Wanzlick made the first unsuccessful attempt to isolate free N-heterocyclic carbenes from their dimerized derivative.³ In 1968, Wanzlick and Öfele reported applications of the N-heterocyclic carbenes as ligands for mercury and chromium complexes (**Scheme 1, A** and **B**, respectively).^{4,5} Later in 1970s, Lappert and coworkers assessed the potential of NHCs for metal complexing with a wide range of metals.⁶⁻⁸ After a decade, the report of a highly stable crystalline NHC 1,3-di-1-adamantylimidazol-2-ylidene by Arduengo initiated a thriving development in this field (**Scheme 1, C**).⁹ These N-heterocyclic carbenes are represented by the cyclic species which are stabilized by the presence of heteroatom interacting with the carbene center (a general structure of NHCs is illustrated in **Figure 1**), this structure is also embraced by another distillable stable phosphinosilylcarbene (**Scheme 1, D**).¹⁰

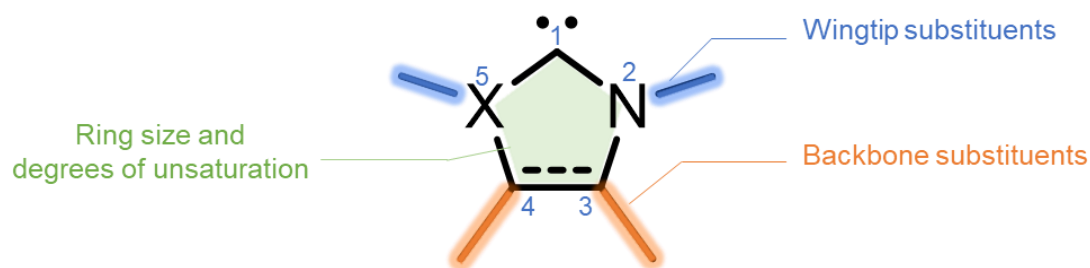
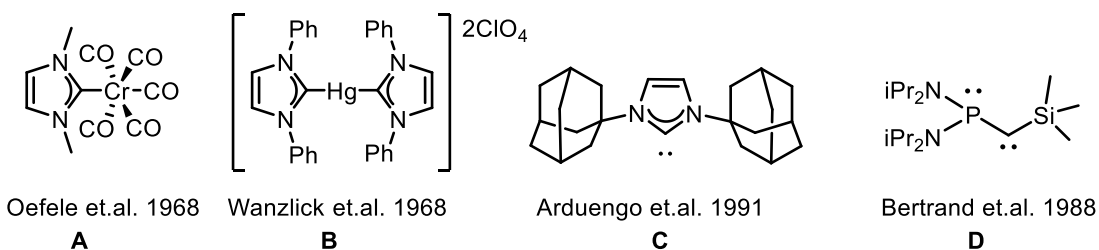
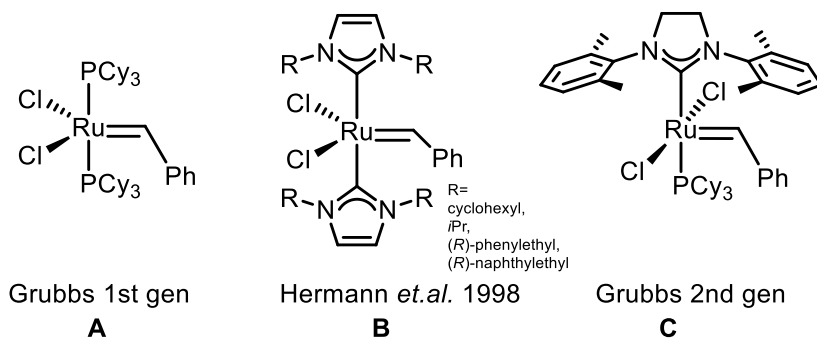


Figure 1. General structural features of NHCs., X = N, O, S, etc.

Scheme 1. Carbene structures reported by Öfele, Wanzlick, Arduengo and Bertrand.^{4,5,9,10}

There is no doubt that the catalysis is one of the main themes for the early stage of NHCs studies. Compared to phosphine ligands, NHCs are strong σ -donor but weak π -acceptor and bind strongly to the metal center. These properties make NHCs attractive alternatives to phosphine ligands as the nucleophilic ligands in catalyst design. Together with other advantages such as easy preparation and coordination versatility, the metal complexes of NHCs was concluded as a new candidate for catalysts in homogeneous catalysis by Herrmann in 1995.^{11,12} The best-known example is probably the development of ruthenium-based Grubb's olefin metathesis catalysts: Grubb's 1st generation catalyst offers simpler handling and higher compatibility with functional groups of substrates compared than previous transition metal catalysts.¹³⁻¹⁵ However, this phosphine complex suffers low thermal stability which arises from its weak P-C bond. Herrmann substituted the phosphine with NHC ligands and a similar catalytic reactivity was observed but with improved stability and more potentials for modification.¹⁶



Scheme 2. Structures of (A) 1st generation Grubb's catalyst^{14,15} (B) first NHC-Ru metathesis catalyst by Herrmann¹⁶ and (C) 2nd generation Grubb's catalyst^{17,18}.

Extensive studies revealed that the activation of 1st generation Grubb's catalyst in olefin metathesis relies on the phosphine dissociation progress from the ruthenium.¹⁹⁻²² Later in 2002, inspired by earlier insightful studies conducted by Herrmann,¹⁶ the 2nd generation Grubb's catalyst substituted one phosphine with NHCs ligand. The stronger σ -donating and weaker π -accepting properties of NHCs render their binding strongly to the metal center and result in a significant improvement in air and moisture stability. Furthermore, the increased σ -donor character of NHCs enhances the affinity of olefin substrates to the ruthenium center, leading to improved catalytic ability.^{17,20,23}

1.2 Structure of N-heterocyclic Carbenes

The unique properties make NHCs an integral part of modern organometallic chemistry, in which the previously mentioned homogeneous olefin metathesis catalysis is just one of the many applications.²⁴ A thorough understanding of the structure of NHCs is essential to apply it in more catalysis fields, and to promote the design of new NHCs. Arduengo-type carbenes are usually referred to heterocyclic species containing one carbene carbon at C² position and the nitrogen atom in the ring (see **Figure 2**).²⁵⁻²⁷ In this kind of carbene, the cyclic structure forces the C² carbon to adapt sp^2 hybridization in the ring plane which leaves one empty p -orbital (p_z) perpendicular to the plane. The hybridized sp^2

orbitals form one electron lone pair and two σ -bond with two nitrogen atoms in the ring plane, while the empty perpendicular p_z orbital receives donating of electron from nitrogen atoms. Therefore, the highest occupied molecular orbital (HOMO) is best described as the empty perpendicular p_z orbital and the lowest unoccupied molecular orbital (LUMO) corresponds to hybridized sp^2 with a lone pair.^{28,29}

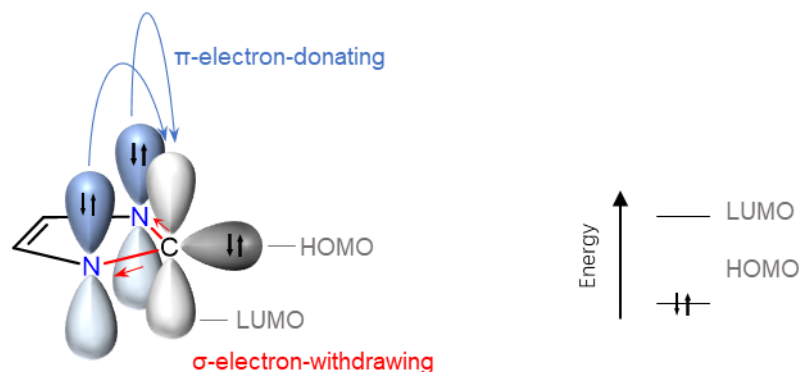
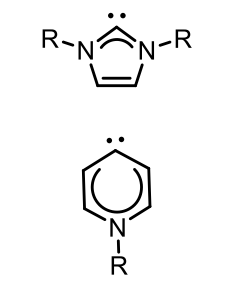
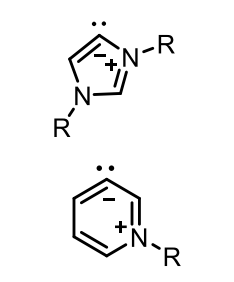
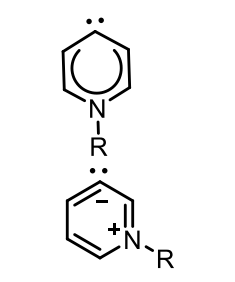
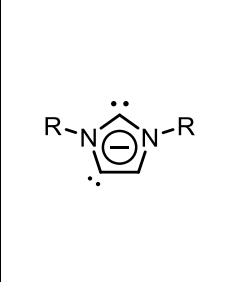


Figure 2. Ground-state electronic structure of N-heterocyclic carbenes, exemplarily demonstrated with imidazolylidene. Substitution groups of the ligand were omitted for clarity. The σ -electron-withdrawing and π -electron-donating effect help to stabilize the singlet carbene structure by donating electrons to the empty p_z orbital (LUMO) on C^2 and withdrawing electrons from hybrid sp^2 orbitals (HOMO).

The σ -electron-withdrawing and π -electron-donating nitrogen atoms stabilize the structure of Arduengo-type carbenes by lowering the energy of the occupied σ orbital and by donating electron density into the empty p_z orbital. In the further study of the structure, it was found that it is not required to have two adjacent nitrogen atoms to stabilize the carbene center.³⁰ Cyclic carbenes bearing alternative heteroatoms (sulfur/oxygen/boron atoms) and at least one nitrogen can also be used in NHCs, constituting another important class of carbenes with equal or lower heteroatom stabilization.³⁰ In a mesoionic ring system, it is required to assign positive and negative formal charges.³¹ In this case, a resonance structure couldn't be obtained with all-neutral formal charges. These carbenes are classified as abnormal carbenes (aNHC) or mesoionic carbenes (MIC).³² In addition to normal carbenes (nNHCs) and abnormal carbenes

(aNHCs), remote carbenes (rNHCs) represent another class of carbenes, featuring the carbene center nonadjacent to any heteroatom. The normal and abnormal carbene mode can be combined in the same ligand moiety yielding an anionic dicarbene or N-heterocyclic dicarbene (NHDC).³³ Imidazolium and pyridinium-derived NHCs were used to demonstrate the classification in **Table 1**.

Table 1. Currently accepted major classes of NHC ligands.

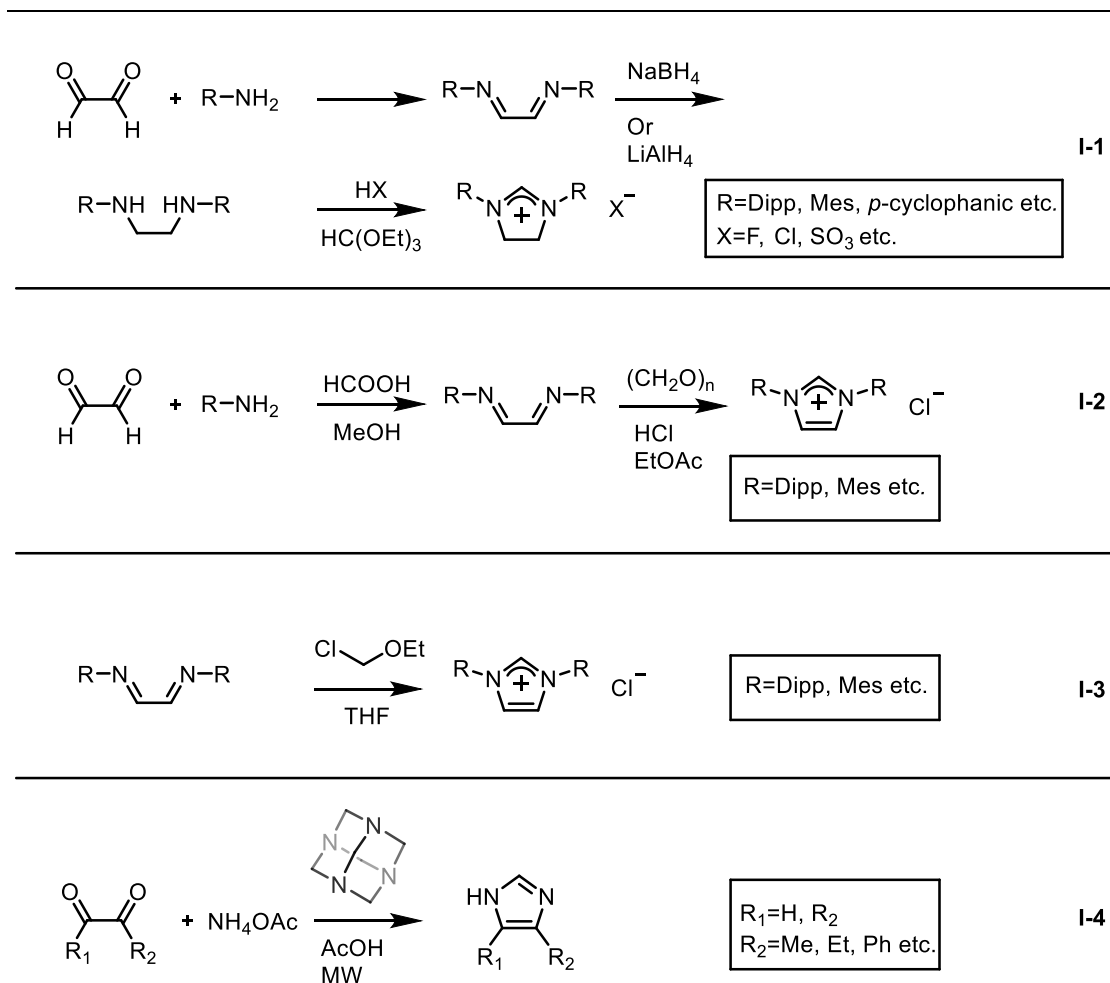
Type of NHC	Normal	Abnormal or mesoionic	Remote	Anionic dicarbene
s	The free nNHC must have a resonance form with all-neutral formal charges	The free aNHC must be mesoionic.	The carbene carbon must not be α to any heteroatom. May be an aNHC or an nNHC	Both normal and abnormal carbene centers exist in one ring system
Example				

1.3 Synthesis of N-heterocyclic Carbenes

1.3.1 Synthetic Approaches towards N-heterocyclic Carbene Ligand Precursors

From the prementioned examples, the structure of NHC could be concluded as a carbene bearing aromatic cyclic structure with at least one nitrogen atom. Unlike phosphine ligands (PR_3), whose properties can only be altered by changing R group, properties of NHCs can be specifically tuned by altering substituents on wingtip/backbone or cyclic structure to meet certain demands. Given the amount of nitrogen containing heterocycles, the potential in the development of NHCs is vast.

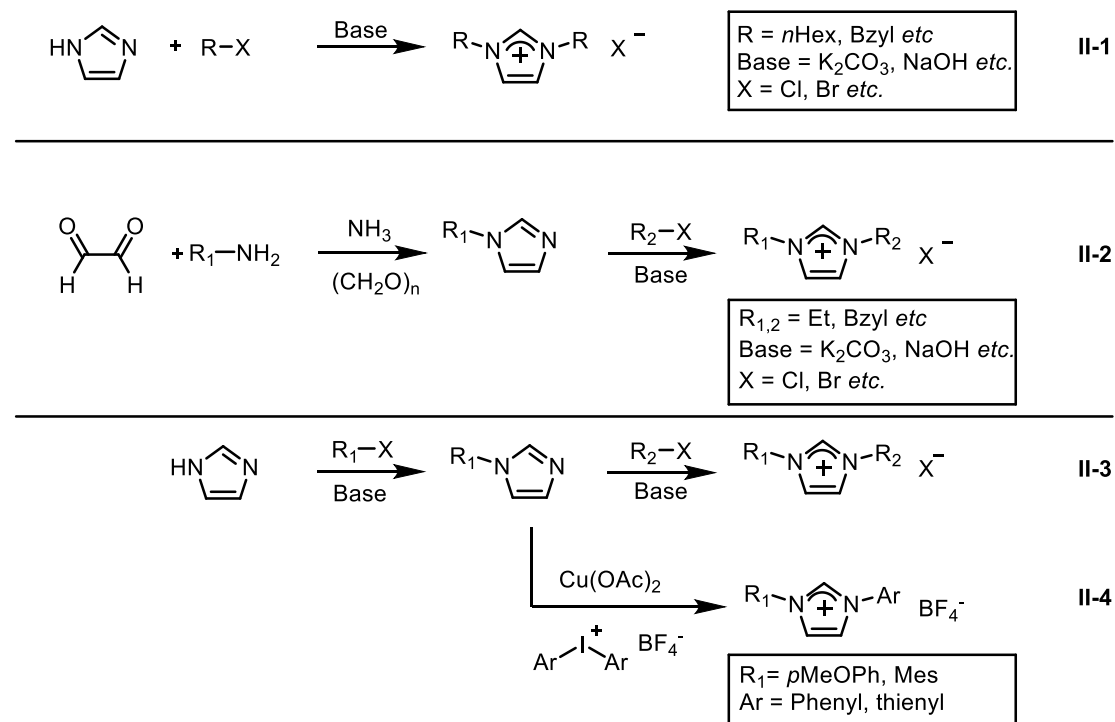
NHCs are usually synthesized by deprotonation of the azolium salt (e.g. imidazolium, triazolium, tetrazolium, pyrazolium, benzimidazolium, oxazolium, thiazolium salts). Of all the mentioned azolium salts, imidazolium/imidazolinium salts are abundantly used for NHCs. When deprotonated, the imidazolium salt is converted to the corresponding imidazolylidene, containing unsaturated five-membered diazaheterocycle. The synthesis of imidazolium salts follows two broad strategies: (I) cyclization of amine/imine with carbon components; (II) alkylation of the parent heterocycle.³⁴ Numerous methods following the two broad strategies have been reported, representative examples are described in **Scheme 3 - 5**:



Scheme 3. Synthesis of imidazolium NHC precursors (**I-1**, **2**, **3**) and imidazole (**I-4**) via cyclization strategy.

The synthetic route **I-1** in **Scheme 3** is a very popular method to access symmetrical imidazolium salts. A diimine is formed by condensation of an amine with glyoxal in the first step. Subsequently, it is reduced to the corresponding diamine, isolated as the free base or as the dihydrochloride salt. Cyclization with triethyl orthoformate in the presence of acid afford the imidazolium salts.³⁵ By adjusting the anion of HX, imidazolium salts with desired anions could be obtained easily. Synthesis of imidazolium salts bearing aromatic, very bulky or functionalized N,N'-substituents benefits from this multi-component cyclization method.³⁶ Nolan reported an improved efficient and scalable synthetic method **I-2**.¹⁷ Mixing the primary amines with glyoxal in methanol with a catalytic amount of acid leads to the rapid precipitation of the

diazabutadienes. Subsequent addition of bisimines and paraformaldehyde in the presence of hydrogen chloride affords symmetrical imidazolium salts with bulky N,N'-substitutions.³⁶⁻³⁸ **I-3** used chloromethylalkyl ethers as the cyclization component. This route was applied to the synthesis of imidazolium with very bulky substitutions such as 2,6-terphenyl group.^{35,39-41} Microwave-assisted method **I-4** starting from 1,2-diketones and urotropine in the presence of ammonium acetate, enables the synthesis of 4,5-substituted imidazoles.⁴² This synthetic strategy offers a new perspective for the rapid synthesis of diverse substituted imidazoles, which can be further utilized for the synthesis of imidazolium salts following the strategy **II**.

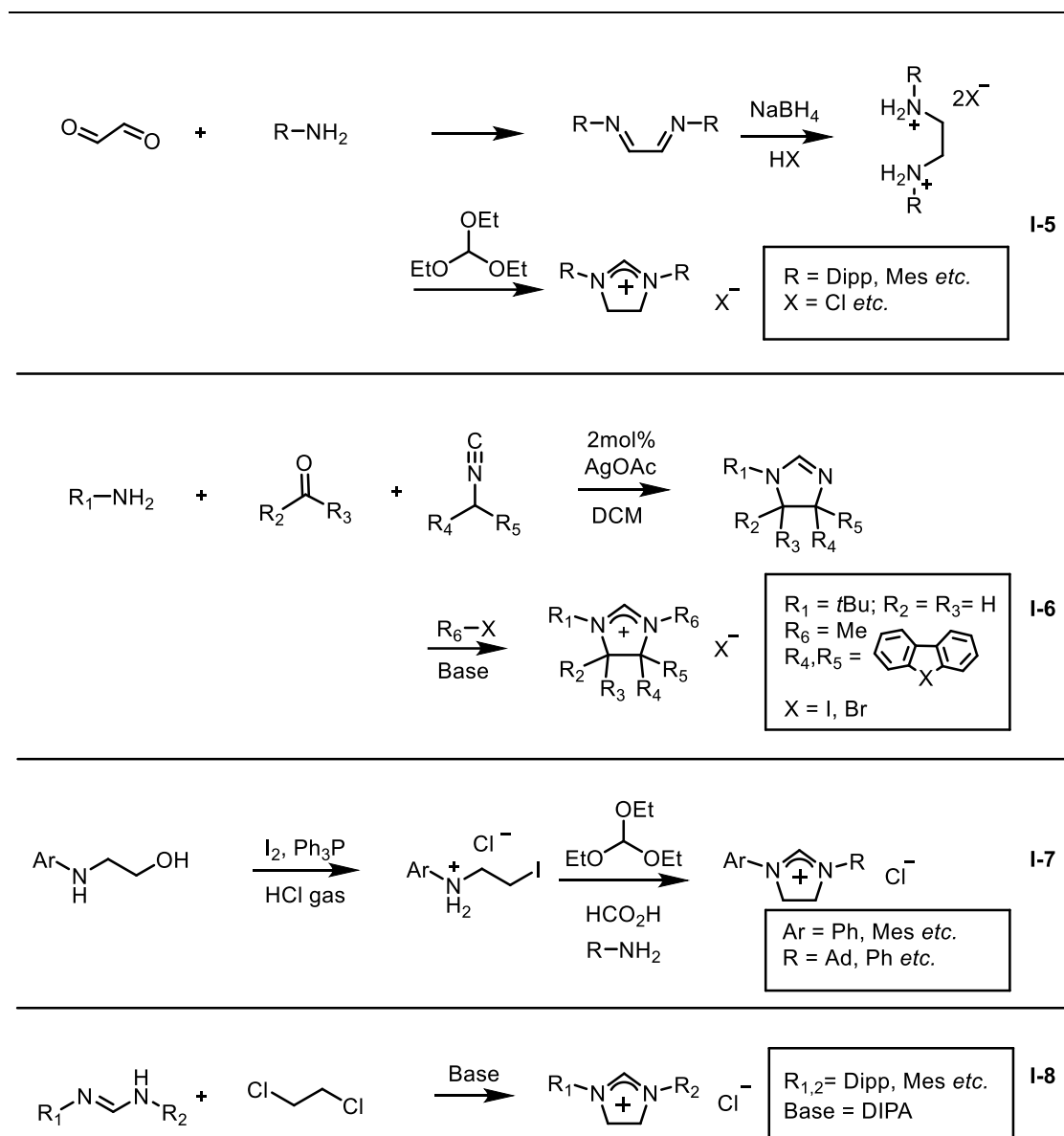


Scheme 4. Synthesis of imidazolium NHC precursors *via* alkylation of the parent heterocycles.

Following strategy **II**, N,N'-substituted azolium salts could be obtained by alkylation of the nitrogen atoms of imidazole with alkyl halide in the presence of base (**Scheme 4, II-1 and II-3**).³⁸ However, systems with sterically demanding substituents are generally not feasible *via* these simple substitution reactions,

cyclization strategy is generally more applicable.³⁴ Unsymmetrically substituted imidazolium salts can be synthesized with multi-component cyclization method, and by stepwise reaction with different alkyl halides (**II-2**). In addition to the base assisted alkylation, copper-catalyzed Ullman-coupling reaction can produce aryl imidazolium salts in good yields from N-substituted imidazoles and diaryliodonium salts.⁴³

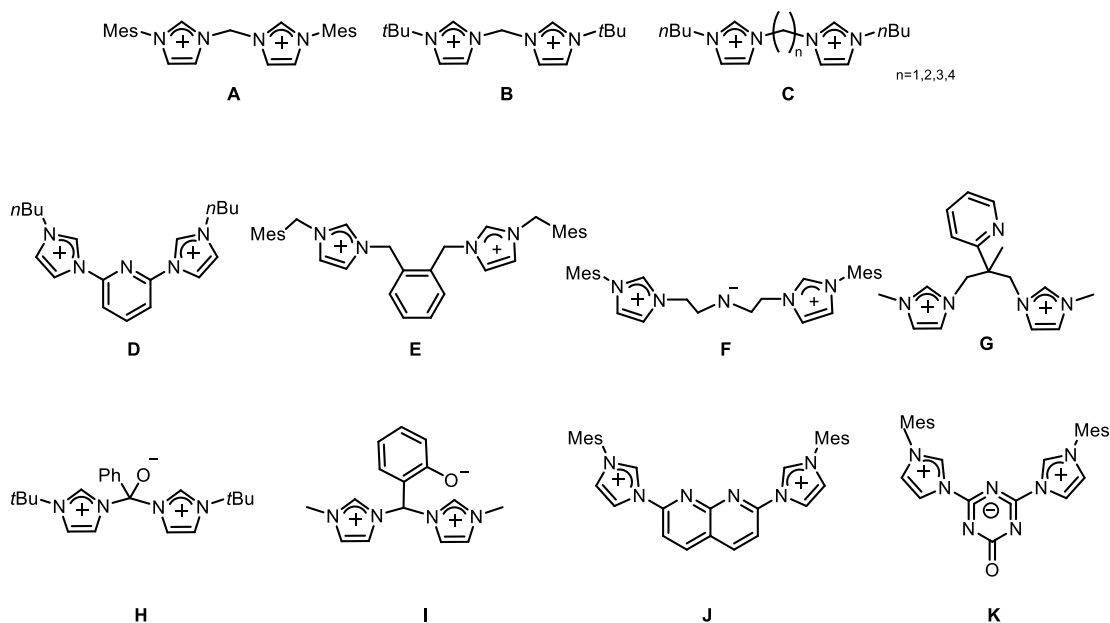
Imidazolinium salts are frequently used in Grubbs catalysts.¹⁷ They are generally obtained with modified methods for imidazolium salts, examples of the cyclization strategy are briefly introduced in **Scheme 5**: The **I-5** synthetic route starting from glyoxal reported by Arduengo *et al.* is a convenient method to get imidazolinium salts with sterically demanding substitution groups.^{35,44} Modular synthetic protocol developed upon this route offers chiral and achiral alkyl, as well as bulky substituted imidazolinium salts;^{45,46} Multi-component route **I-6** leads to unsymmetrical imidazolinium salts. The one-pot condensation reaction between amines, aldehydes and isocyanides with silver acetate catalyst reported by Orru *et al.* is particularly interesting for the synthesis of imidazolinium salts with C4, C5 backbone modifications;⁴⁷⁻⁴⁹ Another route **I-7** towards unsymmetrical imidazolinium salts starts from the amino alcohol with iodo-amine intermediate provides an expedient route to a variety of symmetrical, unsymmetrical, and chiral imidazolinium salt with high compatibility;^{45,46,50} Route **I-8** presented by Grubbs and Kuhn involves formamidine reactions with dichloroethane and a base.⁵¹ Numerous imidazolinium chlorides could be obtained along this route in excellent yields with simple purification.⁵¹



Scheme 5. Synthesis routes toward substituted imidazolium salts.

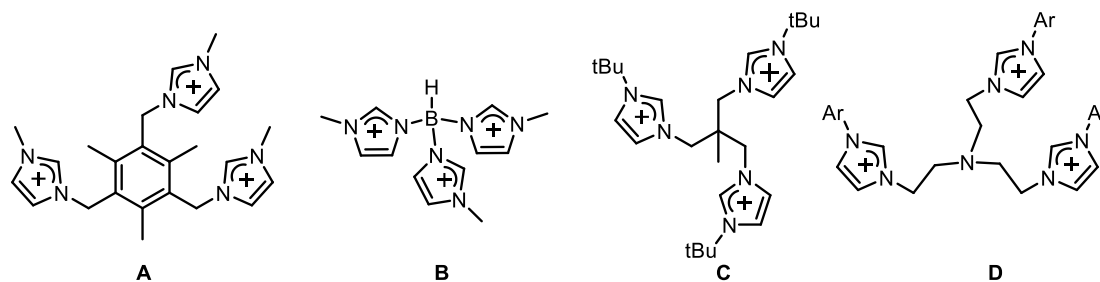
Structural-versatile basic azolium salts can serve as rigid, cationic building blocks in large poly-NHC frameworks. The simple methylene-bridged bis(imidazole) entities reported by Herrmann *et al.* were generated by reacting N-alkylimidazole with dibromomethane.⁵² Bis(imidazole) with longer ethylene, propylene and butylene bridges was later reported by Crabtree and Peris *et al.*⁵²⁻⁵⁵ (Scheme 6 A, B, C) This synthetic strategy consists of a direct reaction between N-alkylimidazole and an alkyl bridge entity which could be easily modified by introducing groups both in the bridging alkyl chain and N-substituents. In this way, the electronic properties, bite angles, chirality and

fluxional behavior of ligands could be finely tuned.⁵²⁻⁵⁵ Many bis-NHCs are developed in this fashion to obtain certain functions, for example, high stability due to the chelating effect in homogeneous catalysts by Peris *et al.*⁵⁶ Other examples are listed in **Scheme 6 D**⁵⁶, **E**⁵⁷, **F**⁵⁸, **G**⁵⁹ and **H** to **K**⁶⁰⁻⁶³ demonstrate the versatility of this type of dicarbene precursors in constructing poly-NHC ligands with different structural parameters.



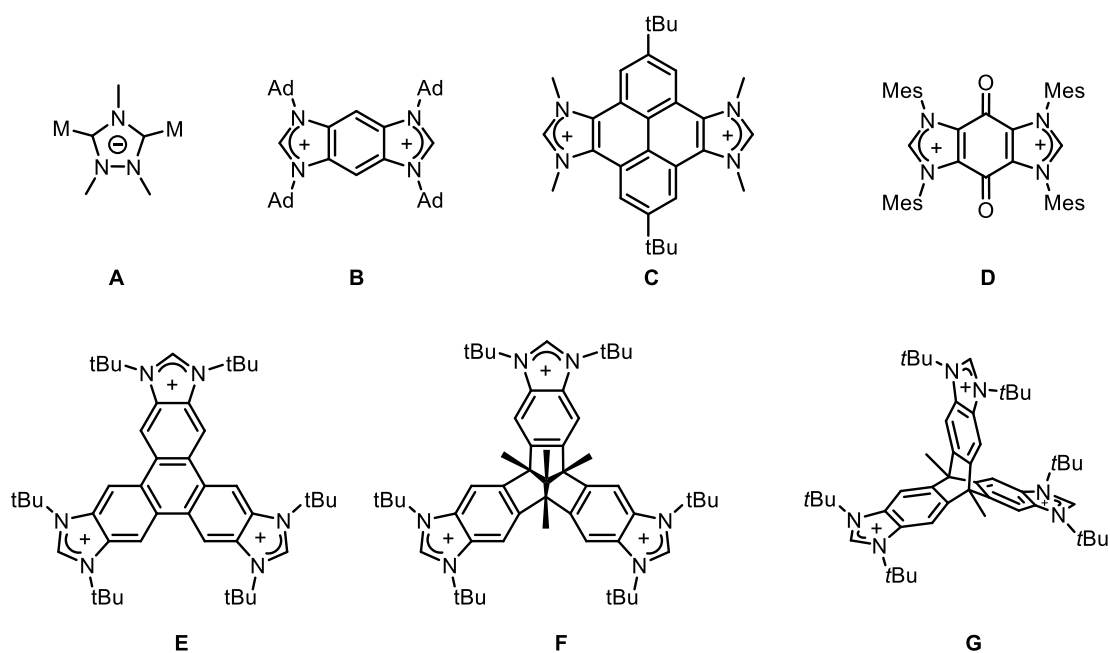
Scheme 6. Examples of chelating bis-NHC ligand precursors **A**⁵², **B**⁵³, **C**^{54,55}, **D**⁵⁶, **E**⁵⁷, **F**⁵⁸, **G**⁵⁹, **H**⁶⁰, **I**⁶¹, **J**⁶², **K**⁶³ with different bridging units.⁵²⁻⁶³

More complicated tridentate poly-NHC ligand precursors can be obtained either by adding donor function on the bridging part or by introducing tripodal bridges. In the latter method, tripodal triscarbene ligands featuring a central connection group (carbon, amino or borate) have been explored as tripodal (fac) topology is significant in determining the catalytic properties of the complex.^{64,65} The first discovery of tridentate poly-NHC is reported by Rasika Dias and Jin.⁶⁶ Representative structures of tripodal triscarbene ligand precursors are summarized in **Scheme 7**.



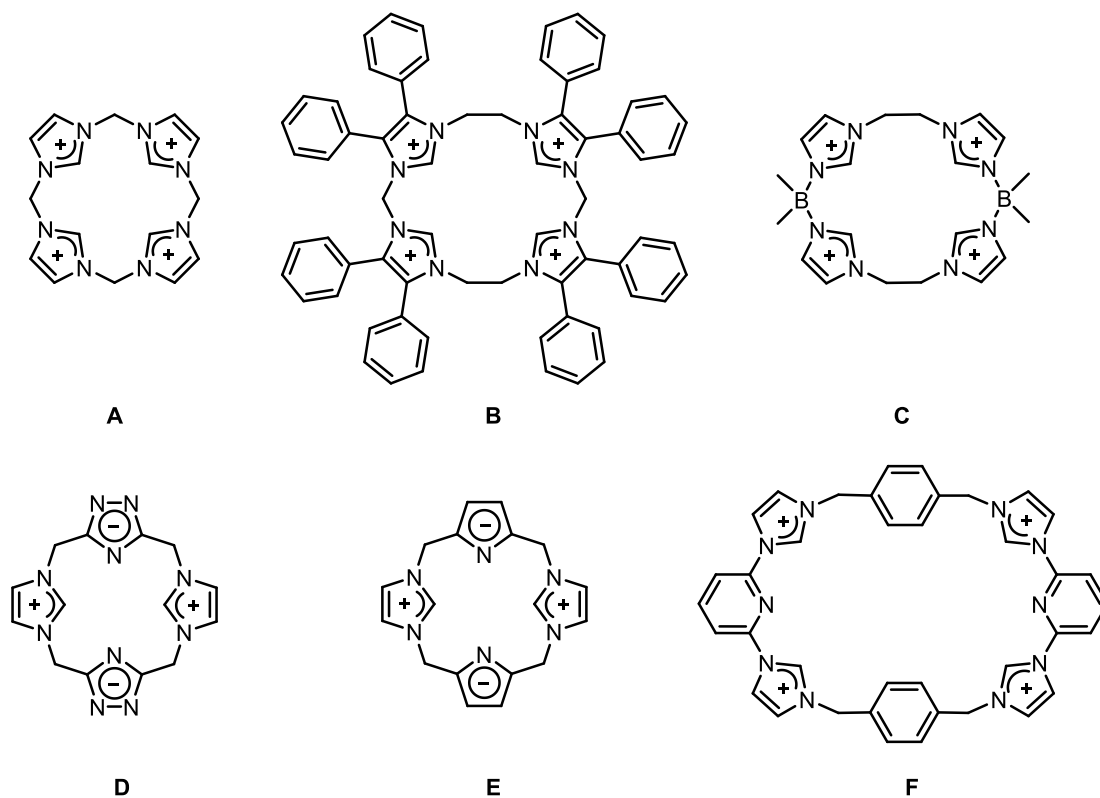
Scheme 7. Examples of chelating tris-NHC ligand precursors **A**⁶⁶, **B**^{67,68}, **C**⁶⁹, **D**⁷⁰.

“Janus-type” ligands is another important class of poly-NHC ligands featuring electronic communications between two linearly opposed NHC moieties. Bielawski and coworkers described this series of benzobis(imidazolylidene)s as NHC ligands in 2005-2006.⁷¹⁻⁷⁴ Peris *et al* demonstrated the simplest Janus-type ligand 1,2,4-trimethyltriazolium tetrafluoroborate (**Scheme 8, A**) which bridges between two metallic centers, with lower electron-donating ability than any known NHCs.^{75,76} However, the interest in this type of poly-NHC ligands stems mainly from their unique structures. Their conjugated bridging makes the electronic communication of two metal centers possible, which was hardly observed with other ligands.⁷⁷ Since then, these π -delocalized aromatic systems have gained increasing attention. In addition to the planar di-NHCs⁷⁷⁻⁸⁰, tri-NHCs Janus ligand (**Scheme 8, E, F**) and the three-dimensional Cerberus ligand **G** was subsequently reported by Bielawski.⁸¹ However, complexes of the 3D Cerberus ligand were rarely reported, further investigations are required for its applications.^{81,82}



Scheme 8. Examples of di - NHC ligand precursors **A**^{75,76}, **B**⁷¹, **C**⁷⁷, **D**⁸³ and tri-NHC ligand precursors **E**⁸², **F**⁸⁴, **G**^{81,82} from Peris and Bielawski.^{71-74,81}

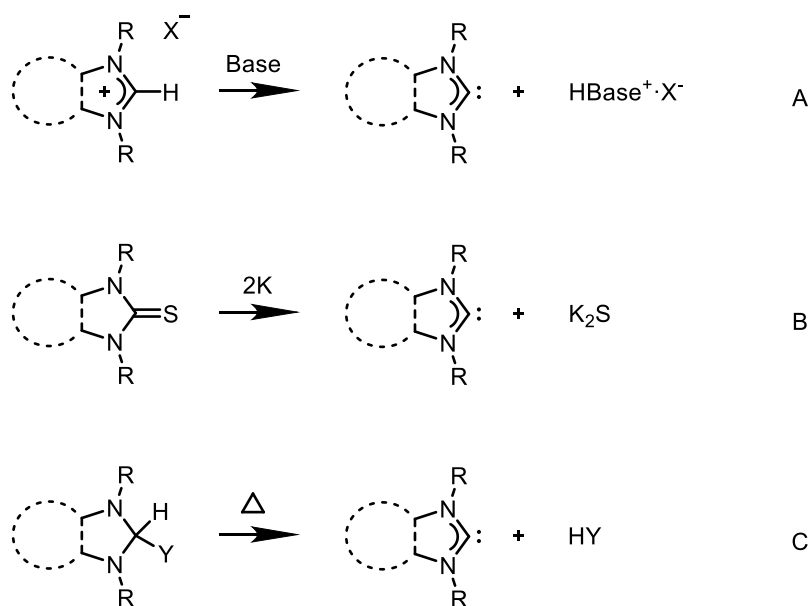
Macrocyclic ligands are known to form extremely robust complex structures due to the synergistic effect of both kinetic and thermodynamic stabilization.^{85,86} However, macrocyclic ligands featuring NHC donor groups have been rarely reported until recently. Method for the synthesis of bis(imidazole) in **Scheme 6** was adapted by groups of Kühn⁸⁷ and Jenkins⁸⁸ to synthesize tetracarbene ligand precursors **A** to **C**, **Scheme 9**. It is worth mentioning that **A** was initially synthesized by Kim and coworkers.⁸⁹ Kim and coworkers reported the calix[*n*]imidazolium ring structure makes **A** a good anion receptor,⁸⁹ then Kühn and coworkers investigated the coordination carbene chemistry with **A**.⁸⁷ When reacting the bis(imidazole) entity with alkyl bis(trifluoromethanesulfonates) with different chain lengths or bromodimethylborane, bridged tetraimidazolium salts **A**, **B**, **C** can be obtained. Triazole/pyrrole/benzene/pyridine units can also be used to form hybrid cyclophane **D**, **E**, **F**, **Scheme 9**. This small selection underlines the versatility of macrocyclic NHC ligands, their potentials as scaffolds to construct multiple dimensional supramolecular frameworks will be discussed in detail in Section 2.3.



Scheme 9. Examples of potential macrocyclic NHC ligand precursors **A**⁸⁷, **B**⁸⁸, **C**⁸⁸, **D**⁹⁰, **E**⁹¹, **F**⁹², there is no reported metal complex of **E** until June 2021.

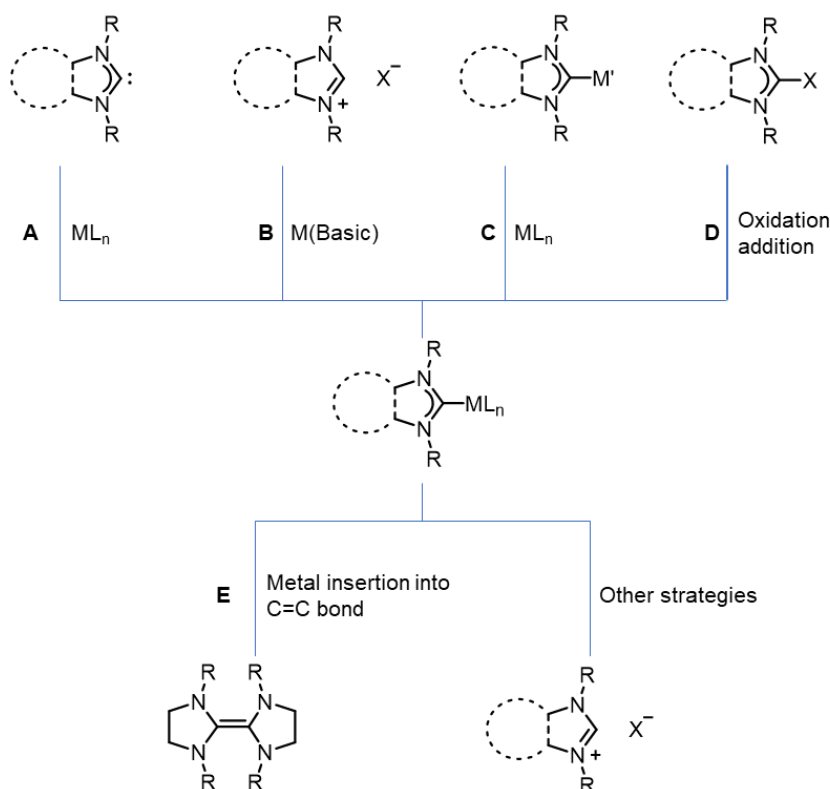
1.3.2 Synthetic Approaches towards Metal N-heterocyclic Carbene Complexes

Free carbenes can be accessed via deprotonation at the C2 position of different types of imidazolium, imidazolinium and benzimidazolium salt. The pioneer in this field, Arduengo, demonstrated the first successful free NHC synthesis with sodium hydride in THF in the presence of catalytic amounts of dimethyl sulfoxide, known as the Arduengo method.⁹ Potassium hydride, sodium hydride and potassium *tert*-butoxide are often used as bases (**Scheme 10, A**).^{35,93} This deprotonation method was later supplemented by Kuhn, who introduced the reductive desulfurization of thiones with potassium metal for the preparation of stable imidazolylidenes (**Scheme 10, B**).⁹⁴ Another method to obtain stable N-heterocyclic carbenes (imidazolidinylidene) from various imidazolidines is thermally induced α -elimination reactions (**Scheme 10, C**).^{95,96} Some imidazolinium salts bearing bulky N substituents or triazoliums could not be deprotonated with base, but can be utilized to get free carbene via thermally induced α -elimination (Scheme 10 C).⁹⁵



Scheme 10. Illustrations of selected synthetic strategies to obtain free carbene.^{35,93-96} Dashed circles and lines are used to represent possible aromatic structures and saturated/unsaturated heterocycles.

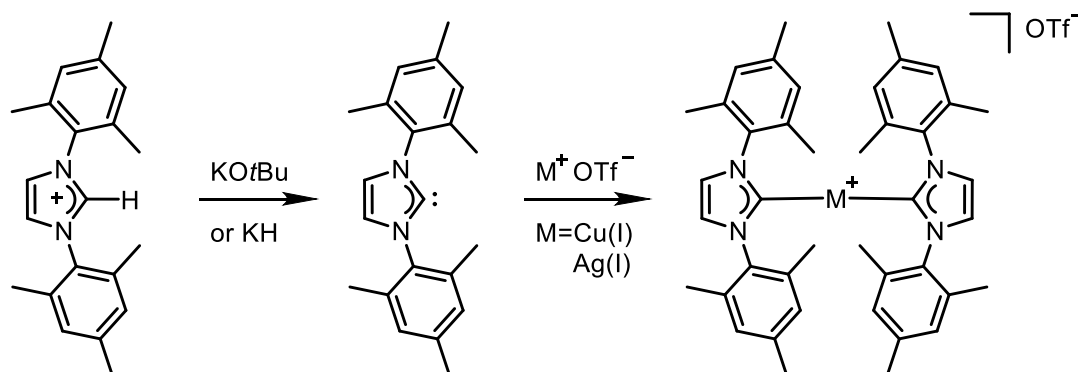
N-heterocyclic carbene complex has been described for all transition metals in various oxidation states.³⁰ Various methods of synthesizing complexes have been reported. The main synthetic routes leading to the formation of N-heterocyclic carbene complexes are depicted in **Scheme 11**. The most popular routes are **A**, **B** and **C**. Route **A** consists of generating the free carbene followed by coordination to a metal center. Method **B** generates the free carbene *in situ* by using a base in the presence of metal precursor, leading to the coordination of the NHC. Method **C** employs a carbene transfer reagent that can generate the NHC complex, then the intermediate complex undergoes a transmetalation reaction to afford the desired NHC-metal complex. Method **D** consists of a C–X bond activation at C2 position *via* oxidative addition, which demonstrates a useful method to get low-valence metal complexes. Route **E** was popular in the early stage of NHC researches, it consists the formation of imidazolidinylidene complexes by C=C bond activation of the dimerized imidazolidinylidene. As the interest in efficient synthesis is increasing in recent years, new methods to synthesize NHC complexes will also be discussed in this section.



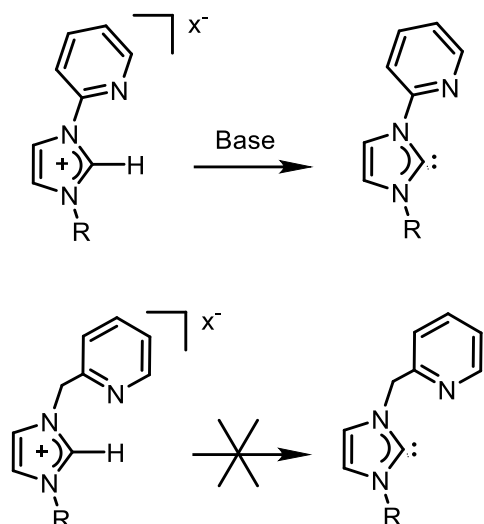
Scheme 11. Main synthetic strategies for the formation of NHC complexes.

1.3.2.1 Free Carbene Route

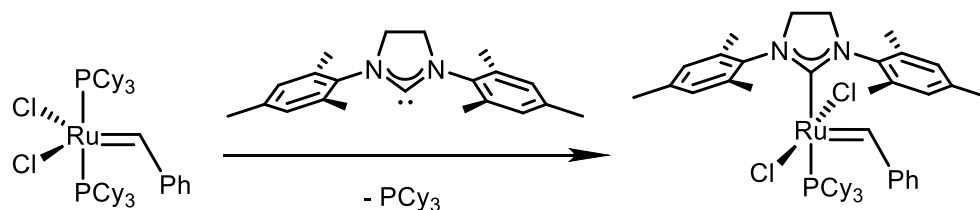
Reacting pre-formed free carbene with metal precursors can yield organometallic NHC complexes. **Scheme 12** shows an example of this synthesis route, the free carbene was generated *via* deprotonation reaction by potassium hydride or potassium *tert*-butoxide. Subsequently, the isolated free carbene was reacted with Cu/Ag triflates to offer corresponding complexes.⁹⁷ This method has been applied successfully for other metals including Ni, Pd, Ir, etc.^{35,68,93,98,99} However, this method requires careful control of reaction conditions. Basic condition required to generate free carbene can also lead to the undesired deprotonation of other acidic protons in the ligand. This occasionally triggers the decomposition of the ligand system, particularly in ligands where methylene groups are α to the nitrogen atoms on the N-heterocyclic carbene (**Scheme 13**).¹⁰⁰⁻¹⁰⁶ Glovebox technique is usually required when the free carbene is not air-stable.¹⁰⁷



Scheme 12. Free carbene route towards NHC complexes.⁹⁷

Scheme 13. Attempts to obtain free carbenes.¹⁰⁰⁻¹⁰⁶

The metal precursor in this free carbene route can be complexes beside metal salts. The precursor should bear ligands that can be easily replaced by the NHC, e.g., phosphines, cyclooctadiene, carbonyl or dimethyl sulfide.¹⁰⁸⁻¹¹⁰ Exemplarily, Grubbs *et al.* used the *bis*-phosphine olefin metathesis catalyst to react with free N-heterocyclic carbene to generate a more thermodynamic stable N-heterocyclic carbene complex (**Scheme 14**).¹⁸ Both classical (Fischer- and Schrock-type) and N-heterocyclic carbene complexes could be found in this family of Ru complexes, which makes them excellent benchmark structures for both types of carbenes.¹¹¹⁻¹¹³ The metal carbene bonds are rather long (~210 pm) for N-heterocyclic carbene complexes, while in Fischer- and Schrock-type complexes these distances are significantly below 200 pm due to the pronounced π backbonding (double bond for metal-carbene bonding).¹² This proves that NHC is analog to other σ -donor ligands like phosphine in terms of their coordination chemistry and metal-binding properties.¹²



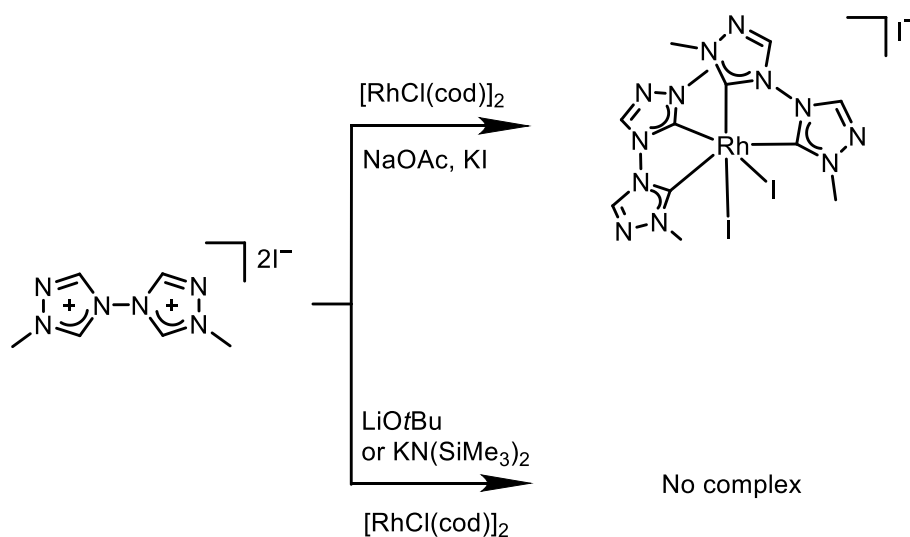
Scheme 14. Example for synthesis of NHC complexes from bis-phosphine metal precursor.

1.3.2.2 External Base Route

An alternative method in the synthesis of the N-heterocyclic carbene complex is *in situ* deprotonation of the pro-ligand in the presence of a metal complex. This *in situ* deprotonation-coordination route does not require the isolation of free carbene in the free carbene route, therefore simplifies the reaction work-up. The base could either come from an external source, or from basic ligands of metal complex.

Several strong bases used in the free carbene route are also used in this route. NaH, *n*BuLi, KO*t*Bu, NaOEt, and non-nucleophilic MN(SiMe₃)₂ (M=Na/K/Li) are among the most widely used bases. The use of the strong base ensures a complete deprotonation of the NHC pro-ligands. However, the strong base often requires inert conditions and low temperature to avoid unwanted activation/undesired side reactions of pro-ligands. To overcome these drawbacks, weak bases are often used to proceed deprotonation under less basic conditions. NEt₃, Cs₂CO₃, and NaOAc often serve as weak external bases devoted to the synthesis of Au, Ni, Pd, Cu, Ag-NHC complexes. Peris, Crabtree and coworkers have proven these bases are efficient for the synthesis of a series of catalytic-active Rh,^{54,56,61,114-120} Ir,¹²⁰⁻¹²⁶ and Ru^{55,127} NHC complexes under mild conditions. In some chelating NHC systems, it is important to use weak bases.¹²⁸ **Scheme 15** demonstrated the synthesis route from triazolium precursor salt to 1,1'-dimethyl-4,4'-bi-1,2,4-triazol-5,5'-ylidene Rh complex, one of the simplest possible chelating tetracarbene Rh complex.¹¹⁹ As depicted in **Scheme 15**, the precursor salt reacts with [RhCl(cod)]₂ in MeCN in the presence of the mild base NaOAc to give the bis-chelating complex. When the strong bases *t*BuOLi or KN(SiMe₃)₂ are used in synthesis, the triazolium precursor salt could not be transferred to complexes. Instead, the triazole precursor undergoes an unexpected rearrangement in the strong basic condition in the absence of metal precursor, which proves the importance of

using weak rather than strong bases in combination with bis(triazolium) salts.¹²⁹



Scheme 15. Base effect in the synthesis of bis-chelate Rh(III) complexes.¹¹⁹

In this regard, it is meaningful to compare the pK_a of base and C2-H acidity of corresponding NHC precursors. Streitwieser and Yates studied the basicity of NHCs experimentally^{130,131} and theoretically¹³² in different solvents. The pK_a values of these prementioned weak bases are lower by several orders of magnitude compared to the pK_a of the NHC precursors, and therefore their deprotonation should not occur.¹²⁸ Despite the unmatched pK_a , the use of excessive base and elevated temperature, as well as the formation of a thermodynamic favored metal carbene bond leads to the continuous removal of nascent free NHCs from the equilibrium and thus the reaction is driven to the product side.¹²⁸

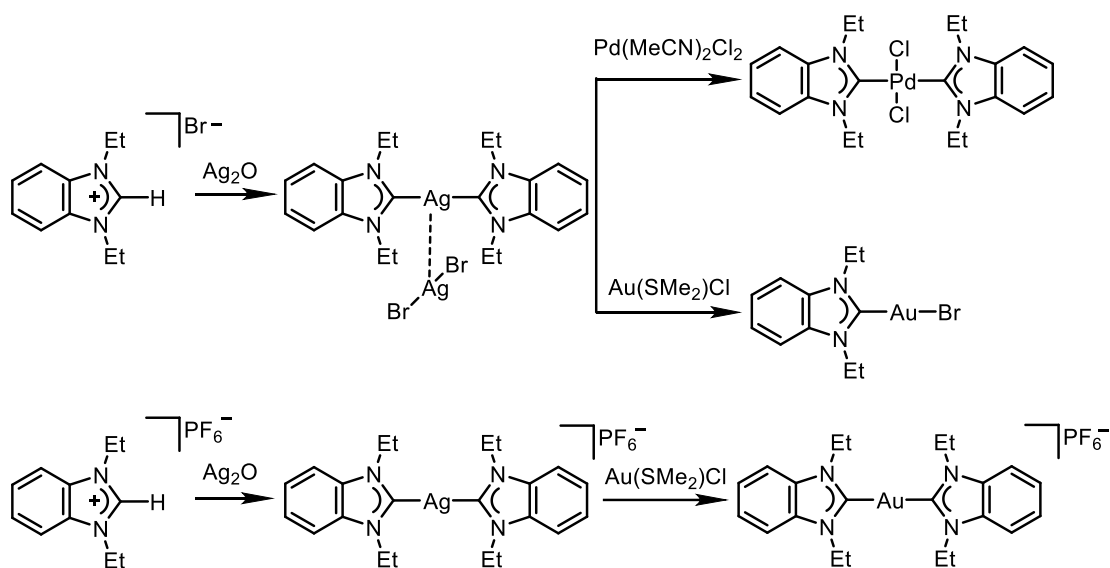
Deprotonation with liquid ammonia or mixtures of liquid ammonia with organic amines or polar-aprotic solvents was introduced by Herrmann in 1996.¹³³ The liquid ammonia exhibits excellent solubility towards singly charged ionic and aromatic compound as it promotes hydrogen bonding, and this route enables the synthesis of imidazolynylidenes bearing linear, branched, cyclic, heteroatom-substituted (O, N, P) and chiral hydrocarbon residues, which are not accessible through known methods at that time.¹³³

The use of two reactants (metal precursor + base) usually results in the

formation of by-products as compared to only one reactant in the case of an internal base. Some common metal complexes, such as salts with acetate, alkoxide, hydride and carbonate as the anion, are frequently used. In fact, utilizing $\text{Hg}(\text{OAc})_2$ and $[\text{CrH}(\text{CO})_5]^-$ as metal precursor, first discovered NHC complexes were obtained along this method by Wanzlick and Öfele (see **Scheme 1**).^{4,5}

1.3.2.3 Transmetalation Route

Herein, a variety of silver bases such as Ag_2O , AgOAc , and Ag_2CO_3 must be mentioned. When attempting to look for the possible ligand-unsupported $\text{Ag}(\text{I})$ - $\text{Ag}(\text{I})$ interactions in silver compounds in 1998, Lin and Wang used AgBr and Ag_2O as metal precursors for preparing silver NHC complexes from imidazolylidene.¹³⁴ The route from AgBr requires NaOH as an external base and a phase transfer catalyst $[\text{Bu}_4\text{N}]\text{Br}$ to process. The more convenient method is to treat N,N' -diethylbenzimidazolium salt with Ag_2O , which serves as a mild base, to yield the $\text{Ag}(\text{I})$ complexes in high yield (see **Scheme 16**).¹³⁴ Subsequently, the $\text{Ag}(\text{I})$ complexes can be used as carbene transfer agents for the synthesis of other transition-metal carbene complexes. This route is a valuable way for obtaining carbene complexes as it avoids the water and oxygen-free reaction conditions required in conventional base deprotonation methods. Its simple workup and mild reaction condition has made it popular for laboratory gram scale reactions for years.¹³⁵ In a typical transmetalation reaction, metal complex (usually with halide) is added to $\text{Ag}(\text{I})$ NHC complex, the lability of the $\text{Ag}-\text{C}_{\text{NHC}}$ bond and the low solubility of the silver halide promote the reaction equilibrium moves to the product side. The successful synthesis of NHC complexes with a variety of metals such as Cu , Ni , Pd , Pt , Rh , Ir , and Ru has proven the versatility of this route.¹³⁶



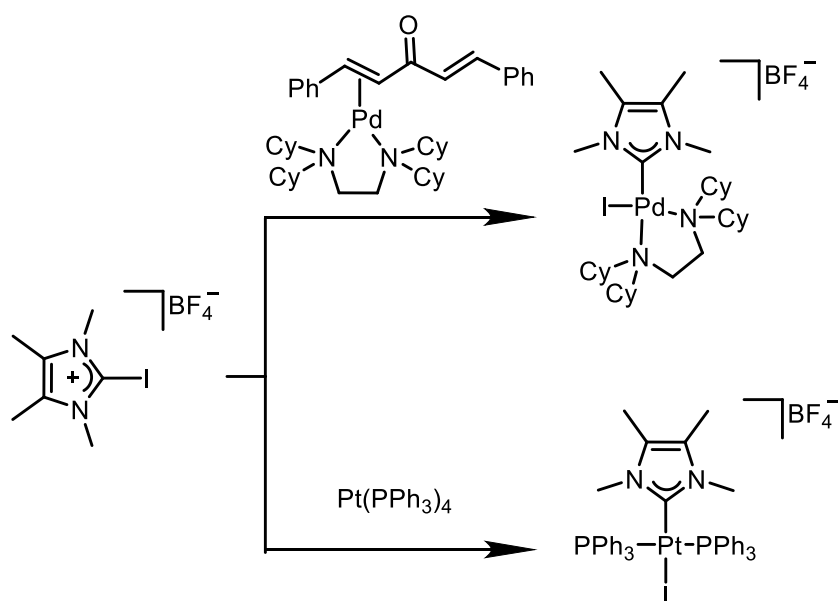
Scheme 16. Synthesis routes of Ag(I) NHC complexes and different transmetalation products.¹³⁴

Despite the convenience of execution, these transmetalation reactions from silver NHC complexes suffer from poor atom economy and can only be considered in large scale applications when the Ag byproducts can be recycled.¹³⁴ Under this manner, Cu₂O was used for its cheaper price.¹³⁷ Research on this carbene transfer agent is still in the early stages, a small range of transition metals complexes such as Au, Pd, Ni, Ir and Rh complexes synthesized from Cu₂O have been reported.^{138,139}

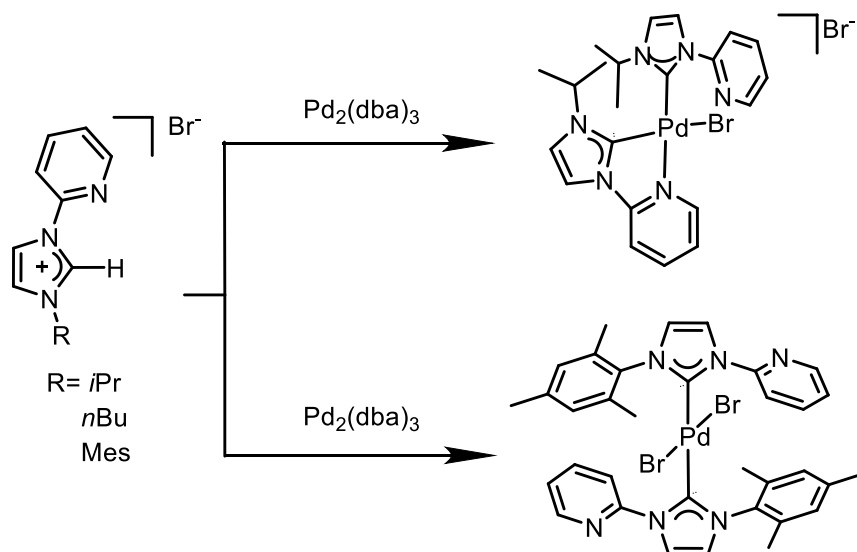
1.3.2.4 Oxidative Addition Route

In some cases, the metalation of the imidazolium precursor occurs without the use of a base via the oxidative addition of the C2-X bonds (X = halogen^{140,141}, S¹⁴², Me¹⁴³ and H^{143,144}) to a low-valence metal complex. This method was studied by Stone and coworkers in 1973 with 2-chloro-methylthiazolium salt.^{143,144} After almost 30 years, Cavell and Yates extended the selection of precursors to 2-iodo-imidazolium and studied the oxidative addition process of 2-halogen imidazolium, 2-H imidazoliums and 2-alkylimidazoliums to group 10 complexes (**Scheme 17**). This study showed for the first time that oxidative

addition method to get NHC complexes is possible.¹⁴⁵ In the same year, oxidative addition of C2-H bonds of imidazolium salts to low valent metals was first observed by Nolan and coworkers, they proposed an NHC-Pd-H intermediate in the catalytic cycle of the dehalogenation of aryl halides with $\text{Pd}(\text{dba})_2$ in the presence of imidazolium salts.¹⁴⁶ Crabtree and Faller reported another sample of this approach months later. The reaction between a pyridine-imidazolium salt and $\text{Pd}_2(\text{dba})_3$ afforded the preparation of bis NHC Pd(II) complexes by C2-H oxidative addition (**Scheme 18**).¹⁴⁷ More recently, Hahn and coworkers reported that neutral 2-chloro-substituted benzimidazoles can also undergo oxidative addition to transition metal complexes, which provides facile alternatives for the synthesis of complexes bearing protic NH-NHC ligands.^{148,149}



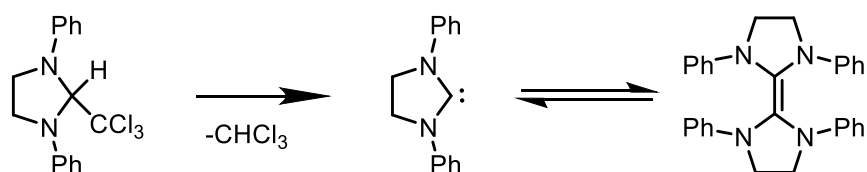
Scheme 17. Oxidative addition of 2-iodo-imidazolium to Pt(0) and Pd(0) complexes by Cavell and Yates.¹⁴⁵



Scheme 18. Examples of oxidative addition route to palladium(0) NHC complexes from N-(2-pyridyl)imidazolium salts.¹⁴⁷

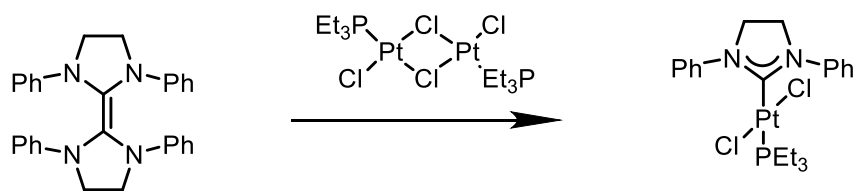
1.3.2.5 Metal Insertion into C=C Bond and Other Strategies

In the pursuit of free carbene, Wanzlick proposed the synthetic route in **Scheme 19**. Tetraaminoethylene was obtained by an α -elimination of chloroform from 1,3-diphenyl-2-(trichloromethyl)imidazolidine. He assumed there is an equilibrium between tetraaminoethylene and carbene.¹⁵⁰⁻¹⁵² This postulation was subsequently confirmed from an experimental and theoretical point of view.¹⁵³⁻¹⁵⁶



Scheme 19. Equilibrium between free carbene and tetraaminoethylene.¹⁵⁰⁻¹⁵²

Tetraaminoethylene heated with metal precursors can provide corresponding NHC complexes. **Scheme 20** demonstrates the first Pt-NHC complex generated from this method. Mn, Fe, Ru, Cr, Co, Ni and Rh-NHC complexes were also reported, proven the success of this method.¹⁵⁷⁻¹⁶⁰

Scheme 20. First Pt(II) complex synthesized from enetetramine.¹⁶¹

The electro-synthesis of NHC complexes has been receiving increasing attention recently for its atom economy and easy workup.^{162,163} The procedure has rarely been used in the preparation of NHC complexes, only Cu,¹⁶² Ni,¹⁶² and Au¹⁶³ have been reported, but a clear synthetic application can be envisaged. A carboxylates-mediation method described by Crabtree and coworkers is worth mentioning, which utilizes imidazolium-2-carboxylates as highly efficient precursors to Rh, Ir, Ru and Pd-NHC complexes under very mild conditions.¹⁶⁴

1.4 Properties of N-heterocyclic Carbenes

1.4.1 Electronic Stabilization

N-heterocyclic carbenes have made a tremendous impact in the area of material chemistry^{165,166} and homogeneous catalysis¹⁶⁷. The main reason for its popularity is due to the myriad stereo-electronic properties, which not only allow easy preparation but also allow fine tuning for specific coordination needs. As introduced in section 1.1, when coordinated to a metal, the NHCs are generally considered to be strong σ -donor and weak π acceptor. However, it cannot be regarded as a subclass of Fischer type carbene: experimental evidence by Herrmann made it clear that Be(II) NHC complexes do not depend on the backbonding from the metal center.¹⁶⁸ At the same time, it cannot be considered as Fischer type carbenes, since in most cases the NHC exhibit a singlet ground-state electronic configuration.¹⁶⁹ Consequently, the N-heterocyclic carbons constitute their own class of nucleophilic singlet carbenes.

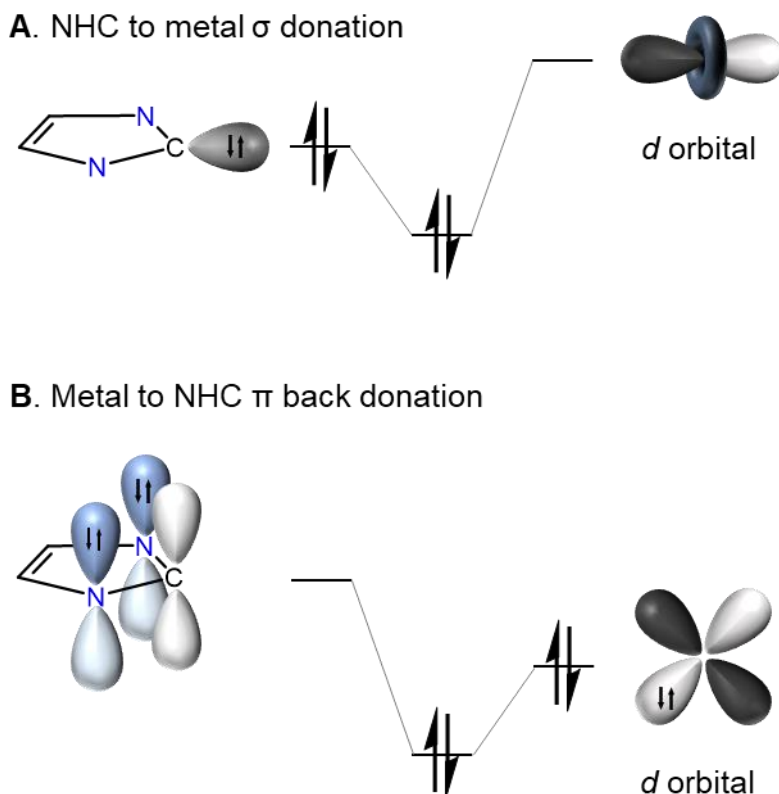


Figure 3. Illustration of **A** σ -bonding from the singlet carbene lone pair to the metal d orbital and **B** π -backbonding from metal d orbital to the empty orbital of the NHC ligand. Substitutions on nitrogen atoms are omitted for clearance.

The orbital contributions shown in **Figure 3** demonstrate the possible electronic interactions between metal and NHC ligand. In general, the σ -bonding predominate the M-NHC interactions,¹⁷⁰ however, some studies showed significant back donation also exists in NHC complexes.¹⁷¹⁻¹⁷⁸ For example, Tulloch reported that the $C_{\text{carbene}}\text{-Cu}$ distance was found shorter than the average C-Cu σ -bonds.¹⁷⁹ Structural evidence from Meyer and Frenking later suggested that electron-rich metal center is more likely to participate in π -backbonding.^{174,175}

1.4.2 pK_a values of Ligand Precursors

In the previous section, different routes to NHC complexes have been demonstrated. One of the key issues in synthesis is the deprotonation of pro-

ligands, which yield the desired NHC *in situ* or in isolated form. On the other hand, the basicity of NHCs was found to have a profound effect on catalytic activities.^{180,181} Hence, the pK_a values of NHCs are important in the design and synthesis of NHC complexes for catalysis and other applications.

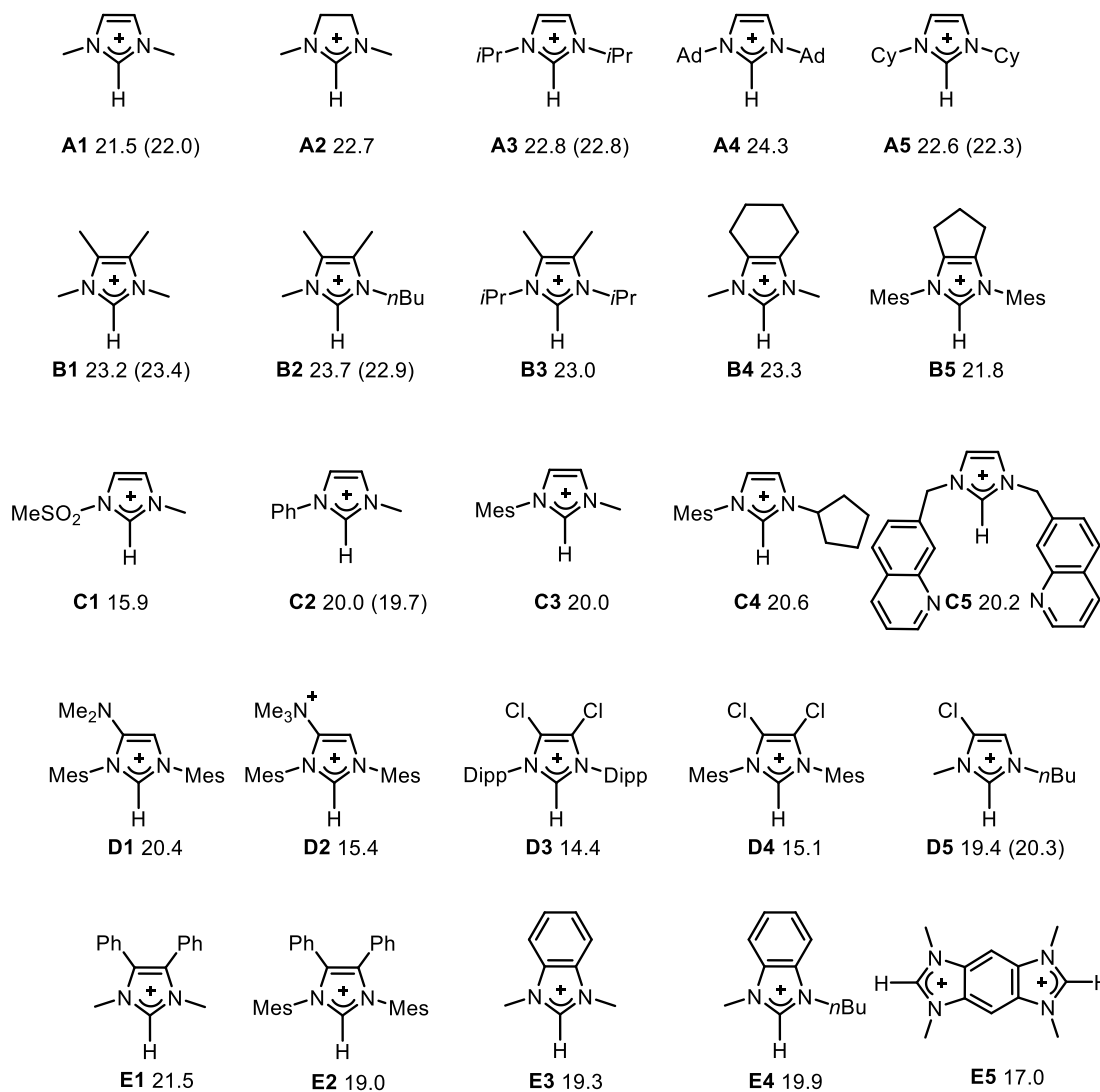


Figure 4. Selection of NHC precursors and their calculated pK_a values in DMSO,¹⁸²⁻¹⁸⁴ Values obtained from spectroscopic methods are included in bracket.^{181,185}

Figure 4 lists pK_a values of some selected NHC precursors.^{181,185} Some trends that arise from modification on N-substitution and backbone parts could be observed. Imidazolium salts are slightly more acidic than unsaturated imidazolinium salts (**A1** vs. **A2**). Flexible N-substitution Cy group shows little effect on the acidity (**A1** vs. **A5**), while bulky N,N'-substitutions (**A3** vs. **A4**) can

lead to larger attenuation in the acidity. The addition of methyl group in backbone position usually results in a decrease of ~1 unit (**B1**, **B2**, **B3**), but it seems the addition of cyclic alkyl chains (**B4**, **B5**) have the same degree of effect. The electron-withdrawing sulfonyl group (RSO_2) in **C1** dramatically increases the acidity, larger than aromatic N-substitution **C2-C5**. Mono/di-substitution of electronic withdrawing NMe_3^+ and Cl at backbone significantly increases the acidities of the corresponding salts (**D2** vs. **D1**, **D3** and **D4** vs. **D5**), which could be ascribed to the strong electron-withdrawing ability of halide. The benzimidazolium derivatives **E3**, **E4**, and dicarbene precursor **E5** are ca. 1.5- 4.5 pK units stronger than the parent imidazolium salts (**E3**, **E5** vs. **A1**), or non-conjugated phenyl substituted derivatives (**E3** vs **E1**), which might be due to the stabilization of the deprotonated species (NHCs) through the additional conjugation.

1.4.3 σ -Donation Properties of NHCs

pK_a is not the only parameter that can be tuned in the designing of NHCs. Donor strength of NHCs can also be modified through structural alteration such as variation of the groups attached to the NHC nitrogen atoms or backbone, change of unsaturation/size of the NHC ring, *etc.* In the search for quantitative measurement of donation ability of phosphine ligands, Tolman introduced an infrared (IR)-derived descriptor based on the pioneering work by Strohmeier¹⁸⁶ and Bigorgne¹⁸⁷. The infrared (IR) spectroscopic measurements on the highest CO stretch from tetrahedral nickel complex $[\text{Ni}(\text{CO})_3\text{L}]$ (L = ligand in question) were extracted and used as an indicator of ligand σ -donating ability.¹⁸⁸ The mechanism is straightforward, compared with weak σ -donating ligand, the strong σ -donating ligand can promote the electron-rich metal center to further increase the degree of π^* anti-bonding orbital into the CO ligands and thus reducing their bond order and stretching frequency. This IR-based descriptor

was named the Tolman electronic parameter (TEP) in the 1970s.¹⁸⁸ From the measurement for TEP in **Figure 5**, some trends can be observed.¹⁸⁹ The donor ability of saturated NHC is weaker than unsaturated NHC (**A1** vs **A2**). The TEP decreases as the size of the N-substitution group increases (**A1** vs. **A3**, **A4**, **A5**). Increasing NHC ring size from five-membered ring to six makes better donors (**C5** vs. **A1**). NHCs with extended π -systems (**B4**, **B5**) form weaker donors. The substitution at backbone positions of NHCs has a major effect on TEP, e.g., the donor power increases significantly in the order $R = \text{NO}_2 < \text{Cl} < \text{CO}_2\text{Me} < \text{H} < \text{Me}$. The triazolium based NHC **C4** is weaker in donor ability than **A1**, **A2**.

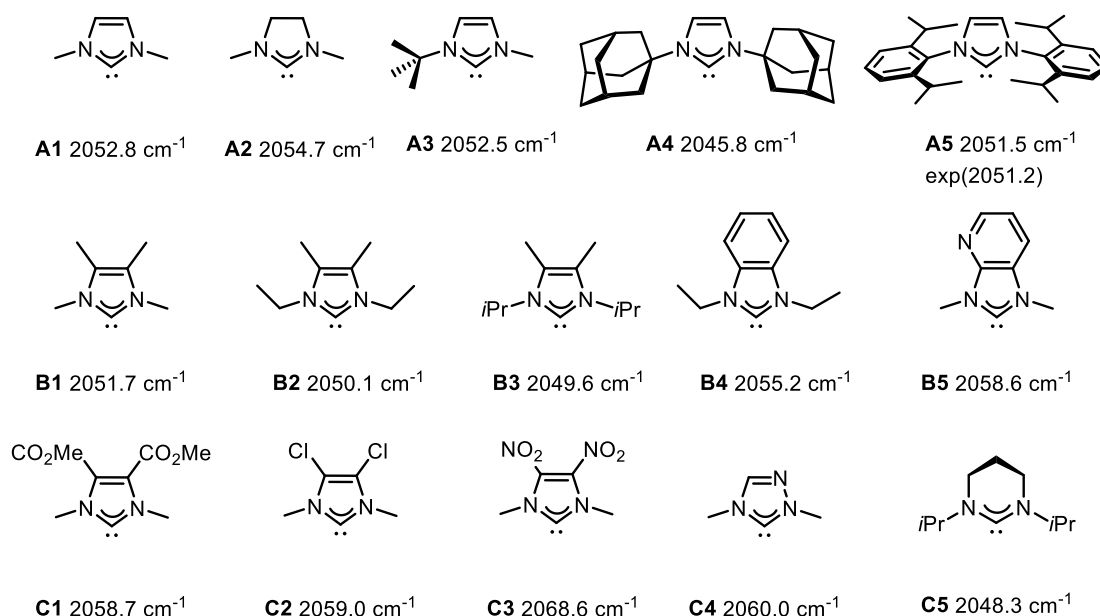


Figure 5. Selection of NHCs and their calculated gas-phase ν_{CO} derived TEP values, values obtained from spectroscopic methods are included in bracket.¹⁸⁹

Gusev and Peris introduced a calculated $\Delta(\text{TEP})$ descriptor as a measure of the electronic communication between two metal centers in dinuclear $\text{M-NHC-M}'$ complexes.¹⁹⁰ Such communication is often assessed through cyclic voltammetric measurements, this $\Delta(\text{TEP})$ based on DFT calculations provides an effective alternative to the electrochemical method.¹⁹⁰ However, TEP poses some limitations: the IR spectrum is highly solvent-dependent; the resolution of the IR spectrometer also has a large influence on the results.^{191,192}

Huynh's electronic parameter (HEP) is a σ -donating strength descriptor utilizes the $^{13}\text{C}_{\text{carbene}}$ NMR chemical shift. The easy-accessible $\text{trans-}[\text{PdBr}_2(\text{iPr}_2\text{bimy})\text{L}]^n$ is used as a spectroscopic probe to assess the σ -donating strength of NHCs, phosphines, isocyanides and classic Werner type ligands.^{193,194} Compared with IR spectroscopy based TEP or cyclic voltammetry, $^{13}\text{C}_{\text{carbene}}$ NMR data used by HEP offers superior accuracy.¹⁹⁵ These quantitative electronic descriptors provide many facilities for the design of NHC ligands, for example in the design of the fluorescent material rhenium(I) tricarbonyl chloride complexes with pyridine-functionalized N-heterocyclic carbenes $\text{Re}(\text{CO})_3(\text{L})\text{Cl}$, (L = 3-methyl-1-(2-pyridyl)imidazol-2-ylidene, 3-methyl-1-(2-pyridyl)benzimidazolin-2-ylidene), 1-methyl-4-(2-pyridyl)-1,2,4-triazoline-5-ylidene) an increase in the emission wavelengths in the order $\text{Re}(\text{CO})_3(\text{L}_{\text{triazolineylidene}})\text{Cl} > \text{Re}(\text{CO})_3(\text{L}_{\text{imidazolylidene}})\text{Cl} > \text{Re}(\text{CO})_3(\text{L}_{\text{benzimidazolinylidene}})\text{Cl}$ could be associated with the different electronic donor capacities of the NHCs.¹⁹⁶

1.4.4 Steric Properties of NHCs

From the trend of donor ability of different N-substituted NHC, we can see that the electronic and steric effects of NHCs are tightly related and difficult to separate.¹⁸⁸ In the research of phosphine complexes, Tolman developed the Tolman cone angle θ , which is measured with the metal at the vertex and the atoms at the perimeter of the cone.¹⁸⁸ Limited to its two-dimensional nature, this parameter was later proven insufficient for structurally elaborate ligands and complicated NHC systems.¹² Initially designed for the direct comparison of steric requirements of NHCs and tertiary phosphines, the "buried volume" parameter ($\%V_{\text{bur}}$) developed by Nolan, Cavallo and coworkers offers a more convenient descriptor for the quantified steric measurement.¹⁹⁷ The parameter is defined as the volume of overlapping between ligand atoms and a sphere

centered on the metal. The M-C_{carbene} length d was usually set to be 2 Å and the sphere radius r was set to 3 Å (see **Figure 6**). SambVca (Salerno molecular buried volume calculation) software developed by Cavallo and coworkers is now available online for easy calculation of the buried volume parameter.¹⁹⁹

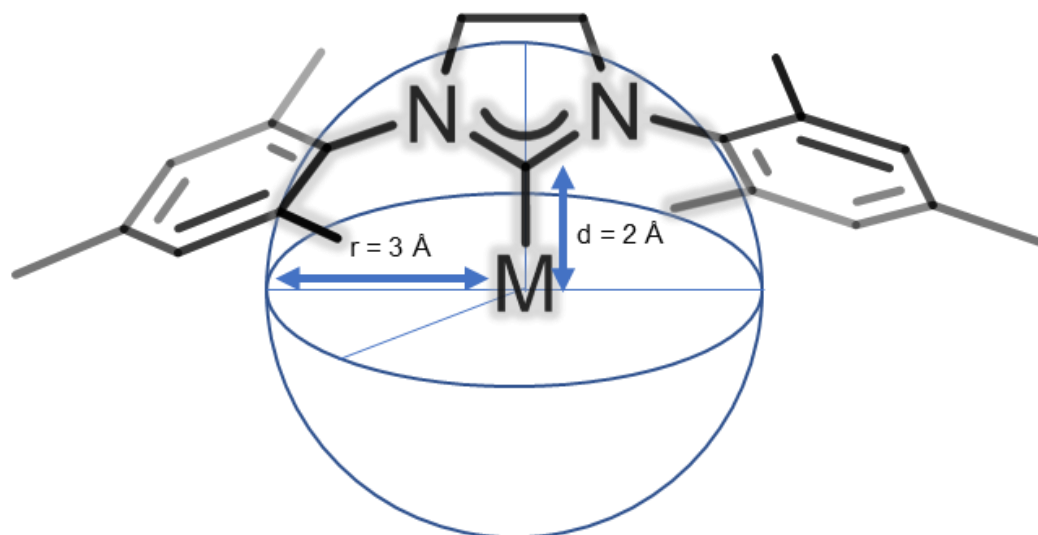


Figure 6. Illustration of buried volume parameter (% V_{bur}) by Nolan *et al.*¹⁹⁷

Interesting results could be found using the % V_{bur} as the steric descriptor. When relative M-C_{carbene} bond dissociation energy values of a range of metathesis catalysts ([Cp* $Ru(NHC)Cl$], Cp* = C₅Me₅) are plotted against buried volume % V_{bur} of their NHC ligands, a linear negative correlation could be observed.¹⁹⁷ In other words, the metal carbene bond strength is essentially controlled by the steric requirements % V_{bur} of the NHC ligands.

There are more descriptors available to facilitate the design and predict the properties of NHC ligands, for example, the Lever electronic parameter (LEP) introduced in 1990.^{200,201} Suresh and coworkers have published a substantial body of work focused on calculated molecular electrostatic potentials (MESP) from which both steric and electronic descriptors can be determined.^{202,203} These calculated methods avoid elaborate experimental measurements and associated limitations and, in particular, can be used for proposed ligands not yet experimentally available.

1.5 Conclusion of Chapter 1

The N-heterocyclic carbene (NHC) is a unique compound class in modern chemistry. In this chapter, the basic structure of NHCs was introduced, emphasizing the structural versatility and unique properties. From the synthetic point of view, the properties of NHCs can be fine-tuned by modifying the structure of its precursors. A section is devoted to the synthetic strategies developed for the formation of NHC precursors with structural variations, followed by introducing main pathways from NHC precursors to NHC free carbene and complexes with examples. The properties of N-heterocyclic carbenes were explained from the electronic and steric aspects, highlighting quantitative descriptors to assess them and the factors that predominantly influence these properties.

1.6 References of Chapter 1

1. W. von E. Doering and A. K. Hoffmann, *J. Am. Chem. Soc.*, 1954, **76**, 6162-6165.
2. E. Fischer and A. Maasböl, *Angew. Chem. Int. Ed. Engl.*, 1964, **3**, 580-581.
3. H. W. Wanzlick, *Angew. Chem. Int. Ed. Engl.*, 1962, **1**, 75-80.
4. H. W. Wanzlick and H. J. Schönherr, *Angew. Chem. Int. Ed. Engl.*, 1968, **7**, 141-142.
5. K. Öfele, *J. Organomet. Chem.*, 1968, **12**, P42-P43.
6. D. Cardin, B. Cetinkaya, M. Lappert, L. Manojlović-Muir and K. Muir, *J. Chem. Soc. D.*, 1971, **8**, 400-401.
7. B. Cetinkaya, P. Dixneuf and M. F. Lappert, *J. Chem. Soc., Dalton Trans.*, 1974, **16**, 1827-1833.
8. D. Cardin, B. Cetinkaya, E. Cetinkaya and M. Lappert, *J. Chem. Soc., Dalton Trans.*, 1973, **5**, 514-522.

9. A. J. Arduengo III, R. L. Harlow and M. Kline, *J. Am. Chem. Soc.*, 1991, **113**, 361-363.
10. A. Igau, H. Grutzmacher, A. Baceiredo and G. Bertrand, *J. Am. Chem. Soc.*, 1988, **110**, 6463-6466.
11. W. A. Herrmann, M. Elison, J. Fischer, C. Köcher and G. R. Artus, *Angew. Chem. Int. Ed. Engl.*, 1995, **34**, 2371-2374.
12. W. A. Herrmann, *Angew. Chem. Int. Ed.*, 2002, **41**, 1290-1309.
13. R. R. Schrock, J. S. Murdzek, G. C. Bazan, J. Robbins, M. DiMare and M. O'Regan, *J. Am. Chem. Soc.*, 1990, **112**, 3875-3886.
14. P. Schwab, M. B. France, J. W. Ziller and R. H. Grubbs, *Angew. Chem. Int. Ed. Engl.*, 1995, **34**, 2039-2041.
15. P. Schwab, R. H. Grubbs and J. W. Ziller, *J. Am. Chem. Soc.*, 1996, **118**, 100-110.
16. T. Weskamp, W. C. Schattenmann, M. Spiegler and W. A. Herrmann, *Angew. Chem. Int. Ed.*, 1998, **37**, 2490-2493.
17. L. Jafarpour, A. C. Hillier and S. P. Nolan, *Organometallics*, 2002, **21**, 442-444.
18. M. Scholl, T. M. Trnka, J. P. Morgan and R. H. Grubbs, *Tetrahedron Lett.*, 1999, **40**, 2247-2250.
19. E. L. Dias, S. T. Nguyen and R. H. Grubbs, *J. Am. Chem. Soc.*, 1997, **119**, 3887-3897.
20. M. S. Sanford, J. A. Love and R. H. Grubbs, *J. Am. Chem. Soc.*, 2001, **123**, 6543-6554.
21. C. Adlhart, C. Hinderling, H. Baumann and P. Chen, *J. Am. Chem. Soc.*, 2000, **122**, 8204-8214.
22. L. Cavallo, *J. Am. Chem. Soc.*, 2002, **124**, 8965-8973.
23. J. A. Love, M. S. Sanford, M. W. Day and R. H. Grubbs, *J. Am. Chem. Soc.*, 2003, **125**, 10103-10109.
24. L. Mercks and M. Albrecht, *Chem. Soc. Rev.*, 2010, **39**, 1903-1912.

25. A. Burini, J. P. Fackler Jr, R. Galassi, T. A. Grant, M. A. Omary, M. A. Rawashdeh-Omary, B. R. Pietroni and R. J. Staples, *J. Am. Chem. Soc.*, 2000, **122**, 11264-11265.
26. P. de Fremont, N. Marion and S. P. Nolan, *Coord. Chem. Rev.*, 2009, **253**, 862-892.
27. D. Bourissou, O. Guerret, F. P. Gabbai and G. Bertrand, *Chem. Rev.*, 2000, **100**, 39-92.
28. C. Heinemann, T. Müller, Y. Apeloig and H. Schwarz, *J. Am. Chem. Soc.*, 1996, **118**, 2023-2038.
29. J. F. Lehmann, S. G. Urquhart, L. E. Ennis, A. P. Hitchcock, K. Hatano, S. Gupta and M. K. Denk, *Organometallics*, 1999, **18**, 1862-1872.
30. F. E. Hahn and M. C. Jahnke, *Angew. Chem. Int. Ed.*, 2008, **47**, 3122-3172.
31. Á. Vivancos, C. Segarra and M. Albrecht, *Chem. Rev.*, 2018, **118**, 9493-9586.
32. M. Melaimi, M. Soleilhavoup and G. Bertrand, *Angew. Chem. Int. Ed.*, 2010, **49**, 8810-8849.
33. Y. Wang, Y. Xie, M. Y. Abraham, P. Wei, H. F. Schaefer, P. v. R. Schleyer and G. H. Robinson, *J. Am. Chem. Soc.*, 2010, **132**, 14370-14372.
34. L. Benhamou, E. Chardon, G. Lavigne, S. Bellemin-Laponnaz and V. César, *Chem. Rev.*, 2011, **111**, 2705-2733.
35. A. J. Arduengo, R. Krafczyk, R. Schmutzler, H. A. Craig, J. R. Goerlich, W. J. Marshall and M. Unverzagt, *Tetrahedron*, 1999, **55**, 14523-14534.
36. A. Arduengo III, *Chem. Eur. J.*, 1996, **2**, 1627-1636.
37. V. P. Böhm and W. A. Herrmann, *Angew. Chem. Int. Ed.*, 2000, **39**, 4036-4038.
38. V. P. W. Böhm, T. Weskamp, C. W. K. Gstöttmayr and W. A. Herrmann, *Angew. Chem. Int. Ed.*, 2000, **39**, 1602-1604.
39. H. Sato, T. Fujihara, Y. Obora, M. Tokunaga, J. Kiyosu and Y. Tsuji, *Chem.*

- Commun.*, 2007, **3**, 269-271.
40. C. Kison and T. Opatz, *Synthesis*, 2006, **6**, 3727-3738.
41. S. G. Alexander, M. L. Cole and J. C. Morris, *New J. Chem.*, 2009, **33**, 720-724.
42. G. Bratulescu, *Synthesis*, 2009, **9**, 2319-2320.
43. T. Lv, Z. Wang, J. You, J. Lan and G. Gao, *J. Org. Chem.*, 2013, **78**, 5723-5730.
44. A. J. Arduengo III, J. R. Goerlich and W. J. Marshall, *J. Am. Chem. Soc.*, 1995, **117**, 11027-11028.
45. A. Paczal, A. C. Bényei and A. Kotschy, *J. Org. Chem.*, 2006, **71**, 5969-5979.
46. S. Saba, A. Brescia and M. K. Kaloustian, *Tetrahedron Lett.*, 1991, **32**, 5031-5034.
47. R. S. Bon, B. van Vliet, N. E. Sprenkels, R. F. Schmitz, F. J. J. de Kanter, C. V. Stevens, M. Swart, F. M. Bickelhaupt, M. B. Groen and R. V. A. Orru, *J. Org. Chem.*, 2005, **70**, 3542-3553.
48. R. S. Bon, F. J. J. de Kanter, M. Lutz, A. L. Spek, M. C. Jahnke, F. E. Hahn, M. B. Groen and R. V. A. Orru, *Organometallics*, 2007, **26**, 3639-3650.
49. R. S. Bon, C. Hong, M. J. Bouma, R. F. Schmitz, F. J. J. de Kanter, M. Lutz, A. L. Spek and R. V. A. Orru, *Org. Lett.*, 2003, **5**, 3759-3762.
50. B. A. B. Prasad and S. R. Gilbertson, *Org. Lett.*, 2009, **11**, 3710-3713.
51. K. M. Kuhn and R. H. Grubbs, *Org. Lett.*, 2008, **10**, 2075-2077.
52. M. G. Gardiner, W. A. Herrmann, C. P. Reisinger, J. Schwarz and M. Spiegler, *J. Organomet. Chem.*, 1999, **572**, 239-247.
53. W. A. Herrmann, J. Schwarz and M. G. Gardiner, *Organometallics*, 1999, **18**, 4082-4089.
54. J. A. Mata, A. R. Chianese, J. R. Miecznikowski, M. Poyatos, E. Peris, J. W. Faller and R. H. Crabtree, *Organometallics*, 2004, **23**, 1253-1263.

55. M. Poyatos, E. Mas-Marzá, M. Sanaú and E. Peris, *Inorg. Chem.*, 2004, **43**, 1793-1798.
56. M. Poyatos, E. Mas-Marzá, José A. Mata, M. Sanaú and E. Peris, *Eur. J. Inorg. Chem.*, 2003, **6**, 1215-1221.
57. I. Özdemir, S. Demir, O. Şahin, O. Büyükgüngör and B. Çetinkaya, *Appl. Organomet. Chem.*, 2008, **22**, 59-66.
58. P. L. Arnold, I. S. Edworthy, C. D. Carmichael, A. J. Blake and C. Wilson, *Dalton Trans.*, 2008, **28**, 3739-3746.
59. S. Yasar, K. J. Cavell, B. D. Ward and B. Kariuki, *Appl. Organomet. Chem.*, 2011, **25**, 374-382.
60. P. L. Arnold, M. Rodden, K. M. Davis, A. C. Scarisbrick, A. J. Blake and C. Wilson, *Chem. Commun.*, 2004, **14**, 1612-1613.
61. E. Mas-Marzá, M. Poyatos, M. Sanaú and E. Peris, *Organometallics*, 2004, **23**, 323-325.
62. J. Ye, S. Jin, W. Chen and H. Qiu, *Inorg. Chem. Commun.*, 2008, **11**, 404-408.
63. A. Pöthig and T. Strassner, *Organometallics*, 2011, **30**, 6674-6684.
64. R. Fränkel, C. Birg, U. Kernbach, T. Habereeder, H. Nöth and W. P. Fehlhammer, *Angew. Chem. Int. Ed.*, 2001, **40**, 1907-1910.
65. J. A. Mata, M. Poyatos and E. Peris, *Coord. Chem. Rev.*, 2007, **251**, 841-859.
66. H. V. R. Dias and W. Jin, *Tetrahedron Lett.*, 1994, **35**, 1365-1366.
67. R. Fränkel, U. Kernbach, M. Bakola-Christianopoulou, U. Plaia, M. Suter, W. Ponikwar, H. Nöth, C. Moinet and W. P. Fehlhammer, *J. Organomet. Chem.*, 2001, **617**, 530-545.
68. U. Kernbach, M. Ramm, P. Luger and W. P. Fehlhammer, *Angew. Chem. Int. Ed. Engl.*, 1996, **35**, 310-312.
69. X. Hu, I. Castro-Rodriguez and K. Meyer, *Organometallics*, 2003, **22**, 3016-3018.

70. X. Hu, I. Castro-Rodriguez and K. Meyer, *J. Am. Chem. Soc.*, 2003, **125**, 12237-12245.
71. A. J. Boydston, K. A. Williams and C. W. Bielawski, *J. Am. Chem. Soc.*, 2005, **127**, 12496-12497.
72. A. J. Boydston, J. D. Rice, M. D. Sanderson, O. L. Dykhno and C. W. Bielawski, *Organometallics*, 2006, **25**, 6087-6098.
73. D. M. Khramov, A. J. Boydston and C. W. Bielawski, *Angew. Chem.*, 2006, **118**, 6332-6335.
74. A. J. Boydston and C. W. Bielawski, *Dalton Trans.*, 2006, **34**, 4073-4077.
75. E. Mas-Marzá, J. A. Mata and E. Peris, *Angew. Chem. Int. Ed.*, 2007, **46**, 3729-3731.
76. A. Zanardi, R. Corberán, J. A. Mata and E. Peris, *Organometallics*, 2008, **27**, 3570-3576.
77. S. Gonell and E. Peris, *ACS Catal.*, 2014, **4**, 2811-2817.
78. D. M. Khramov, A. J. Boydston and C. W. Bielawski, *Angew. Chem. Int. Ed.*, 2006, **45**, 6186-6189.
79. S. Gonell, M. Poyatos and E. Peris, *Chem. Eur. J.*, 2014, **20**, 9716-9724.
80. A. G. Tennyson, R. J. Ono, T. W. Hudnall, D. M. Khramov, J. A. V. Er, J. W. Kamplain, V. M. Lynch, J. L. Sessler and C. W. Bielawski, *Chem. Eur. J.*, 2010, **16**, 304-315.
81. K. A. Williams and C. W. Bielawski, *Chem. Commun.*, 2010, **46**, 5166-5168.
82. S. Gonell, M. Poyatos and E. Peris, *Angew. Chem. Int. Ed.*, 2013, **52**, 7009-7013.
83. B. M. Neilson, A. G. Tennyson and C. W. Bielawski, *J. Phys. Org. Chem.*, 2012, **25**, 531-543.
84. C. Segarra, J. Linke, E. Mas-Marzá, D. Kuck and E. Peris, *Chem. Commun.*, 2013, **49**, 10572-10574.
85. D. K. Cabbiness and D. W. Margerum, *J. Am. Chem. Soc.*, 1969, **91**,

- 6540-6541.
86. R. K. Jyothi and J.-Y. Lee, *Sci. Rep.*, 2016, **6**, 27668.
 87. M. R. Anneser, S. Haslinger, A. Pöthig, M. Cokoja, J.-M. Basset and F. E. Kühn, *Inorg. Chem.*, 2015, **54**, 3797-3804.
 88. H. M. Bass, S. A. Cramer, J. L. Price and D. M. Jenkins, *Organometallics*, 2010, **29**, 3235-3238.
 89. Y. Chun, N. Jiten Singh, I.-C. Hwang, J. Woo Lee, S. U. Yu and K. S. Kim, *Nat. Commun.*, 2013, **4**, 1797.
 90. E. Alcalde, N. Mesquida, L. Pérez-García, S. Ramos, M. Alemany and M. L. Rodríguez, *Chem. Eur. J.*, 2002, **8**, 474-484.
 91. R. S. Simons, J. C. Garrison, W. G. Kofron, C. A. Tessier and W. J. Youngs, *Tetrahedron Lett.*, 2002, **43**, 3423-3425.
 92. H.-Y. Gong, B. M. Rambo, E. Karnas, V. M. Lynch and J. L. Sessler, *Nat. Chem.*, 2010, **2**, 406-409.
 93. A. J. Arduengo, H. V. R. Dias, R. L. Harlow and M. Kline, *J. Am. Chem. Soc.*, 1992, **114**, 5530-5534.
 94. N. Kuhn and T. Kratz, *Synthesis (Stuttgart)*, 1993, **6**, 561-562.
 95. M. C. Jahnke and F. E. Hahn, *N-Heterocyclic Carbenes: From Laboratory Curiosities to Efficient Synthetic Tools (2)*, The Royal Society of Chemistry, 2017, pp. 1-45.
 96. D. Enders, K. Breuer, G. Raabe, J. Runsink, J. H. Teles, J.-P. Melder, K. Ebel and S. Brode, *Angew. Chem. Int. Ed. Engl.*, 1995, **34**, 1021-1023.
 97. A. J. Arduengo, H. V. R. Dias, J. C. Calabrese and F. Davidson, *Organometallics*, 1993, **12**, 3405-3409.
 98. P. J. Quinlivan, A. Loo, D. G. Shlian, J. Martinez and G. Parkin, *Organometallics*, 2021, **40**, 166-183.
 99. A. J. Arduengo, S. F. Gamper, J. C. Calabrese and F. Davidson, *J. Am. Chem. Soc.*, 1994, **116**, 4391-4394.
 100. A. n. Caballero, E. Díez-Barra, F. A. Jalón, S. Merino and J. Tejada, *J.*

- Organomet. Chem.*, 2001, **617**, 395-398.
101. O. Guerret, S. Solé, H. Gornitzka, G. Trinquier and G. Bertrand, *J. Organomet. Chem.*, 2000, **600**, 112-117.
102. A. n. Caballero, E. Díez-Barra, F. A. Jalón, S. Merino and J. Tejada, *J. Organomet. Chem.*, 2001, **617**, 395-398.
103. D. S. McGuinness and K. J. Cavell, *Organometallics*, 2000, **19**, 741-748.
104. V. César, S. Bellemin-Laponnaz and L. H. Gade, *Organometallics*, 2002, **21**, 5204-5208.
105. W. Chen, B. Wu and K. Matsumoto, *J. Organomet. Chem.*, 2002, **654**, 233-236.
106. X. Wang, S. Liu and G.-X. Jin, *Organometallics*, 2004, **23**, 6002-6007.
107. P. de Frémont, N. M. Scott, E. D. Stevens and S. P. Nolan, *Organometallics*, 2005, **24**, 2411-2418.
108. K. M. Lee, C. K. Lee and I. J. B. Lin, *Angew. Chem. Int. Ed. Engl.*, 1997, **36**, 1850-1852.
109. K. Öfele, W. A. Herrmann, D. Mihalios, M. Elison, E. Herdtweck, W. Scherer and J. Mink, *J. Organomet. Chem.*, 1993, **459**, 177-184.
110. T. Weskamp, V. P. W. Böhm and W. A. Herrmann, *J. Organomet. Chem.*, 2000, **600**, 12-22.
111. J. R. Norton, R. G. Finke and J. P. Collman., *Principles and Applications of Organotransition Metal Chemistry*. Oxford University Press, Oxford, **XII**, 1987, pp. 1145-1146.
112. P. Schwab, M. B. France, J. W. Ziller and R. H. Grubbs, *Angew. Chem. Int. Ed. Engl.*, 1995, **34**, 2039-2041.
113. P. Schwab, R. H. Grubbs and J. W. Ziller, *J. Am. Chem. Soc.*, 1996, **118**, 100-110.
114. M. Poyatos, M. Sanaú and E. Peris, *Inorg. Chem.*, 2003, **42**, 2572-2576.
115. M. Albrecht, R. H. Crabtree, J. Mata and E. Peris, *Chem. Commun.*, 2002, **1**, 32-33.

-
116. E. Mas-Marzá, M. Poyatos, M. Sanaú and E. Peris, *Inorg. Chem.*, 2004, **43**, 2213-2219.
117. E. Mas-Marzá, M. Sanaú and E. Peris, *J. Organomet. Chem.*, 2005, **690**, 5576-5580.
118. M. Poyatos, W. McNamara, C. Incarvito, E. Peris and R. H. Crabtree, *Chem. Commun.*, 2007, **22**, 2267-2269.
119. M. Poyatos, W. McNamara, C. Incarvito, E. Clot, E. Peris and R. H. Crabtree, *Organometallics*, 2008, **27**, 2128-2136.
120. M. Albrecht, J. R. Miecznikowski, A. Samuel, J. W. Faller and R. H. Crabtree, *Organometallics*, 2002, **21**, 3596-3604.
121. J. R. Miecznikowski and R. H. Crabtree, *Polyhedron*, 2004, **23**, 2857-2872.
122. J. R. Miecznikowski and R. H. Crabtree, *Organometallics*, 2004, **23**, 629-631.
123. M. Viciano, E. Mas-Marzá, M. Poyatos, M. Sanaú, R. H. Crabtree and E. Peris, *Angew. Chem. Int. Ed.*, 2005, **44**, 444-447.
124. M. Viciano, M. Poyatos, M. Sanaú, E. Peris, A. Rossin, G. Ujaque and A. Lledós, *Organometallics*, 2006, **25**, 1120-1134.
125. R. Corberán, V. Lillo, J. A. Mata, E. Fernandez and E. Peris, *Organometallics*, 2007, **26**, 4350-4353.
126. A. Pontes da Costa, M. Viciano, M. Sanaú, S. Merino, J. Tejada, E. Peris and B. Royo, *Organometallics*, 2008, **27**, 1305-1309.
127. M. Poyatos, J. A. Mata, E. Falomir, R. H. Crabtree and E. Peris, *Organometallics*, 2003, **22**, 1110-1114.
128. E. A. Martynova, N. V. Tzouras, G. Pisanò, C. S. J. Cazin and S. P. Nolan, *Chem. Commun.*, 2021, **57**, 3836-3856.
129. M. Raynal, C. S. J. Cazin, C. Vallée, H. Olivier-Bourbigou and P. Braunstein, *Organometallics*, 2009, **28**, 2460-2470.
130. R. Alder, P. Allen and S. Williams, Kim YJ, Streiwieser AJ, *J. Am. Chem.*

- Soc., 1995, **124**, 5757.
131. Y.-J. Kim and A. Streitwieser, *J. Am. Chem. Soc.*, 2002, **124**, 5757-5761.
132. A. M. Magill, K. J. Cavell and B. F. Yates, *J. Am. Chem. Soc.*, 2004, **126**, 8717-8724.
133. W. A. Herrmann, C. Köcher, L. J. Gooßen and G. R. J. Artus, *Chem. Eur. J.*, 1996, **2**, 1627-1636.
134. H. M. J. Wang and I. J. B. Lin, *Organometallics*, 1998, **17**, 972-975.
135. J. C. Garrison and W. J. Youngs, *Chem. Rev.*, 2005, **105**, 3978-4008.
136. T. Scattolin and S. P. Nolan, *Trends. Chem.*, 2020, **2**, 721-736.
137. Y. D. Bidal, M. Lesieur, M. Melaimi, D. B. Cordes, A. M. Z. Slawin, G. Bertrand and C. S. J. Cazin, *Chem. Commun.*, 2015, **51**, 4778-4781.
138. M. R. L. Furst and C. S. J. Cazin, *Chem. Commun.*, 2010, **46**, 6924-6925.
139. F. Nahra, A. Gómez-Herrera and C. S. J. Cazin, *Dalton Trans.*, 2017, **46**, 628-631.
140. T. Kösterke, T. Pape and F. E. Hahn, *Chem. Commun.*, 2011, **47**, 10773-10775.
141. Y. Han and H. V. Huynh, *Dalton Trans.*, 2011, **40**, 2141-2147.
142. J. A. Cabeza, I. da Silva, I. del Río and M. G. Sánchez-Vega, *Dalton Trans.*, 2006, **33**, 3966-3971.
143. P. J. Fraser, W. R. Roper and F. G. A. Stone, *J. Organomet. Chem.*, 1973, **50**, C54-C56.
144. P. J. Fraser, W. R. Roper and F. G. A. Stone, *J. Chem. Soc., Dalton Trans.*, 1974, **7**, 760-764.
145. D. S. McGuinness, K. J. Cavell, B. F. Yates, B. W. Skelton and A. H. White, *J. Am. Chem. Soc.*, 2001, **123**, 8317-8328.
146. M. S. Viciu, G. A. Grasa and S. P. Nolan, *Organometallics*, 2001, **20**, 3607-3612.
147. S. Gründemann, M. Albrecht, A. Kovacevic, J. W. Faller and R. H. Crabtree, *J. Chem. Soc., Dalton Trans.*, 2002, **10**, 2163-2167.

148. R. Das, A. Hepp, C. G. Daniliuc and F. E. Hahn, *Organometallics*, 2014, **33**, 6975-6987.
149. T. Kösterke, T. Pape and F. E. Hahn, *J. Am. Chem. Soc.*, 2011, **133**, 2112-2115.
150. H. W. Wanzlick and E. Schikora, *Angew. Chem.*, 1960, **72**, 494-494.
151. H.-W. Wanzlick and E. Schikora, *Chem. Ber.*, 1961, **94**, 2389-2393.
152. H. W. Wanzlick and H. J. Kleiner, *Angew. Chem.*, 1961, **73**, 493-493.
153. Y. Liu, P. E. Lindner and D. M. Lemal, *J. Am. Chem. Soc.*, 1999, **121**, 10626-10627.
154. M. K. Denk, K. Hatano and M. Ma, *Tetrahedron Lett.*, 1999, **40**, 2057-2060.
155. F. E. Hahn, L. Wittenbecher, D. Le Van and R. Fröhlich, *Angew. Chem. Int. Ed.*, 2000, **39**, 541-544.
156. D. C. Graham, K. J. Cavell and B. F. Yates, *J. Phys. Org. Chem.*, 2005, **18**, 298-309.
157. P. B. Hitchcock, M. F. Lappert, P. Terreros and K. P. Wainwright, *J. Chem. Soc., Chem. Commun.*, 1980, **24**, 1180-1181.
158. M. F. Lappert, *J. Organomet. Chem.*, 1988, **358**, 185-213.
159. P. B. Hitchcock, M. F. Lappert and P. L. Pye, *J. Chem. Soc., Dalton Trans.*, 1978, **7**, 826-836.
160. M. F. Lappert and P. L. Pye, *J. Chem. Soc., Dalton Trans.*, 1977, **21**, 2172-2180.
161. D. J. Cardin, B. Cetinkaya, M. F. Lappert, L. Manojlović-Muir and K. W. Muir, *J. Chem. Soc. D*. 1971, **8**, 400-401.
162. B. Liu, Y. Zhang, D. Xu and W. Chen, *Chem. Commun.*, 2011, **47**, 2883-2885.
163. C. Galuppo, J. Alvarenga, A. C. Queiroz, I. Messias, R. Nagao and C. Abbehausen, *Electrochem. Commun.*, 2020, **110**, 106620.
164. A. M. Voutchkova, L. N. Appelhans, A. R. Chianese and R. H. Crabtree,

- J. Am. Chem. Soc.*, 2005, **127**, 17624-17625.
165. G. Gasser, I. Ott and N. Metzler-Nolte, *J. Med. Chem.*, 2011, **54**, 3-25.
166. H. V. Huynh, *The Organometallic Chemistry of N-Heterocyclic Carbenes*, John Wiley & Sons, 2017.
167. E. Peris, *Chem. Rev.*, 2018, **118**, 9988-10031.
168. W. A. Herrmann, O. Runte and G. Artus, *J. Organomet. Chem.*, 1995, **501**, C1-C4.
169. J. C. Bernhammer, G. Frison and H. V. Huynh, *Chem. Eur. J.*, 2013, **19**, 12892-12905.
170. A. Comas-Vives and J. N. Harvey, *Eur. J. Inorg. Chem.*, 2011, **32**, 5025-5035.
171. H. Karabıyık, B. Yiğit, M. Yiğit, İ. Özdemir and H. Karabıyık, *Acta Crystallogr., Sect. C: Cryst. Struct. Commun.*, 2019, **75**, 941-950.
172. M. D. Sanderson, J. W. Kamplain and C. W. Bielawski, *J. Am. Chem. Soc.*, 2006, **128**, 16514-16515.
173. C. Boehme and G. Frenking, *Organometallics*, 1998, **17**, 5801-5809.
174. X. Hu, I. Castro-Rodriguez, K. Olsen and K. Meyer, *Organometallics*, 2004, **23**, 755-764.
175. D. Nemcsok, K. Wichmann and G. Frenking, *Organometallics*, 2004, **23**, 3640-3646.
176. H. Jacobsen, A. Correa, C. Costabile and L. Cavallo, *J. Organomet. Chem.*, 2006, **691**, 4350-4358.
177. D. Benitez, N. D. Shapiro, E. Tkatchouk, Y. Wang, W. A. Goddard and F. D. Toste, *Nat. Chem.*, 2009, **1**, 482-486.
178. X. Xu, S. H. Kim, X. Zhang, A. K. Das, H. Hirao and S. H. Hong, *Organometallics*, 2013, **32**, 164-171.
179. A. A. D. Tulloch, A. A. Danopoulos, S. Kleinhenz, M. E. Light, M. B. Hursthouse and G. Eastham, *Organometallics*, 2001, **20**, 2027-2031.
180. N. Wang, J. Xu and J. K. Lee, *Org. Biomol. Chem.*, 2018, **16**, 8230-8244.

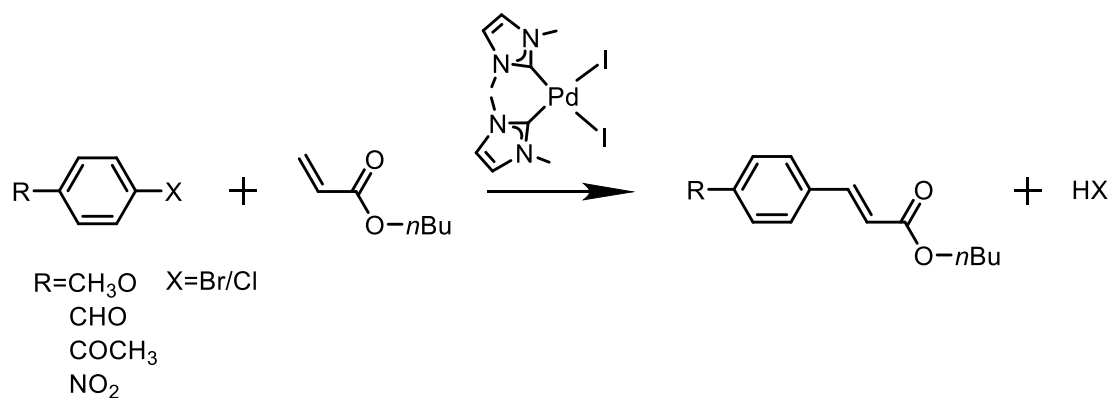
181. Z. Wang, X. S. Xue, Y. Fu and P. Ji, *Chem. Asian J.*, 2020, **15**, 169-181.
182. C. Yang, X. S. Xue, J. L. Jin, X. Li and J. P. Cheng, *J. Org. Chem.*, 2013, **78**, 7076-7085.
183. C. Yang, X. S. Xue, X. Li and J. P. Cheng, *J. Org. Chem.*, 2014, **79**, 4340-4351.
184. V. S. Bernales, A. V. Marenich, R. Contreras, C. J. Cramer and D. G. Truhlar, *J. Phys. Chem. B.*, 2012, **116**, 9122-9129.
185. R. W. Alder, P. R. Allen and S. J. Williams, *J. Chem. Soc., Chem. Commun.*, 1995, **12**, 1267-1268.
186. W. Strohmeier and F. J. Müller, *Chem. Ber.*, 1967, **100**, 2812-2821.
187. G. Bouquet, A. Loutellier and M. Bigorgne, *J. Mol. Struct.*, 1968, **1**, 211-237.
188. C. A. Tolman, *Chem. Rev.*, 1977, **77**, 313-348.
189. D. G. Gusev, *Organometallics*, 2009, **28**, 6458-6461.
190. D. G. Gusev and E. Peris, *Dalton Trans.*, 2013, **42**, 7359-7364.
191. D. J. Nelson and S. P. Nolan, *Chem. Soc. Rev.*, 2013, **42**, 6723-6753.
192. T. Dröge and F. Glorius, *Angew. Chem. Int. Ed.*, 2010, **49**, 6940-6952.
193. Q. Teng and H. V. Huynh, *Dalton Trans.*, 2017, **46**, 614-627.
194. H. V. Huynh, Y. Han, R. Jothibasua and J. A. Yang, *Organometallics*, 2009, **28**, 5395-5404.
195. H. V. Huynh, *Chem. Rev.*, 2018, **118**, 9457-9492.
196. X. W. Li, H. Y. Li, G. F. Wang, F. Chen, Y.-Z. Li, X.-T. Chen, Y.-X. Zheng and Z.-L. Xue, *Organometallics*, 2012, **31**, 3829-3835.
197. A. C. Hillier, W. J. Sommer, B. S. Yong, J. L. Petersen, L. Cavallo and S. P. Nolan, *Organometallics*, 2003, **22**, 4322-4326.
198. H. Clavier and S. P. Nolan, *Chem. Commun.*, 2010, **46**, 841-861.
199. A. Poater, B. Cosenza, A. Correa, S. Giudice, F. Ragone, V. Scarano and L. Cavallo, *Eur. J. Inorg. Chem.*, 2009, **13**, 1759-1766.
200. A. B. P. Lever, *Inorg. Chem.*, 1990, **29**, 1271-1285.

201. A. B. P. Lever, *Inorg. Chem.*, 1991, **30**, 1980-1985.
202. J. Mathew and C. H. Suresh, *Inorg. Chem.*, 2010, **49**, 4665-4669.
203. J. Mathew and C. H. Suresh, *Organometallics*, 2011, **30**, 3106-3112.

2. Applications of N-heterocyclic Carbenes Complexes

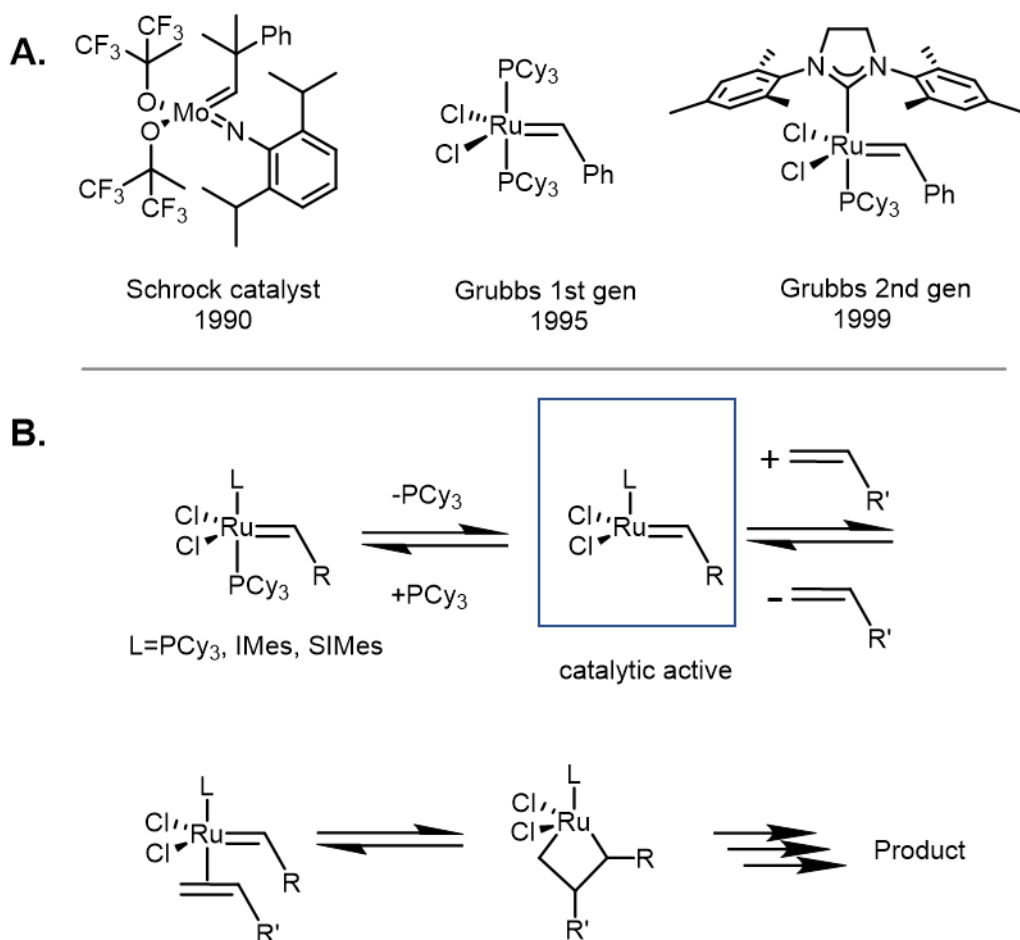
2.1 Applications of NHCs in Catalysis

As mentioned in the concept chapter, since the initial disclosure by Wanzlick & Öfele and the first isolation by Arduengo, NHCs have gained great attention in areas such as catalysis,¹⁻³ photoluminescent material,⁴ and metallopharmaceuticals⁵. By far the largest application of NHC complexes is the homogeneous catalysis of organic transformations. The basis of NHCs in catalysis application was established by Herrmann in 1995 (see **Scheme 21**).⁶ This Pd-NHC catalyst was shown to have far superior thermal and hydrolytic stabilities than previous phosphine and phosphite catalysts.⁶



Scheme 21. The first NHC Pd(II) complex catalyzes Mizoroki–Heck reaction reported by Herrmann in 1995.⁶

Nowadays, NHC complexes with various transition metals are catalysts in a myriad of academically and commercially important processes.⁴ Some of the most important reactions catalyzed by NHC metal complexes include Ir- and Ru-catalyzed hydrogenation and hydrogen transfer,⁷ gold-catalyzed activation of π -bonds,⁸ hydrosilylation mediated by Rh- and Pt-complexes,⁹ palladium-catalyzed cross-coupling,¹⁰ and ruthenium-catalyzed olefin metathesis¹¹.



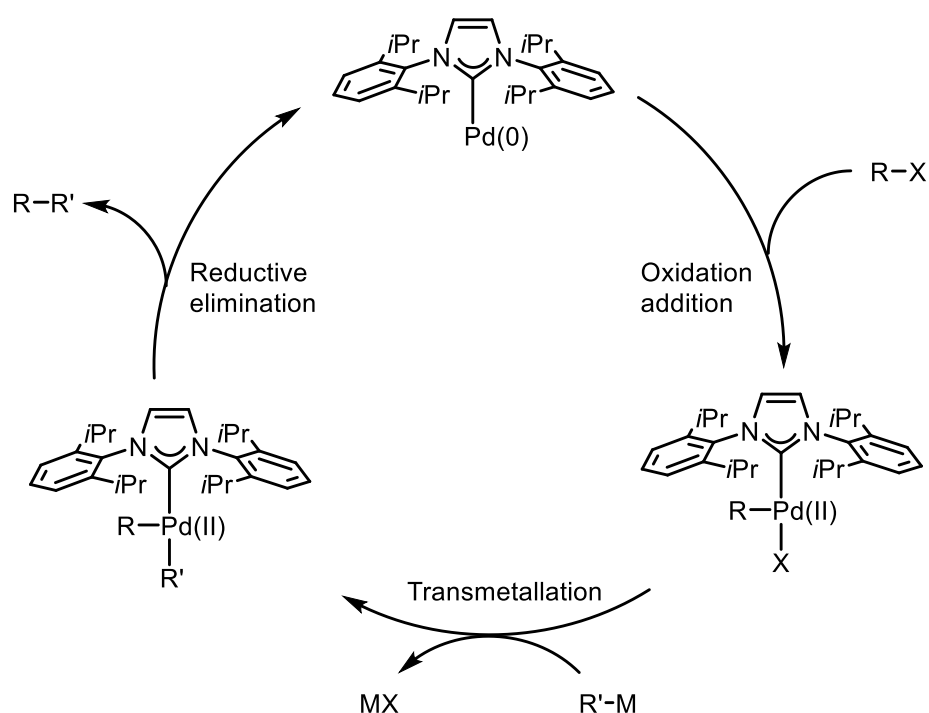
Scheme 22. **A** Structures of Schrock catalyst^{12,13} and two generations Grubbs catalysts for olefin metathesis^{14,15}; **B** The general initiation mechanism of alkene metathesis reactions^{16,17}.

As introduced in Chapter 1, the ruthenium-based olefin metathesis catalysts have been the focus of great attention. The introduction of the metal catalyst in olefin metathesis begins in the 1990s, Schrock and coworkers proved the molybdenum alkylidene complexes have high reactivity and applicability to a broad range of substrates (**Scheme 22, A**).^{12,13,18} However, the low functional group tolerance to substrates and sophisticated handling characteristics hindered its further development. Meanwhile, Grubbs's 1st generation ruthenium phosphine complex exhibits air/moisture stability but relatively low thermal stability and inferior reactivity. Hoveyda and coworkers have serendipitously discovered another internal metal-oxygen chelate ruthenium-based catalyst, which has similar performance and disadvantages.¹⁹ The

breakthrough in this catalysis is the introduction of NHC ligands IMes and SIMes into the ruthenium-based Grubbs 1st generation catalyst (**Scheme 22, A**). According to several theoretical and experimental studies, the mechanism of alkene metathesis reactions was depicted in **Scheme 22, B**, with metallacyclobutane (MCB) to be the intermediate species.¹⁶ It was recognized that the dissociation of phosphine step is closely related to the reactivity, and the steric bulkiness of the ligand L directly contributes to the phosphine dissociation. In comparison to the 1st generation catalyst, the SIMes-Ru(II) complex (2nd gen Grubbs) exhibits approximately 5 kcal mol⁻¹ higher Ru-ligand binding strength, which contributes to its thermal stability.^{20,21} In the next step, the binding of alkene substrates to catalytic active species is more favored than reassociation with PCy₃. The initial binding of the coordinatively unsaturated metal center to the π -accepting olefin occurs with an affinity four times of magnitude greater for the NHC catalyst than for the phosphine analogue.¹⁷ To conclude, benefits from the steric and electronic interactions between NHC and ruthenium core, 2nd generation Grubbs catalyst exhibits substantially greater thermal stability and higher reactivity than the 1st generation Grubbs catalyst for cross- and ring-closing metathesis, ring-opening metathesis polymerization.¹⁹ In addition, the 2nd generation ruthenium NHC catalysts achieved better *E/Z* selectivity in cross-metathesis reactions and ring-closing metathesis reactions, which gives access to unprecedented reactivity pathways and selectivity paradigms that are not feasible using other catalysis systems.²²⁻²⁴

The Heck-Mizoraki reaction catalyzed by the Pd-NHC complex showed in **Scheme 21**, demonstrates another example that great improvements were achieved by the introduction of NHC ligands. Since the first NHC complex catalyzed Heck reaction was reported by Herrmann,⁶ developments in this research area have grown rapidly.^{25,26} The general mechanisms for cross-coupling reactions are similar (see **Scheme 23**). The pre-catalyst of Pd is activated to obtain the Pd(0) species, then the Pd(0) undergoes the oxidative

addition of the halogenated substrates (X can also be pseudohalide, such as triflate). During this step, the difficulty of oxidation involving in the coupling typically decreases in the order of $R-Cl > R-Br > R-I$, which correlates to the $R-X$ bond strengths. The NHC ligated $Pd(0)$ poses an electron-rich catalytically active metal center, which was found to be suitable for the oxidative addition into the $R-X$ bond of the substrates.²⁷ Hence, organochlorides such as aryl chlorides with strong $C-Cl$ bonds that resist oxidative addition, can be activated by these $Pd-NHC$ catalysts.^{10,28,29}



Scheme 23. General cross-coupling mechanism between organic halides and organometallic reagents ($R, R' =$ aryl, heteroaryl, alkyl; $X =$ halide or pseudohalide; $M = B(OR)_2$ (Suzuki–Miyaura), SnR_3 (Stille), ZnR (Negishi), and HNR_2 (Buchwald–Hartwig), *etc.*).^{25,26} Coordinating solvent molecules were omitted for clarity.

Different transmetalation agents are involved in the transmetalation step: boronic acids or esters are involved in the Suzuki–Miyaura reaction; organotin reagents are used in the Stille reaction; Negishi coupling employs organozinc and Buchwald–Hartwig reaction use amides. In Negishi coupling carried out in the $Pd-PEPPSI$ (pyridine-enhanced precatalyst preparation, stabilization, and

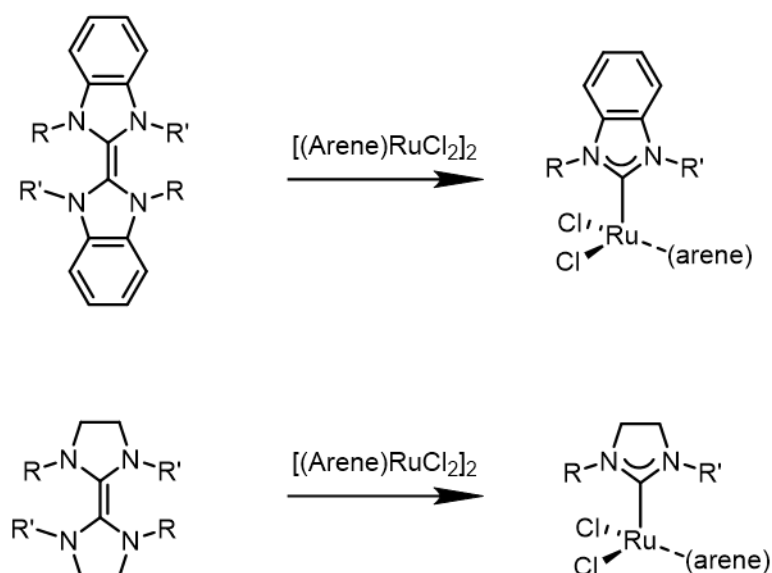
initiation) catalyst system, the steric demanding NHC ligand helps to facilitate the rate-limiting reductive elimination step in the catalytic transformation.³⁰

The intuitive modifiability of NHCs is a key factor in their great suitability as steering ligands in the many catalysis areas. Apart from mentioned homogeneous catalysis, NHCs are widely used in areas of water-soluble homogeneous catalysis,³¹ asymmetric catalysis,³² and catalyst immobilization.³³ Reflecting their importance, a huge variety of review articles and book chapters have been dedicated to the design and synthesis of diverse types of NHC-based catalysts.³⁴⁻³⁸

2.2 Medicinal Applications of NHCs

Compared to the flourishing of NHC complexes in the field of catalysis, applications of NHC complexes in biomedical chemistry are scarce but experiencing rapid development.^{5,39,40} One of the major advancements at the early stages that shaped the current understanding of metallodrugs is certainly the discovery of the Cisplatin by Rosenberg in the 1970s.^{41,42} After a decade, Cetinkaya made the first attempt to investigate the *in vitro* activity antimicrobial property of ruthenium(II) and rhodium(I) NHC complexes.^{43,44} Following the metal insertion method, a library of ruthenium complexes were synthesized by reacting $[(\eta^6\text{-arene})\text{RuCl}_2]_2$ with corresponding tetraamines (see **Scheme 24**).^{43,44} Subsequently, the antimicrobial activity of these Ru(II) NHC complexes was examined against *Enterococcus faecalis*, *Staphylococcus aureus*, *Escherichia coli*, and *Pseudomonas aeruginosa*.^{43,44} Some of them were further tested against *Candida albicans* and *Candida tropicalis* for antifungal activity.^{43,44} The result showed none of the Ru-NHC complexes had greater performance than the Ampicillin in antimicrobial efficacy.^{43,44} However, Ru complexes bearing imidazolynylidenes with bulky N-substituted $\text{CH}_2\text{CH}_2\text{OMe}$ or $p\text{-CH}_2\text{C}_6\text{H}_4\text{N}(\text{Me})_2$ exhibited activity against Gram-positive bacteria and fungi.^{43,44} In general, more potent activity was observed with Ru(II)

NHC complexes bearing more lipophilic substituents as compared to their analogues. This finding is consistent with previous studies on the antimicrobial activity of imidazolium salts,^{45,46} suggests the lipophilic side chain is an essential component for NHC complexes to cross the bacterial cellular membrane to perform their antimicrobial activity.



Arene	R	R'
<i>p</i> -MeC ₆ H ₄ iPr	Me	
<i>p</i> -MeC ₆ H ₄ iPr	Et	
C ₆ H ₃ Me ₃	Me	
C ₆ H ₃ Me ₃	Et	
C ₆ Me ₆	Me	
C ₆ Me ₆	Et	
<i>p</i> -MeC ₆ H ₄ iPr	Me	CH ₂ CH ₂ OMe
<i>p</i> -MeC ₆ H ₄ iPr	CH ₂ CH ₂ OMe	CH ₂ CH ₂ OMe
<i>p</i> -MeC ₆ H ₄ iPr	<i>p</i> -CH ₂ C ₆ H ₄ OMe	<i>p</i> -CH ₂ C ₆ H ₄ OMe
<i>p</i> -MeC ₆ H ₄ iPr	<i>p</i> -CH ₂ C ₆ H ₄ N(Me) ₂	<i>p</i> -CH ₂ C ₆ H ₄ N(Me) ₂
<i>p</i> -MeC ₆ H ₄ iPr	<i>p</i> -CH ₂ C ₆ H ₄ N(Me) ₂ ·HCl	<i>p</i> -CH ₂ C ₆ H ₄ N(Me) ₂ ·HCl
C ₆ Me ₆	Me	CH ₂ CH ₂ OMe
C ₆ Me ₆	CH ₂ CH ₂ OMe	CH ₂ CH ₂ OMe
C ₆ Me ₆	<i>p</i> -CH ₂ C ₆ H ₄ OMe	<i>p</i> -CH ₂ C ₆ H ₄ OMe
C ₆ Me ₆	<i>p</i> -CH ₂ C ₆ H ₄ N(Me) ₂	<i>p</i> -CH ₂ C ₆ H ₄ N(Me) ₂
C ₆ Me ₆	<i>p</i> -CH ₂ C ₆ H ₄ N(Me) ₂ ·HCl	<i>p</i> -CH ₂ C ₆ H ₄ N(Me) ₂ ·HCl

Scheme 24. Synthetic routes to ruthenium(II) carbene complexes by Cetinkaya in 1996.⁴³

In recent years, Ru-based drugs have received attention for their potentials as antitumor and antimetastatic agents in platinum-resistant tumors or as alternatives to Cisplatin and its derivatives.⁴⁷ NAMI-A (imidazolium *trans*-[tetrachlorido(1*H*-imidazole)(*S*-dimethyl sulfoxide)ruthenate(III)]) was the first Ru-based anticancer agent to enter phase I clinical trials. It was found to be able to slow down the progression of metastasis *in vitro*.⁴⁸ However, it failed in the phase II trials.⁴⁹ The indazole-based ruthenium(III) complex KP1019 (indazolium *trans*-[tetrachloridobis(1*H*-indazole)ruthenate(III)]) is the second Ru-based anticancer agent to enter clinical trials. KP1019 has been reported to exhibit potent cytotoxicity against primary tumors, particularly for colorectal cancer.^{50,51} Bio-active Ru-NHC complexes have also made great strides. A range of NHC ligands were incorporated in a well-established [Ru(II)(η^6 -arene)(en)Cl]⁺ (en = ethylenediamine, RAEDs) (**Figure 7, A**) family, to afford enzyme inhibitors (e.g., thioredoxin reductase (TrxR), cathepsin B).^{52,53} **Figure 7, B** demonstrated the most cytotoxic and lipophilic compound in a range of Ru-based complexes studied bearing bidentate NHC-pyridyl ligands.⁵³ **Figure 7, C** was also reported to be the most active and lipophilic compound within a series of non-chelating ruthenium NHC complexes, which highlights the importance of lipophilicity.⁵⁴ In addition, **C** in **Figure 7** was able to inhibit PC-3 cell lines by inducing cell cycle arrest at the G2/M phase, and exhibited a better binding to DNA than the complexes bearing less lipophilic terminal groups.⁵⁴

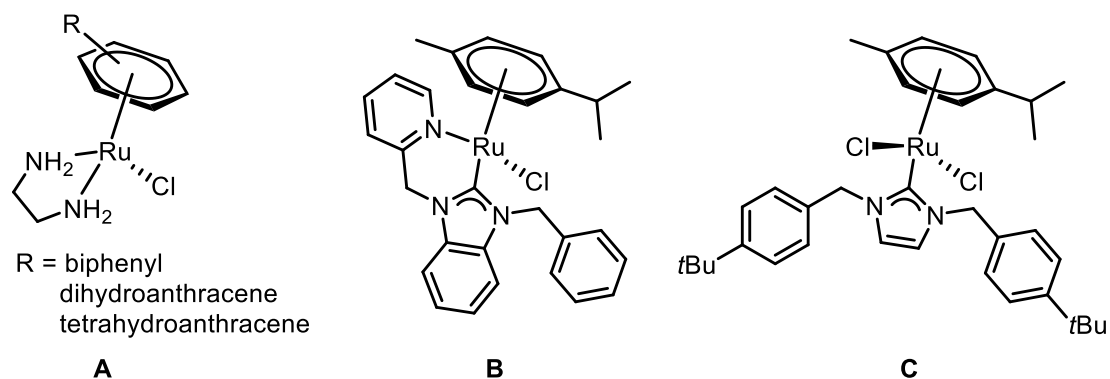
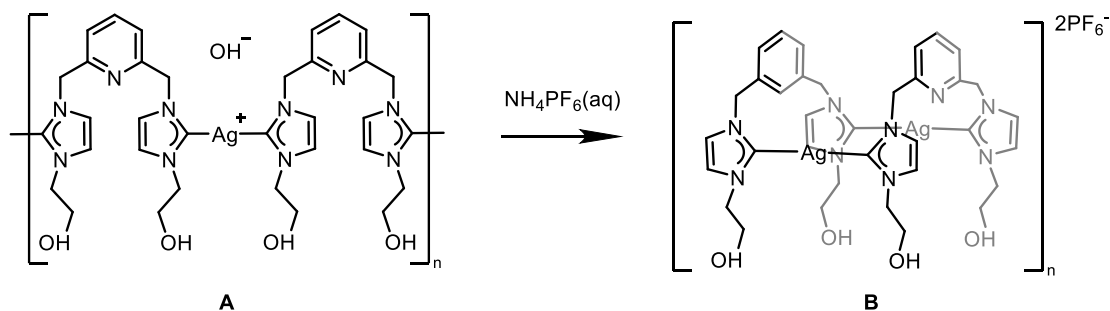


Figure 7. Examples of cytotoxic ruthenium complexes.⁵²⁻⁵⁴

Coinage metal complexes have yielded fruitful results in medicinal applications.⁵⁵ Since the introduction of silver nitrate in the 17th century, the popularity of silver has not faded.⁵⁶ In particular, Moyer and coworkers discovered the powerful antibacterial properties of silver against resistant organisms such as *Pseudomonas aeruginosa*, *Proteus mirabilis*, and *Proteus morgani*, offering doctors an alternative to penicillin and other antibiotics.⁵⁷ Another example is silver sulfadiazine, which has remained the most popular and effective drug for the treatment of topical burns since it was reported by Fox in 1968.⁵⁸ The antimicrobial activity of Ag(I) NHC complexes was first reported by Youngs *et al.* in 2004.⁵⁹ The pyridine bridged dicarbene units coordinated to Ag(I) cation and polymerized to form a water-soluble coordination polymer (**Scheme 25, A**).⁵⁹ The addition of NH_4PF_6 to this polymer yielded an insoluble discrete dinuclear Ag(I) NHC complex (**Scheme 25, B**).⁵⁹ The soluble polymer was shown to exhibit better antimicrobial ability against *Escherichia coli*, *Staphylococcus aureus*, and *Pseudomonas aeruginosa* than silver nitrate, and the good solubility in water makes it an excellent therapeutic agent for *in vivo* applications.⁵⁹



Scheme 25. Structures of Ag-NHC complexes with antimicrobial properties by Young and coworkers.⁵⁹

The good antimicrobial activity of this Ag-NHC polymer was explained by the release of Ag^+ ions from the pincer-type complex.⁵⁹ Interestingly, encapsulating this bio-active polymer into TecophilicTM polymer fiber mat greatly enhanced its antimicrobial activity.⁶⁰ This was explained by the slow releasing of silver

nanoparticles from polymer embedded mat, which sustained the antimicrobial activity of the mat over a long period of time.⁶⁰

An increasing number of publications have focused on the medicinal applications of gold NHC complexes.⁶¹⁻⁶⁴ In contrast to silver NHC complexes that often exhibit antimicrobial activities, gold NHC complexes frequently emerge as antimicrobial and anticancer agents.⁶⁵ It is generally accepted that inhibition of the seleno-enzyme thioredoxin reductase (TrxR) is the source of the cytotoxic actions of gold(I) and gold(III) anti-cancer agents, as strong TrxR inhibition may eventually lead to apoptosis through a mitochondrial pathway.⁶⁶⁻⁶⁹ Hence, a large effort has been dedicated to synthesizing gold complex with antimitochondrial effects. Following the successful application of gold phosphine complexes in this area, Berners-Price and coworkers reported two key structures of gold metallodrugs (**Figure 8, A**⁷⁰ and **B**^{71,72}). **Figure 8, A** was synthesized in analog to bis-chelated gold phosphine complexes, but exhibited a better mitochondrial uptake.⁷⁰ In the following studies, the mononuclear complex **Figure 8, B** was evaluated. *N*-substituted group of structure B was modified to adjust lipophilicity and the cationic dicarbene resulted in a delocalized lipophilic cation (DLC) structure, which promoted the complex to accumulate inside mitochondria and display strong antimitochondrial effects.⁷³ Due to the complexity of NHC ligand structures, the studies focus on structure-activity-relationship are still in the early stages.^{61,74,75}

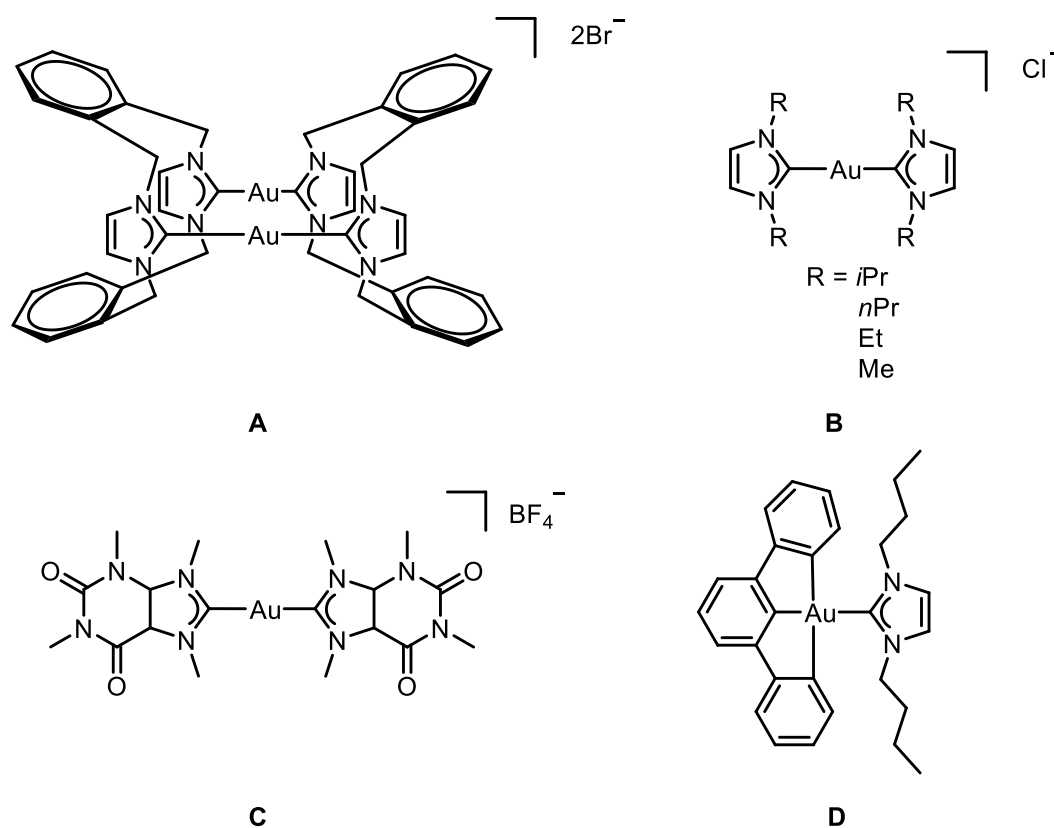


Figure 8. **A.** First di-nuclear gold(I) NHC complexes used by Berners-Price and coworkers.⁷⁰ **B.** mono-nuclear gold(I) NHC complex used to investigate structure-activity-relationship by Berners-Price and coworkers.^{71,72} **C.** Biscarbene Au(I) complex targeting G-quadruplex by Casini and co-workers.⁷⁶ **D.** pincer gold(III) NHC complex engages multiple molecular targets by Che.⁷⁷

The success of gold NHC complexes in targeting TrxR has inspired several other attractive research topics.⁵⁵ Dicarbene complex **C** in **Figure 8** is synthesized from caffeine and exhibits a good cytotoxic effect and behaves like a selective G-quadruplex stabilizer in DNA secondary structures.⁷⁶ Furthermore, pincer gold(III) NHC complex (**Figure 8, D**) displayed specific engagement with multiple cellular targets, including HSP60, vimentin, nucleophosmin, and YB-1, accompanied by expected downstream mechanisms of actions.⁷⁷

Beyond medicinal chemistry, N-heterocyclic carbene complexes found their way into a plethora of further fields of research. Exemplarily, organometallic complexes of group 11 usually require fine-tuning of metallophilic interactions to impart the desired luminescence.⁴ By changing the N-substituents in the

wingtip or aromaticity in the backbone of the NHCs, it is possible to change the electronic properties and therefore to obtain suitable characteristics for luminescent materials.⁴ NHCs have also been found valuable in a variety of applications in materials science. This includes the use of NHCs as functionalization agents on planar metallic and metalloid surfaces,⁷⁸⁻⁸¹ as stabilizers on nanoparticles⁸²⁻⁸⁵ and clusters,⁸⁶⁻⁸⁸ in addition to building blocks in coordination polymers⁸⁹⁻⁹¹ and metal-organic frameworks (MOFs)⁹²⁻⁹⁴.

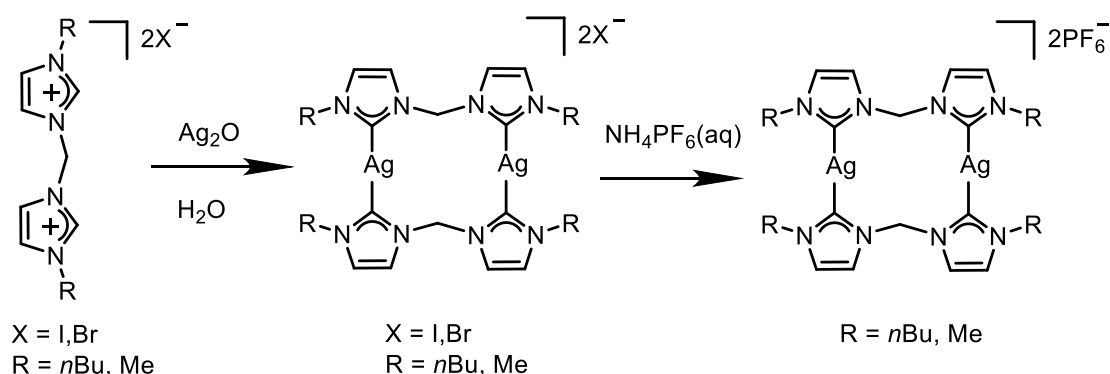
2.3 Supramolecular Chemistry Based on NHC Complexes

In the past years, noteworthy progress has been attained in the concept of designing coordination-driven discrete supramolecular architectures.⁹⁵⁻¹⁰⁰ However, most of these frameworks were assembled based on classical/Werner-type coordination chemistry, in which the directional metal-ligand bond controls the self-assembly process and allows for an empirical design of topology.¹⁰¹ The most representative application in this area is metal-organic frameworks (MOFs), in which organic ligands bearing donor atoms act as connectors between metal cations and form repeating coordination entities in two or three dimensions.¹⁰² When ligands and metal nodes are combined in a geometrically convergent fashion, supramolecular coordination complexes (SCCs) exhibiting discrete two- or three-dimensional structures, can be obtained.¹⁰³

In contrast to the classical SCCs built of metal nodes and linkers by classic coordination chemistry using heteroatom donors or those whose ligands (normally η^5 -Cp or η^6 -arene) cap the metal nodes, their organometallic counterpart features metal-carbon bonds for the connection between linkers and nodes. Given the advantage of easy preparation and structural versatility, the N-heterocyclic carbene complexes have gained rapid advancements towards complex three-dimensional structures. From the perspective of coordination chemistry, conventional Werner-type metal-ligand bonding in complexes is often regarded as a dynamic linkage, which can reversibly form and disrupt in response to environmental stimulation.¹⁰⁴⁻¹⁰⁶ While in the case of organometallic M-C_{NHC} bonding, due to the strong bond strength,¹⁰⁷ late transition metal NHC complex are generally regarded as having a 'static' structure, meaning the complex disfavors a reversible dissociation.¹⁰⁸

Hereby, supramolecular complexes assembled with NHC-donor, alkynyl or metal-arene donor groups can be named supramolecular organometallic complexes (SOCs).¹⁰⁸

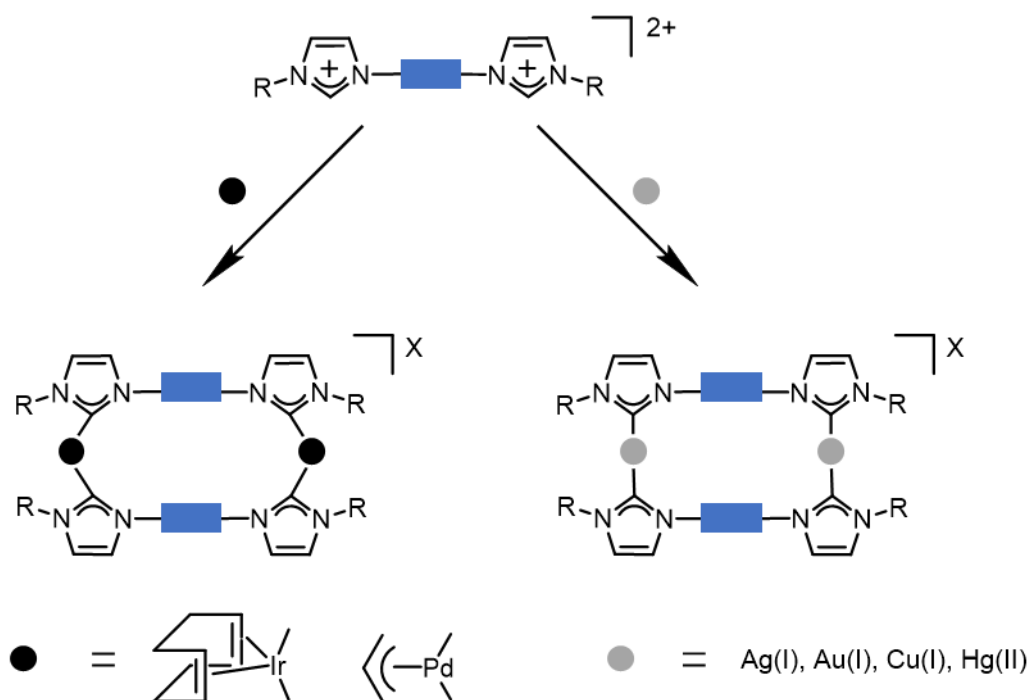
The number of organometallic-based supramolecular assemblies has grown fast. At this point, it is worthwhile to mention the group 11 (coinage metal) cations are widely used for the assembly of NHC-based SOC. ¹⁰⁹ The reason for this is that these coinage metals Cu, Ag, and Au, often display linear coordination modes in their +1 oxidation state, that facilitate trans coordination of the NHC ligands. Molecular rectangles obtained from bis-NHC ligands constitute the simplest derivatives in supramolecular NHC chemistry. **Scheme 26** demonstrated the synthesis of the first dinuclear molecular rectangles from linear bidentate NHC ligands with silver cations.¹¹⁰ The methylene bridged bisimidazolium salt was reacted with Ag_2O in water, yielded nearly quantitative formation of light-sensitive dinuclear complexes.¹¹⁰ The dinuclear complexes can undergo an anion exchange reaction with NH_4PF_6 to afford the more stable PF_6^- complexes.¹¹⁰



Scheme 26. Synthesis route of dinuclear molecular rectangles by Youngs and coworkers.¹¹⁰

The modular design strategy of these dinuclear molecular rectangles has been extensively exploited by Hahn, Han, and Bielawski.^{109,111} Several

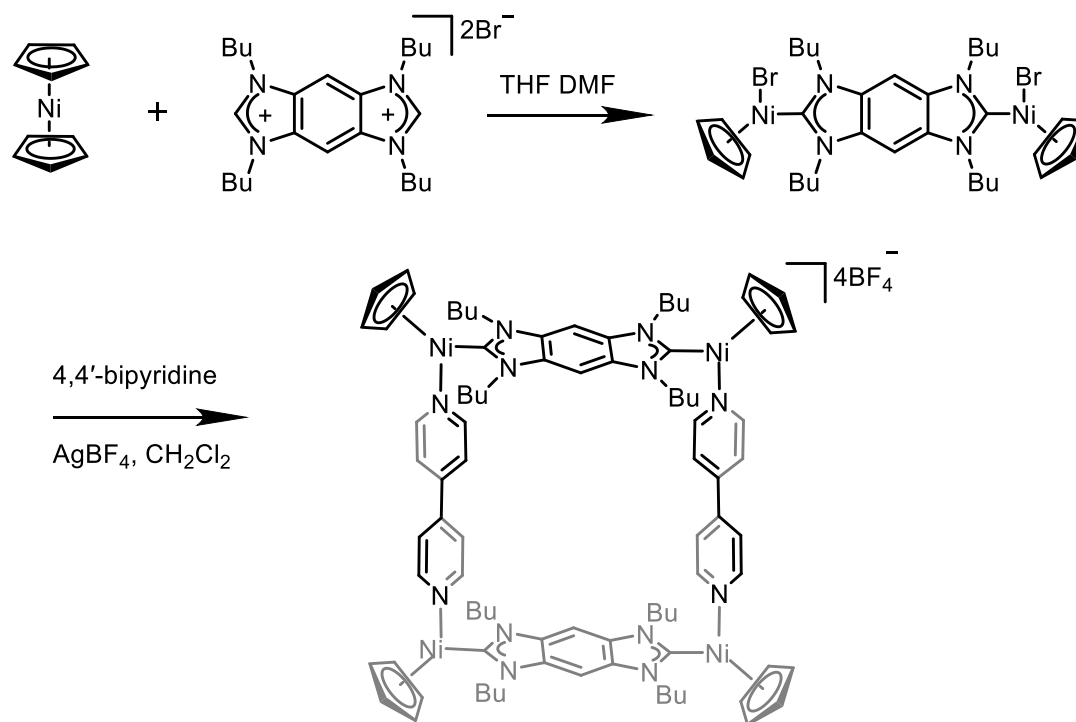
metals other than Cu, Ag, and Au have been found in the formation of a large variety of dinuclear molecular rectangles (refer to the schematic diagram in **Scheme 27**).^{109,111} Different bridging entities between imidazolium have been designed with various wingtip terminal groups.¹⁰⁹ However, due to the flexibility of the bridging moiety, none of the assemblies with structures demonstrated in **Scheme 27** were able to encapsulate guest molecules.¹⁰⁹



Scheme 27. Schematic representation of two design strategy towards metallacycles, the blue rectangle represents flexible to semi-rigid bridging functional groups, include alkyl, alkenyl, ether etc.^{109,111}

Following this modular approach, Hahn introduced the planar poly-conjugated poly-NHC ligands to form more rigid metallorightangles.^{112,113} The first tetranuclear metallorightangle was prepared *via* step-wise assembly as depicted in **Scheme 28**.¹¹³ The end-capped Ni(II) dicarbene intermediate was isolated in 50% yield by deprotonating the bisimidazolium salt with nickelocene in a THF/DMF mixture. The subsequent reaction of the Ni(II) dicarbene intermediate with 4,4'-bipyridine ligands in the presence of AgBF_4 produced the air and water

stable metallorectangle in 43% yield. According to the single crystal X-ray diffraction result, biscarbene ligands were found to have an almost coplanar arrangement with an 11.3 Å separation, and $C_{NHC}-Ni-N$ angles were found to be $94.6(3)-95.4(3)^\circ$.¹¹³

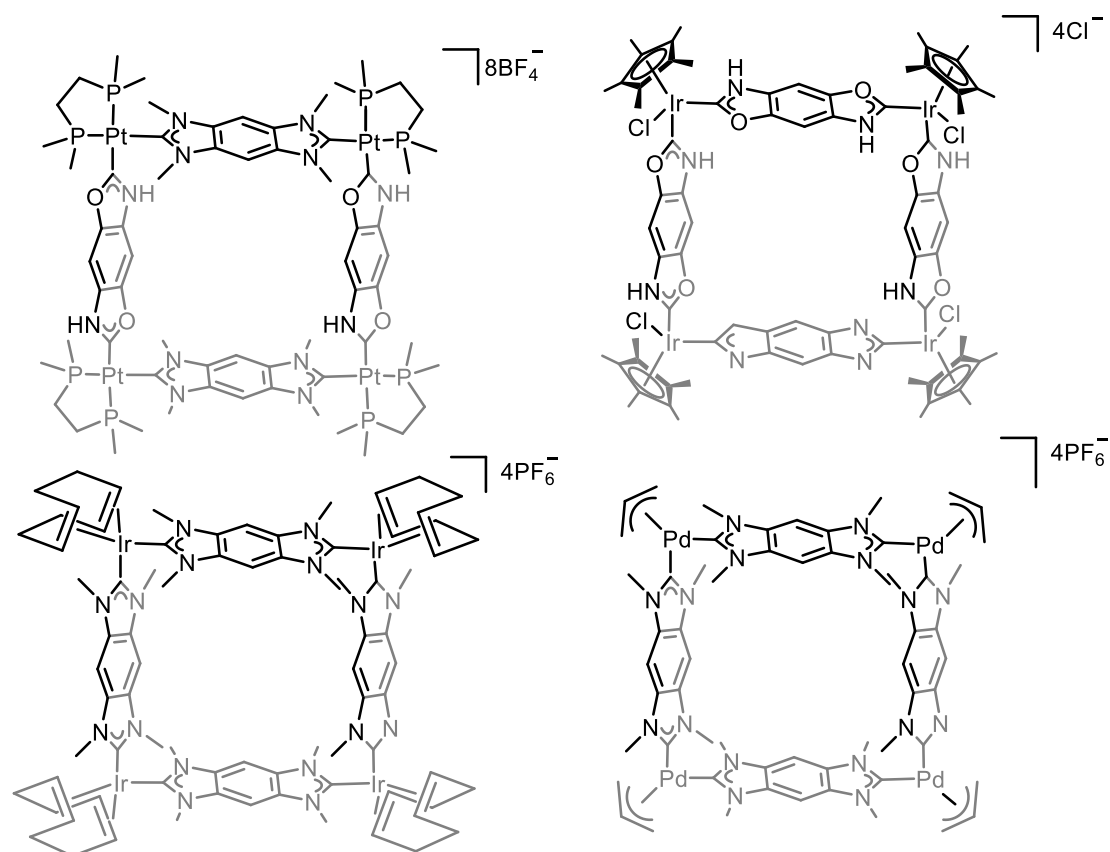


Scheme 28. Step-wise synthesis towards the first Ni(II) metallorectangle.¹¹³

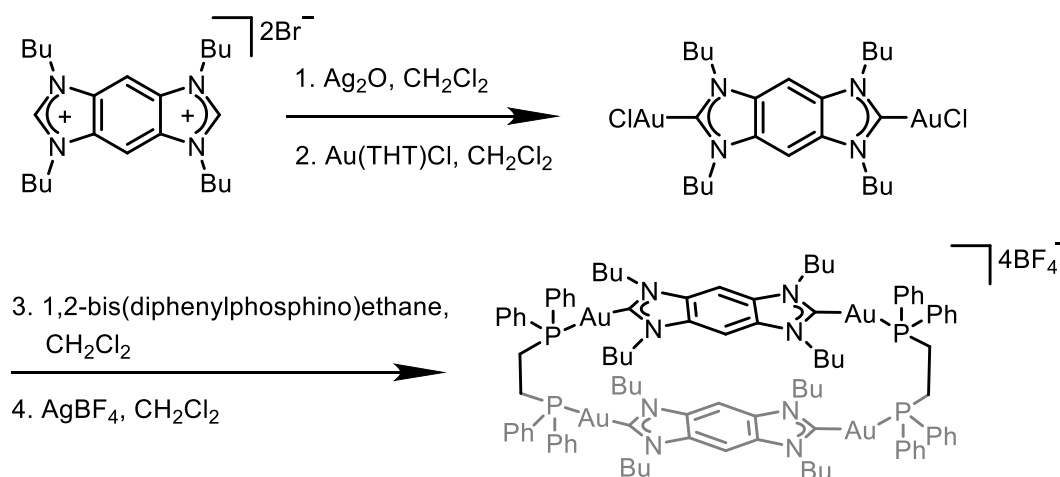
The established successful synthetic strategy was applied to a series of metals, include iridium^{114,115}, platinum¹¹⁶, and palladium¹¹⁴, together with a structurally similar di(NH,O)-NHC ligand and corresponding capping groups (**Scheme 29** top row). Ir(II) and Pd(II) metallosquares were synthesized through the straightforward one-pot strategy, as demonstrated in the synthesis of metallacycles.¹¹⁴ Bisimidazolium salts reacted with [Pd(allyl)Cl]₂ and [IrCl-(COD)]₂ in the presence of Cs₂CO₃ in acetonitrile to produce tetranuclear Pd(II) and Ir(I) octacarbene metallosquares as shown in **Scheme 29** second row.¹¹⁴

The first tetranuclear gold(I) metallorectangle was prepared *via* step-wise assembly described in **Scheme 30**. An initial reaction of the dicationic

benzobisimidazolium salt and Ag_2O yielded the dinuclear silver(I) complex, then *in situ* transmetalation with $\text{Au}(\text{THT})\text{Cl}$ afforded the dinuclear gold(I) complex in 95% yield.¹¹² Then the dinuclear gold intermediate reacted with phosphine bridging ligands in the presence AgBF_4 to produce the gold(I) molecular rectangles in 68% yield. Single crystal X-ray diffraction result revealed that the two phenyl rings were co-planar arranged with 3.3 Å separation.¹¹² The co-planar moieties formed a confined space with surrounding *n*Butyl chains, but only one molar equivalent of diethyl ether was found trapped inside. Peris *et al.* proposed that the distance between two potential coordination sites of dicationic benzobisimidazolium proligand is too short, which prevents large non-solvent guest molecules from entering the supramolecular cavity.¹¹⁷



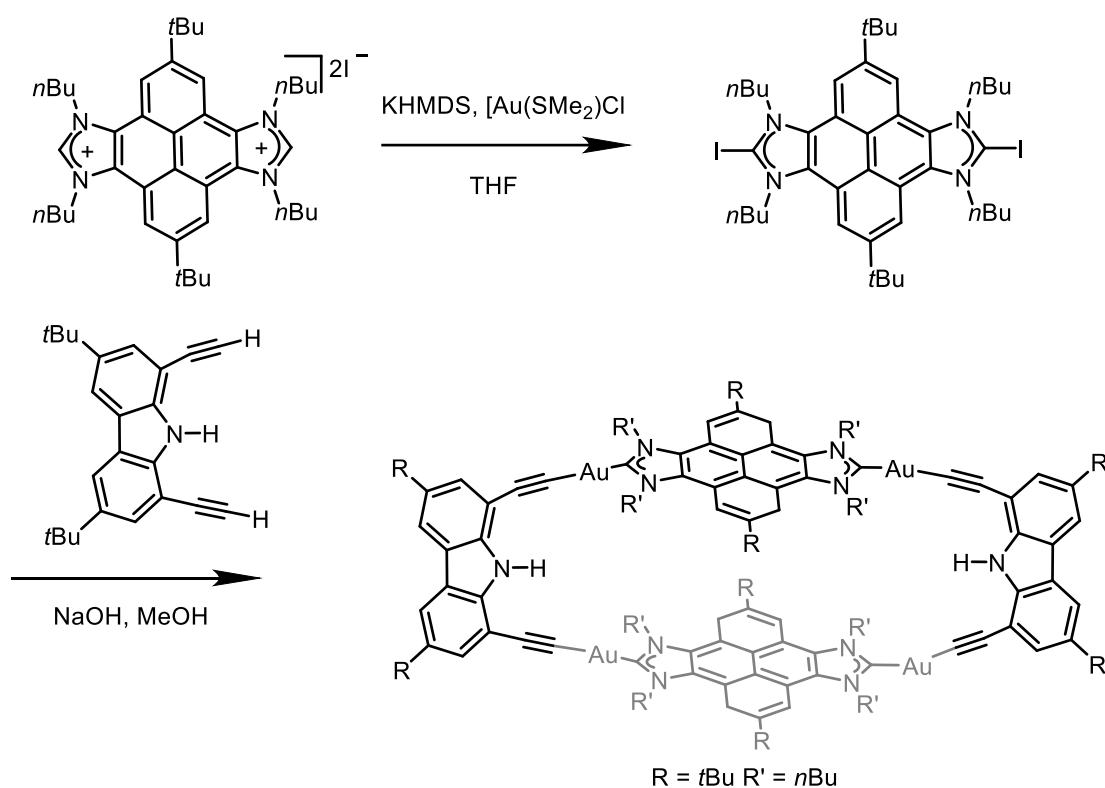
Scheme 29. Examples of iridium, platinum, and palladium NHC-based metallosquares described by Hahn.¹¹⁴⁻¹¹⁶



Scheme 30. Synthesis route of first tetranuclear Au(I) metallorectangle with phosphine and NHC ligands.¹¹²

In the past twenty years, Peris and Bielawski have conducted a series of ground-breaking works in the field of poly-conjugated NHCs.¹¹⁸ Section 1.2.1 in the previous chapter has shown a series of di- and tri- carbenes bearing π -extended cores prepared from these works.¹¹⁹⁻¹²³ The distance between two coordination centers on each edge of metallorectangle can therefore be extended from 10.5 Å for benzobis-(imidazolylidene) ligand to 13.1 Å for pyrenebis(imidazolylidene) ligand.¹¹⁸ The step-wise assembly procedure is depicted in **Scheme 31**. The corresponding pyrenebis(azolium) salt was metallated with $\text{Au}(\text{SMe}_2)\text{Cl}$ in the presence of non-nucleophilic base KHMDS to afford Au(I) dicarbene intermediate in 60% yield. Then the metallorectangle structure was completed by reacting with di-*tert*-butyldiethynyl-carbazole in the presence of NaOH in 71% yield.¹²⁴ The single-crystal X-ray diffraction revealed the co-facial polycyclic-conjugated ligands were separated by 6.6 Å, while the distance between the gold centers bound to the same bis-carbene ligand was 13.1 Å.¹²⁴ The tetragold(I) metallorectangle was found to be able to encapsulate a series of polycyclic aromatic hydrocarbons(PAHs), include anthracene, pyrene, triphenylene, perylene, coronene, and corannulene, which makes this complex a *de facto* metallocage.¹²⁴ The binding affinity

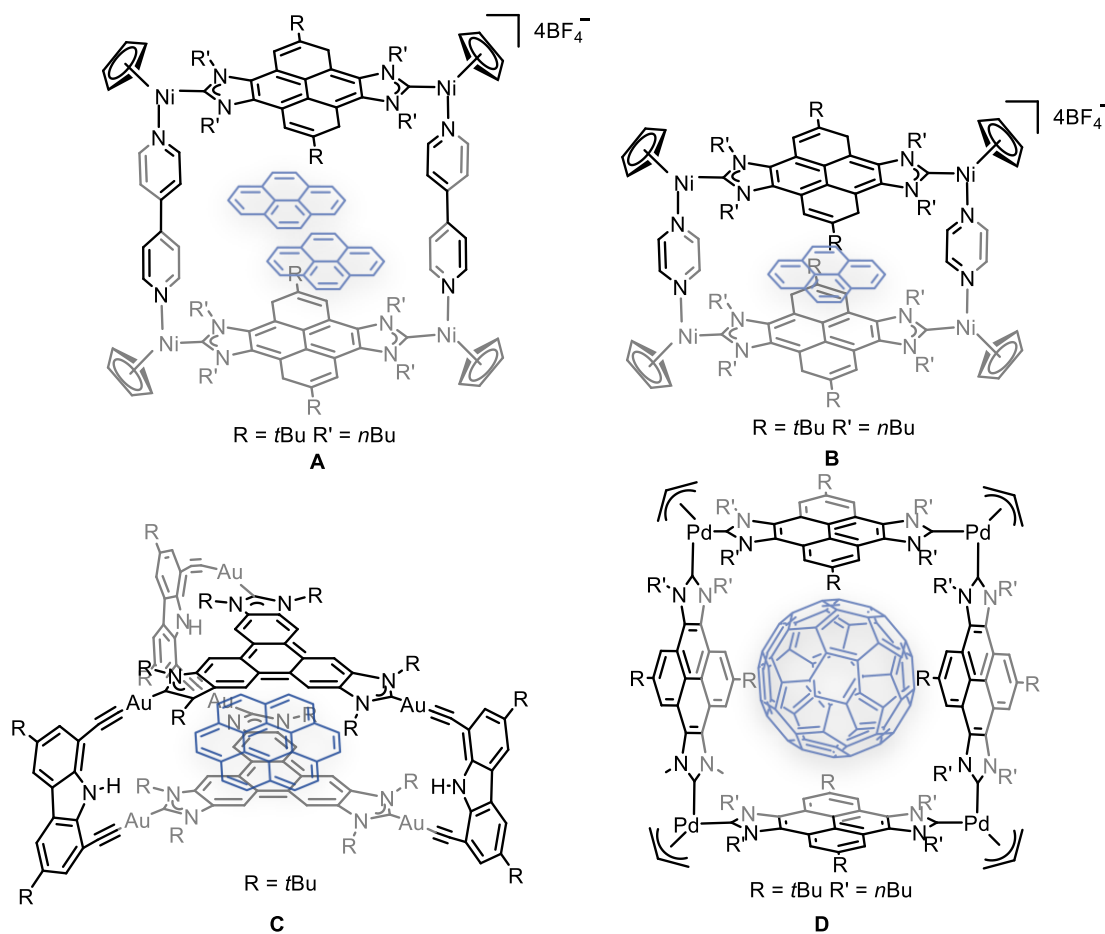
of the host-guest system in CD_2Cl_2 was revealed to exponentially increase with the number of π -electrons of the guest ($1.3 > \log K > 6.6$), with the exception of nonplanar bowl-shaped corannulene. The excellent binding constants are among the highest reported for a metal-containing receptor and are also competitive with organic-based cationic hosts.^{125,126} The binding between host metallogage with nonplanar corannulene molecule resulted in significant compression of the corannulene (16%) and concomitant expansion of the host metallogage, thus shows an unusual case of artificial mutual induced-fit arrangement.¹²⁴



Scheme 31. Synthesis route of tetranuclear Au(I) metallorectangle with conjugated a pyrenebis(imidazolylidene) ligand.¹¹⁸

The di-carbenes bearing π -extended pyrene core were also introduced to the assembly of Ni(II) metallosquares following the synthetic route in **Scheme 28**. In addition, the separation between coplanar NHC ligands modulated by either using 4,4'-bipyridine (**Scheme 32, A**) or shorter pyrazine moiety (**Scheme 32, B**).¹²⁷ Both metallogages were able to

encapsulate small PAHs, such as pyrene.¹²⁷ ¹H NMR spectroscopy titration showed different host-guest stoichiometry of inclusion complexes formed: 1:1 for the pyrazine-based host, and 1:2 for the host containing bipyridine, in accordance with the larger dimensions of the latter.¹²⁷ Similarly, a tris-carbene ligand bearing π -extended cores was used in metallocage assembly following step-wise assembly of **Scheme 31** to afford **Scheme 32, C**, which also exhibits the ability to encapsulate PAHs.¹²⁸

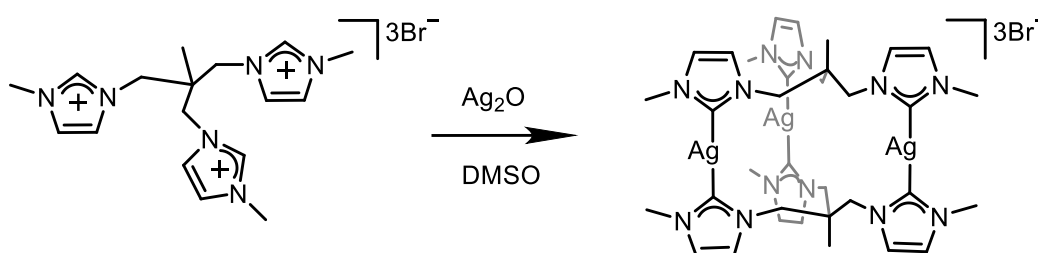


Scheme 32. Examples of metallocages assembled from poly-conjugated "Janus" NHCs.¹²⁷⁻¹²⁹

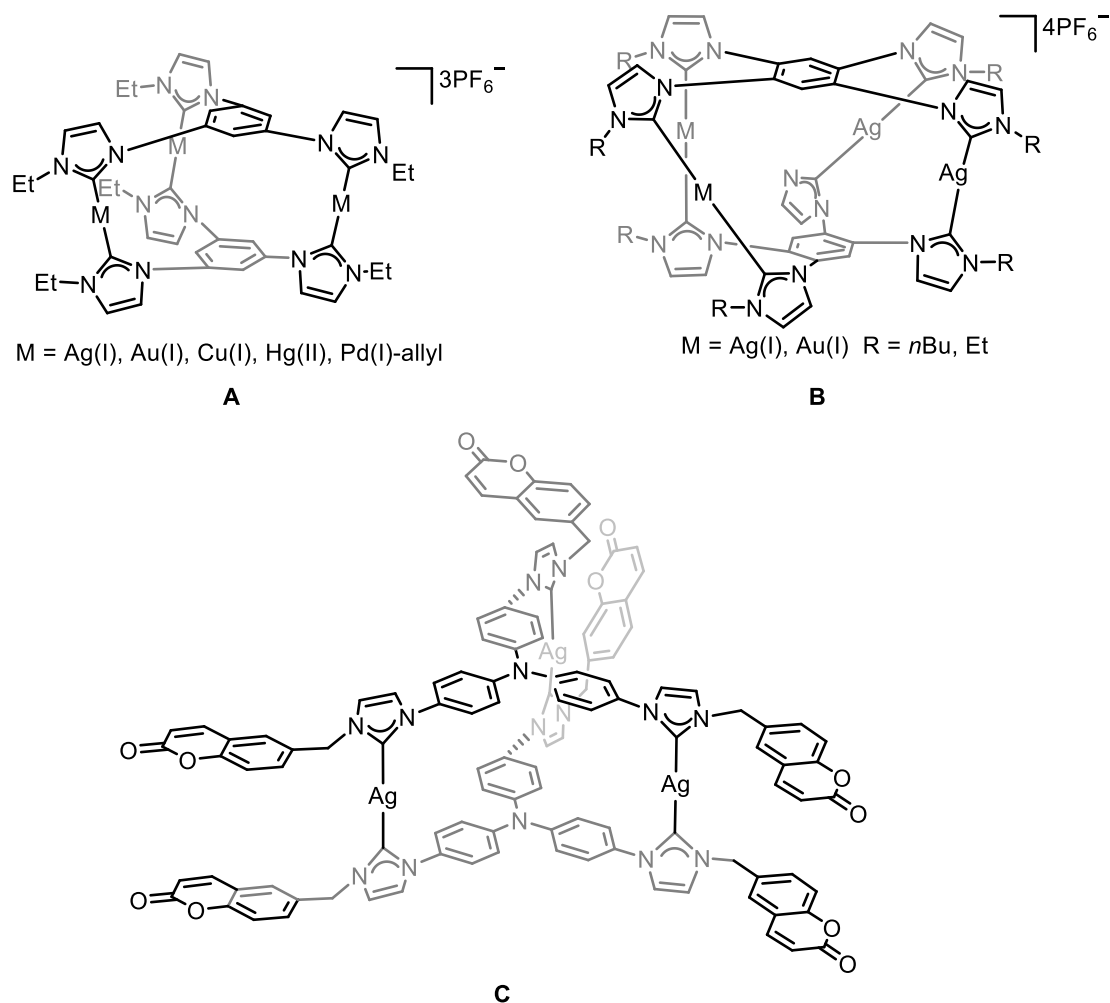
Using the one-pot strategy in the synthesis of metallacycles, the pyrenebis(imidazolylidene) ligand was used for the preparation of palladium(II) metallocage (**Scheme 32, D**).¹²⁸ The palladium(II) metallocage was used to encapsulate fullerenes (C_{60} and C_{70}).¹²⁸ The

metallo-square is shape-adaptable, i.e., its shape can adjust to accommodate the encapsulated fullerene.^{128,130} The host-guest systems were later shown to be efficient photochemically stable singlet oxygen photosensitizers, which underline the potentials of supramolecular systems in the catalysis applications.¹³¹

The first prismatic supramolecular assembly was demonstrated by Meyer and coworkers in 2002.^{132,133} As demonstrated in **Scheme 33**, tripodal pro-ligand was prepared and utilized to prepare cylinder-like metallocages assemblies through a straightforward one-pot strategy.^{132,133} Peris, Han, and Hahn developed several molecular cylinders from diverse triscarbene,¹³⁴⁻¹³⁷ tetracarbene,¹³⁸ and hexacarbene¹³⁹ ligands. A small range of representative molecular cylinders were depicted in **Scheme 34**. It is worth noting that the cylinder **C** in **Scheme 34** could undergo three [2+2]-cycloaddition reactions at their coumarin terminals in the presence of UV-irradiation, the resulting complex is the first example for organometallic complexes bearing cage-like three-dimensional hexacarbene ligands. Subsequent removal of the metal ions resulted in the formation of a three-dimensional hexakisimidazolium cage.¹³⁶



Scheme 33. Synthesis route of first trinuclear Ag(I) cylinder.^{132,133}

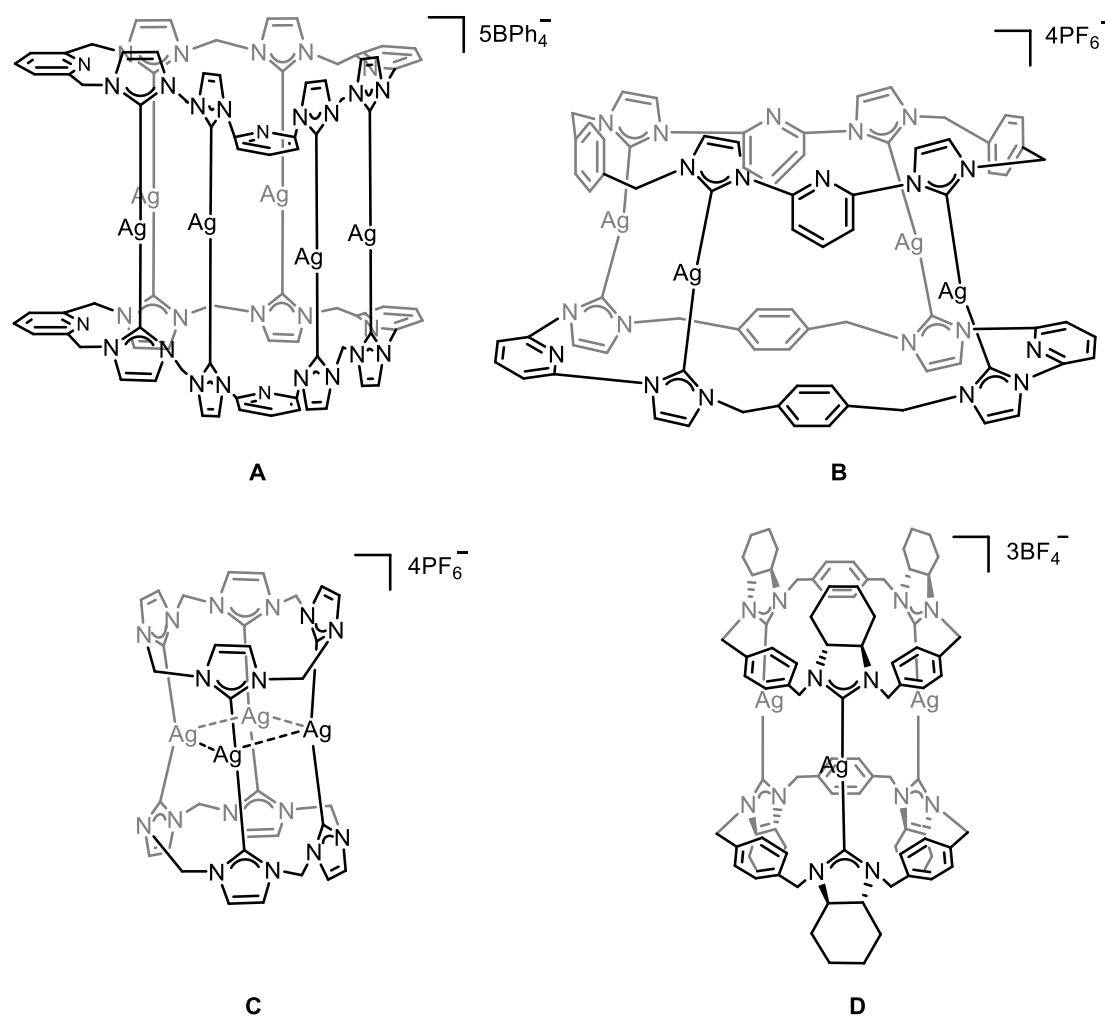
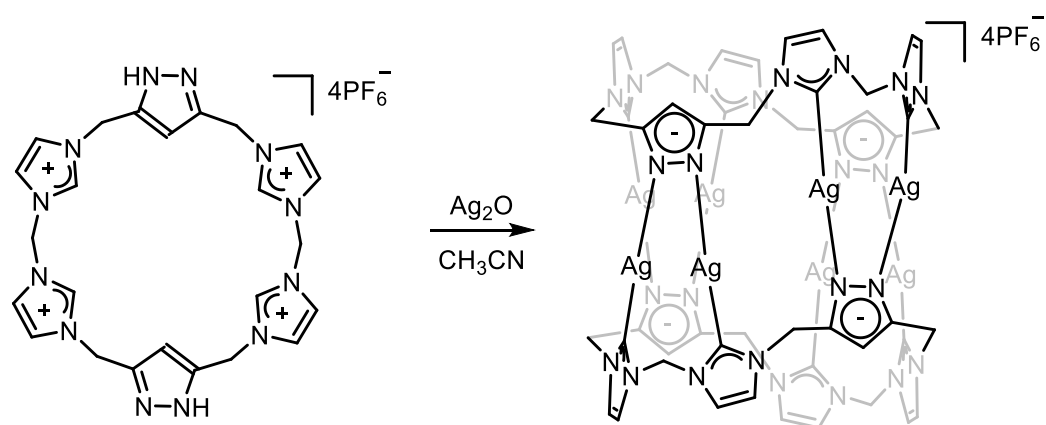


Scheme 34. Examples of molecular cylinders assembled from triscarbene¹³⁴⁻¹³⁶ and tetracarbene¹³⁸ NHC ligands.

In the pursuit of three-dimensional organometallic assemblies, Hahn reported that a hexasilver dodecacarbene cylinder can be obtained serendipitously from two equivalents of a cyclic lutidine bridged hexakisimidazolium salt and Ag₂O in 10% yield (**Scheme 35, A**).¹⁴⁰ The single crystal X-ray diffraction revealed a sandwich-like hexanuclear silver(I) complex structure. The silver atoms formed a slightly distorted hexagonal coordination between the two hexacarbene ligands.¹⁴⁰ Two years later, Sessler and Hahn reported that a structurally similar lutidine and *m*-xylene bridged cyclic tetraimidazolium ligand could react with silver nitrate in the presence of NH₄OH in a water/acetonitrile solvent mixture and produced the

tetrasilver molecular cylinder (**Scheme 35, B**) in 60% yield.¹⁴¹ The single crystal X-ray diffraction result revealed a well-defined, cage-like species that consists of two macrocyclic NHC ligands bridged by four silver atoms. Furthermore, the successful synthesis of tetrasilver molecular cylinder from methylene-bridged tetra(imidazolium) precursor¹⁴² (**Scheme 35, C**) and trissilver chiral molecular cylinder from *p*-xylene-bridged tris(imidazolium) precursor¹⁴³ (**Scheme 35, D**) serves to highlight further the potential utility of imidazolium macrocycles as the template for supramolecular assembly.

Pöthig's research group contributed to this field of macrocycle-templated NHC-based supramolecular assembly in 2016 (see **Scheme 36**).¹⁴⁴ A macrocyclic tetra(imidazolium)octadentate ligand precursor was used as a flexible organic template for the construction of an octanuclear molecular cylinder with defined shape.¹⁴⁴ "Pillarplex" was named for this family of complexes. Pillarplexes possess a tubular shape with a pore that allows for the highly selective encapsulation of linear molecules and were the first kind of supramolecular organometallic complexes to be explicitly used as metallocavitands (as defined by Frischmann and MacLachlan).¹⁴⁵ In 2017, pillarplex was employed as ring components in mechanically interlocked architectures (organometallic rotaxanes).¹⁴⁶

Scheme 35. Examples of molecular cylinders assembled from macrocyclic NHC ligands.¹⁴⁰⁻¹⁴³Scheme 36. Macrocycle-templated supramolecular assembly of octanuclear Ag(I) Pillarplex.¹⁴⁴

2.4 Conclusion of Chapter 2

In two decades of development, the N-heterocyclic carbenes attracted tremendous attention and lead to a multitude of applications across many different fields. The first two sections in this chapter gave an essential introduction to applications of NHCs in catalysis and medicinal chemistry with examples. The strength and stability of the metal-C_{NHC} bonding, and the ability to readily fine-tune the properties of NHC complexes through structural modification of the ligand, explain the importance of NHCs in these applications. The last section of this chapter was dedicated to introducing supramolecular architectures assembled based upon NHCs. Prominent supramolecular scaffolds were summarized with respect to their building strategies and geometries.

2.5 References of Chapter 2

1. H. W. Wanzlick and H. J. Schönherr, *Angew. Chem. Int. Ed. Engl.*, 1968, **7**, 141-142.
2. K. Öfele, *J. Organomet. Chem.*, 1968, **12**, P42-P43.
3. A. J. Arduengo III, R. L. Harlow, M. Kline, *J. Am. Chem. Soc.*, 1991, **113**, 361-363.
4. R. Visbal and M. C. Gimeno, *Chem. Soc. Rev.*, 2014, **43**, 3551-3574.
5. L. Oehninger, R. Rubbiani and I. Ott, *Dalton Trans.*, 2013, **42**, 3269-3284.
6. W. A. Herrmann, M. Elison, J. Fischer, C. Köcher and G. R. J. Artus, *Angew. Chem. Int. Ed. Engl.*, 1995, **34**, 2371-2374.
7. L. D. Vazquez-Serrano and J. M. Buriak, *N - Heterocyclic Carbenes in Synthesis*, 2006, pp. 241-255.
8. P. J. Pérez and M. M. Díaz-Requejo, *N - Heterocyclic Carbenes in Synthesis*, 2006, pp. 257-274.

9. G. Berthon-Gelloz and I. E. Markó, *N - Heterocyclic Carbenes in Synthesis*, 2006, pp. 119-161.
10. M. S. Viciu, R. F. Germaneau, O. Navarro-Fernandez, E. D. Stevens and S. P. Nolan, *Organometallics*, 2002, **21**, 5470-5472.
11. T. Weskamp, W. C. Schattenmann, M. Spiegler and W. A. Herrmann, *Angew. Chem. Int. Ed.*, 1998, **37**, 2490-2493.
12. R. R. Schrock, J. S. Murdzek, G. C. Bazan, J. Robbins, M. DiMare and M. O'Regan, *J. Am. Chem. Soc.*, 1990, **112**, 3875-3886.
13. G. C. Bazan, E. Khosravi, R. R. Schrock, W. J. Feast, V. C. Gibson, M. B. O'Regan, J. K. Thomas and W. M. Davis, *J. Am. Chem. Soc.*, 1990, **112**, 8378-8387.
14. M. Scholl, T. M. Trnka, J. P. Morgan and R. H. Grubbs, *Tetrahedron Lett.*, 1999, **40**, 2247-2250.
15. P. Schwab, M. B. France, J. W. Ziller and R. H. Grubbs, *Angew. Chem. Int. Ed. Engl.*, 1995, **34**, 2039-2041.
16. L. Cavallo, *J. Am. Chem. Soc.*, 2002, **124**, 8965-8973.
17. D. J. Nelson, S. Manzini, C. A. Urbina-Blanco and S. P. Nolan, *Chem. Commun.*, 2014, **50**, 10355-10375.
18. G. C. Bazan, J. H. Oskam, H. N. Cho, L. Y. Park and R. R. Schrock, *J. Am. Chem. Soc.*, 1991, **113**, 6899-6907.
19. S. Beligny and S. Blechert, *N - Heterocyclic Carbenes in Synthesis*, 2006, pp. 1-25.
20. J. Huang, H. J. Schanz, E. D. Stevens and S. P. Nolan, *Organometallics*, 1999, **18**, 5375-5380.
21. J. Huang, E. D. Stevens, S. P. Nolan and J. L. Petersen, *J. Am. Chem. Soc.*, 1999, **121**, 2674-2678.
22. T. Ritter, A. Hejl, A. G. Wenzel, T. W. Funk and R. H. Grubbs, *Organometallics*, 2006, **25**, 5740-5745.
23. D. Bourgeois, A. Pancrazi, L. Ricard and J. Prunet, *Angew. Chem. Int.*

- Ed.*, 2000, **39**, 725-728.
24. A. Gradillas and J. Pérez-Castells, *Angew. Chem. Int. Ed.*, 2006, **45**, 6086-6101.
 25. N. Marion and S. P. Nolan, *Acc. Chem. Res.*, 2008, **41**, 1440-1449.
 26. E. A. B. Kantchev, C. J. O'Brien and M. G. Organ, *Angew. Chem. Int. Ed.*, 2007, **46**, 2768-2813.
 27. J.-P. Corbet and G. Mignani, *Chem. Rev.*, 2006, **106**, 2651-2710.
 28. M. S. Viciu, R. M. Kissling, E. D. Stevens and S. P. Nolan, *Org. Lett.*, 2002, **4**, 2229-2231.
 29. M. S. Viciu, R. F. Germaneau and S. P. Nolan, *Org. Lett.*, 2002, **4**, 4053-4056.
 30. J. Nasielski, N. Hadei, G. Achonduh, E. A. B. Kantchev, C. J. O'Brien, A. Lough and M. G. Organ, *Chem. Eur. J.*, 2010, **16**, 10844-10853.
 31. L.-A. Schaper, S. J. Hock, W. A. Herrmann and F. E. Kühn, *Angew. Chem. Int. Ed.*, 2013, **52**, 270-289.
 32. F. Wang, L.-j. Liu, W. Wang, S. Li and M. Shi, *Coord. Chem. Rev.*, 2012, **256**, 804-853.
 33. R. Zhong, A. C. Lindhorst, F. J. Groche and F. E. Kühn, *Chem. Rev.*, 2017, **117**, 1970-2058.
 34. W. A. Herrmann, *Angew. Chem. Int. Ed.*, 2002, **41**, 1290-1309.
 35. F. E. Hahn and M. C. Jahnke, *Angew. Chem. Int. Ed.*, 2008, **47**, 3122-3172.
 36. T. Scattolin and S. P. Nolan, *Trends. Chem.* 2020, **2**, 721-736.
 37. G. C. Vougioukalakis and R. H. Grubbs, *Chem. Rev.*, 2010, **110**, 1746-1787.
 38. T. Dröge and F. Glorius, *Angew. Chem. Int. Ed.*, 2010, **49**, 6940-6952.
 39. T. Zou, C. T. Lum, C. N. Lok, J. J. Zhang and C. M. Che, *Chem. Soc. Rev.*, 2015, **44**, 8786-8801.
 40. M. Jalal, B. Hammouti, R. Touzani, A. Aouniti and I. Ozdemir, *Mater.*

- Today-Proc.* 2020, **31**, S122-S129.
41. B. Rosenberg, L. Van Camp and T. Krigas, *Nature*, 1965, **205**, 698-699.
 42. B. Rosenberg, L. Van Camp, J. E. Trosko and V. H. Mansour, *Nature*, 1969, **222**, 385-386.
 43. B. Cetinkaya, E. Cetinkaya, H. Küçükbay and R. Durmaz, *Arzneimitt. Forsch.*, 1996, **46**, 821-823.
 44. B. Cetinkaya, I. Ozdemir, B. Binbaşıoğlu, R. Durmaz and S. Günal, *Arzneimitt. Forsch.*, 1999, **49**, 538-540.
 45. E. Çetinkaya, A. Denizci, I. Özdemir, H. T. Öztürk, I. Karaboz and B. Çetinkaya, *J. Chemother.*, 2002, **14**, 241-245.
 46. J. Pernak and A. Skrzypczak, *Eur. J. Med. Chem.*, 1996, **31**, 901-903.
 47. E. S. Antonarakis and A. Emadi, *Cancer Chemother. Pharmacol.*, 2010, **66**, 1-9.
 48. A. Vacca, M. Bruno, A. Boccarelli, M. Coluccia, D. Ribatti, A. Bergamo, S. Garbisa, L. Sartor and G. Sava, *Br. J. Cancer.*, 2002, **86**, 993-998.
 49. S. Leijen, S. A. Burgers, P. Baas, D. Pluim, M. Tibben, E. van Werkhoven, E. Alessio, G. Sava, J. H. Beijnen and J. H. M. Schellens, *Invest. New Drugs.*, 2015, **33**, 201-214.
 50. E. Alessio and L. Messori, *Molecules*, 2019, **24**, 1995.
 51. C. G. Hartinger, M. A. Jakupec, S. Zorbas-Seifried, M. Groessler, A. Egger, W. Berger, H. Zorbas, P. J. Dyson and B. K. Keppler, *Chem. Biodivers.*, 2008, **5**, 2140-2155.
 52. B. S. Murray, M. V. Babak, C. G. Hartinger and P. J. Dyson, *Coord. Chem. Rev.*, 2016, **306**, 86-114.
 53. S. Movassaghi, S. Singh, A. Mansur, K. K. H. Tong, M. Hanif, H. U. Holtkamp, T. Söhnle, S. M. F. Jamieson and C. G. Hartinger, *Organometallics*, 2018, **37**, 1575-1584.
 54. G. Lv, L. Guo, L. Qiu, H. Yang, T. Wang, H. Liu and J. Lin, *Dalton Trans.*, 2015, **44**, 7324-7331.

55. F. Guarra, A. Pratesi, C. Gabbiani and T. Biver, *J. Inorg. Biochem.*, 2021, **217**, 111355.
56. H. J. Klasen, *Burns*, 2000, **26**, 117-130.
57. C. A. Moyer, L. Brentano, D. L. Gravens, H. W. Margraf and W. W. Monafo, JR., *Arch Surg.*, 1965, **90**, 812-867.
58. C. L. Fox, Jr., *Arch Surg.*, 1968, **96**, 184-188.
59. A. Melaiye, R. S. Simons, A. Milsted, F. Pingitore, C. Wesdemiotis, C. A. Tessier and W. J. Youngs, *J. Med. Chem.*, 2004, **47**, 973-977.
60. A. Melaiye, Z. Sun, K. Hindi, A. Milsted, D. Ely, D. H. Reneker, C. A. Tessier and W. J. Youngs, *J. Am. Chem. Soc.*, 2005, **127**, 2285-2291.
61. B. Dominelli, J. D. G. Correia and F. E. Kühn, *J. Organomet. Chem.*, 2018, **866**, 153-164.
62. M. Mora, M. C. Gimeno and R. Visbal, *Chem. Soc. Rev.*, 2019, **48**, 447-462.
63. İ. Özdemir, A. Denizci, H. T. Öztürk and B. Çetinkaya, *Appl. Organomet. Chem.*, 2004, **18**, 318-322.
64. M. N. Lone, Zubaid-ul-khazir, G. N. Yattoo, J. A. Banday and I. A. Wani, *Advances in Metallodrugs: Preparation and Applications in Medicinal Chemistry*, 2020, pp. 247-271.
65. B. Bertrand and A. Casini, *Dalton Trans.*, 2014, **43**, 4209-4219.
66. S. J. Berners-Price and A. Filipovska, *Metallomics*, 2011, **3**, 863-873.
67. O. Rackham, A.-M. J. Shearwood, R. Thyer, E. McNamara, S. M. K. Davies, B. A. Callus, A. Miranda-Vizueté, S. J. Berners-Price, Q. Cheng, E. S. J. Arnér and A. Filipovska, *Free Radic. Biol. Med.*, 2011, **50**, 689-699.
68. S. P. Fricker, *Metallomics*, 2010, **2**, 366-377.
69. A. Bindoli, M. P. Rigobello, G. Scutari, C. Gabbiani, A. Casini and L. Messori, *Coord. Chem. Rev.*, 2009, **253**, 1692-1707.
70. P. J. Barnard, M. V. Baker, S. J. Berners-Price and D. A. Day, *J. Inorg.*

- Biochem.*, 2004, **98**, 1642-1647.
71. M. V. Baker, P. J. Barnard, S. J. Berners-Price, S. K. Brayshaw, J. L. Hickey, B. W. Skelton and A. H. White, *Dalton Trans.*, 2006, **30**, 3708-3715.
 72. J. L. Hickey, R. A. Ruhayel, P. J. Barnard, M. V. Baker, S. J. Berners-Price and A. Filipovska, *J. Am. Chem. Soc.*, 2008, **130**, 12570-12571.
 73. S. Sundelacruz, M. Levin and D. L. Kaplan, *Stem Cell Rev. Rep.*, 2009, **5**, 231-246.
 74. R. Rubbiani, S. Can, I. Kitanovic, H. Alborzinia, M. Stefanopoulou, M. Kokoschka, S. Mönchgesang, W. S. Sheldrick, S. Wölfl and I. Ott, *J. Med. Chem.*, 2011, **54**, 8646-8657.
 75. R. Rubbiani, L. Salassa, A. de Almeida, A. Casini and I. Ott, *ChemMedChem.*, 2014, **9**, 1205-1210.
 76. D. Wragg, A. de Almeida, R. Bonsignore, F. E. Kühn, S. Leoni and A. Casini, *Angew. Chem. Int. Ed.*, 2018, **57**, 14524-14528.
 77. S. K. Fung, T. Zou, B. Cao, P.-Y. Lee, Y. M. E. Fung, D. Hu, C.-N. Lok and C.-M. Che, *Angew. Chem. Int. Ed.*, 2017, **56**, 3892-3896.
 78. C. M. Crudden, J. H. Horton, I. I. Ebralidze, O. V. Zenkina, A. B. McLean, B. Drevniok, Z. She, H.-B. Kraatz, N. J. Mosey, T. Seki, E. C. Keske, J. D. Leake, A. Rousina-Webb and G. Wu, *Nat. Chem.*, 2014, **6**, 409-414.
 79. C. M. Crudden, J. H. Horton, M. R. Narouz, Z. Li, C. A. Smith, K. Munro, C. J. Baddeley, C. R. Larrea, B. Drevniok, B. Thanabalasingam, A. B. McLean, O. V. Zenkina, I. I. Ebralidze, Z. She, H.-B. Kraatz, N. J. Mosey, L. N. Saunders and A. Yagi, *Nat. Commun.*, 2016, **7**, 12654.
 80. A. V. Zhukhovitskiy, M. G. Mavros, T. Van Voorhis and J. A. Johnson, *J. Am. Chem. Soc.*, 2013, **135**, 7418-7421.
 81. G. Wang, A. Rühling, S. Amirjalayer, M. Knor, J. B. Ernst, C. Richter, H.-J. Gao, A. Timmer, H.-Y. Gao, N. L. Doltsinis, F. Glorius and H. Fuchs, *Nat. Chem.*, 2017, **9**, 152-156.

82. J. D. Scholten, G. Ebeling and J. Dupont, *Dalton Trans.*, 2007, **47**, 5554-5560.
83. J. F. DeJesus, L. M. Sherman, D. J. Yohannan, J. C. Becca, S. L. Strausser, L. F. P. Karger, L. Jensen, D. M. Jenkins and J. P. Camden, *Angew. Chem. Int. Ed.*, 2020, **59**, 7585-7590.
84. L. Du, N. A. Nosratabad, Z. Jin, C. Zhang, S. Wang, B. Chen and H. Mattoussi, *J. Am. Chem. Soc.*, 2021, **143**, 1873-1884.
85. R. W. Y. Man, C. H. Li, M. W. A. MacLean, O. V. Zenkina, M. T. Zamora, L. N. Saunders, A. Rousina-Webb, M. Nambo and C. M. Crudden, *J. Am. Chem. Soc.*, 2018, **140**, 1576-1579.
86. L. Deng and R. H. Holm, *J. Am. Chem. Soc.*, 2008, **130**, 9878-9886.
87. C. Fliedel and P. Braunstein, *Organometallics*, 2010, **29**, 5614-5626.
88. L. Jin, D. S. Weinberger, M. Melaimi, C. E. Moore, A. L. Rheingold and G. Bertrand, *Angew. Chem. Int. Ed.*, 2014, **53**, 9059-9063.
89. S. Thanneeru, K. M. Ayers, M. Anuganti, L. Zhang, C. V. Kumar, G. Ung and J. He, *J. Mater. Chem. C*, 2020, **8**, 2280-2288.
90. A. M. Ortiz, P. Gómez-Sal, J. C. Flores and E. de Jesús, *Organometallics*, 2014, **33**, 600-603.
91. S. Gonell, M. Poyatos and E. Peris, *Chem. Eur. J.*, 2014, **20**, 5746-5751.
92. C. I. Ezugwu, N. A. Kabir, M. Yusubov and F. Verpoort, *Coord. Chem. Rev.*, 2016, **307**, 188-210.
93. Y. Jiang, X. Zhang and H. Fei, *Dalton Trans.*, 2020, **49**, 6548-6552.
94. Y. Dong, W.-H. Li and Y. B. Dong, *J. Org. Chem.*, 2021, **86**, 1818-1826.
95. R. Chakrabarty, P. S. Mukherjee and P. J. Stang, *Chem. Rev.*, 2011, **111**, 6810-6918.
96. T. R. Cook and P. J. Stang, *Chem. Rev.*, 2015, **115**, 7001-7045.
97. M. Fujita and K. Ogura, *Bull. Chem. Soc. Jpn.*, 1996, **69**, 1471-1482.
98. S. R. Seidel and P. J. Stang, *Acc. Chem. Res.*, 2002, **35**, 972-983.
99. L. J. Chen, H. B. Yang and M. Shionoya, *Chem. Soc. Rev.*, 2017, **46**,

- 2555-2576.
100. P. Wang, X. Miao, Y. Meng, Q. Wang, J. Wang, H. Duan, Y. Li, C. Li, J. Liu and L. Cao, *ACS Appl. Mater. Interfaces.*, 2020, **12**, 22630-22639.
 101. T. Rodenas, I. Luz, G. Prieto, B. Seoane, H. Miro, A. Corma, F. Kapteijn, F. X. L. i Xamena and J. Gascon, *Nat. Mater.* 2015, **14**, 48-55.
 102. W. Xuan, C. Zhu, Y. Liu and Y. Cui, *Chem. Soc. Rev.*, 2012, **41**, 1677-1695.
 103. T. R. Cook, Y. R. Zheng and P. J. Stang, *Chem. Rev.*, 2013, **113**, 734-777.
 104. J. M. Lehn, *Aust. J. Chem.*, 2010, **63**, 611-623.
 105. J. M. Lehn, *Chem. Soc. Rev.*, 2007, **36**, 151-160.
 106. P. T. Corbett, J. Leclaire, L. Vial, K. R. West, J. L. Wietor, J. K. M. Sanders and S. Otto, *Chem. Rev.*, 2006, **106**, 3652-3711.
 107. C. Boehme and G. Frenking, *Organometallics*, 1998, **17**, 5801-5809.
 108. A. Pöthig and A. Casini, *Theranostics*, 2019, **9**, 3150-3169.
 109. M.-M. Gan, J. Q. Liu, L. Zhang, Y. Y. Wang, F. E. Hahn and Y. F. Han, *Chem. Rev.*, 2018, **118**, 9587-9641.
 110. C. A. Quezada, J. C. Garrison, M. J. Panzner, C. A. Tessier and W. J. Youngs, *Organometallics*, 2004, **23**, 4846-4848.
 111. N. Sinha and F. E. Hahn, *Acc. Chem. Res.*, 2017, **50**, 2167-2184.
 112. C. Radloff, J. J. Weigand and F. E. Hahn, *Dalton Trans.*, 2009, **43**, 9392-9394.
 113. F. E. Hahn, C. Radloff, T. Pape and A. Hepp, *Organometallics*, 2008, **27**, 6408-6410.
 114. N. Sinha, F. Roelfes, A. Hepp and F. E. Hahn, *Chem. Eur. J.*, 2017, **23**, 5939-5942.
 115. F. M. Conrady, R. Fröhlich, C. Schulte to Brinke, T. Pape and F. E. Hahn, *J. Am. Chem. Soc.*, 2011, **133**, 11496-11499.
 116. H. V. R. Dias and W. Jin, *Tetrahedron Lett.*, 1994, **35**, 1365-1366.

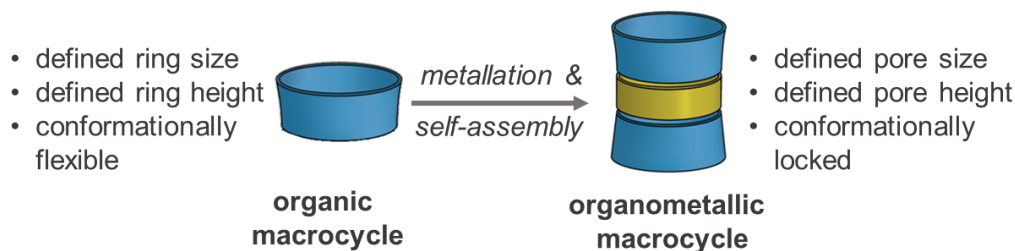
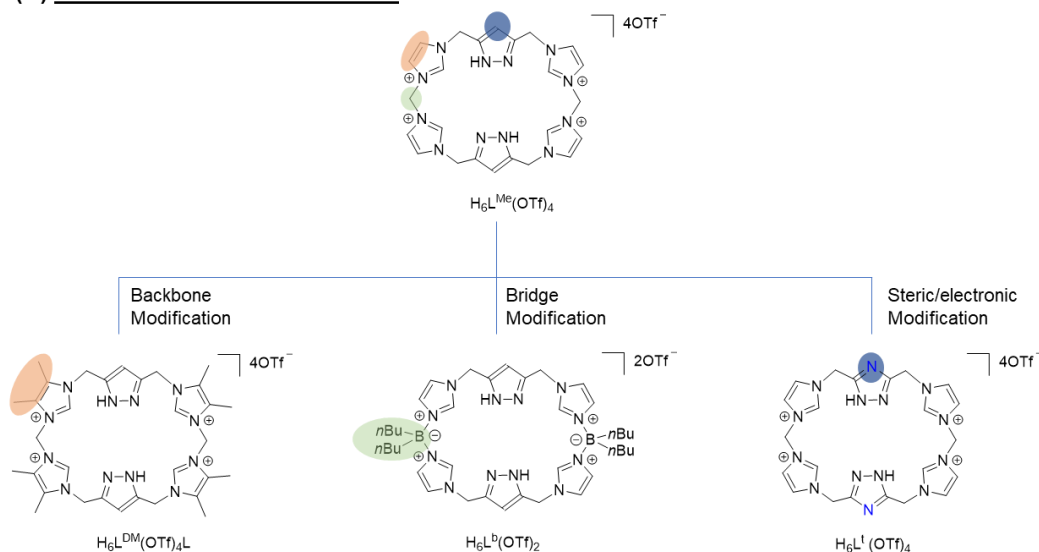
117. S. Ibáñez, M. Poyatos and E. Peris, *Acc. Chem. Res.*, 2020, **53**, 1401-1413.
118. E. Peris, *Chem. Commun.*, 2016, **52**, 5777-5787.
119. A. J. Boydston, K. A. Williams and C. W. Bielawski, *J. Am. Chem. Soc.*, 2005, **127**, 12496-12497.
120. A. J. Boydston, J. D. Rice, M. D. Sanderson, O. L. Dykhno and C. W. Bielawski, *Organometallics*, 2006, **25**, 6087-6098.
121. D. M. Khramov, A. J. Boydston and C. W. Bielawski, *Angew. Chem.*, 2006, **118**, 6332-6335.
122. A. J. Boydston and C. W. Bielawski, *Dalton Trans.*, 2006, **34**, 4073-4077.
123. K. A. Williams and C. W. Bielawski, *Chem. Commun.*, 2010, **46**, 5166-5168.
124. S. Ibáñez and E. Peris, *Angew. Chem. Int. Ed.*, 2020, **59**, 6860-6865.
125. J. C. Barnes, M. Juriček, N. L. Strutt, M. Frasconi, S. Sampath, M. A. Giesener, P. L. McGrier, C. J. Bruns, C. L. Stern, A. A. Sarjeant and J. F. Stoddart, *J. Am. Chem. Soc.*, 2013, **135**, 183-192.
126. E. J. Dale, N. A. Vermeulen, A. A. Thomas, J. C. Barnes, M. Juriček, A. K. Blackburn, N. L. Strutt, A. A. Sarjeant, C. L. Stern, S. E. Denmark and J. F. Stoddart, *J. Am. Chem. Soc.*, 2014, **136**, 10669-10682.
127. V. Martínez-Agramunt, S. Ruiz-Botella and E. Peris, *J. Am. Chem. Soc.*, 2017, **23**, 6675-6681.
128. S. Ibáñez and E. Peris, *Angew. Chem. Int. Ed.*, 2019, **58**, 6693-6697.
129. V. Martínez - Agramunt, T. Eder, H. Darmandeh, G. Guisado - Barrios and E. Peris, *Angew. Chem. Int. Ed.*, 2019, **58**, 5682-5686.
130. E. V. Peris, C. Vicent, V. Martinez-Agramunt, V. Gandhi, C. Larriba-Andaluz and D. Gusev, *Angew. Chem. Int. Ed.*, 2021, DOI: 10.1002/anie.202100914.
131. V. Martínez-Agramunt and E. Peris, *Inorg. Chem.*, 2019, **58**, 11836-11842.

132. X. Hu, Y. Tang, P. Gantzel and K. Meyer, *Organometallics*, 2003, **22**, 612-614.
133. X. Hu, I. Castro-Rodriguez, K. Olsen and K. Meyer, *Organometallics*, 2004, **23**, 755-764.
134. R. Maity, A. Rit, C. Schulte to Brinke, C. G. Daniliuc and F. E. Hahn, *Chem. Commun.*, 2013, **49**, 1011-1013.
135. A. Rit, T. Pape and F. E. Hahn, *Organometallics*, 2011, **30**, 6393-6401.
136. L. Y. Sun, N. Sinha, T. Yan, Y. S. Wang, T. T. Tan, L. Yu, Y. F. Han and F. E. Hahn, *Angew. Chem. Int. Ed.*, 2018, **57**, 5161-5165.
137. Y.-W. Zhang, R. Das, Y. Li, Y.-Y. Wang and Y.-F. Han, *Chem. Eur. J.*, 2019, **25**, 5472-5479.
138. A. Rit, T. Pape, A. Hepp and F. E. Hahn, *Organometallics*, 2011, **30**, 334-347.
139. C. Segarra, G. Guisado-Barrios, F. E. Hahn and E. Peris, *Organometallics*, 2014, **33**, 5077-5080.
140. F. E. Hahn, C. Radloff, T. Pape and A. Hepp, *Chem. Eur. J.*, 2008, **14**, 10900-10904.
141. C. Radloff, H.-Y. Gong, C. Schulte to Brinke, T. Pape, V. M. Lynch, J. L. Sessler and F. E. Hahn, *Chem. Eur. J.*, 2010, **16**, 13077-13081.
142. P. J. Altmann, D. T. Weiss, C. Jandl and F. E. Kühn, *Chem. Asian J.*, 2016, **11**, 1597-1605.
143. D. Wang, B. Zhang, C. He, P. Wu and C. Duan, *Chem. Commun.*, 2010, **46**, 4728-4730.
144. P. J. Altmann and A. Pöthig, *J. Am. Chem. Soc.*, 2016, **138**, 13171-13174.
145. P. D. Frischmann and M. J. MacLachlan, *Chem. Soc. Rev.*, 2013, **42**, 871-890.
146. P. J. Altmann and A. Pöthig, *Angew. Chem. Int. Ed.*, 2017, **56**, 15733-15736.

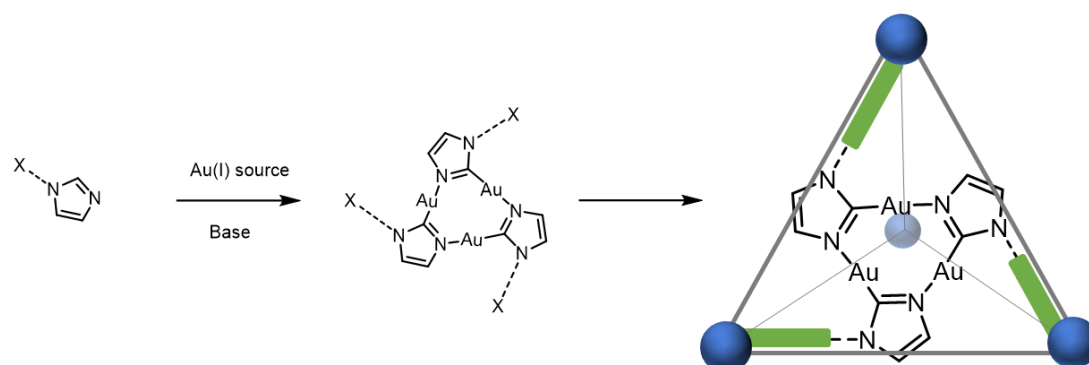
3. Objective

Macrocyclic ligand templated supramolecular assembly has recently been demonstrated to form organometallic pillarplex (concept of the templation approach shown in **Scheme 37, A**). According to the definition by Schmidt and Würthner, this kind of NHC based macrocyclic building blocks fulfills the criteria of “supramolecular element”. Given the advantage of easy preparation, structural and electronic versatility of NHC ligands, it is envisioned that a facile functionalization of the original pillarplex ligand towards desired supramolecular properties could be easily achieved. Hence, based on the successful pillarplex assembly with pyrazolate/imidazolate hybrid proligand $\text{H}_6\text{L}^{\text{Me}}(\text{OTf})_4$, three ligand modification approaches were envisaged as depicted in **Scheme 37, B**. Therefore, the initial aim of this work is to synthesize three tetracarbene macrocycle ligand precursors. Subsequently, the macrocyclic ligand scaffolds shall be attempted for supramolecular assembly. Furthermore, the molecular structure of the respective coinage metal complexes was examined, to evaluate the influence of ligand modification on final complex structures.

In the light of recent advancements in self-assembled tetrahedral coordination cage, a new type of supramolecular compound was designed. Cyclic trinuclear complexes (CTCs) – the simplest polynuclear metal cluster – could act as the building block. An illustration of the concept is shown in **Scheme 38**. To evaluate the potential of CTCs for supramolecular organometallic complexes (SOCs) assembly, the synthesis, non-covalent interactions and relevant photophysical properties of imidazolate-based Au(I) CTCs were studied.

(A) Macrocytic Templatation Strategy**(B) Potential Modifications Route**

Scheme 37. **A.** Concept of macrocycle template approach for SOC assembly; **B.** Potential modifications of tetracarbenic macrocycle ligand precursors.



Scheme 38. Envisioned supramolecular structure synthesized from N-substituted imidazole, X represents functional group utilized for supramolecular assembly, blue balls represent nodes moieties of a tetrahedron supramolecular structure, green rectangles represent linkage between cyclic trinuclear complex and tetrahedron nodes.

4. Result and Discussion

4.1 Biological Activity & Stability Studies of Pillarplex*

*This chapter uses material from “Pöthig, A., Ahmed, S., Winther-Larsen, H. C., Guan, S., Altmann, P. J., Kudermann, J., ... & Høgmoen Åstrand, O. A. (2018). Antimicrobial activity and cytotoxicity of Ag (I) and Au (I) pillarplexes. *Frontiers in Chemistry*, 6, 584.” Reproduced with the Copyright © 2018 Pöthig, Ahmed, Winther-Larsen, Guan, Altmann, Kudermann, Santos Andresen, Gjøen and Høgmoen Åstrand.

4.1.1 Abstract

UV-Vis titration studies of four pillarplex compounds featuring different metals and anions were carried out to check for stability depending on pH and chloride concentration changes and evaluate the applicability in physiological media. The biological activity of four pillarplex compounds was evaluated by determining the toxicity against four bacterial strains (*B. subtilis* (ATCC6633), *S. aureus* (ATCC6538), *E. coli* (UVI isolate), *P. aeruginosa*), one fungus (*C. albicans*) and a human cell line (HepG2). All compounds are bioactive: the silver compounds are less stable than gold compounds and showed higher activity against bacteria and fungi. The corresponding gold pillarplexes are more stable but less toxic against human cells.

4.1.2 Introduction

Since the early 2000s, coinage metal complexes featuring N-heterocyclic carbenes (NHC) – a ligand class with a facile tunability towards steric bulkiness, electronics and solubility – have been employed as bioactive compounds.¹⁻³ As

introduced in Chapter 2.2, Youngs and coworkers investigated the antimicrobial behavior of silver(I) NHC complexes (see **Figure 9, A**).^{4,5} In this example, the slow release of silver ions originating from the decomposition of the NHC complex is expected to be the cause of its antimicrobial ability against *Escherichia coli*, *Staphylococcus aureus*, and *Pseudomonas aeruginosa*.⁶ Its effect can be rationalized by the comparably labile metal-carbene bond (with respect to other late transition metal-NHC bonds).⁶ Beyond silver complexes, more stable gold(I) NHC complexes were also employed in studies investigating their antibiotic potential.⁷ One possible target is enzymes bearing residual thiol or selenol groups, e.g. thioredoxin reductase, accompanied by the inhibition of the enzyme, which is similar to the mode of action proposed for the approved metallodrug Auranofin.^{8,9} This is expected in particular for gold(I) mono-carbene complexes, which can dissociate one (labile non-NHC) ligand to coordinate the sulfur or selenium atom.¹⁰⁻¹⁸ Apart from the enzymatic targeting, Casini and coworkers reported a class of Au(I) di-caffeine NHC complexes (**Figure 9, B**) were able to stabilize G4 quadruplex DNA structures, inhibiting telomerase activity.¹⁹⁻²² Hereby, the overall structure of the intact complex (being planar, cationic, and possessing a conjugated system for stacking) determines its ability to interact in a non-covalent binding, forming supramolecular aggregates.

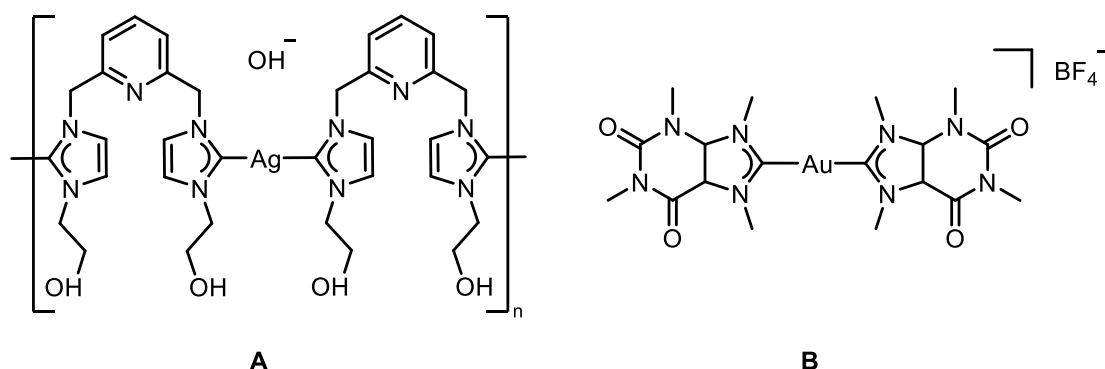


Figure 9. Examples of coinage metal NHC complexes with biomedical applications.^{4,5,19-21}

A related supramolecular recognition of biomolecules causing bioactivity was discovered by Hannon and coworkers, who were using cylindrical metal helicates $[\text{Fe}_2\text{L}_3]\text{Cl}_4$ ($\text{L} = \text{N,N}'\text{-(methylenebis(4,1-phenylene))bis(1-pyridinyl-methanimine)}$), **Figure 10** – a class of supramolecular coordination complexes (SCCs) – to specifically recognize various unusual DNA or RNA structures, e.g. Y-shaped three-way junctions.²³⁻²⁸ The remarkable supramolecular recognition arises from the two features of the Fe(II) complex: high overall positive charge with Fe^{2+} ions located on the terminal promotes the electrostatic interaction between the cationic helicates and negatively charged DNA phosphate moiety; hydrophobic surfaces constructed with aromatic parts of the ligands tend to form π -stacking structures with thymine and adenine at the Y-shaped three-way junctions.²⁷ In general, such supramolecular coordination compounds are often regarded as promising candidates for future applications as metallodrugs or drug delivery systems.²⁹

Another class of SCCs that emerged in biomedical applications is the metallocage. In contrast to small bioactive metal complexes that only have intrinsic anticancer properties, large-sized metallocages were often studied as drug delivery systems in addition to the intrinsic properties of their building components.^{30,31} Mukherjee and coworkers reported a tubular cage $[\text{Pt}_8\text{L}_4(\text{en})_3](\text{NO}_3)_{16}$ ($\text{en} = \text{ethane-1,2-diamine}$, $\text{L} = \text{tetrapyridinyl-benzo}[c][1,2,5]\text{thiadiazole-4,7-diamine}$, **Figure 10**) can be used to inhibit the growth of Gram-positive and Gram-negative bacteria.³⁰ In addition, its hydrophobic cavity can accommodate hydrophobic drugs like curcumin in an aqueous medium.³²

The pillarplex compound, reported by Pöthig and Altmann in 2016, is a new family of SOCs (see **Figure 10**).³³ This family of compound has a cylindrical shape, which constitutes an octanuclear coinage metal core with two coordinating macrocyclic NHC ligands on the rim. Compared with Mukherjee's tubular cage, which can encapsulate aromatic molecules³³, the pillarplex has a

slim pore, which only allows for encapsulation of linear guest molecules.³⁰ The organic relative of pillarplex – the pillararene^{34,35}, have been applied in biomedical applications recently.³⁶ Zhang and Sun reported the encapsulated complex of carboxylated pillar[6]arene and oxaliplatin exhibited reduced cytotoxicity towards normal cells and improved anticancer ability than oxaliplatin.³⁶ In this application, the pillararene showed no bioactivity and acted as carriers for actual metallodrug, modulate the release of metallodrug.³⁶ In the case of pillarplexes, due to their in-built functionality (e.g. luminescence, easily tunable solubility) caused by the coinage metal-complex character, the pillarplexes are more versatile than pillararenes.^{34,35} Pillarplexes combine the possibilities to behave as metallodrug, i.e., exhibit intrinsic cellular toxic properties, with the possible applications of cavitands.

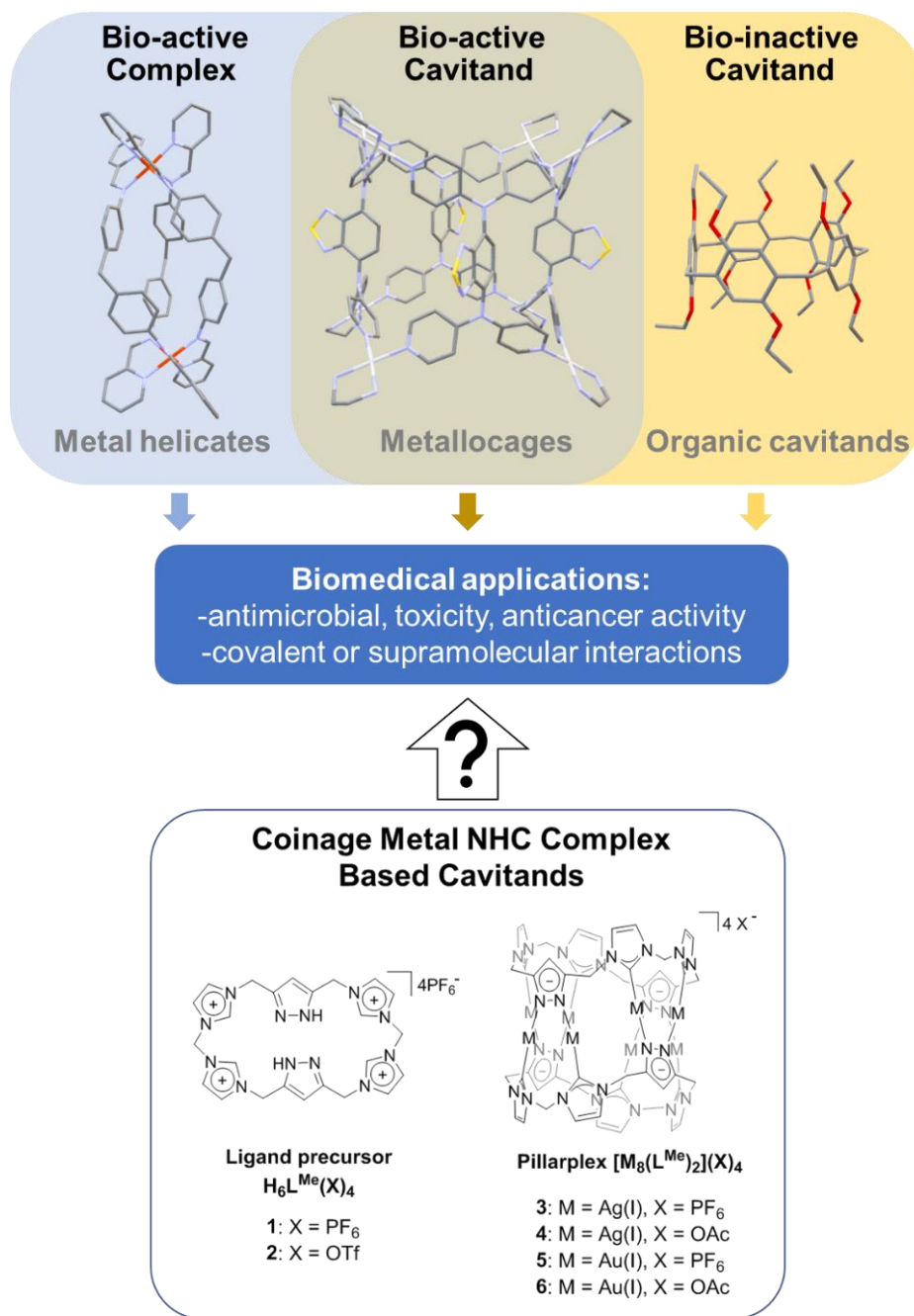


Figure 10. Up: Overview of related known biomedical relevant compound classes.^{27,30,32,37} Down: NHC-based organometallocavitands including precursor investigated in this study. Adapted with permission from Ref. 38.

Therefore, to explore the future potential of pillarplexes in the biomedical context, co-authors and I conducted toxicity and stability studies. Winther-Larsen and Santos Andresen tested the antimicrobial activity of the four metal complexes (**Figure 10, 3-6**), the metal salts as well as the ligand precursor salts

(**Figure 10, 1, 2**) towards four different bacterial strains (*B. subtilis* (ATCC6633), *S. aureus* (ATCC6538), *E. coli* (UVI isolate), *P. aeruginosa*) and one fungus (*C. albicans*). Miconazole nitrate, Tetracycline, Gentamycin sulphate as well as AgNO_3 and AuCl_3 were included as controls. The toxicity of the complexes towards a human cell line (HepG2) was also evaluated to clarify if related future research directions might be promising to follow. Finally, I conducted a stability study of the pillarplexes towards changes in pH and chloride ion concentration, which has implications on the use of the compounds under physiological conditions.

4.1.3 Results and Discussion

4.1.3.1 Antimicrobial Activity Studies

Antimicrobial activity was measured using the disc diffusion assay by Winther-Larsen and Santos Andresen. The antimicrobial experiment results and discussion were reproduced from Ref. 38. Details of experiments can be found in Ref. 38. Results revealed that both silver pillarplexes (**3** and **4**) shown antimicrobial activity against all bacterial strains as well as the fungus. Compared with the Miconazole nitrate, Tetracycline, Gentamycin sulphate, the overall activity of **3** and **4** is moderate, however, (by means of statistic uncertainty) it is identical to that of AgNO_3 , which has been used as an antibiotic since ancient times.³⁹ Hence, it was suspected that the release of silver ions *via* decomposition of the pillarplexes, is responsible for the antimicrobial activity. Such effect is in agreement with the general behavior of silver(I) NHC complexes, as reported by Youngs and coworkers.^{4,5}

The gold pillarplexes (**5** and **6**) show lower to no bioactivity, when compared with their silver congeners. Compound **6**, the completely water-soluble acetate, shows no activity against any of the microbes, whereas the more lipophilic compound **5** shows a selective moderate activity against Gram-negative *E. coli*

and Gram-positive *S. aureus*. In contrast, the gold(III) salt AuCl_3 shows activity against all bacterial strains in control tests, which of course might be additionally influenced by the redox activity of the gold(III) ion. However, a more probable reason is that the gold pillarplexes are more stable in the physiological environment, therefore not releasing uncoordinated metal ions, which would explain the lower activity. Similarly, if the gold complexes would decompose, similar toxicity as free ligand precursors would be expected. In general, such imidazolium salts are known to be potentially toxic, depending on different factors, e.g. lipophilicity or anions.⁴⁰ In this study, the two macrocyclic polyimidazolium ligand precursors (**1** and **2**, with different anions) show only moderate and very selective toxicity only against the Gram-positive bacteria *S. aureus* and *B. subtilis*. Gram-positive bacteria lack the outer membrane surrounding the cell wall. This outer membrane excludes, by various mechanisms, certain drugs from penetrating the bacterial cell⁴¹ and could be the reason for antimicrobial selectivity of compound **2**. For the latter, no activity at all was observed in the case of the gold pillarplexes, therefore the decomposition of gold complex was ruled out.

4.1.3.2 Cell Toxicity Studies

The toxicity study against human HepG2 liver cells was carried out by Winther-Larsen and Santos Andresen. The results and discussion were reproduced from Ref. 38. Details of experiments can be found in Ref. 38. In general, all tested compounds (**1** to **6**) exhibit biological activity. The silver pillarplexes appear to be more toxic and more active than their gold counterparts.

4.1.3.3 Stability Tests

To evaluate possible reasons for the observations made during the bacterial and cell tests, I conducted a UV-Vis titration study. In detail, I checked the

influence of varying chloride and proton concentrations on the stability or solubility of the pillarplex compounds. I first evaluated the absorption properties of the two water-soluble pillarplex acetates **4** and **6** in aqueous solution, as well as the ligand precursor (**Figure 11, A**). All compounds absorb in the UV range: the silver complex **4** shows an absorption maximum at 226 nm whereas the gold complex **6** absorbs at 245 nm. The ligand precursor **1,2** absorbs at 209 nm. The molar extinction coefficients for the pillarplex compounds at the wavelengths of the individual maximal absorption are $9.33 \cdot 10^4 \pm 6.41 \cdot 10^2 \text{ M}^{-1} \text{ cm}^{-1}$ (**4**) and $1.21 \cdot 10^5 \pm 4.64 \cdot 10^3 \text{ M}^{-1} \text{ cm}^{-1}$ (**6**).

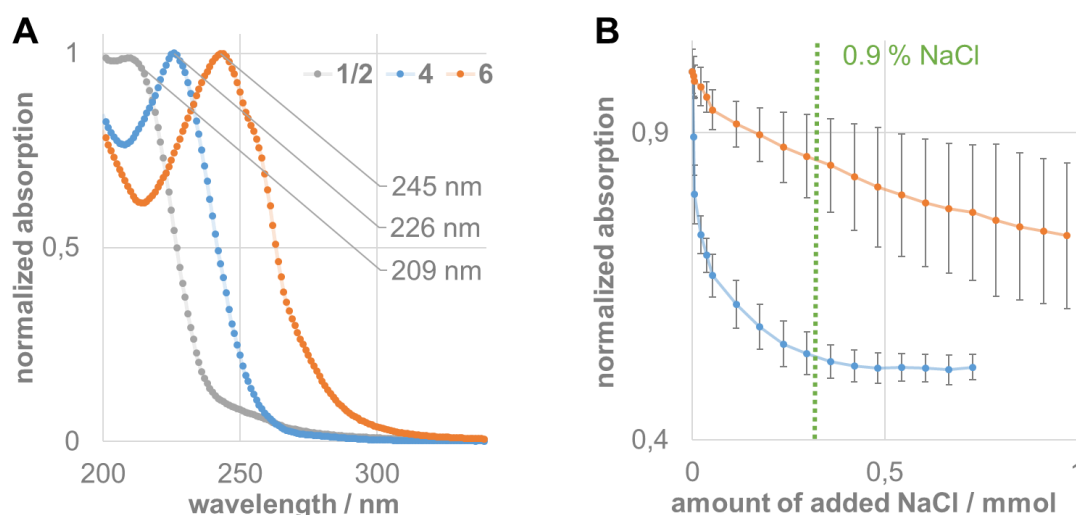


Figure 11.**A**: Normalized UV-Vis absorption spectra of the ligand precursor (grey) and pillarplexes **4** (blue) and **6** (orange). **B**: Titration experiment of compounds **4** (blue) and **6** (orange) against sodium chloride, showing the decay of the normalized signal at the individual absorption maximum (226 nm for **4**, 245 nm for **6**) including statistical uncertainties. Reproduced with permission from Ref. 38.

The titration results of the pillarplexes against an increasing amount of chloride ions present in aqueous solution show a very different behavior of the silver compared to the gold compound (**Figure 11, B**). The absorption signal of silver complex **4** immediately drops up to addition of 0.5 mmol NaCl (which is about 17000-fold excess of chloride). After that, no significant change can be observed in the absorption spectra upon the addition of more equivalents of chloride. In the biological tests, precipitation was observed when adding silver

pillarplexes to 0.9% NaCl solution. The precipitation might be a possible explanation reason for the absorption behavior of **4** in >0.9% chloride concentration solutions.

The gold compound **6** also shows a decay of the absorption signal upon chloride addition. However, the drop is less pronounced and at 0.9% chloride concentration, there is still a significant absorption (85% of the initial value). At higher chloride contents I observed a higher variation of the measured values, which I cannot explain up to now. However, even after the addition of 1 mmol NaCl (about 35000-fold excess), the characteristic absorption band at 245 nm can be observed for compound **6**, strongly indicating that the gold complex is significantly less affected by chloride addition and still present in solution under physiological conditions.

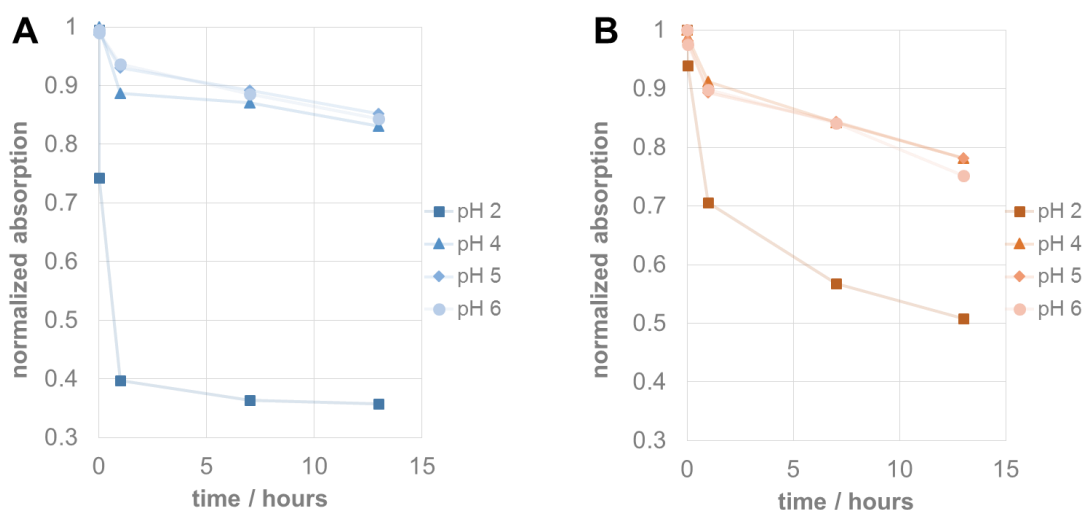


Figure 12. **A**: Stability test at different pH values showing the decay of normalized absorption of silver pillarplex **4** (blue) at 226 nm over time. **B**: Stability test at different pH values showing the decay of normalized absorption of gold pillarplex **6** (blue) at 245 nm over time. Reproduced with permission from Ref. 38.

Figure 12 shows the pH-dependent decay of pillarplex compounds **4** and **6** over time. From the previous work on pillarplex rotaxanes, in the case of silver, the metal ions can be released quickly in the presence of an excess of the strong trifluoromethanesulfonic acid.⁴² This was reproduced also in the case of the empty pillarplex **4** (**Figure 12, A**) for which an immediate drop of absorption

signal at 226 nm was observed at pH 2, indicating very fast decomposition to the protonated imidazolium precursor. The resulting UV-Vis spectrum is also in agreement with that measured for the ligand precursor (**Figure 11, A**). At higher pH values, the decomposition is significantly slower and almost identical for pH 4 – pH 6. A similar behavior was observed for the gold complex **6**, though the decay at pH 2 is significantly slower than that of **4**. Interestingly, at the higher pH values the relative drop if the absorption signal is more pronounced compared to the silver complex. However, in the case of **6**, the resulting absorption spectrum after the assumed decomposition is not resembling that of the ligand precursor, and rather corresponds to the spectrum of **6** just with lower absorption intensity. Therefore, I conducted an NMR experiment to check for protonation of the NHC ligands at pH 2. As a result, no protonated species was detected strongly indicating that the gold pillarplexes are stable even at low pH (see Appendix **Figure S1**).

4.1.4 Conclusion

In general, the silver pillarplexes behaved like similar silver complexes in that they showed antimicrobial and antifungal activity as well as moderate toxicity towards human HepG2 cells. The corresponding gold complexes were inactive against most bacterial strains and fungi, as well as had lower HepG2 toxicity. The observed effects are most likely due to the increased stability of the gold pillarplexes compared to the silver pillarplexes, as evident by the UV-Vis titration experiments and the ^1H NMR study. The fact that the gold complexes seemed so non-toxic and stable could open up the possibility of them being used as drug carriers for selective drug delivery or modified release of drugs that could fit inside the cavity in the pillarplexes.

4.1.5 References of Section 4.1

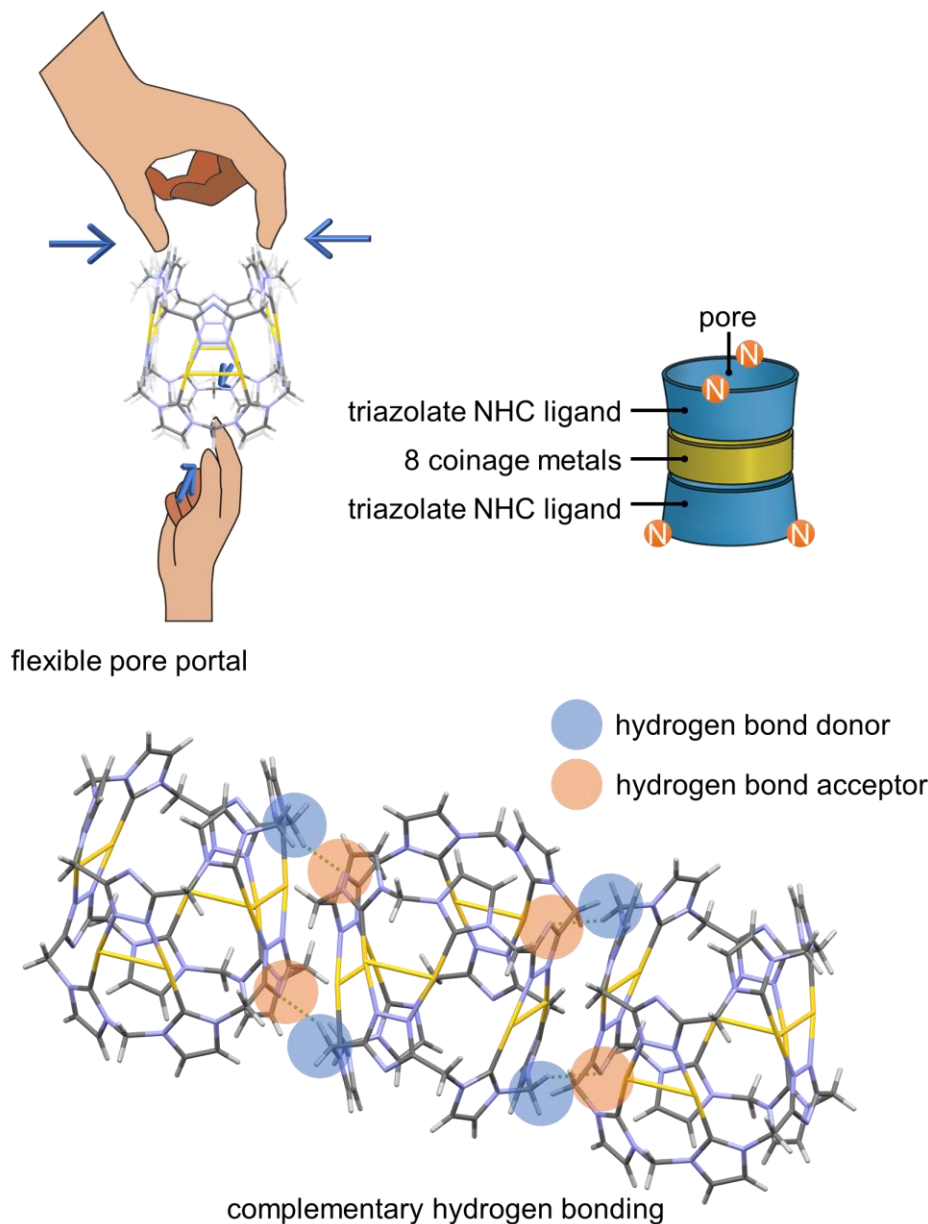
1. W. A. Herrmann, *Angew. Chem. Int. Ed.*, 2002, **41**, 1290-1309.
2. M. N. Hopkinson, C. Richter, M. Schedler and F. Glorius, *Nature*, 2014, **510**, 485-496.
3. L. Mercks and M. Albrecht, *Chem. Soc. Rev.*, 2010, **39**, 1903-1912.
4. A. Kascatan-Nebioglu, M. J. Panzner, J. C. Garrison, C. A. Tessier and W. J. Youngs, *Organometallics*, 2004, **23**, 1928-1931.
5. A. Melaiye, R. S. Simons, A. Milsted, F. Pingitore, C. Wesdemiotis, C. A. Tessier and W. J. Youngs, *J. Med. Chem.*, 2004, **47**, 973-977.
6. A. Kascatan-Nebioglu, M. J. Panzner, C. A. Tessier, C. L. Cannon and W. J. Youngs, *Coord. Chem. Rev.*, 2007, **251**, 884-895.
7. F. Lazreg and C. S. J. Cazin, *N - Heterocyclic Carbenes*, 2014, pp. 173-198.
8. M. V. Baker, P. J. Barnard, S. J. Berners-Price, S. K. Brayshaw, J. L. Hickey, B. W. Skelton and A. H. White, *J. Organomet. Chem.*, 2005, **690**, 5625-5635.
9. E. Schuh, C. Pfluger, A. Citta, A. Folda, M. P. Rigobello, A. Bindoli, A. Casini and F. Mohr, *J. Med. Chem.*, 2012, **55**, 5518-5528.
10. R. Rubbiani, S. Can, I. Kitanovic, H. Alborzinia, M. Stefanopoulou, M. Kokoschka, S. Moenchgesang, W. S. Sheldrick, S. Woelfl and I. Ott, *J. Med. Chem.*, 2011, **54**, 8646-8657.
11. R. Rubbiani, E. Schuh, A. Meyer, J. Lemke, J. Wimberg, N. Metzler-Nolte, F. Meyer, F. Mohr and I. Ott, *MedChemComm*, 2013, **4**, 942-948.
12. X. Cheng, P. Holenya, S. Can, H. Alborzinia, R. Rubbiani, I. Ott and S. Woelfl, *Mol. Cancer*, 2014, **13**, 221/221-221/215.
13. A. Meyer, L. Oehninger, Y. Geldmacher, H. Alborzinia, S. Woelfl, W. S. Sheldrick and I. Ott, *ChemMedChem*, 2014, **9**, 1794-1800.
14. B. Bertrand, A. S. Romanov, M. Brooks, J. Davis, C. Schmidt, I. Ott, M.

- O'Connell and M. Bochmann, *Dalton Trans.*, 2017, **46**, 15875-15887.
15. O. Karaca, V. Scalcon, S. M. Meier-Menches, R. Bonsignore, J. M. J. L. Brouwer, F. Tonolo, A. Folda, M. P. Rigobello, F. E. Kuehn and A. Casini, *Inorg. Chem.*, 2017, **56**, 14237-14250.
 16. C. Schmidt, B. Karge, R. Misgeld, A. Prokop, R. Franke, M. Broenstrup and I. Ott, *Chem. Eur. J.*, 2017, **23**, 1869-1880.
 17. C. Zhang, M.-L. Maddelein, R. Wai-Yin Sun, H. Gornitzka, O. Cuvillier and C. Hemmert, *Eur. J. Med. Chem.*, 2018, **157**, 320-332.
 18. J. F. Arambula, R. McCall, K. J. Sidoran, D. Magda, N. A. Mitchell, C. W. Bielawski, V. M. Lynch, J. L. Sessler and K. Arumugam, *Chem. Sci.*, 2016, **7**, 1245-1256.
 19. B. Bertrand, L. Stefan, M. Pirrotta, D. Monchaud, E. Bodio, P. Richard, P. Le Gendre, E. Warmerdam, M. H. de Jager, G. M. M. Groothuis, M. Picquet and A. Casini, *Inorg. Chem.*, 2014, **53**, 2296-2303.
 20. C. Bazzicalupi, M. Ferraroni, F. Papi, L. Massai, B. Bertrand, L. Messori, P. Gratteri and A. Casini, *Angew. Chem., Int. Ed.*, 2016, **55**, 4256-4259.
 21. O. Karaca, S. M. Meier-Menches, A. Casini and F. E. Kühn, *Chem. Commun.*, 2017, **53**, 8249-8260.
 22. S. M. Meier-Menches, B. Neuditschko, K. Zappe, M. Schaier, M. C. Gerner, K. G. Schmetterer, G. Del Favero, R. Bonsignore, M. Cichna-Markl, G. Koellensperger, A. Casini and C. Gerner, *Chem. Eur. J.*, 2020, **26**, 15528-15537.
 23. I. Meistermann, V. Moreno, M. J. Prieto, E. Moldrheim, E. Sletten, S. Khalid, P. M. Rodger, J. C. Peberdy, C. J. Isaac, A. Rodger and M. J. Hannon, *Proc. Natl. Acad. Sci. U. S. A.*, 2002, **99**, 5069-5074.
 24. A. Oleksi, A. G. Blanco, R. Boer, I. Uson, J. Aymami, A. Rodger, M. J. Hannon and M. Coll, *Angew. Chem., Int. Ed.*, 2006, **45**, 1227-1231.
 25. M. J. Hannon, *Chem. Soc. Rev.*, 2007, **36**, 280-295.
 26. C. Ducani, A. Leczkowska, N. J. Hodges and M. J. Hannon, *Angew.*

- Chem., Int. Ed.*, 2010, **49**, 8942-8945.
27. S. Phongtongpasuk, S. Paulus, J. Schnabl, R. K. O. Sigel, B. Spingler, M. J. Hannon and E. Freisinger, *Angew. Chem., Int. Ed.*, 2013, **52**, 11513-11516.
 28. J. Malina, M. J. Hannon and V. Brabec, *Sci. Rep.*, 2016, **6**, 29674.
 29. A. Casini, B. Woods and M. Wenzel, *Inorg. Chem.*, 2017, **56**, 14715-14729.
 30. S. Bhattacharyya, M. Venkateswarulu, J. Sahoo, E. Zangrando, M. De and P. S. Mukherjee, *Inorg. Chem.*, 2020, **59**, 12690-12699.
 31. T. C. Johnstone, K. Suntharalingam and S. J. Lippard, *Chem. Rev.*, 2016, **116**, 3436-3486.
 32. I. A. Bhat, R. Jain, M. M. Siddiqui, D. K. Saini and P. S. Mukherjee, *Inorg. Chem.*, 2017, **56**, 5352-5360.
 33. P. J. Altmann and A. Pöthig, *J. Am. Chem. Soc.*, 2016, **138**, 13171-13174.
 34. T. Ogoshi, S. Kanai, S. Fujinami, T.-A. Yamagishi and Y. Nakamoto, *J. Am. Chem. Soc.*, 2008, **130**, 5022-5023.
 35. T. Ogoshi, T. A. Yamagishi and Y. Nakamoto, *Chem. Rev.*, 2016, **116**, 7937-8002.
 36. Q. Hao, Y. Chen, Z. Huang, J.-F. Xu, Z. Sun and X. Zhang, *ACS Appl. Mater. Interfaces*, 2018, **10**, 5365-5372.
 37. G. Yu, M. Xue, Z. Zhang, J. Li, C. Han and F. Huang, *J. Am. Chem. Soc.*, 2012, **134**, 13248-13251.
 38. A. Pöthig, S. Ahmed, H. C. Winther-Larsen, S. Guan, P. J. Altmann, J. Kudermann, A. M. Santos Andresen, T. Gjøen and O. A. Høgmoen Åstrand, *Front. Chem.*, 2018, **6**, 584.
 39. G. Danscher and L. J. Locht, *Histochem. Cell Biol.*, 2010, **133**, 359-366.
 40. J. Gravel and A. R. Schmitzer, *Org. Biomol. Chem.*, 2017, **15**, 1051-1071.
 41. R. E. W. Hancock, *Trends Microbiol.*, 1997, **5**, 37-42.
 42. J. Altmann Philipp and A. Pöthig, *Angew. Chem., Int. Ed.*, 2017, **56**,

15733-15736.

4.2 Rim-Modified Pillarplexes



*The picture illustrates the basic concept of macrocycle-templated NHC-based supramolecular organometallic complexes (SOCs) formation, as well as the structure and intermolecular interactions of the first shape-adaptive triazolane-based pillarplex.

**This chapter uses material from “S. Guan, T. Pickl, C. Jandl, L. Schuchmann,

X. Zhou, P. J. Altmann and A. Pöthig, Triazolate-based pillarplexes: shape-adaptive metallocavitands *via* rim modification of macrocyclic ligands, *Org. Chem. Front.*, 2021, Advance Article, DOI: 10.1039/D1QO00588J.” Reproduced by permission of The Royal Society of Chemistry.

4.2.1 Abstract

The success of pyrazolate based pillarplex has driven the development of supramolecular metallocavitand. The unique structure of pillarplexes and its easy synthesis have promoted me to extend this supramolecular family. With similar macrocycle synthesis strategies, new classes of hybrid imidazolium cyclophane ($\text{H}_6\text{L}^{\text{t}}(\text{OTf})_4$, $\text{H}_6\text{L}^{\text{DM}}(\text{OTf})_4$, $\text{H}_6\text{L}^{\text{b}}(\text{OTf})_2$) with defined ring sizes were prepared and investigated as ligand precursors, serving as supramolecular elements in the subsequent supramolecular organometallic complexes (SOCs) self-assembly.

Out of three kinds of imidazolium based macrocyclic ligand precursors investigated, the hybrid imidazolium/triazole cyclophane $\text{H}_6\text{L}^{\text{t}}(\text{OTf})_4$ demonstrated the successful supramolecular assembly. The new pillarplexes in part behave similarly to previously reported pyrazolate-based congeners, e.g., regarding luminescence or host-guest properties. In contrast, for the Au(I) complex, an unprecedented shape adaptive behavior is observed in the solid-state, caused by the additional nitrogen atoms being present in the rim and rationalized by DFT calculations. Additionally, complementary hydrogen bonding between the cationic complexes is observed, proving that the rim modification not only modulates the flexibility of the cavitand but is also a tool to introduce further functionality into the SOC.

4.2.2 Introduction

The supramolecular organometallic complexes (SOCs) have been introduced in Chapter 2. Some representative examples of two- and three-dimensional NHC-based SOC were selected and shown in **Figure 13**. Pioneering work towards SOC synthesis was performed by Bielawski and coworkers,^{1,2} who established Janus-type bis-NHC ligands. Following a modular macrocyclization strategy, Hahn explored the assembly of rectangular- and square-shaped SOC with different planar benzobis-NHC ligands (**Figure 13, A**).^{3,4} Han and coworkers extended the structural variety of these compounds by variation of the bridging motifs between the metal centers, with examples ranging from di- and tetranuclear metallorectangles,⁵⁻⁷ to tetranuclear metallosquares (2D),⁸ and tri-, tetra, and hexa-nuclear metalloprisms/cylinders (3D) (**Figure 13, B**).⁹⁻¹¹ While many SOC based on this structural motif have been reported, few of them were tested for host-guest applications.^{12,13} Among them, Peris and coworkers recently introduced metallocages consisting of extended π -conjugated bis-NHC linkers (**Figure 13, C–D**) used for the efficient encapsulation of polycyclic aromatic hydrocarbons.¹⁴⁻¹⁷

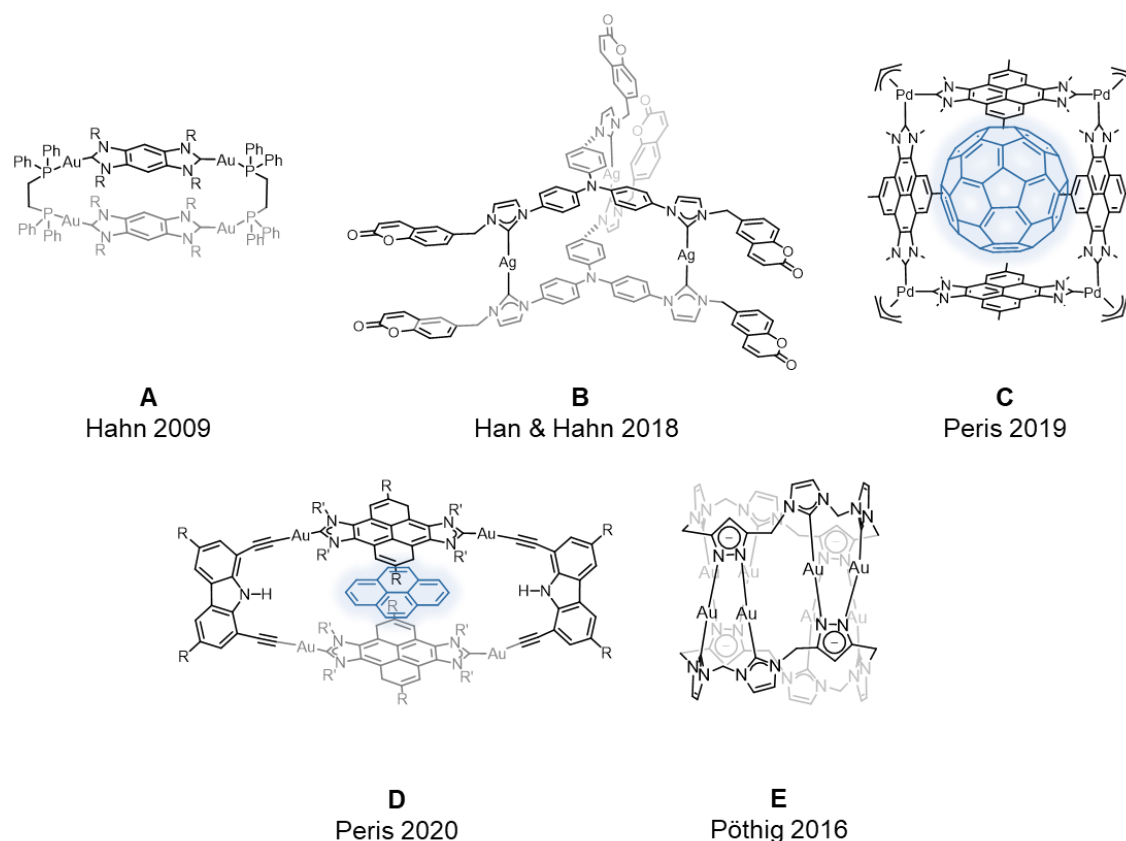
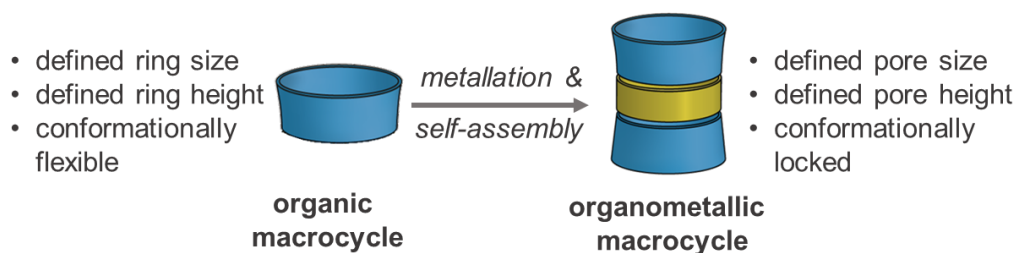
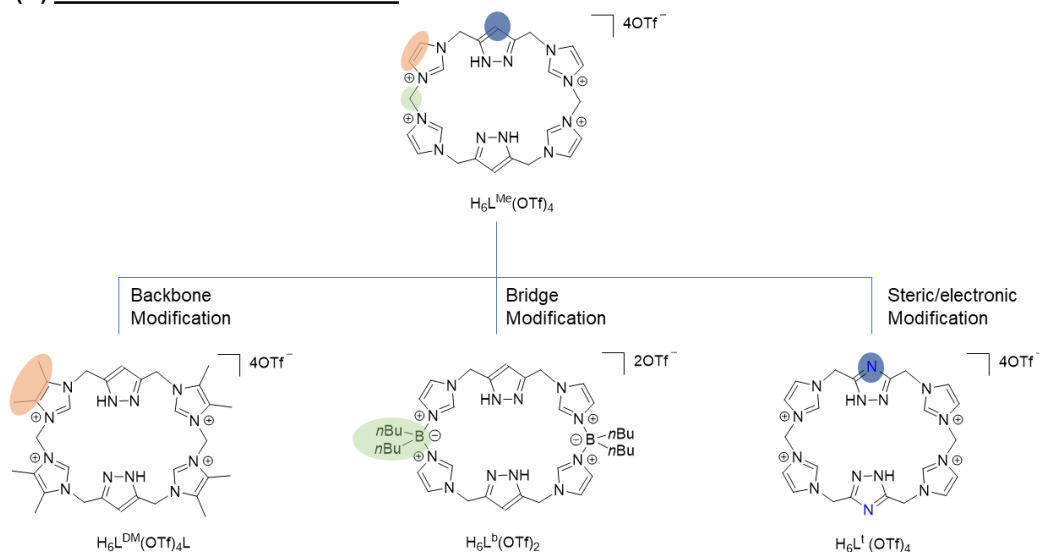


Figure 13. Examples of NHC-based supramolecular organometallic complexes (SOCs) and metallocavitands.^{3,4,8-11,14-18} Reproduced with permission from Ref. 19.

My group's (PD Dr. Pöthig group) first contribution to the field of macrocycle-templated NHC-based SOC in host-guest assemblies was reported in 2016.¹⁸ Altmann and Pöthig demonstrated that a macrocyclic imidazolium salt, a compound class prominent in supramolecular chemistry,^{20,21} can act as an NHC ligand precursor for a new SOC sub-family: the pillarplexes $[M_8L^{Me_2}](X)_4$ ($M = Ag, Au$; $X = OAc, OTf, PF_6$) (**Figure 13E**).^{18,22,23} Here, the multidentate NHC ligand serves as a template for the SOC. This fulfills the criteria of a "supramolecular element", as recently coined by Schmidt and Würthner.²⁴ The derived pillarplexes possess a tubular shape with a pore that allows for the highly selective encapsulation of linear molecules and was the first SOC to be explicitly used as metallocavitands (as defined by Frischmann and MacLachlan).²⁵

(A) Macrocylic Templatation Strategy**(B) Potential Modifications Route**

Scheme 39. **A.** Concept of macrocycle template approach for SOC assembly; **B.** Potential modifications of tetracarbenic macrocycle ligand precursors. Adapted from Ref. 19 with permission from The Royal Society of Chemistry.

Herein, to further explore the macrocycle template approach for SOC formation (**Scheme 39, A**), three macrocyclic ligands as potential supramolecular elements were envisioned as depicted in **Scheme 39, B**. Compared to the pyrazolate/imidazolate hybrid proligand $H_6L^{Me}(OTf)_4$ used in initially reported pillarplexes, proligand $H_6L^{DM}(OTf)_4$ bearing 4,5-dimethyl-1*H*-imidazolium have additional steric-demanding methyl groups. It was envisaged that the four methyl groups could be assembled to a taller SOC than initially reported pillarplexes. There are only three reports that described the coordination nature of methyl backbone modified imidazol-2-ylidene,²⁶⁻²⁸ and none of its coinage metal complexes has been reported, this further motivated me to investigate this species.

In the design of $\text{H}_6\text{L}^{\text{b}}(\text{OTf})_2$ proligand, the incorporation of a negative-charged borate bridge into the macrocyclic framework would, in this context, be beneficial for several reasons. A major drawback of initially reported pillarplex compounds is their charge, as the high oxidation state restrains their solubility to polar solvents.¹⁸ Jenkins and coworkers reported the first neutral metal tetracarbene complexes prepared from macrocyclic imidazolium borate ligand precursors, which exhibit good solubility in nonpolar solvents, paved the pathway of this strategy.²⁹ Additionally, borate building blocks should lead to an improved electron-donating ability of the carbene carbon atoms, which might result in enhanced stabilization of the metal centers. This electron donation comparison can be investigated through spectroscopic methods as introduced in Chapter 1.4,³⁰ as well as DFT calculations.^{31,32}

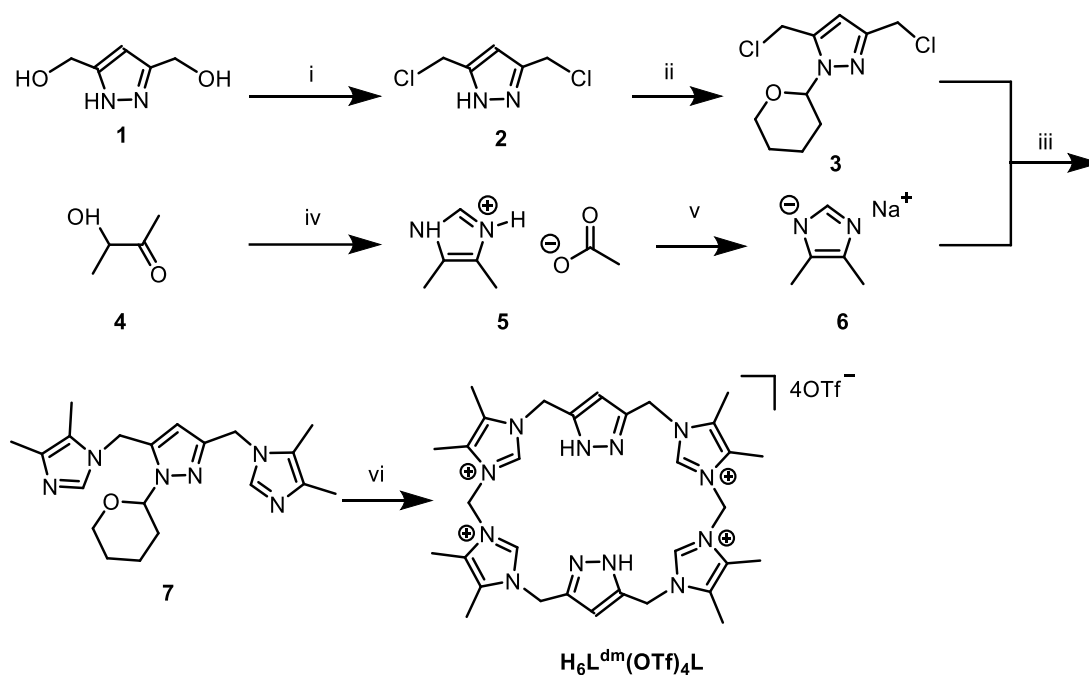
The introduction of a macrocyclic 1,2,4-triazolate/imidazolate hybrid proligand $\text{H}_6\text{L}^{\text{t}}(\text{OTf})_4$ as a supramolecular element allows the tuning in both electronic and steric properties of resulting SOCs. Compared to pyrazole, 1,2,4-triazole has an additional *N*-donor site. In principle, this allows for more variable coordination chemistry. For example, a bridging mode of non-adjacent nitrogen atoms has been observed in dinuclear ruthenium and osmium complexes of triazoles with chelating substituents.³³⁻³⁶ In some instances, all three nitrogens of triazole are involved in coordinative bonding, e.g., to bridge three metal ions, as observed in a Zn complex and some MOFs.^{34,37,38} 1,2,4-triazoles have even already been incorporated into macrocyclic imidazolium ligands in early works by Alcalde et al.^{39,40} However, the reported Ru complexes only show monodentate N-coordination of the triazole ligand.⁴¹ The motivation for the introduction of triazole as a substitute for pyrazole into the ligand design of pillarplexes is manifold: First, in agreement with the above examples, different coordination modes of the macrocyclic NHC ligand could be expected, leading to a coinage metal complex with a geometry different from the pillarplexes. If successfully incorporated into pillarplex architectures, the triazolate-based

ligands could also structurally change the rim of the tubular compound: In total, four unbound nitrogen atoms were envisioned to alter the interactions of the cationic pillarplex with its counterions (as compared to the CH groups of the initially reported pillarplexes) (**Figure 13, E**). These changes in functionality potentially affect the sterics (with N being less sterically demanding than CH) as well as the intermolecular interactions, now offering a Lewis basic atom at the rim of the pillarplex. Therefore, I first pursued the synthesis of the macrocyclic triazolone/imidazolium salt used as an NHC precursor and subsequently aimed for the pillarplex formation by metalation with coinage metal precursors.

4.2.3 Results and Discussion

4.2.3.1 Backbone Modified NHC Proligand

Proligand $\text{H}_6\text{L}^{\text{DM}}(\text{OTf})_4$ was synthesized following a similar route with its pyrazole derivative $\text{H}_6\text{L}^{\text{Me}}(\text{OTf})_4$. Dichloro-precursor **3** was prepared from **1** in two steps following a procedure reported in the literature.⁴² The 4,5-dimethyl-1*H*-imidazole (**5**) was obtained by conversion of acetoin (**4**) in excess formamide *via* thermal condensation as introduced in Chapter 1.3.1.⁴³ The ring closure of bis(4,5-dimethylimidazolyl)-functionalized pyrazole **7** with methylene bis(triflate) afforded the macrocyclic calix[4](3,4 dimethylimidazolylidene)[2]pyrazolato proligand $\text{H}_6\text{L}^{\text{DM}}(\text{OTf})_4$.



Scheme 40. Synthesis pathway towards calix[4](3,4 dimethylimidazolylidene)[2]pyrazolato proligand **H₆L^{DM}(OTf)₄**: (i) SOCl₂ (neat), 95 °C, 0.5 h; (ii) 3,4-dihydro-2*H*-pyran (DCM), r.t., 16 h; (iii) sodium 4,5-dimethylimidazolide (MeCN), 70 °C, 3 d; (iv) formamide, 160 °C, 6 h; (v) sodium hydride (THF), r.t., 1 h; (vi) CH₂(OTf)₂ (MeCN), -40 °C to r.t., 16 h; Tf₂O/H₂O (EtOH), r.t., 30 min.

Subsequently, water-soluble **H₆L^{DM}(OTf)₄** underwent an anion exchange reaction to obtain its hexafluorophosphate salt. The deprotonation reaction of the hexafluorophosphate salt with Ag₂O in acetonitrile was then attempted. After fractional precipitation with diethyl ether, an off-white solid was obtained. The ¹H NMR spectrum indicated the successful deprotonation of imidazoliums. Eleven signals between 6.5 and 1.5 ppm can be assigned to the compound, signal sets consists of one singlet for the pyrazole proton, three pairs of doublets for the protons of the methylene bridges between the imidazole and pyrazole unities, and four singlets for the methyl groups of the imidazole backbone (see **Figure S2** in appendix). Suitable crystals for SC-XRD measurement were grown by slow evaporation of an acetonitrile solution of the product. Eventually, single crystal X-ray diffraction measurement was conducted, and a crystal composite of **[Ag₁₁L^{DM}₃](PF₆)_{2.32}(OTf)_{2.68}** was revealed (see **Figure 14**). The anion scrambling probably resulted from the

unsuccessful (incomplete) anion exchange step. This anion exchange and metalation reaction should be repeated in future studies in order to get the silver complex with only one kind of anion.

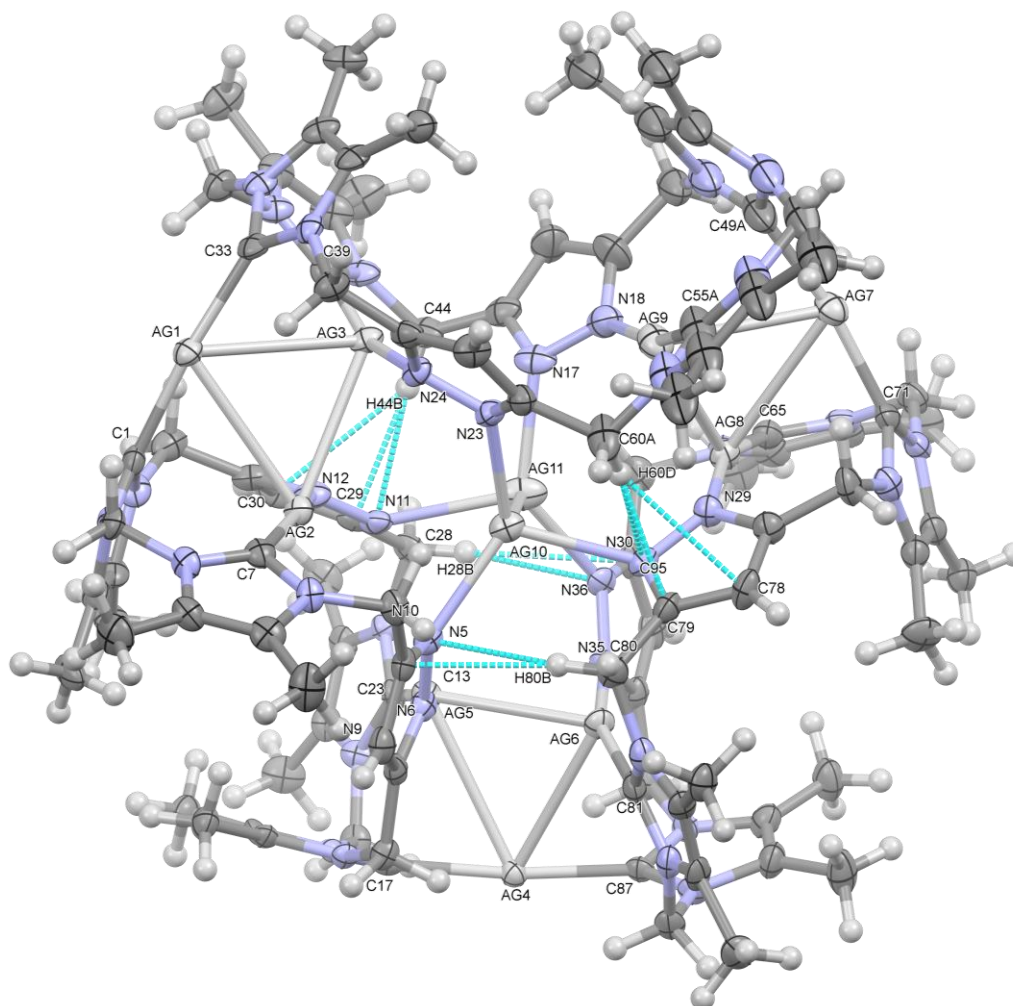


Figure 14. Solid-state molecular structure of the cationic fragment of $[\text{Ag}_{11}\text{L}^{\text{DM}_3}](\text{PF}_6)_{2.32}(\text{OTf})_{2.68}$. Ellipsoids are shown at 50% probability. Counter ions are omitted for clarity. Selected structural parameters: Ag1–Ag2 3.213(1) Å, Ag1–Ag3 3.165 Å, Ag2–Ag3 3.113(6) Å, Ag4–Ag6 3.161(3) Å, Ag5–Ag6 3.120(5) Å, Ag4–Ag5 3.283(6) Å, Ag7–Ag8 3.212(2) Å, Ag7–Ag9 3.150(7) Å, Ag8–Ag9 3.176(6) Å, Ag10–Ag11 2.750(7) Å, Ag1–C1 2.080(8) Å, Ag1–C33 2.074(7) Å, Ag2–N12 2.161(5) Å, Ag2–C7 2.153(6) Å, Ag3–N24 2.152(6) Å, Ag3–C39 2.120(2) Å, Ag4–C17 2.089(9) Å, Ag4–C87 2.085(3) Å, Ag5–N6 2.147(5) Å, Ag5–C23 2.137(2) Å, Ag6–N35 2.151(5) Å, Ag6–C81 2.120(1) Å, Ag7–C49A 2.057(9) Å, Ag7–C71 2.080(4) Å, Ag8–N29 2.180(5) Å, Ag8–C65 2.146(8) Å, Ag9–N18 2.151(8) Å, Ag9–C55A 2.082(9) Å, Ag10–N5 2.271(8) Å, Ag10–N23 2.225(2) Å, Ag10–N30 2.324(3) Å, Ag11–N11 2.46 Å, Ag11–N17 2.232(2) Å, Ag11–N36 2.246(8) Å, C1–Ag1–C33 171.5(1)°, N24–Ag3–C39 162.3(2)°, C7–Ag2–N12 162.9(4)°, N23–Ag10–N5

127.3(4)°, N23-Ag10-N5 127.3(4)°, N6-Ag5-C23 162.8(3)°, C17-Ag4-C87
 173.3(6)°, C81-Ag6-N35 161.1(8)°, N5-Ag10-N30 110.6(4)°, N30-Ag10-N23
 111.1(5)°, N17-Ag11-N11 107.2(6)°, N11-Ag11-N36 113.7(9)°, N17-Ag11-N36
 128.8(9)°, N18-Ag9-C55A 165.1°, C49A-Ag7-C71 170.3(6)°, N29-Ag8-C65
 160.1(4)°. Donor-acceptor distances (H...X [C...X])/angles/angles: (C28-H28...N36)
 2.553 [3.534] Å / 170.9°, (C28-H28...C95) 2.718 [3.649] Å / 156.8°, (C44-H44B...N11) 2.430
 [3.418] Å / 175.6°, (C44-H44B...C29) 2.402 [3.302] Å / 150.8°, (C44-H44B...C30) 2.840 [3.609]
 Å / 135°, (C60A-H60D...C78) 2.899 [3.708] Å / 139.5°, (C60A-H60D...C79) 2.560 [3.479] Å /
 154.4°, (C60A-H60D...N30) 2.563 [3.547] Å / 172.58°, (C80-H80B...C13) 2.548 [3.457] Å /
 152.7°, (C80-H80B...N5) 2.416 [3.403] Å / 175.5°.

The molecular structure of $[\text{Ag}_{11}\text{L}^{\text{DM}_3}](\text{PF}_6)_{2.32}(\text{OTf})_{2.68}$ was solved and refined in the triclinic space group *P*-1 (No. 2). The unit cell consists of two $[\text{Ag}_{11}\text{L}^{\text{DM}_3}]^{5+}$ cations. The center of the cationic fragment is the Ag10-Ag11 barbell moiety, each of the silver atoms coordinate to three pyrazole-N atoms (Ag10 coordinated to N5, N23, N30; Ag11 coordinated to N11, N17, N36), and the argentophilic contact between Ag10 & Ag11 was observed. The six pyrazole moieties are located on three ligands. In this way, the Ag10-Ag11 barbell moiety connects the three ligands. Inside the moiety of each ligand, two C-Ag-N bonds are observed between NHC and pyrazole-N atoms (Ag2 coordinates to N2, C7/ Ag5 coordinates to N6, C23 on the left ligand in **Figure 14**; Ag3 coordinates to N24, C36/ Ag9 coordinates to N18, C55A on the top ligand in **Figure 14**; Ag6 coordinates to N35, C81/ Ag8 coordinates to N29, C65 on the right ligand in **Figure 14**). The remaining NHC moieties are tilted towards adjacent NHCs from neighboring ligands, and form the linkage C1-Ag1-C33, C17-Ag4-C87 and C49A-Ag7-C71. Furthermore, the connections between neighboring ligands are reinforced by argentophilic contacts Ag2-Ag3, Ag5-Ag6, Ag8-Ag9. Additional argentophilic contacts Ag1-Ag2, Ag1-Ag3, Ag4-Ag5, Ag4-Ag6, Ag7-Ag8, Ag7-Ag9 are observed, this arrangement gives three silver triangles, with each silver atom coordinated in a t-shaped manner, forming an equilateral triangle shape (Ag1-Ag3-Ag2 = 61.56° / Ag3-Ag2-Ag1 = 60.01° / Ag2-Ag1-Ag3 = 58.44° / Ag1-Ag2 = 3.213(1) Å, Ag1-Ag3 = 3.165 Å, Ag2-Ag3 = 3.113(6) Å; Ag8-Ag9-Ag7 = 61.02° / Ag9-Ag7-Ag8 = 59.89° / Ag7-Ag8-Ag9 = 59.09° / Ag7-

Ag8 = 3.212(2) Å, Ag7-Ag9 = 3.150(7) Å, Ag8-Ag9 = 3.176(6) Å; Ag4-Ag5-Ag6 = 59.1° / Ag5-Ag6-Ag4 = 63.02° / Ag6-Ag4-Ag5 = 57.88° / Ag4-Ag6 = 3.161(3) Å, Ag5-Ag6 = 3.120(5) Å, Ag4-Ag5 = 3.283(6) Å. Argentophilic contacts within Ag1-Ag3-Ag2/ Ag7-Ag8-Ag9/ Ag4-Ag5-Ag6 triangles are found to have distances between 3.113(6) to 3.283(6) Å, a shorter argentophilic contact was observed between the Ag10 and Ag11 atoms (2.750(7) Å), all of them are significantly shorter than the sum of the van der Waals radii of silver (3.44 Å).^{44,45} The coordination geometries of the Ag1/Ag4/Ag7, which coordinates to two NHCs, are almost linear with values of 171.5(1)° / 173.3(6)° / 170.3(6)°, for the C-Ag-C angles. While the coordination geometries of Ag2/Ag3/Ag5/Ag6/Ag8/Ag9, which coordinate to NHC and pyrazole-N atoms, are slightly bent with values from 160.1(4)° to 165.1(0)°, for the C-Ag-N angles. The Ag-C bond lengths are in agreement with previously reported silver pillarplex $[\text{Ag}_8\text{L}^{\text{Me}_2}](\text{OTf})_4$, ranging from 2.057(9) to 2.153(6) Å.¹⁸ A closer inspection of the $[\text{Ag}_{11}\text{L}^{\text{DM}_3}]^{5+}$ structure reveals there are intramolecular hydrogen bonding between neighboring ligands. The hydrogen on the CH₂ bridging moieties forms multiple hydrogen bonds to pyrazole ring (C28-H28...N36 / C28-H28...C95; C44-H44B...N11 / C44-H44B...C29 / C44-H44B...C30; C60A-H60D...C78 / C60A-H60D...C79 / C60A-H60D...N30; C80-H80B...C13 / C80-H80B...N5).

The utilization of obtained $[\text{Ag}_{11}\text{L}^{\text{DM}_3}](\text{PF}_6)_{2.32}(\text{OTf})_{2.68}$ as carbene transfer agent for its gold(I) congener was not successful, the stronger aurophilic interaction forms shorter metal-metal bonds than weaker argentophilic interaction⁴⁶, which probably make the cationic structure unstable. The reaction of the proligand $\text{H}_6\text{L}^{\text{DM}}(\text{OTf})_4$ with NaHCO₃ in the presence of four equivalent of Au(I) precursor Au(THT)Cl in DMF at 120 °C, afforded a purple reaction solution. A purple solid was obtained by fractional precipitation with diethyl ether. The purple color is probably from the gold nanoparticles. ¹H NMR spectrum showed that the purple solid shows four doublets between 5.0 and 7.0 ppm (see **Figure**

15). Subsequent ESI-MS analysis (**Figure S18**) indicates the formation of $[\text{Au}_8\text{L}^{\text{DM}}]^{4+}$. However, as can be observed from the weak signal on NMR spectrum, the yield of the desired product is very low. After repeating the reaction eight times, it was still not possible to obtain enough product for crystal growth and further measurement analysis. Modifications on multiple reaction parameters have been attempted, but none of them afforded the desired product with better yield.

Table 2. Unsuccessful reaction parameters for deprotonation and metalation of proligand $\text{H}_6\text{L}^{\text{DM}}(\text{OTf})_4$.

Metal Precursors	Base	Temperature/ $^{\circ}\text{C}$	Solvent
Au(THT)Cl	K_2CO_3	20	DMF (HPLC grade / dry & degassed)
Au(THT)Cl	K_2CO_3	40	DMF (HPLC grade / dry & degassed)
Au(THT)Cl	K_2CO_3	60	DMF (HPLC grade / dry & degassed)
Au(THT)Cl	K_2CO_3	80	DMF (HPLC grade / dry & degassed)
Au(THT)Cl	Cs_2CO_3	20	DMF (HPLC grade / dry & degassed)
Au(THT)Cl	Cs_2CO_3	40	DMF (HPLC grade / dry & degassed)

Au(THT)Cl	Cs ₂ CO ₃	60	DMF (HPLC grade / dry & degassed)
Au(THT)Cl	Cs ₂ CO ₃	80	DMF (HPLC grade / dry & degassed)
Au(THT)Cl	KN(SiMe ₃) ₂	20	MeCN (dry & degassed)
Au(THT)Cl	KN(SiMe ₃) ₂	40	MeCN (dry & degassed)
Au(THT)Cl	KN(SiMe ₃) ₂	60	MeCN (dry & degassed)
Au(THT)Cl	KN(SiMe ₃) ₂	80	MeCN (dry & degassed)
(AuPPh ₃) ₃ OBF ₄		40	MeCN (dry & degassed)
(AuPPh ₃) ₃ OBF ₄		60	MeCN (dry & degassed)
(AuPPh ₃) ₃ OBF ₄		80	MeCN (dry & degassed)

*(AuPPh₃)₃OBF₄ = Tris(triphenylphosphino)aurio(I)oxonium tetrafluoroborate

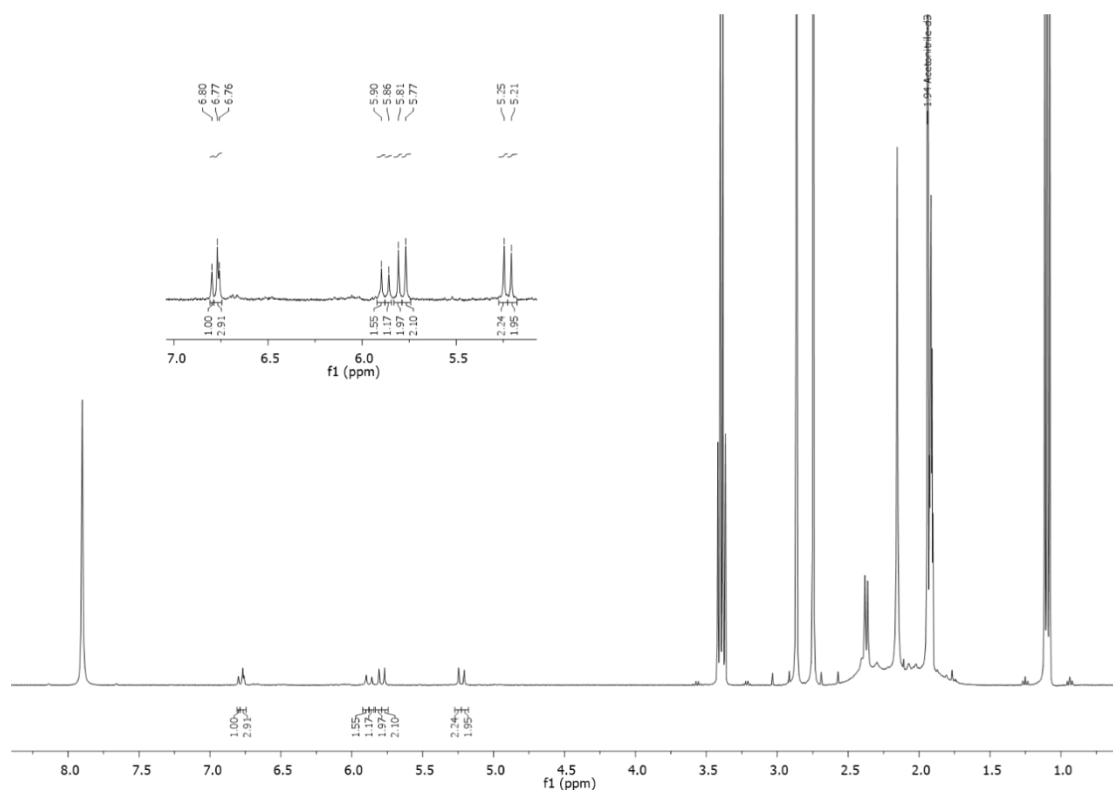
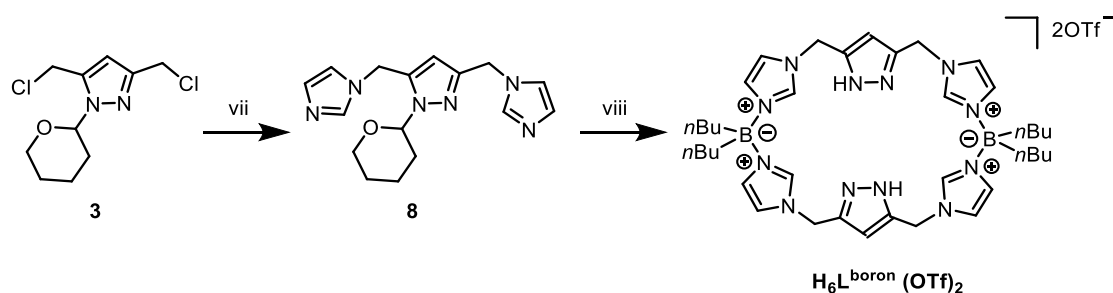


Figure 15. ¹H NMR of deprotonation and metalation product of proligand $\text{H}_6\text{L}^{\text{DM}}(\text{OTf})_4$. Solvent $\text{MeCN-}d_3$. Spectrum was measured at 400.13 MHz.

4.2.3.2 Charged Modified, Borate-Bridged NHC Proligand

Proligand $\text{H}_6\text{L}^{\text{b}}(\text{OTf})_2$ was synthesized following a similar route with its pyrazole derivative $\text{H}_6\text{L}^{\text{Me}}(\text{OTf})_4$ (Scheme 41). Synthesis to **8** has been reported.^{47,48} The macrocyclization protocol from **8** to $\text{H}_6\text{L}^{\text{b}}(\text{OTf})_2$ was adapted from the reported synthesis of $\text{H}_6\text{L}^{\text{Me}}(\text{OTf})_4$.^{47,48} The ring closure of bis(imidazolyl)-functionalized triazole **8** with dibutylboryl triflate afforded macrocyclic proligand $\text{H}_6\text{L}^{\text{b}}(\text{OTf})_2$. After purification by recrystallization with 1 volume% of MeOH in acetone, transparent crystals were filtered out as the final product. The ¹H NMR spectrum of the proligand shows the successful transformation from precursor **8** (see Figure S4). Subsequently, the single-crystal X-ray diffraction unambiguously proved the formation of the $\text{H}_6\text{L}^{\text{b}}(\text{OTf})_2$. (Figure 16) Suitable crystals for X-ray diffraction were obtained by vapor diffusion of diethyl ether into methanol solution of proligand.



Scheme 41. Synthesis pathway towards **H₆L^b(OTf)₂**: (vii) sodium imidazole (MeCN), r.t., 16 h; (viii) *n*Bu₂BOTf (MeCN), -40 °C to r.t., 16 h; HTfO (MeOH), r.t., 30 min

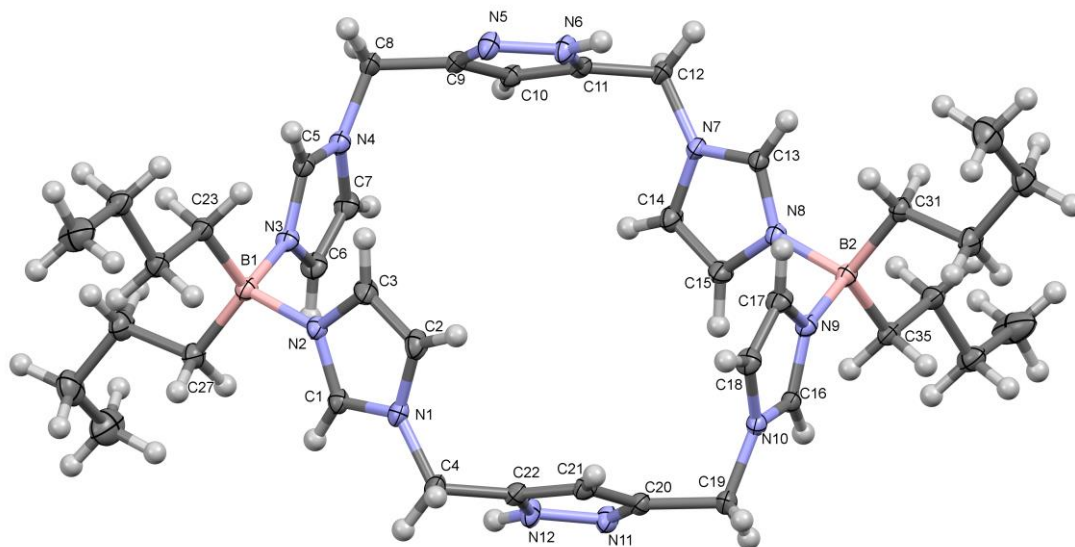


Figure 16. Solid-state molecular structure of the cationic fragment of **H₆L^b(OTf)₂**. Ellipsoids are shown at 50% probability. Counter ions are omitted for clarity. Selected structural parameters: N2-B1-N3 104.0(2)°, C23-B1-C27 115.7(1)°, N9-B2-N8 104.0(2)°, C31-B2-C35 115.7(2)°, C20-C19-N10 111.1(8)°, C22-C4-N1 113.3(5)°, N4-C8-C9 111.9(2)°, C11-C12-N7 111.8°.

The molecular structure of **H₆L^b(OTf)₂** was solved and refined in the triclinic space group *P*-1 (No. 2). The unit cell consists of two **H₆L^b 2⁺** cations and four triflate anions. The cationic macrocyclic ring is centrosymmetric, the center of inversion located at the Wyckoff position *2i*. The macrocyclic ring structures in the unit cell are arranged in parallel along the *c* axis, forming a columnar stack with triflate anions in-between (between Wyckoff position *1h* and *1f*). The remaining triflate anions disordered around position *1d* (for packing diagrams see **Figure 17, Top**).

The structure of **H₆L^b 2⁺** cation is illustrated in **Figure 16**. Pyrazolate rings C20-

C21/C22/N12/N11 and C9/C10/C11/N6/N5 are arranged in a parallel fashion, with protonated N6 and N12 pointing to opposite directions. The remaining imidazolium rings (C13/N7/C14/C15/N8 & C1/N1/C2/C3/N2; C5/N3/C6/C7/N4 & C16/N9/C17/C18/N10) follow the same arrangement, each pair of rings are parallel and pointing to opposite directions. Nevertheless, the neighboring borate bridged imidazolium ring point to the opposite direction with regard to the ring next to it (C1/N1/C2/C3/N2 & C5/N3/C6/C7/N4; C13/N7/C14/C15/N8 & C16/N9/C17/C18/N10). This alternate twisting arrangement was described previously by Siebert^{49,50} and Jenkins²⁹ for imidazolium-borate macrocycles of smaller size. This orientation implies that the macrocyclic ring has a high strain, it might be hard to orient the imidazoliums toward one direction to facilitate SOC assembly.

Multiple hydrogen bondings between triflate and cation are observed inside the unit cell. From the Hirshfeld surface analysis, charge-assisted hydrogen bonds (**Figure 17**, interaction 1-9 and 11) with triflate oxygen atoms (O1, O1A, O3A, O4, O6) as hydrogen bond acceptors dominate the non-covalent interactions (17.3% of all contacts). Interaction 1 represents a classical hydrogen bond formed from the C-H group on the butyl chain to the oxygen atoms of disordered triflate anion. Oxygen atoms of the same triflate anion form other four hydrogen bonds with hydrogen atoms of pyrazolate (H12) and proximal imidazolium (H1) (interaction 2 to 5). Oxygen atoms O4 of triflate anions between Wyckoff position *1h* and *1f* form classical hydrogen bonds with imidazolium backbone protons H2 & H18 and pyrazolate H21 & H6 atom (interaction 6, 7, 8, 11). Attractive non-classical charge-assisted hydrogen bonds (interaction 9) can be found between triflates F4 atoms and imidazolium backbone protons H17, with trifluoromethyl group on central symmetrical triflate anions acting as a CF-acceptor. Interaction 10 shows hydrogen bonds between triflate sulfur atoms (S2) and pyrazolate hydrogen atoms (H6).

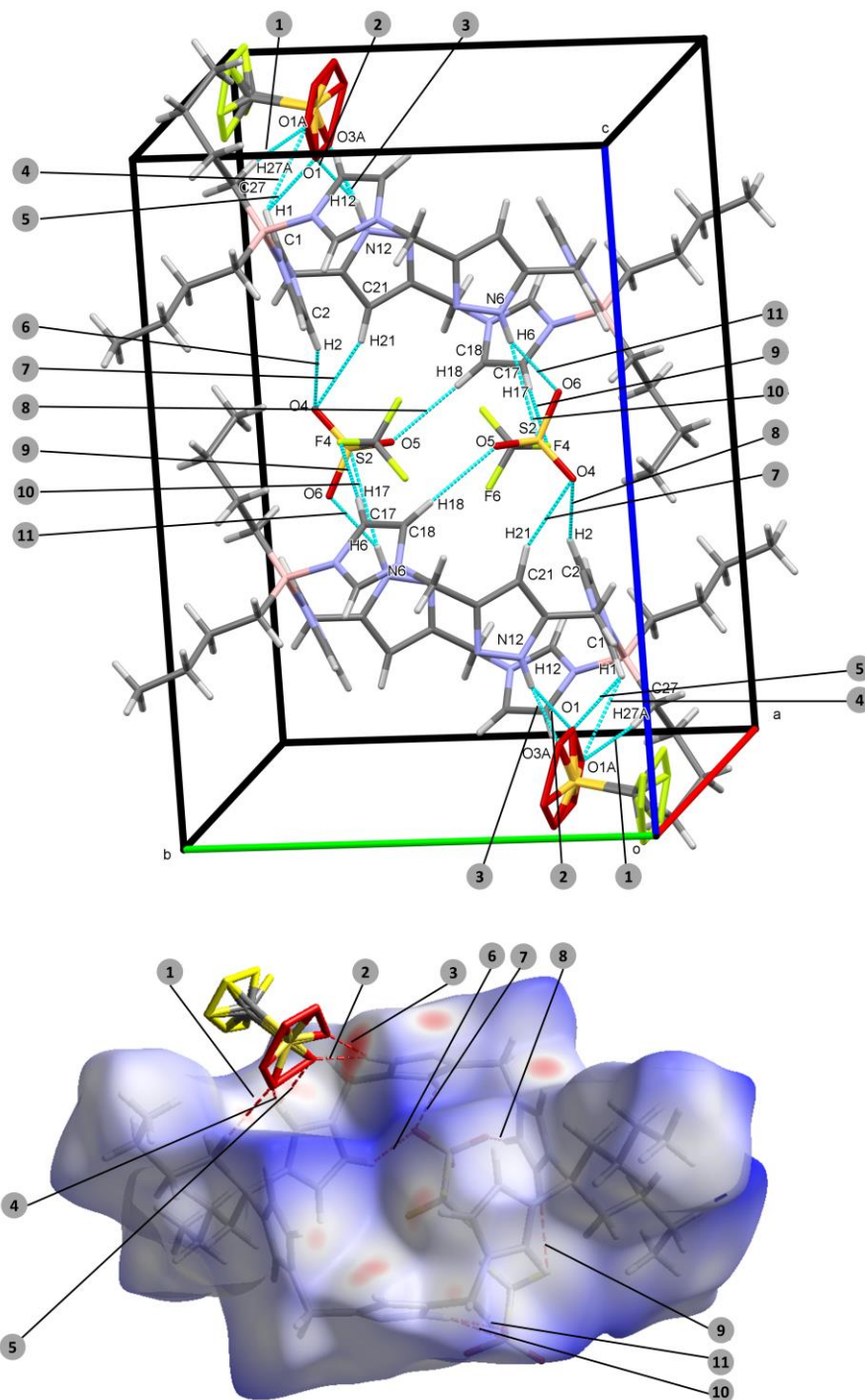


Figure 17. Top: Non-covalent interaction of triflate anions with the H_6L^{b2+} cation in the unit cell. Down: Hirshfeld surface analysis of different non-covalent interactions around H_6L^{b2+} cation. Donor-acceptor distances (H...X [C...X])/angles: (C2-H2...O4) 2.656[3.287] Å / 156°, (C17-H17...F4) 2.492[3.44] Å / 175.7°, N6-H6...O6 2.043[2.878] Å / 157.9°, C21-H21...O4 2.573[3.365] Å / 141°, C18-H18...O5 2.449[3.394] Å / 172.7°, N12-H12...O1 1.948[2.784] Å / 158°, C1-H1...O1 2.485[3.089] Å / 121.5°, C27-H27A...O1A 2.528[3.49] Å / 164°, N12-H12...O3A 1.813[2.67] Å / 164°, C10-H10...O3 2.523[3.378] Å / 149.8°.

Attempts to synthesize a stable silver or gold complex with $\text{H}_6\text{L}^{\text{b}}(\text{OTf})_2$ were not successful yet. Despite trying a wide variety of bases, solvents, and temperatures, no evidence of complex formation could be observed on the mass spectrum or ^1H NMR spectrum. Attempted reactions with parameters were summarized in Table 3.

Table 3. Attempted reaction parameters to synthesize complex of $\text{H}_6\text{L}^{\text{b}}(\text{OTf})_2$.

Metal Precursors	Base	Temperature/ $^{\circ}\text{C}$	Solvent
	Ag_2O	20	MeCN (HPLC grade)
	Ag_2O	40	MeCN (HPLC grade)
	Ag_2O	60	MeCN (HPLC grade)
	Ag_2O	80	MeCN (HPLC grade)
	Ag_2O	20	DMF (HPLC grade)
	Ag_2O	40	DMF (HPLC grade)
	Ag_2O	60	DMF (HPLC grade)
	Ag_2O	80	DMF (HPLC grade)
AgOTf	<i>n</i> BuLi	-40	THF (dry & degassed)
AgOTf	<i>n</i> BuLi	-20	THF (dry & degassed)
AgOTf	<i>n</i> BuLi	0	THF (dry & degassed)

			degassed)
AgOTf	NaOH	20	MeCN (HPLC grade)
AgOTf	NaOH	40	MeCN (HPLC grade)
AgOTf	NaOH	60	MeCN (HPLC grade)
AgOTf	NaOH	80	MeCN (HPLC grade)
AgOTf	K ₂ CO ₃	20	MeCN (HPLC grade)
AgOTf	K ₂ CO ₃	40	MeCN (HPLC grade)
AgOTf	K ₂ CO ₃	60	MeCN (HPLC grade)
AgOTf	K ₂ CO ₃	80	MeCN (HPLC grade)
AgOTf	KN(SiMe ₃) ₂	20	MeCN (HPLC grade)
AgOTf	KN(SiMe ₃) ₂	40	MeCN (HPLC grade)
AgOTf	KN(SiMe ₃) ₂	60	MeCN (HPLC grade)
AgOTf	KN(SiMe ₃) ₂	80	MeCN (HPLC grade)
Ag ₂ O	<i>in situ</i> transmetallation with Au(THT)Cl	40	MeCN (HPLC grade)
Ag ₂ O	<i>in situ</i>	60	MeCN (HPLC grade)

	transmetallation with Au(THT)Cl		grade)
Au(THT)Cl	<i>n</i> BuLi	-40	THF (dry & degassed)
Au(THT)Cl	<i>n</i> BuLi	-20	THF (dry & degassed)
Au(THT)Cl	<i>n</i> BuLi	0	THF (dry & degassed)
Au(THT)Cl	K ₂ CO ₃	20	MeCN (HPLC grade / dry & degassed)
Au(THT)Cl	K ₂ CO ₃	40	MeCN (HPLC grade / dry & degassed)
Au(THT)Cl	K ₂ CO ₃	60	MeCN (HPLC grade / dry & degassed)
Au(THT)Cl	K ₂ CO ₃	80	MeCN (HPLC grade)
Au(THT)Cl	KN(SiMe ₃) ₂	20	MeCN (dry & degassed)
Au(THT)Cl	KN(SiMe ₃) ₂	40	MeCN (dry & degassed)
Au(THT)Cl	KN(SiMe ₃) ₂	60	MeCN (dry & degassed)
Au(THT)Cl	KN(SiMe ₃) ₂	80	MeCN (dry & degassed)
Au(PPh ₃)Cl	<i>n</i> BuLi	-40	THF (dry & degassed)

Au(PPh ₃)Cl	<i>n</i> BuLi	-20	THF (dry & degassed)
Au(PPh ₃)Cl	<i>n</i> BuLi	0	THF (dry & degassed)
Au(PPh ₃)Cl	K ₂ CO ₃	20	MeCN (HPLC grade / dry & degassed)
Au(PPh ₃)Cl	K ₂ CO ₃	40	MeCN (HPLC grade / dry & degassed)
Au(PPh ₃)Cl	K ₂ CO ₃	60	MeCN (HPLC grade / dry & degassed)
Au(PPh ₃)Cl	K ₂ CO ₃	80	MeCN (HPLC grade / dry & degassed)

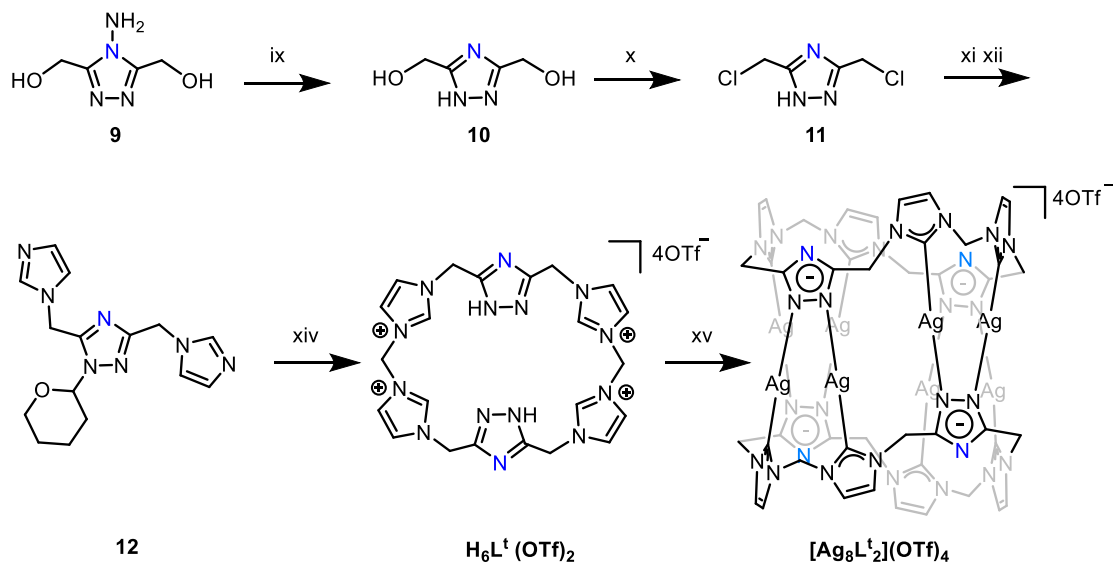
Several rationales could explain the failure of forming stable SOC from **H₆L^b(OTf)₂**. The steric bulky butyl substituted borate entity might prevent the assembly of the coinage metal complex from the macrocyclic ligand. From the structure of the previously reported pyrazolate based pillarplex, it can be observed that coordination sites on imidazolium and pyrazolate entities are oriented towards one direction. In the case of **H₆L^b(OTf)₂**, it can be noticed that all of the five-membered entities within the macrocycle adapt alternate twisting arrangement, which requires rearrangement to obtain necessary conformation for pillarplex's assembly.¹⁸ Jenkins described the failure of metalation reaction with a similar imidazolium-borate macrocyclic NHC ligand system bearing alternate twisting arranged imidazolium moieties.²⁹ Furthermore, the acidity of C2 imidazolium proton might influence the deportation/metalation reaction. As depicted in Chapter 1.4.2, the electronic withdrawing N-substitution on

imidazolium increases the acidity of C2 imidazolium proton,⁵¹⁻⁵³ and vice versa, the weak acidity of C2 imidazolium proton resulted from the electron-rich borate entity prevent the deportation/metalation reaction from happening.

4.2.3.3 Steric/Electronic Modified, Triazolate NHC proligand

Macrocyclic proligand **H₆L^t(OTf)₄** was synthesized similarly to its pyrazole derivative **H₆L^{Me}(OTf)₄**. Starting from 4-amino-3,5-bis(hydroxymethyl)-1,2,4-triazole (**9**), dichloro precursor **11** was prepared in two steps following a procedure reported in the literature.⁵⁴ The macrocyclization protocol from **11** to **H₆L^t(OTf)₄** was adapted from the reported synthesis of **H₆L^{Me}(OTf)₄**.^{47,48} The ring closure of bis(imidazolyl)-functionalized triazole **12** with methylene bis(triflate) afforded calix[4]imidazolylidene[2]tri-azolato proligand **H₆L^t(OTf)₄**. Subsequently, an excess of silver(I) oxide was directly added acting as a metalation agent and as a base to deprotonate the imidazolium and triazole groups (**Scheme 3**). After fractional precipitation with diethyl ether and acetonitrile, an off-white solid was obtained. The ¹H NMR spectrum of the product shows four doublets between 5.0 and 7.0 ppm (see Figure S9) suggesting that the protons of the methylene groups bridging the azoles are magnetically inequivalent. A similar pattern can also be found for the pyrazole-based pillarplex, which indicates the formation of the targeted triazolate-based pillarplex. Additional analytic results obtained from ESI-MS and elemental analysis supported the composition of the product to be **[Ag₈L^t]₂(OTf)₄**. Eventually, single-crystal X-ray diffraction unambiguously proved the formation of the desired pillarplex (**Figure 18**). Suitable crystals were grown by diffusion of diethyl ether into an acetonitrile solution of **[Ag₈L^t]₂(OTf)₄**. The compound crystallizes in the orthorhombic space group *Pnma* (No. 62). The unit cell consists of four individual **[Ag₈L^t]₂⁴⁺** cations and sixteen trifluoromethanesulfonate (triflate) anions. The cationic complexes are located at the Wyckoff position *4c*, with site symmetry *m*, which means that in the asymmetric

unit only half of the pillarplex is present, while the second half is symmetry-generated by a mirror plane.



Scheme 42. Synthesis pathway towards $\text{H}_6\text{L}^{\text{b}}(\text{OTf})_2$: (ix) NaNO_2 ; (x) SOCl_2 (neat), 95°C , 0.5 h; (xi) 3,4-dihydro-2*H*-pyran (DCM), r.t., 16 h; (xii) sodium imidazolide (MeCN), r.t., 16 h; (xiv) $\text{CH}_2(\text{OTf})_2$ (MeCN), -40°C to r.t., 16 h; $\text{Tf}_2\text{O}/\text{H}_2\text{O}$ (EtOH), r.t., 30 min (xv) Ag_2O , r.t. 16 h. Reproduced with permission from Ref. 19.

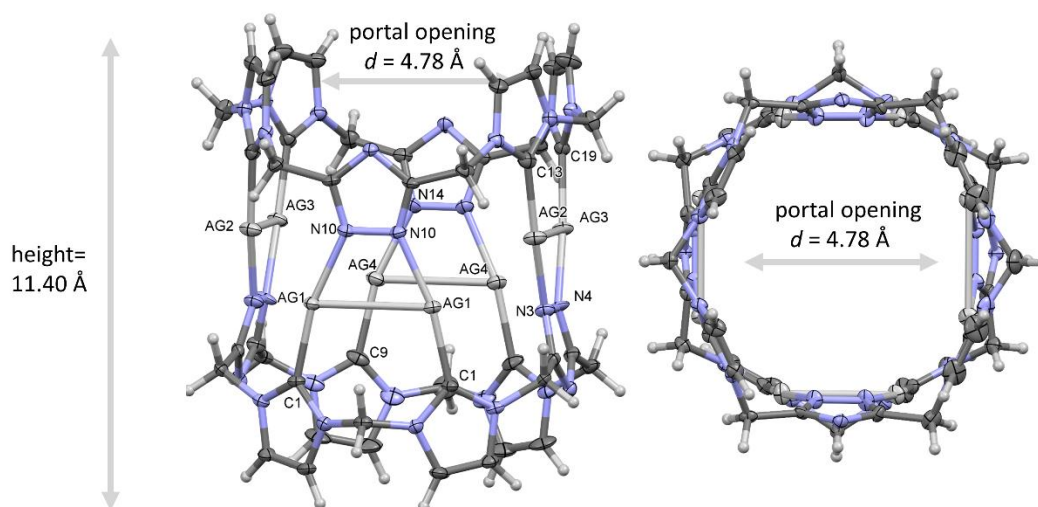
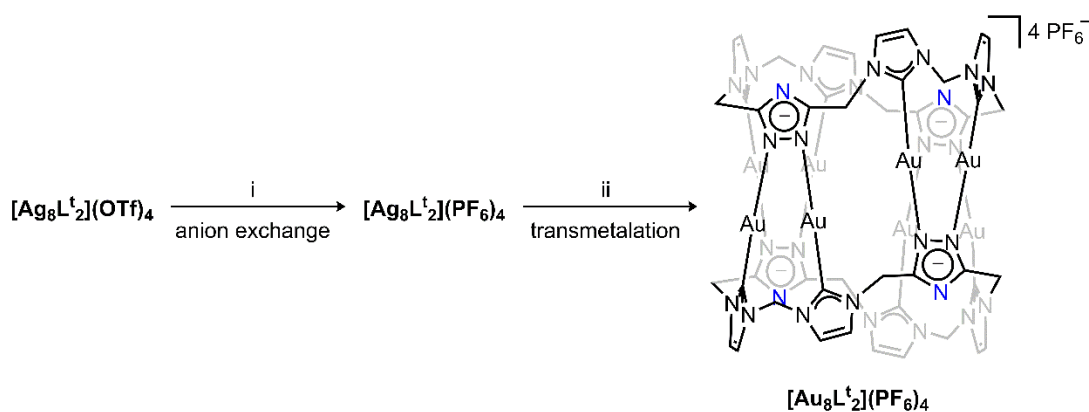


Figure 18. Front view (**left**) and top view (**right**) of the solid-state molecular structure of the cationic pillarplex fragment of $[\text{Ag}_8\text{L}^{\text{b}}_2](\text{OTf})_4$. Ellipsoids are shown at 50% probability. Counter ions and solvents are omitted for clarity. Selected structural parameters: $\text{Ag1}-\text{Ag1}$ 3.161 Å, $\text{Ag2}-\text{Ag3}$ 3.098(2) Å, $\text{Ag4}-\text{Ag4}$ 3.174 Å, $\text{Ag1}-\text{C1}$ 2.077(5) Å, $\text{Ag2}-\text{C13}$ 2.070(2) Å, $\text{Ag3}-\text{C19}$ 2.080(7) Å, $\text{Ag4}-\text{C9}$ 2.086(4) Å, $\text{C1}-\text{Ag1}-\text{N10}$ $166.8(5)^\circ$, $\text{C13}-\text{Ag2}-\text{N3}$ $168.3(8)^\circ$, $\text{C19}-\text{Ag3}-\text{N4}$ $168.4(2)^\circ$, $\text{C9}-\text{Ag4}-\text{N14}$ $165.8(2)^\circ$. Reproduced with permission from Ref. 19.

As in the case of the pyrazolate pillarplexes,¹⁸ SC-XRD revealed eight metal ions to be present in the solid-state structure of the cationic fragment, coordinated by the two octadentate NHC ligands (**Figure 18**). Argentophilic contacts were also observed (3.098(2) to 3.174(0) Å), which are significantly shorter than the sum of the van der Waals radii of silver (3.44 Å).^{44,45} The Ag–C bond lengths are in agreement with previously reported silver complexes, ranging from 2.070(2) to 2.086(3) Å.¹⁸ The cavity diameter of the metallocavitand was estimated to be 4.78 Å with a height of roughly 11.40 Å. The molecular geometry of the cation almost perfectly matches that of the initially reported silver(I) pyrazolate-based pillarplex.²²

Eventually, I exchanged the triflate anions of water-soluble $[\text{Ag}_8\text{L}^t_2](\text{OTf})_4$ to hexafluorophosphate to obtain $[\text{Ag}_8\text{L}^t_2](\text{PF}_6)_4$. The latter salt exhibits increased solubility in non-aqueous solvents – a trait that showed to facilitate the transmetalation of the silver(I) complex to its gold(I) congener. The reaction of $[\text{Ag}_8\text{L}^t_2](\text{PF}_6)_4$ with chloro(tetrahydrothiophene)gold(I) afforded $[\text{Au}_8\text{L}^t_2](\text{PF}_6)_4$ in 48% yield (**Scheme 2**). ¹H NMR spectroscopy shows a very signal pattern of the gold(I) complex compared to the one of $[\text{Ag}_8\text{L}^t_2](\text{PF}_6)_4$ (ESI Figure S11, Figure S14). Results obtained from ESI-MS and elemental analysis confirmed the expected composition of the transmetalation product.



Scheme 43. Synthesis of $[\text{Au}_8\text{L}^t_2](\text{PF}_6)_4$ starting from $[\text{Ag}_8\text{L}^t_2](\text{OTf})_4$: (i) NH_4PF_6 ($\text{NH}_3(\text{aq})$), (ii) $\text{Au}(\text{THT})\text{Cl}$ (MeCN), 60 °C, 16 h. Reproduced with permission from Ref. 19.

Crystals of $[\text{Au}_8\text{L}^{\text{t}_2}](\text{PF}_6)_4$ suitable for SC-XRD analysis were obtained by diffusion of diethyl ether into an acetonitrile solution. The molecular structure of $[\text{Au}_8\text{L}^{\text{t}_2}](\text{PF}_6)_4$ was solved and refined in the tetragonal space group $I4/mcm$ (No. 140). The unit cell consists of four $[\text{Au}_8\text{L}^{\text{t}_2}]^{4+}$ cations and sixteen hexafluorophosphate anions. The cationic pillarplex fragments are located at the Wyckoff position $4b$, whose site symmetry ($-42m$) exactly coincides with the point group (D_{2d}) of the pillarplexes. The pores of the pillarplex cations are oriented along the c axis forming a columnar stack with PF_6^- anions in-between (Wyckoff position $4d$). The remaining hexafluoro-phosphates are located at Wyckoff positions $4a$ and disordered around position $8h$ (for packing diagrams see **Figure 19**). Residual electron density originating from disordered solvent molecules was found in the cation pores, but could not be refined explicitly and therefore was removed using the PLATON/SQUEEZE procedure.⁵⁵

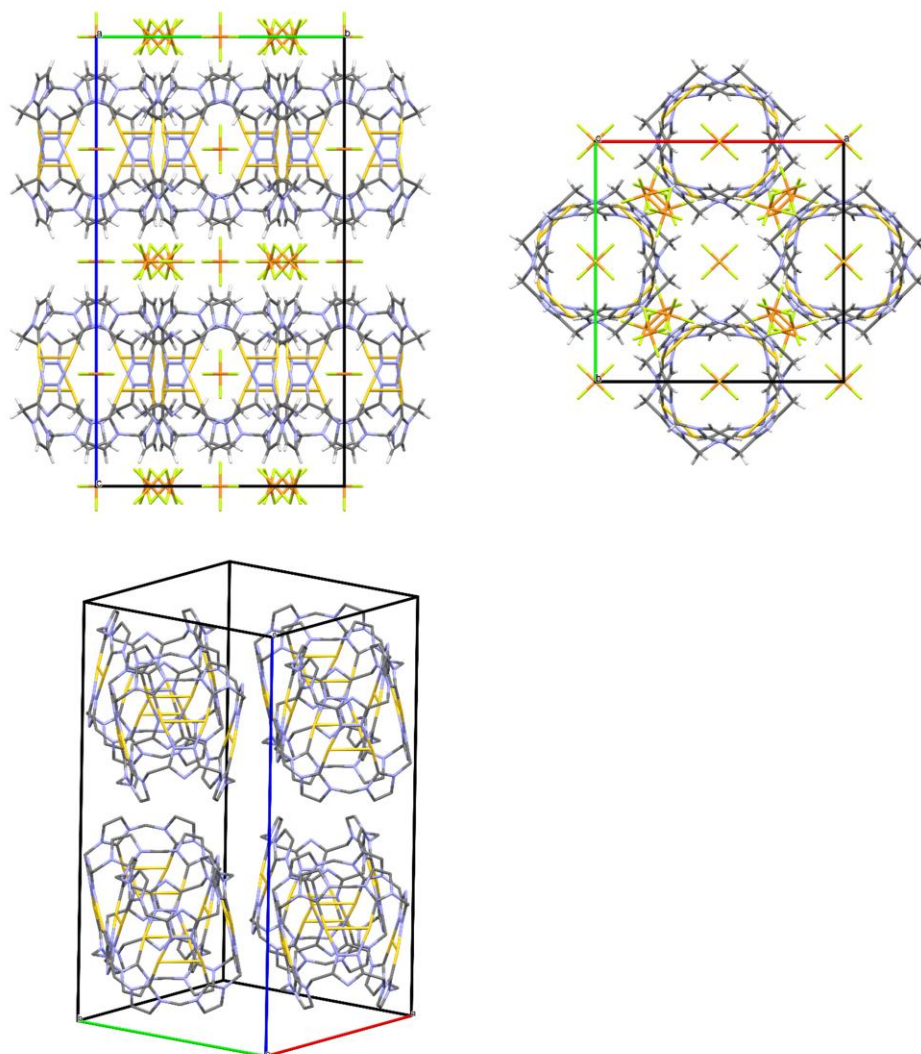


Figure 19. Packing of $[\text{Au}_8\text{L}_2](\text{PF}_6)_4$ in the solid-state. **Top left:** view along the crystallographic *a*-axis; **Top right:** view along the crystallographic *c*-axis; **Bottom:** packing of the cations (hydrogen atom omitted) Reproduced with permission from Ref. 19.

The molecular structure of gold(I) pillarplex $[\text{Au}_8\text{L}_2](\text{PF}_6)_4$ is illustrated in **Figure 20**. As can be seen, the composition and connectivity of the complex are identical to that of previously reported gold pillarplexes.¹⁸ The coordination geometries of the gold ions are almost linear with values of $171.6(2)^\circ$ for the N–Au–C angles, and $1.986(1) \text{ \AA}$ for the Au–C bond lengths. Auophilic contacts were observed with distances of $3.002(7) \text{ \AA}$, again being significantly shorter than the sum of the respective van der Waals radii.⁴⁴

However, although the connectivity is identical, the overall shape of the pillarplex differs. In detail, the methylene-bridged imidazolylidene moieties

within the macrocyclic ligands are bent towards each other in a pairwise fashion. As a result, the tubular shape of the pillarplex is distorted as the portals of the cavity are compressed, exhibiting smaller portal diameters of approximately 2.93 Å (compared to 4.78 Å in the undistorted case; see **Figure 14**). This is remarkable, since in principle, the pore opening governs the efficiency and selectivity of the host-guest interactions, as can be seen for example for cucurbit[5]uril (CB[5]).⁵⁶ The latter can only host small molecules like N₂ due to the small portal diameter of 2.4 Å, although the inner diameter of 4.4 Å should be large enough to host even larger guest molecules, e.g., linear hydrocarbons.

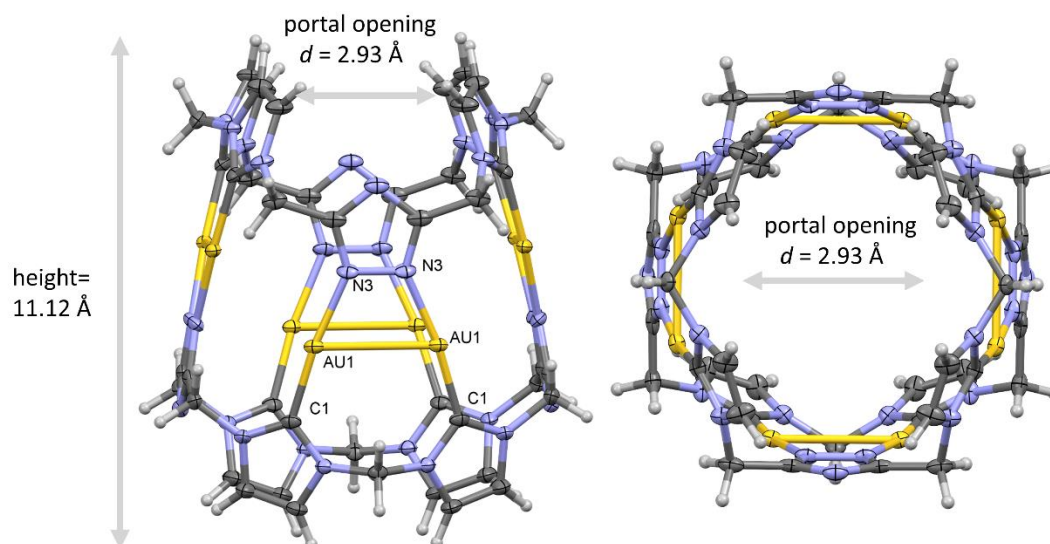


Figure 20. Front view (**left**) and top view (**right**) of the solid-state molecular structure of the cationic pillarplex fragment of $[\text{Au}_8\text{L}'_2](\text{PF}_6)_4$. Ellipsoids are shown at 50% probability. Counter ions and solvents are omitted for clarity. Selected structural parameters: Au1-Au1' 3.0028(7) Å, Au1-C1 1.986(4) Å, Au1-N3 2.040(4) Å, C1-Au1-N3 171.6(2)°. Symmetry operator ('): $1/2-y, 1/2-x, +z$. Reproduced with permission from Ref. 19.

A closer inspection of the packing of $[\text{Au}_8\text{L}'_2](\text{PF}_6)_4$ reveals the origin of the distortion, namely intermolecular hydrogen bonding to the pillarplex cation shown in **Figure 21**. The most prominent interaction observed is that between the PF_6^- anion on Wyckoff position $4d$ to the rim of the pillarplex (**Figure 21, A**, interaction 1). Two symmetry-related fluorine atoms (F3, F3') form four non-classical hydrogen bonds to the four symmetry-equivalent proximal

imidazolylidene backbone protons (H2-H2'') of one pillarplex rim. This attractive interaction apparently causes the aforementioned bending of the methylene-bridged bis-NHC moieties towards the center of the tubular pore, narrowing the cavity portal. Such a pronounced squeezing has not been observed for the pyrazolate-based pillarplexes before, and possibly is enabled by the lower steric demand induced by the triazolate nitrogen atom (N4) compared to the CH group in the pyrazolate-based pillarplex. Note: The identical hydrogen bonding can be observed in the other direction of the PF_6^- anion towards the next pillarplex cation, leading to the above-mentioned stack-formation in the packing along the crystallographic *c*-axis. Additional to this very prominent feature, further hydrogen bonding interactions were observed in the packing (**Figure 21, B**). The disordered PF_6^- anion at Wyckoff position *8h* is involved in a series of different hydrogen bonds (**Figure 21, B**, interactions 2-7). Hydrogen bonds 2-4 are formed between the imidazolydene-backbone hydrogen atom H3 (proximal to the triazolate moiety at the pillarplex rim) and three different fluorine atoms (F6, F8, F9). Interactions 5-7 are $\text{CH}\cdots\text{F}$ hydrogen bonds bridging the disordered PF_6^- anion to one of the methylene hydrogen atoms (H4B, between two imidazolydienes) of a neighbored, symmetry equivalent pillarplex. Note: As in the case of the PF_6^- anion discussed above, all the interactions are mirrored in crystallographic *c*-direction, bridging two more pillarplex cations (total of four). The third hexafluorophosphate ion at Wyckoff position *4a* only shows one kind of interaction (**Figure 21, B**, 8). Again, this is a $\text{CH}\cdots\text{F}$ hydrogen bond with one of the methylene hydrogen atoms (H5A, between the triazolate and one imidazolylidene) bridging four pillarplex cations in the crystallographic *ab*-plane with a total of 8 hydrogen bonds per PF_6^- ion. Hirshfeld surface analysis of the pillarplex cation showed, that the described $\text{CH}\cdots\text{F}$ interactions (1-8) are dominant and amount to 54.8% of all contacts (see Figure S34).

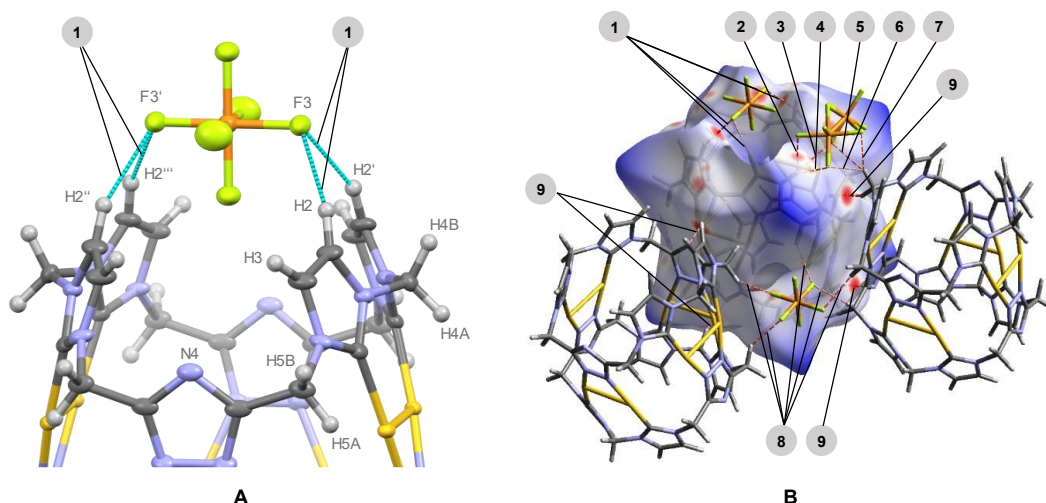


Figure 21 (A) Supramolecular interaction of hexafluorophosphate with the rim of the $[\text{Au}_8\text{L}_2]^{4+}$ cation in the solid state. Charge-assisted hydrogen bonding (blue) is observed from all four symmetry-equivalent imidazolylidene backbone protons to the hexafluorophosphate fluorine acceptor. Ellipsoids are shown at 50% probability. (B) Overview of the different non-covalent interactions in the packing of $[\text{Au}_8\text{L}_2]^{4+} (\text{PF}_6)_4$ as determined by Hirshfeld surface analysis (Note: Due to reasons of clarity not all symmetry equivalent interactions are depicted in the figure). Donor-acceptor distances ($\text{H}\cdots\text{X}[\text{C}\cdots\text{X}]$)/angles: **1** ($\text{C}2\text{-H}2\cdots\text{F}3$) 2.388 [3.287] Å / 156°, **2** ($\text{C}3\text{-H}3\cdots\text{F}8$) 2.471 [3.164] Å / 129.6°, **3** ($\text{C}3\text{-H}3\cdots\text{F}6$) 2.546 [3.469] Å / 163.9°, **4** ($\text{C}3\text{-H}3\cdots\text{F}9$) 2.598 [3.430] Å / 146.4°, **5** ($\text{C}4\text{-H}4\text{B}\cdots\text{F}6$) 2.437 [3.434] Å / 151.9°, **6** ($\text{C}4\text{-H}4\text{B}\cdots\text{F}9$) 2.590 [3.328] Å / 131.3°, **7** ($\text{C}4\text{-H}4\text{B}\cdots\text{F}7$) 2.541 [3.460] Å / 154.4°, **8** ($\text{C}5\text{-H}5\text{A}\cdots\text{F}2$) 2.483 [3.309] Å / 140.8°, **9** ($\text{C}4\text{-H}4\text{A}\cdots\text{N}4$) 2.361 [3.271] Å / 152.2°. Reproduced with permission from Ref. 19.

Interestingly, there is an additional observable interaction that is not a charge-assisted hydrogen bond between cations and anions (as in the case of all previously described examples). Interaction 9 in **Figure 21, B** shows a hydrogen bond between a methylene-group acting as a CH-donor ($\text{C}4\text{-H}4\text{A}$, between two imidazolylidenes) and the triazolate nitrogen atom ($\text{N}4$) of a neighboring pillarplex, acting as a hydrogen bond acceptor. Each of the four sides of the pillarplex (as defined by the pairs of coordinated gold ions) features one hydrogen bond donor (methylene-bridged bis-NHC moiety) and one hydrogen bond acceptor (triazolate) – each part of the opposing macrocyclic NHC ligands within the tubular complex. This leads to an ideal anti-parallel arrangement of four neighboring cations, perfectly synergistic with the attractive charge-assisted hydrogen bonds of type 8 in the crystallographic *ab*-plane. This

attractive inter-cationic self-recognition is a direct consequence of the rim-modification and presence of the additional Lewis-basic nitrogen atom in the macrocyclic ligand precursor. In contrast, the pyrazolate-based pillarplex exclusively possesses CH groups at its rim and, therefore, intrinsically is not able to form such complementary cation-cation hydrogen bonds.

The observations in the solid-state show, on the one hand, that the additionally introduced donor atom can in principle intermolecularly interact with Lewis acids, in this case contributing to a well-ordered, highly symmetric arrangement of the cations. On the other hand, the significant distortion of the macrocyclic ligand along with the charge-assisted hydrogen bonding (**Figure 21, B, 1**) strongly suggests that the rim modification substantially influences the flexibility of the metallocavitand.

To assess for a possible effect of the observed shape adaptive behavior towards supramolecular host-guest chemistry in solution, an NMR titration study identical to that of the original pyrazolate-based pillarplex was then conducted with $[\text{Au}_8\text{L}^{\text{t}_2}](\text{PF}_6)_4$. Upon the addition of 1,8-diaminooctane, the methylene backbone proton resonances of the pillarplex were upfield shifted, in analogy to what had been observed with the pyrazolate-based pillarplex. The stoichiometry of the species involved in the host-guest interaction was determined to be 1:1 by Job-Plot analysis (see **Figure S22**). NMR titration experiments with 1,8-diaminooctane as a model guest were performed for a comparison of the host-guest behavior of $[\text{Au}_8\text{L}^{\text{t}_2}](\text{PF}_6)_4$ and previously reported $[\text{Au}_8\text{L}^{\text{Me}_2}](\text{PF}_6)_4$. For the interaction between $[\text{Au}_8\text{L}^{\text{t}_2}](\text{PF}_6)_4$ and 1,8-diaminooctane, an association constant (K_a) of $(4.6 \pm 3.5) \cdot 10^4 \text{ M}^{-1}$ was determined. This indicates a very similar binding ability to the model guest as reported for the pyrazolate pillarplex $[\text{Au}_8\text{L}^{\text{Me}_2}](\text{PF}_6)_4$ [$K_a = (4.2 \pm 1.2) \cdot 10^4 \text{ M}^{-1}$] (**Figure 22**).^{18,57,58}

Photophysical measurements were conducted to gain further insight into the properties of $[\text{Au}_8\text{L}^{\text{t}_2}](\text{PF}_6)_4$. Similar to the pyrazolate-based pillarplex,

$[\text{Au}_8\text{L}^{\text{t}_2}](\text{PF}_6)_4$ shows solid-state emission in the blue region of the visible spectrum ($\lambda_{\text{max}} = 400 \text{ nm}$, $\lambda_{\text{ex}} = 270 \text{ nm}$) with a quantum yield of 31%. The emission band is in the range of reported emissive gold(I) NHC complexes.⁵⁹

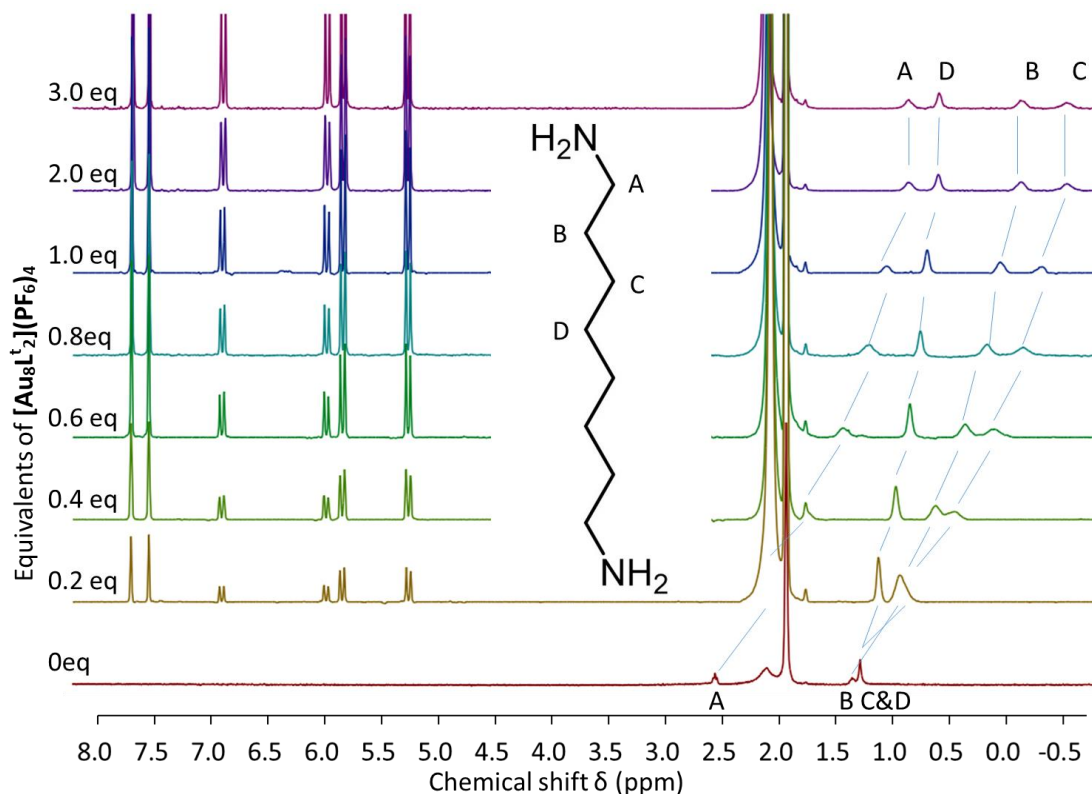


Figure 22. ^1H NMR titration (400 MHz, 298 K) of $[\text{Au}_8\text{L}^{\text{t}_2}](\text{PF}_6)_4$ in $\text{MeCN-}d_3$ into a 1.4 mM solution of 1,8-diaminooctane in $\text{MeCN-}d_3$. The signals between 5 and 8 ppm are assigned to $[\text{Au}_8\text{L}^{\text{t}_2}](\text{PF}_6)_4$. Electronic shielding by the cavity of $[\text{Au}_8\text{L}^{\text{t}_2}](\text{PF}_6)_4$ (host) leads to an upfield shift of the proton resonances (A–D) of 1,8-diaminooctane (guest). A K_a value of $(4.6 \pm 3.5) \cdot 10^4 \text{ M}^{-1}$ was calculated. Reproduced with permission from Ref. 19.

To rationalize the pronounced structural difference between pillarplexes $[\text{Au}_8\text{L}^{\text{t}_2}](\text{PF}_6)_4$ and $[\text{Au}_8\text{L}^{\text{Me}_2}](\text{PF}_6)_4$, Thomas Pickl assessed the influence of the portal opening of both complexes on their total energy by DFT. Calculation details are included in Ref. 19. The geometries of the cationic fragments $[\text{Au}_8\text{L}^{\text{t}_2}]^{4+}$ and $[\text{Au}_8\text{L}^{\text{Me}_2}]^{4+}$ were either fully optimized without any restrictions, or partially optimized by applying a geometric constraint to the pillarplex portal. The distance between the outermost opposing NHC backbone carbon atoms was set to a fixed distance which was incrementally varied. For comparison

with experimental data,¹⁸ the derived portal opening d_{calcd} was defined as the distance between the respective hydrogen atoms attached to the constrained NHC backbone carbons. After each partial geometry optimization of the remaining atoms, the total energy of the complexes was evaluated as a function of d_{calcd} and referenced to the relative energies of the corresponding fully optimized geometries (**Figure 23**). The calculations show that the computed portal openings of the fully optimized gas-phase geometries of $[\text{Au}_8\text{L}^{\text{Me}_2}]^{4+}$ and $[\text{Au}_8\text{L}^{\text{t}_2}]^{4+}$ are considerably smaller than the experimentally derived distances: SC-XRD data reported herein and before by me and Pöthig group,¹⁸ show a more pronounced squeezing of the portal, quantified by $d = 4.80 \text{ \AA}$ for $[\text{Au}_8\text{L}^{\text{Me}_2}]^{4+}$ (vs. $d_{calcd} = 5.63 \text{ \AA}$) and $d = 2.93 \text{ \AA}$ for $[\text{Au}_8\text{L}^{\text{t}_2}]^{4+}$ (vs. $d_{calcd} = 4.75 \text{ \AA}$). The computed distances follow the same trend as the measured ones, namely the portal opening of $[\text{Au}_8\text{L}^{\text{Me}_2}]^{4+}$ is significantly larger than of $[\text{Au}_8\text{L}^{\text{t}_2}]^{4+}$. The deviation of the calculated gas-phase geometries from the experimental solid-state structures may largely originate from the presence of counter ions, packing effects, and interactions between multiple cationic fragments. However, Pickl pointed out that even without including these crucial factors that govern the solid-state structures of both complexes, the comparison of the relative gas-phase energies also indicates that the squeezing of the portal is more favorable for $[\text{Au}_8\text{L}^{\text{t}_2}]^{4+}$ than for $[\text{Au}_8\text{L}^{\text{Me}_2}]^{4+}$: Constraining the portal opening of $[\text{Au}_8\text{L}^{\text{Me}_2}]^{4+}$ to the computed distance of the fully optimized triazole pillarplex $[\text{Au}_8\text{L}^{\text{t}_2}]^{4+}$ ($d_{calcd} = 4.75 \text{ \AA}$) leads to a destabilization of ca. 13 kJ/mol, while constraining it to the experimental value for $[\text{Au}_8\text{L}^{\text{t}_2}]^{4+}$ in the solid-state ($d = 2.93 \text{ \AA}$) is even more unfavorable (ca. 84 kJ/mol). These results suggest that even when excluding the influence of intermolecular interactions in the solid-state, the *N*-substitution from pyrazolate to triazolate alone leads to a more facile portal deformability of the pillarplex.

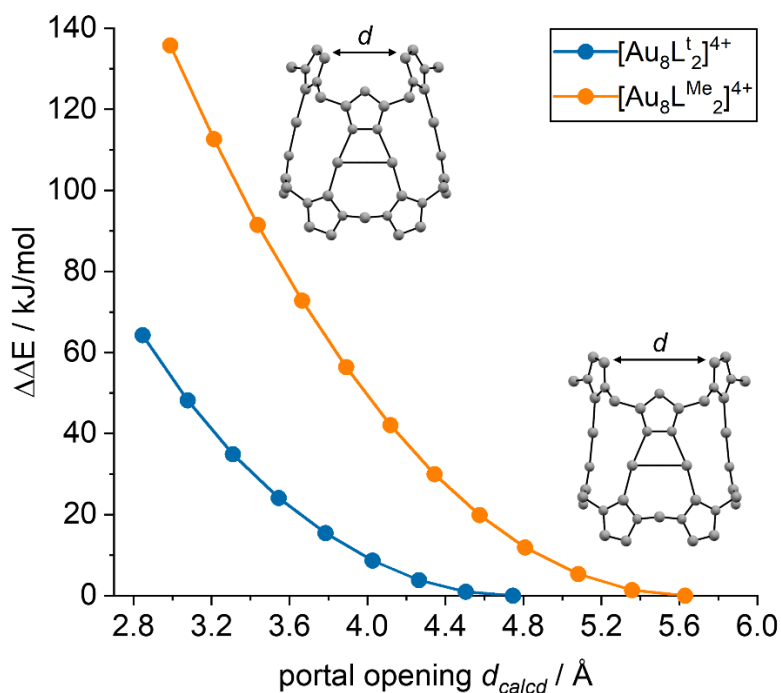


Figure 23. Calculated relative energy difference of $[\text{Au}_8\text{L}^t_2]^{4+}$ and $[\text{Au}_8\text{L}^{\text{Me}}_2]^{4+}$ as a function of the portal opening d_{calcd} . The relative stabilities of the unrestrained geometries of $[\text{Au}_8\text{L}^t_2]^{4+}$ and $[\text{Au}_8\text{L}^{\text{Me}}_2]^{4+}$ serve as reference points and were set to zero. Reproduced with permission from Ref. 19.

4.2.4 Conclusions

In conclusion, I successfully synthesized a new subclass of rim-modified pillarplex SOC's featuring triazolate instead of pyrazolate moieties in the macrocyclic NHC ligands. The triazolate was introduced *via* incorporation in the ligand precursor, a macrocyclic imidazolium cyclophane $\text{H}_6\text{L}^t(\text{OTf})_4$, which acts as a template in the self-assembly, determining the shape and pore size of the SOC. The solid-state structure of the gold(I) hexafluorophosphate complex $[\text{Au}_8\text{L}^t_2](\text{PF}_6)_4$ revealed unprecedented structural flexibility of the new pillarplexes, possibly caused by the lower steric demand of the introduced nitrogen atom at the rim. This is supported by DFT calculations, showing a significantly higher energy penalty for an attempted similar deformation modeled for the pyrazolate-based pillarplexes. Additionally, the triazolate nitrogen atom at the rim has been shown to be a hydrogen bond acceptor,

enabling a self-recognition between the cationic complexes. From a more generalized perspective, this proves that the macrocyclic templation strategy is a valid tool to generally tune structural properties of pillarplexes such as flexibility, but also to introduce additional functionality to the rim regions.

4.2.5 References of Section 4.2

1. A. J. Boydston and C. W. Bielawski, *Dalton Trans.*, 2006, **34**, 4073-4077.
2. A. J. Boydston, K. A. Williams and C. W. Bielawski, *J. Am. Chem. Soc.*, 2005, **127**, 12496-12497.
3. C. Radloff, J. J. Weigand and F. E. Hahn, *Dalton Trans.*, 2009, **43**, 9392-9394.
4. N. Sinha and F. E. Hahn, *Acc. Chem. Res.*, 2017, **50**, 2167-2184.
5. C. X. Wang, Y. Gao, Y. X. Deng, Y. J. Lin, Y. F. Han and G. X. Jin, *Organometallics*, 2015, **34**, 5801-5806.
6. W. Z. Zhang, Y. F. Han, Y. J. Lin and G. X. Jin, *Organometallics*, 2010, **29**, 2842-2849.
7. Y. F. Han, Y. J. Lin, W. G. Jia, G. L. Wang and G. X. Jin, *Chem. Commun.*, 2008, **15**, 1807-1809.
8. Y.-F. Han, H. Li and G.-X. Jin, *Chem. Commun.*, 2010, **46**, 6879-6890.
9. L. Y. Sun, N. Sinha, T. Yan, Y. S. Wang, T. T. Tan, L. Yu, Y. F. Han and F. E. Hahn, *Angew. Chem. Int. Ed.*, 2018, **57**, 5161-5165.
10. L. Zhang, R. Das, C. T. Li, Y. Y. Wang, F. E. Hahn, K. Hua, L. Y. Sun and Y. F. Han, *Angew. Chem.*, 2019, **131**, 13494-13498.
11. W. B. Yu, Y. F. Han, Y. J. Lin and G. X. Jin, *Chem. Eur. J.*, 2011, **17**, 1863-1871.
12. C. X. Lin, X. F. Kong, Q. S. Li, Z. Z. Zhang, Y. F. Yuan and F. B. Xu, *CrystEngComm*, 2013, **15**, 6948-6962.
13. D. Qin, X. Zeng, Q. Li, F. Xu, H. Song and Z.-Z. Zhang, *Chem. Commun.*, 2007, **2**, 147-149.

14. S. Ibáñez and E. Peris, *Angew. Chem. Int. Ed.*, 2020, **59**, 6860-6865.
15. S. Ibáñez and E. Peris, *Angew. Chem. Int. Ed.*, 2019, **58**, 6693-6697.
16. A. Gutiérrez-Blanco, S. Ibáñez, F. E. Hahn, M. Poyatos and E. Peris, *Organometallics*, 2019, **38**, 4565-4569.
17. S. Ibáñez, M. Poyatos and E. Peris, *Acc. Chem. Res.*, 2020, **7**, 1401-1413.
18. P. J. Altmann and A. Pöthig, *J. Am. Chem. Soc.*, 2016, **138**, 13171-13174.
19. S. Guan, T. Pickl, C. Jandl, L. Schuchmann, X. Zhou, P. J. Altmann and A. Pöthig, *Org. Chem. Front.*, **2021**, doi:10.1039/D1QO00588J.
20. Y.-D. Yang, J. L. Sessler and H.-Y. Gong, *Chem. Commun.*, 2017, **53**, 9684-9696.
21. C. J. Serpell, J. Cookson, A. L. Thompson and P. D. Beer, *Chem. Sci.*, 2011, **2**, 494-500.
22. P. J. Altmann and A. Pöthig, *Angew. Chem. Int. Ed.*, 2017, **56**, 15733-15736.
23. A. Pöthig, S. Ahmed, H. C. Winther-Larsen, S. Guan, P. J. Altmann, J. Kudermann, A. M. Santos Andresen, T. Gjøen and O. A. Høgmoen Åstrand, *Front. Chem.*, 2018, **6**, 584.
24. H. W. Schmidt and F. Würthner, *Angew. Chem. Int. Ed.*, 2020, **59**, 8766-8775.
25. P. D. Frischmann and M. J. MacLachlan, *Chem. Soc. Rev.*, 2013, **42**, 871-890.
26. N. Kuhn, T. Kratz, R. Boese and D. Bläser, *J. Organomet. Chem.*, 1994, **470**, C8-C11.
27. N. Kuhn, T. Kratz, D. Bläser and R. Boese, *Chem. Ber.*, 1995, **128**, 245-250.
28. N. Kuhn, T. Kratz, D. Bläser and R. Boese, *Inorg. Chim. Acta*, 1995, **238**, 179-181.
29. H. M. Bass, S. A. Cramer, A. S. McCullough, K. J. Bernstein, C. R.

- Murdock and D. M. Jenkins, *Organometallics*, 2013, **32**, 2160-2167.
30. H. V. Huynh, Y. Han, R. Jothibas and J. A. Yang, *Organometallics*, 2009, **28**, 5395-5404.
31. I. H. Wasbotten and A. Ghosh, *Inorg. Chem.*, 2007, **46**, 7890-7898.
32. K. Nagura, S. Saito, R. Fröhlich, F. Glorius and S. Yamaguchi, *Angew. Chem. Int. Ed.*, 2012, **51**, 7762-7766.
33. J. G. Haasnoot, *Coord. Chem. Rev.*, 2000, **200**, 131-185.
34. M. B. Cingi, A. M. M. Lanfredi, A. Tiripicchio, J. P. Cornelissen, J. G. Haasnoot and J. Reedijk, *Inorg. Chim. Acta.*, 1987, **129**, 217-222.
35. R. Hage, J. G. Haasnoot, H. A. Nieuwenhuis, J. Reedijk, D. J. De Ridder and J. G. Vos, *J. Am. Chem. Soc.*, 1990, **112**, 9245-9251.
36. J. H. Van Diemen, R. Hage, J. G. Haasnoot, H. E. Lempers, J. Reedijk, J. G. Vos, L. De Cola, F. Barigelletti and V. Balzani, *Inorg. Chem.*, 1992, **31**, 3518-3522.
37. T. Asaji, H. Sakai and D. Nakamura, *Inorg. Chem.*, 1983, **22**, 202-206.
38. J. P. Zhang and X. M. Chen, *Chem. Commun.*, 2006, **16**, 1689-1699.
39. N. Mesquida, I. Dinarès, A. Ibáñez and E. Alcalde, *Org. Biomol. Chem.*, 2013, **11**, 6385-6396.
40. E. Alcalde, N. Mesquida, L. Pérez - García, S. Ramos, M. Alemany and M. L. Rodríguez, *Chem. Eur. J.*, 2002, **8**, 474-484.
41. E. Alcalde, P. Pacheco and J. Elguero, *Synth. React. Inorg. Met. Org. Chem.*, 1996, **26**, 1279-1294.
42. P. J. Altmann and A. Pöthig, *J. Am. Chem. Soc.*, 2016, **138**, 13171-13174.
43. E. Bernarducci, P. K. Bharadwaj, K. Krogh-Jespersen, J. A. Potenza and H. J. Schugar, *J. Am. Chem. Soc.*, 1983, **105**, 3860-3866.
44. A. Bondi, *J. Phys. Chem.*, 1964, **68**, 441-451.
45. B. Cordero, V. Gómez, A. E. Platero-Prats, M. Revés, J. Echeverría, E. Cremades, F. Barragán and S. Alvarez, *Dalton Trans.*, 2008, **21**, 2832-2838.

46. L. Magnko, M. Schweizer, G. Rauhut, M. Schütz, H. Stoll and H. J. Werner, *Phys. Chem. Chem. Phys.* 2002, **4**, 1006-1013.
47. M. R. Anneser, S. Haslinger, A. Pöthig, M. Cokoja, J.-M. Basset and F. E. Kühn, *Inorg. Chem.*, 2015, **54**, 3797-3804.
48. P. J. Altmann, C. Jandl and A. Pöthig, *Dalton Trans.*, 2015, **44**, 11278-11281.
49. A. Weiss, V. Barba, H. Pritzkow and W. Siebert, *J. Organomet. Chem.*, 2003, **680**, 294-300.
50. A. Weiss, H. Pritzkow and W. Siebert, *Angew. Chem. Int. Ed.*, 2000, **39**, 547-549.
51. C. Yang, X. S. Xue, J. L. Jin, X. Li and J. P. Cheng, *J. Org. Chem.*, 2013, **78**, 7076-7085.
52. C. Yang, X.-S. Xue, X. Li and J.-P. Cheng, *J. Org. Chem.*, 2014, **79**, 4340-4351.
53. V. S. Bernales, A. V. Marenich, R. Contreras, C. J. Cramer, D. G. Truhlar, *J. Phys. Chem. B.*, 2012, **116**, 9122-9129.
54. J. S. Bradshaw, R. B. Nielsen, P. K. Tse, G. Arena, B. E. Wilson, N. K. Dalley, J. D. Lamb, J. J. Christensen and R. M. Izatt, *J. Heterocycl. Chem.*, 1986, **23**, 361-368.
55. A. L. Spek, *Acta Crystallogr. C*, 2015, **71**, 9-18.
56. J. W. Lee, S. Samal, N. Selvapalam, H.-J. Kim and K. Kim, *Acc. Chem. Res.*, 2003, **36**, 621-630.
57. E. V. Peris, C. Vicent, V. Martinez-Agramunt, V. Gandhi, C. Larriba-Andaluz and D. Gusev, *Angew. Chem. Int. Ed.*, 2021, DOI: 10.1002/anie.202100914.
58. E. V. Peris and S. Ibáñez, *Chem. Eur. J.*, 2021, DOI: 10.1002/chem.202100794.
59. M. Baron, C. Tubaro, A. Biffis, M. Basato, C. Graiff, A. Poater, L. Cavallo, N. Armaroli and G. Accorsi, *Inorg. Chem.*, 2012, **51**, 1778-1784.

4.3 Cyclic trinuclear $\text{Au}_3(1\text{-Methylimidazolate})_3$

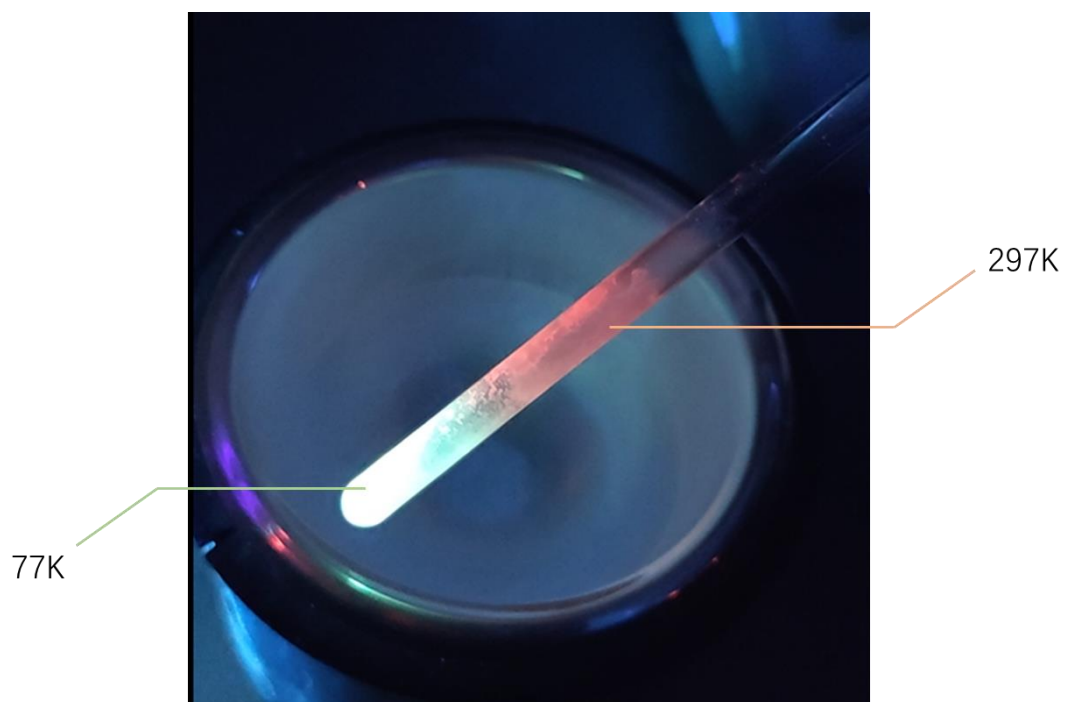


*Photo of thermochromism effect of $\text{Au}_3(1\text{-Methylimidazolate})_3$ solid sample with α structure under 255 nm UV light in a quartz tube. The bottom part of the quartz tube was cooled with liquid nitrogen (77 K), while the upper part was at room temperature (297 K).

4.3.1 Abstract

In the study of rim modified of pillarplex, three backbone modified NHC macrocyclic ligands formed a compound $[\text{Ag}_{11}\text{L}^{\text{DM}_3}]\text{X}_5$ with eleven silver atoms. Inside the $[\text{Ag}_{11}\text{L}^{\text{DM}_3}]^{5+}$ cation, three Ag atoms were attracted by argentophilic interactions to each other and constructed a cyclic trinuclear structure, which helps to stabilize the cationic structure. From a more generalized perspective, the trinuclear triangle structure is the simplest polynuclear structure. A more concise example of the triangle structure is the cyclic trinuclear complex (CTC), which is characterized by its planar or near-planar trimetal nine-membered rings consists of metal atoms that linearly coordinate with N / C atoms in ditopic anionic bridging ligands.¹ Having a great interest in closed-shell coinage-metal-based systems constructed with NHC ligands, I chose the Au(I) imidazolate-based CTCs as a platform to evaluate the potential of CTC for supramolecular organometallic complexes (SOCs) assembly and to investigate the metallophilic interactions as well as relevant photophysical properties.

During the study, the synthesis of $[\text{Au}_3(1\text{-Methylimidazolate})_3]$ – the simplest congener of imidazolate-based Au(I) CTCs – was repeated and a new solvatomorph of $[\text{Au}_3(1\text{-Methylimidazolate})_3]$ has been identified and structurally characterized. Single-crystal X-ray diffraction revealed a dichloromethane solvate exhibiting remarkably short intermolecular Au...Au distances (3.2190(7) Å). This goes along with a dimer formation in the solid state, which is not observed in a previously reported solvent-free crystal structure. Hirshfeld analysis, in combination with DFT calculations, indicates that the dimerization is generally driven by attractive aurophilic interactions, which are commonly associated with the luminescence properties of CTCs. Since $[\text{Au}_3(1\text{-Methylimidazolate})_3]$ has previously been reported to be emissive in the solid-state, I conducted a thorough photophysical study combined with phase analysis utilizing powder X-ray diffraction (PXRD), to correctly attribute

the photophysical active phase of the bulk material. Interestingly, all investigated powder samples accessed via different preparation methods can be assigned to the pristine solvent-free crystal structure, showing no aurophilic interactions. Finally, the observed strong thermochromism of the solid-state material was investigated using variable-temperature PXRD, ruling out a significant phase transition being responsible for the drastic change of the emission properties (hypsochromic shift from 710 nm to 510 nm) when lowering the temperature up down to 77 K.

4.3.2 Introduction

Cyclic trinuclear complexes (CTCs) featuring three coordinated metal atoms in the nine-membered planar or near planar rings represent some of the simplest polynuclear metal clusters. Comprehensive synthetic, structural, theoretical, and photophysical studies have been performed on a variety of cyclic trinuclear complexes, featuring series of angular ditopic bridging ligands, including carbenate, pyrazolate, imidazolate, and triazolate ligands.²⁻⁸ CTCs have found various applications in the field of intermolecular M(I)–M(I) interactions^{9,10}, metalloaromaticity/ π -acidity and basicity¹¹, luminescence¹²⁻¹⁴ and supramolecular assembly¹⁵⁻¹⁷. (**Figure 24, B, C, D**) Imidazolate-based CTCs are the least studied compared to those of carbenate and pyrazolate, only four examples have been reported (**Figure 24, A**). In the 90s, Burini, Wagner and coworkers reported the synthesis of Au₃ imidazolate CTCs bearing methyl or benzyl substituents, while more recently Omary et al. achieved complexes of general formula tris[(μ_2 -1-ethylimidazolato-N³,C²)Au(I)] (Au₃(EtIm)₃) (Et = ethyl).^{4,8,18} These complexes exhibit rich supramolecular chemistry having, e.g. fascinating luminescence properties in sandwich adducts of Au(I) imidazolate CTCs with Ag⁺ and Tl⁺.⁷ Very recently, CTCs were also shown to act as donors with a range of planar π -acceptors and exhibited exceptional strong binding, which envisaged more complicated aromatic donor-acceptor supramolecular

assembly(**Figure 24, C**).^{19,20} Remarkably, Fujita et al. used the tris[(μ_2 -1-methylimidazolato- N^3,C^2)Au(I)] (abbreviated 'Au₃(Melm)₃' in the following, Me = methyl) and Ag⁺ ions formed to form an unprecedented triple-decker ion cluster (Au₃-Ag-Au₃-Ag-Au₃) decker cluster within a self-assembled cage (**Figure 24, D**).¹⁵⁻¹⁷

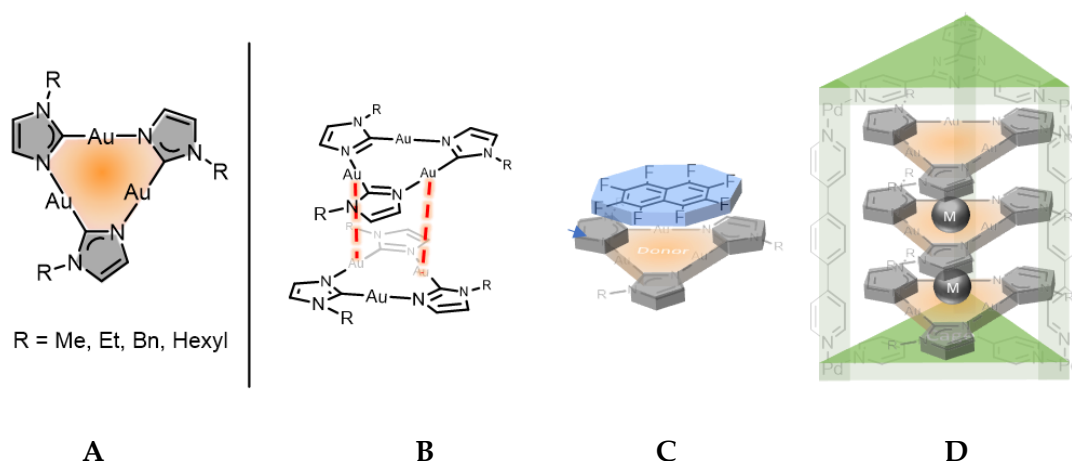


Figure 24. **A**. General structure of imidazolate-based CTCs [Au₃(Melm)]₃;^{8,21} [Au₃(EtIm)]₃; Au₃(BzIm)₃;^[17] Au₃(HexIm)₃;¹⁹ **B**. illustration of metallophilic interaction; **C**. Lewis acidity/basicity of π electron system¹⁹; **D**. supramolecular trigonal prismatic arrays within a palladium coordination cages, M = Ag⁺ cation.¹⁵

In this context, having a great interest in closed-shell coinage-metal-based systems with fascinating photo-physical properties,^{22,23} I further consider the Au(I) imidazolate-type CTCs as a valuable platform to investigate luminescence, inter- and intra-trimer metal-metal interactions and related supramolecular assembly. The simplest CTC - Au₃(Melm)₃ was the first synthesized Au(I) imidazolate CTC by Burini in 1989,⁸ but was not structurally determined until very recently by Ruiz in 2020.²¹ The reported crystal structure showed no co-crystallization of solvent molecules or any pronounced intermolecular aurophilic interactions between Au₃Melm₃. When reinvestigating the synthesis, I serendipitously discovered a new solvatomorph at an unconventional cryogenic crystallization condition, which actually features a dimer formation of Au₃Melm₃ through aurophilic interactions. Such weak metallophilic interactions in linear-

coordinate Au(I) complexes are similar to the energies of hydrogen bonds,^{9,24} and are also involved in the occurrence of polymorphism/ solvatomorphism in the solid state.²⁵⁻²⁷ In addition, aurophilic interactions are closely related to luminescence, pointing towards significant differences in the emission properties of the different solid-state structures. Therefore, I conducted a combined photophysical and structural study, accompanied by DFT-calculations, of Au₃Melm₃ being the archetypal molecule for imidazolate-based CTCs, to investigate which exact polymorph is the photophysical active phase.

4.3.3 Results and Discussion

4.3.3.1 Structural analysis

I prepared Au₃(Melm)₃ mainly following the route described previously by Burini⁸ and Vaughan²⁸ with minor modifications (see Experimental section for details). Numerous attempts have been made to obtain crystals suitable for single-crystal X-ray diffraction analysis, however, the majority of attempts were unsuccessful. For example, slow evaporation of a solution of Au₃(Melm)₃ in dichloromethane or chloroform solution at ambient conditions leads to the formation of a bright yellow solution and colloid gold precipitation. To prevent decomposition, crystallization was then carried out at ultra-low temperature instead of reported room temperature crystallization. After keeping a saturated solution of dichloromethane/hexane (20:1) at 193 K (-80 °C) for two weeks, colorless needle-like crystals suitable for a single-crystal X-ray diffraction study were obtained.

The SC-XRD result revealed the presence of a novel solvatomorph (hereafter referred to as the solvatomorph β) which is completely divergent from the one previously reported (the structure discovered by Ruiz *et al.* is referred as the polymorph α).²¹ In details, the trinuclear complex Au₃(Melm)₃ crystallizes in triclinic system with space group *P*-1, and the structure shows three gold atoms

bridging between three 1-methylimidazolate in a way that the metal ions are bound to one nitrogen and one carbon donor atom from neighboring imidazolates, through N...Au...C linkages. The angles of N-Au-C slightly deviate from linearity, which are similar to Au₃ imidazolium trimers with bulkier substituents (ethyl/benzyl).^{4,18} The distances of intramolecular contacts are slightly exceeding the range of reported Au₃ imidazolium complexes (ethyl/benzyl) (3.436 to 3.465 Å).^{4,18} This molecular monomer structure can be considered identical for structure α and β , despite some minor differences.

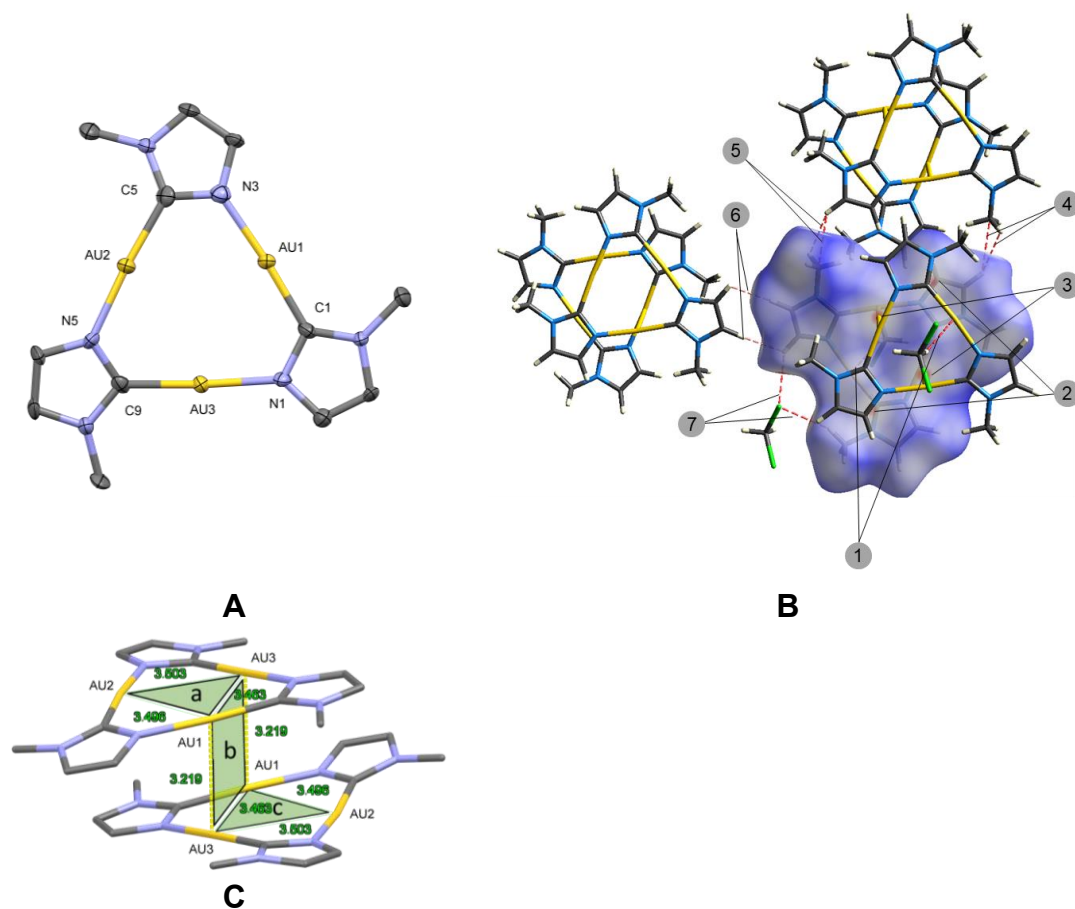


Figure 25. **A.** A view of the molecular structure of the monomer of Au₃(Melm)₃ from solvatomorph β with displacement ellipsoids is shown at 50% probability. Hydrogen atoms are omitted for clarity. (note that the monomer triangle molecules are identical in both polymorphs.) **B.** Overview of the different non-covalent interactions around Au₃(Melm)₃ molecule within dimeric structure in solvatomorph β as determined by Hirshfeld surface analysis. (Note: Due to reasons of clarity not all symmetry equivalent interactions are depicted in the figure) **C.** Dimer-of-trimer formation found in solvatomorph β , shown in ORTEP plot. Solvents are omitted for clarity. Selected bond lengths (Å): Au1...Au2, 3.496(0) Å; Au3...Au2, 3.503(1) Å; Au3...Au1,

3.463(5) Å; Selected angles (Å) C-Au1-N, 175.8(4)°; C-Au2-N, 173.5(4)°; C-Au3-N, 175.3(1)°.

In this solvatomorph β , the imidazolate trimer experiences attractive aurophilic interaction with its neighboring trimer, which is absent in polymorph α . Together with the repulsion from the auxiliary alkyl group, the aurophilic interaction links two trimers (**Figure 25, A**) in a twist-staggered arrangement by 180° relative to each other (**Figure 25, C**). To evidence possible interactions between trimers, Hirshfeld surface analysis was applied for a single trimer in **Figure 25, B**. In the d_{normal} mapping, four interactions (2 & 3) on the Hirshfeld surface between two trimers can be observed, which I attribute to two aurophilic interactions (interaction 3) and two short contacts (interaction 2) between carbon atoms on the heterocyclic rings. The interaction 1 and 7 are related to solvent molecules. Hydrogen bonds 7 C-Cl...H are formed between imidazolate back-bone hydrogen atoms and chlorine on dichloromethane. Interaction 1 (C-H...Au distance: 2.739 Å) show hydrogen bonds between dichloromethane and gold atoms, with CH group on dichloromethane acting as donor and gold acting as hydrogen bond acceptor. A survey was performed using Cambridge Structural Database (CSD), results herein reveal that among all the reported Au₃ cyclotrimers preserving Au...H hydrogen bonding, Au₃(Melm)₃ has the shortest distance between hydrogen to the triangular centroid. The Au...H distance (2.739 Å) shorter than the sum of the van der Waals radii (2.8 Å).²⁹ In an authoritative review of the hydrogen bonding to gold, Schmidbaur et al. summarized different types of Au...H-X bonding. In the discussion of Au₃ or Au₄ clusters, he concluded this kind of bonding is dominated by classical Lewis-adduct formation.²⁹⁻³¹ Interactions 4-6 are CH...C hydrogen bonds bridging the imidazolate back-bone hydrogen atoms to methylene group of neighbored, symmetry equivalent dimers.

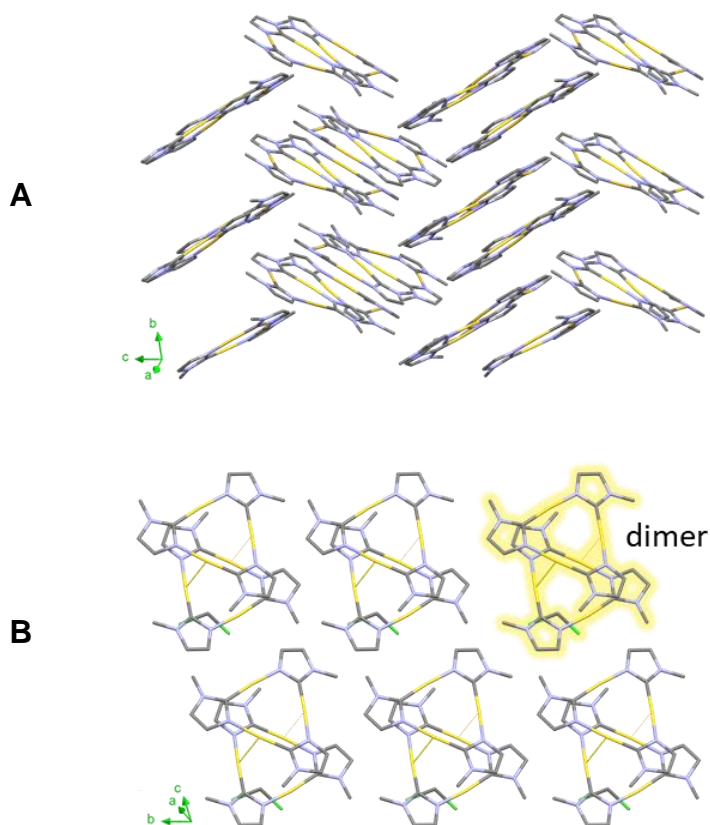


Figure 26. Packing of the different solvatomorphs of $\text{Au}_3(\text{Melm})_3$ in the solid-state: **A**. Solvent-free polymorph α . **B**. Solvatomorph β (dichloromethane solvate). Hydrogen atoms and co-crystallized solvent molecules were omitted for clarity.

The aforementioned $\text{Au}_3(\text{Etlm})_3$ exhibits a similar stair-like dimer-trimer arrangement with the solvatomorph β (compare **Figure 25**).⁴ To quantify the shape similarity, I defined three planes that go through the hexanuclear gold core in the dimer-trimer in **Figure 25, C**. Plane *a* is defined by Au1-Au2-Au3 on the top layer, plane *b* is defined by Au1-Au3 on the top and Au1-Au3 on the bottom, the plane *c* is defined by Au1-Au2-Au3 on the bottom. The plane angles $\angle ab$ and $\angle bc$ are both 88.07° in β , smaller than the plane angles in $\text{Au}_3(\text{Etlm})_3$ (between 95.85 and 101.54°). The centroid *a* and centroid *c* are on parallel planes, their projections on the same plane are separated by 2.04 \AA , while in the case of $\text{Au}_3(\text{Etlm})_3$, the distance is 2.00 \AA and 2.04 \AA . The distance between plane *a* and *b* is shorter in $\text{Au}_3(\text{Etlm})_3$ than solvatomorph β (3.01 \AA vs 3.18 \AA), but the shorter inter-plane distance does not contribute to stronger

aurophilic interactions.

The differences between structure α and β in the intermolecular interactions consequently lead to the aforementioned different packing of the two crystal structures as shown in **Figure 26**. $\text{Au}_3(\text{Etlm})_3$ molecules in the solvent-free monoclinic polymorph α are separated and form zigzag-like layers along the c axis (**Figure 26, A**). Hereby, the intermolecular interactions are dominated by hydrogen bonding, and the closest Au-Au distance is 3.666(0) Å. In contrast, in the solvatomorph β , the dimers of $\text{Au}_3(\text{Etlm})_3$ are packed within layered arrangements in the b - c plane (**Figure 26, B**).

4.3.3.2 DFT studies

The results of the SC-XRD analysis of solvatomorph β together with the conducted Hirshfeld analysis clearly point towards the formation of intermolecular (additionally to coordination induced intramolecular) metallophilic Au-Au interactions in Au_3Melm_3 gold(I) trimer structures, which has never been observed so far. Therefore, to further rationalize the potential M-M interactions of the selected CTC, David Mayer performed electronic structure calculations by density functional theory (DFT), using the M06 meta-hybrid functional by Truhlar³² and the CEP-31G(d) basis set.³³ This approach has successfully been applied in the theoretical description of CTCs^{34,35} and other systems with predominantly non-covalent interactions³⁶. Specifically, Galassi and co-workers used M06/CEP-31G(d) DFT computations to examine d^{10} - d^{10} metal-metal bonding in the abovementioned CTC, $[\text{Au}_2(\mu\text{-C}^2, \text{N}^3\text{-Melm})_2\text{Cu}(\mu\text{-3,5-(CF}_3)_2\text{Pz})]$, which renders a direct comparison to related systems possible.^{34,37}

From the calculation result, David Mayer concluded that the $\text{Au}_3(\text{Melm})_3$ -Dimer formation from monomer species $\text{Au}_3(\text{Melm})_3$ is driven by robust aurophilic interactions. This result is in accordance with the crystallographic analysis. Calculations of the dimer formation free energy underpinned by the dimer

dissociation energy, reveal rather strong aurophilic bonding interactions. Analysis of the bonding situation by different bonding indexes reveals a rather small bonding interaction within the Au_3^{3+} core, but stronger interactions between monomer complexes in the dimer.

The aurophilic interactions are commonly associated with the luminescence properties of CTCs. Given that two different metal-metal bondings can be found in the solid-state of $\text{Au}_3(\text{Melm})_3$. I conducted a thorough photophysical study in combination with phase analysis, to correctly correlate the photophysical active phase of the bulk material.

4.3.3.3 Qualitative phase analysis and photophysical studies

In the attempts to grow samples for single-crystal X-ray diffraction analysis, two crystallization methods were employed: (i) slow evaporation of dichloromethane solution of $\text{Au}_3(\text{Melm})_3$; (ii) vapor diffusion of *n*-hexane or diethyl ether into dichloromethane solution of $\text{Au}_3(\text{Melm})_3$. Additionally, crystallization experiments were carried out at different temperatures to prevent decomposition. Limited to the low diffusion coefficient of solvent at ultra-low temperature, vapor diffusion crystallization experiments with dichloromethane and hexane at 193 K did not yield suitable single crystals, while the slow evaporation of dichloromethane solution offers few single crystals of solvatomorph β serendipitously. In the remaining samples, I found that crystalline products obtained at a temperate higher than 253 K (-20 °C), always offer the polymorph α . Interestingly, dissolution of a sample of the solvatomorph β in dichloromethane followed by evaporation higher than 253 K leads to the formation of α structure.

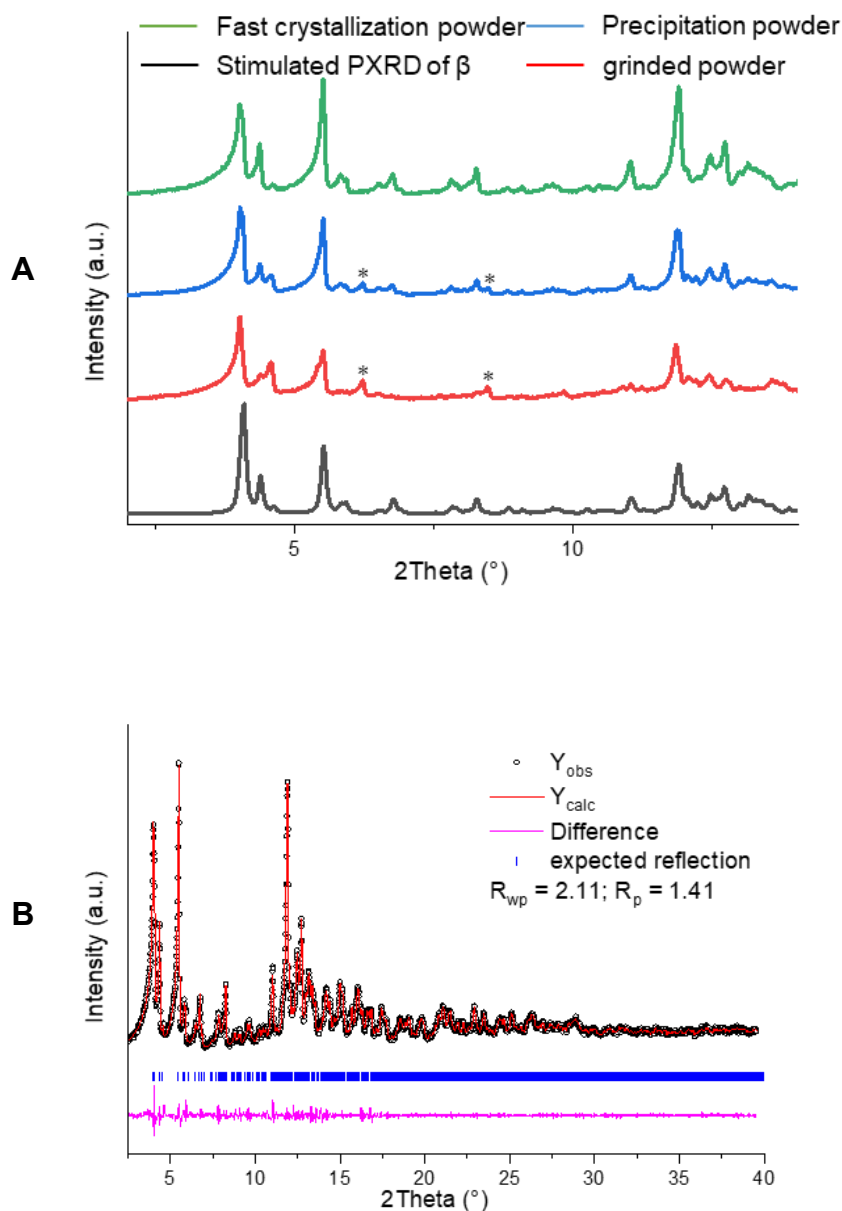


Figure 27. **A.** Rietveld refinement plots ($\lambda = 0.71 \text{ \AA}$) of powder obtained with fast crystallization, precipitation, and grinded powder in ambient condition. Simulated pattern was obtained from SC-XRD of polymorph α . **B.** Pawley fit analysis of fast crystallization powder and calculated data. Observed data sets and calculated data are shown in black symbols and red line, respectively. The pink line shows the difference curve, while the blue marks show Bragg positions.

As the preparation of bulk crystalline samples for luminescence tests is generally conducted at ambient conditions, the formation of the α polymorph should be expected. However, since also different solvent combinations were

used, compared to the preparations of the single crystals, I carefully investigated the solid-state phase of the prepared bulk samples by means of powder X-ray diffraction (PXRD). Hereby, products from (1) fast evaporation of $\text{Au}_3(\text{MeIm})_3$ from DCM/THF solution and (2) precipitation of $\text{Au}_3(\text{MeIm})_3$ with *n*-hexane/ Et_2O from DCM/THF solution were characterized. The powder diffractograms of the samples of the two crystallization methods are shown in **Figure 27, A**. Small differences can be visually observed (marked by asterisks), which I tentatively attribute to a minor side phase I cannot further specify. Pawley analysis was used to compare the simulated PXRD of polymorph α with that of the measured powder sample from fast evaporation, and shows a very good fit of both diffractograms (**Figure 27, B**). Consequently, all bulk crystallization methods at ambient conditions led to the formation of polymorph α , and fast crystallization by solvent removal was identified to yield the most phase-pure material, which then has been used for the luminescence measurements described in the following.

The luminescence measurement of the crystalline sample with polymorph α partially fits with reported results (**Figure 28**).²¹ When excited with 256 nm UV light, polymorph α exhibits the emission maximum at around 710 nm at room temperature. However, Ruiz and co-workers reported that in their luminescence measurement, two emission bands at 722 nm and 810 nm can be found. Given that there might exist multiple solid-state structures in Au_3MeIm_3 samples, I tentatively attribute the peak at 810 nm to the contamination of other phases.

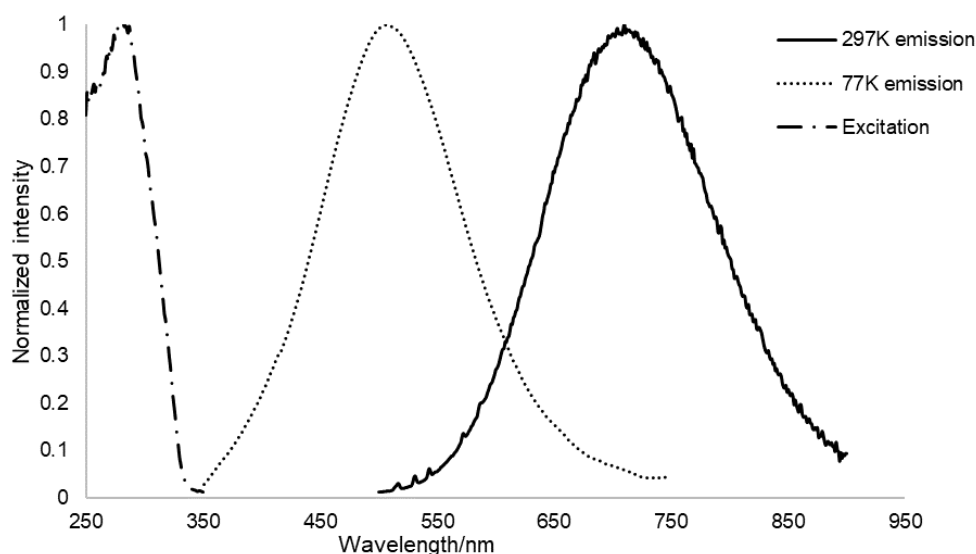


Figure 28. Diffuse reflectance and emission spectra of the solid samples of polymorph α at 297 K and 77 K. The excitation pattern is the same at room temperature and cryogenic temperature. Quantum yield is 15% at 297 K and 60% at 77 K, respectively.

Another attractive photophysical behavior of polymorph α was observed when cooling the sample with liquid nitrogen. At 77 K, the emission maximum moves to 510 nm with a dramatic intensity increase (quantum yield increased from 15 % to 60 %) (**Figure 28**). When warming up to 297 K, the emission was restored. The whole process was fully reversible. The drastic hypsochromic shifting at cryogenic temperature is very rare in CTCs.^{4,38,39} Raithby et al. considered the crystallographic phase transition could be correlated with shifts of the luminescence maxima at different temperatures.⁴⁰ To rule out the possibility of structural deformation with changing temperature. Measurements of unit cell parameters with SC-XRD at different temperatures were conducted, the crystal structure of polymorph α at 296(2) K shows the same space group $P2_1/c$ with <0.5% yet expected thermal expansion versus the 100(2) K structure. Accordingly, calculated density decreases from 3.547 to 3.452 g/cm³; intermolecular Au-Au distances slightly increase from 3.689 Å, 3.751 Å, 4.141 Å to 3.776 Å, 3.778 Å, 4.181 Å, respectively. All the intermolecular Au-Au distances significantly exceed the sum of the vdW radii of Au (3.32 Å),⁹ no

additional aurophilic interactions could be observed at cryogenic temperature. These findings are supported by non-ambient PXRD measurements (**Figure 29**), which also show no change in the diffraction pattern and therefore no phase transition when continuously measured between -180 °C and 40°C. Hence, I think that the minor structural changes in the packing of polymorph α cannot be correlated with the observed distinct thermochromism.

There are other possible explanations for the thermochromism in CTCs. Omary and coworkers observed similar thermochromism in other CTCs.^{4,34} They speculated that thermochromism probably resulted from changes in the relaxation pathway of emission in the molecule. In the case of Au_3EtIm_3 , Omary and coworkers observed the emission bands centers at 425 nm at $T < 200$ K, and shift to 700 nm at $T \geq 200$ K. They suggested that at a high temperature (above 200 K in their case), a non-radiation relaxation to an intermediate excitation state takes place, to give rise to the low energy emission band. At lower temperatures ($T < 200$ K), which give rise to a high excitation state, a higher energy emission would happen (centered at 425 nm). This proposed mechanism is supposed to be further studied in the future.

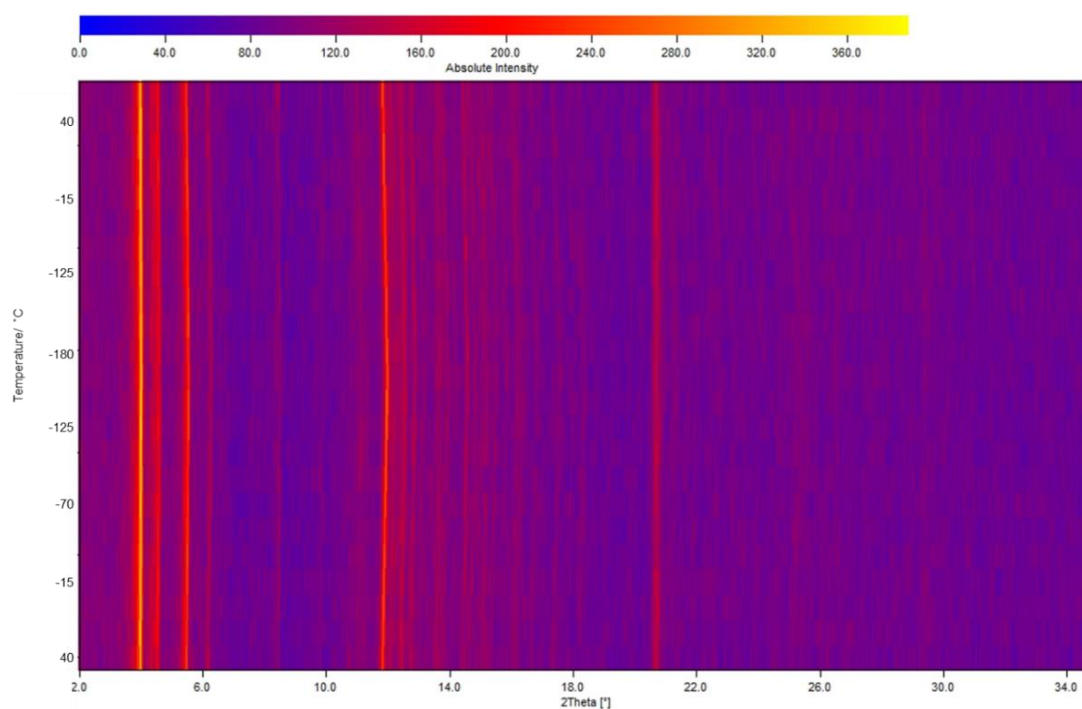


Figure 29. 3D graphic illustration of the powder XRD VT series ($\lambda = 0.71 \text{ \AA}$), the temperature goes from 40 °C to -180 °C and back to 40 °C.

4.3.4 Conclusion

In conclusion, this study revealed a new solvatomorph β (dichloromethane solvate) of $[\text{Au}_3(1\text{-Methylimidazolate})_3]$, the archetypal imidazolate CTC molecule, exhibiting unprecedented short intermolecular aurophilic interactions in the solid-state which were rationalized with DFT calculations. Crystallization conditions were investigated in combination with powder X-ray diffraction monitoring to correctly correlate the photophysical active phase of bulky crystalline material. All investigated powder samples accessed via different preparation methods can be assigned to the pristine solvent-free polymorph α , showing no aurophilic interactions. In addition, a strong thermochromic behavior of polymorph α was observed, which implies that the monomeric Au_3 core is solely responsible for the emissive nature of Au CTC complexes. From a more generalized perspective, this study provides the first example of solvatomorphism induced aurophilic interactions in cyclic trinuclear complexes,

and underlines the importance of a thorough solid-state characterization when deducing properties of molecular materials.

4.3.5 References of Section 4.3

1. J. Zheng, Z. Lu, K. Wu, G.-H. Ning and D. Li, *Chem. Rev.*, 2020, **120**, 9675-9742.
2. M. C. Gimeno and A. Johnson, *Chem. Eur. J.*, 2020, **26**, 11256.
3. L. H. Gade, *Angew. Chem. Int. Ed. Engl.*, 1997, **36**, 1171-1173.
4. M. M. Ghimire, V. N. Nesterov and M. A. Omary, *Inorg. Chem.*, 2017, **56**, 12086-12089.
5. M. A. Rawashdeh-Omary, M. A. Omary, J. P. Fackler, R. Galassi, B. R. Pietroni and A. Burini, *J. Am. Chem. Soc.*, 2001, **123**, 9689-9691.
6. M. M. Olmstead, F. Jiang, S. Attar and A. L. Balch, *J. Am. Chem. Soc.*, 2001, **123**, 3260-3267.
7. A. Burini, J. P. Fackler Jr, R. Galassi, T. A. Grant, M. A. Omary, M. A. Rawashdeh-Omary, B. R. Pietroni and R. J. Staples, *J. Am. Chem. Soc.*, 2000, **122**, 11264-11265.
8. F. Bonati, A. Burini, B. R. Pietroni and B. Bovio, *J. Organomet. Chem.*, 1989, **375**, 147-160.
9. H. Schmidbaur and A. Schier, *Chem. Soc. Rev.*, 2012, **41**, 370-412.
10. H. Schmidbaur and A. Schier, *Chem. Soc. Rev.*, 2008, **37**, 1931-1951.
11. S. M. Tekarli, T. R. Cundari and M. A. Omary, *J. Am. Chem. Soc.*, 2008, **130**, 1669-1675.
12. J. C. Vickery, M. M. Olmstead, E. Y. Fung and A. L. Balch, *Angew. Chem. Int. Ed. Engl.*, 1997, **36**, 1179-1181.
13. A. Hayashi, M. M. Olmstead, S. Attar and A. L. Balch, *J. Am. Chem. Soc.*, 2002, **124**, 5791-5795.
14. M. A. Omary, O. Elbjeirami, C. S. P. Gamage, K. M. Sherman and H. R. Dias, *Inorg. Chem.*, 2009, **48**, 1784-1786.

15. T. Osuga, T. Murase and M. Fujita, *Angew. Chem.*, 2012, **124**, 12365-12367.
16. M. Kiguchi, J. Inatomi, Y. Takahashi, R. Tanaka, T. Osuga, T. Murase, M. Fujita, T. Tada and S. Watanabe, *Angew. Chem.*, 2013, **125**, 6322-6325.
17. T. Osuga, T. Murase, M. Hoshino and M. Fujita, *Angew. Chem. Int. Ed.*, 2014, **53**, 11186-11189.
18. B. Bovio, S. Calogero and F. Wagner, *J. Organomet. Chem.*, 1994, **470**, 275.
19. R. Hahn, F. Bohle, W. Fang, A. Walther, S. Grimme and B. Esser, *J. Am. Chem. Soc.*, 2018, **140**, 17932-17944.
20. A. Burini, R. Bravi, J. P. Fackler Jr, R. Galassi, T. A. Grant, M. A. Omary, B. R. Pietroni and R. J. Staples, *Inorg. Chem.*, 2000, **39**, 3158-3165.
21. J. Ruiz, D. Sol, M. A. Mateo, M. Vivanco and R. Badía-Laiño, *Dalton Trans.*, 2020, **49**, 6561-6565.
22. P. J. Altmann and A. Pöthig, *J. Am. Chem. Soc.*, 2016, **138**, 13171-13174.
23. S. Guan, T. Pickl, C. Jandl, L. Schuchmann, X. Zhou, P. J. Altmann and A. Pöthig, *Org. Chem. Front.*, 2021, doi:10.1039/D1QO00588J.
24. H. Schmidbaur, W. Graf and G. Müller, *Angew. Chem. Int. Ed. Engl.*, 1988, **27**, 417-419.
25. R. J. Davey, *Polymorphism in Molecular Crystals Joel Bernstein*. Oxford University Press, New York, ISBN 0198506058. 2002
26. J. Lefebvre, R. J. Batchelor and D. B. Leznoff, *J. Am. Chem. Soc.*, 2004, **126**, 16117-16125.
27. R. L. White-Morris, M. M. Olmstead and A. L. Balch, *J. Am. Chem. Soc.*, 2003, **125**, 1033-1040.
28. L. G. Vaughan, *J. Am. Chem. Soc.*, 1970, **92**, 730-731.
29. H. Schmidbaur, H. G. Raubenheimer and L. Dobrzańska, *Chem. Soc. Rev.*, 2014, **43**, 345-380.
30. E. Kryachko, A. Karpfen and F. Remacle, *J. Phys. Chem. A.*, 2005, **109**,

- 7309-7318.
31. M. Rigoulet, S. Massou, E. D. S. Carrizo, S. Mallet-Ladeira, A. Amgoune, K. Miqueu and D. Bourissou, *Proc. Natl. Acad. Sci. U.S.A.*, 2019, **116**, 46-51.
 32. Y. Zhao and N. Schultz, *J. Chem. Theory Comput.*, 2006, **2006**, 2.
 33. T. R. Cundari and W. J. Stevens, *J. Chem. Phys.*, 1993, **98**, 5555-5565.
 34. R. Galassi, M. M. Ghimire, B. M. Otten, S. Ricci, R. N. McDougald, R. M. Almotawa, D. Alhmoud, J. F. Ivy, A.-M. M. Rawashdeh and V. N. Nesterov, *Proc. Natl. Acad. Sci. U.S.A.*, 2017, **114**, E5042-E5051.
 35. R. Galassi, S. Ricci, A. Burini, A. Macchioni, L. Rocchigiani, F. Marmottini, S. M. Tekarli, V. N. Nesterov and M. A. Omary, *Inorg. Chem.*, 2013, **52**, 14124-14137.
 36. Y. Zhao and D. G. Truhlar, *Acc. Chem. Res.*, 2008, **41**, 157-167.
 37. N. B. Jayaratna, M. M. Olmstead, B. I. Kharisov and H. R. Dias, *Inorg. Chem.*, 2016, **55**, 8277-8280.
 38. C. Yang, M. Messerschmidt, P. Coppens and M. A. Omary, *Inorg. Chem.*, 2006, **45**, 6592-6594.
 39. M. A. Omary, M. A. Rawashdeh-Omary, M. A. Gonser, O. Elbjeirami, T. Grimes, T. R. Cundari, H. V. Diyabalanage, C. S. P. Gamage and H. R. Dias, *Inorg. Chem.*, 2005, **44**, 8200-8210.
 40. C. H. Woodall, J. Christensen, J. M. Skelton, L. E. Hatcher, A. Parlett, P. R. Raithby, A. Walsh, S. C. Parker, C. M. Beavers and S. J. Teat, *IUCrJ*, 2016, **3**, 367-376.

5 Conclusion and Outlook

The focus of this thesis lies on the synthesis and properties of macrocycle-template synthesized NHC-based SOC “pillarplex”. In addition, the cyclic trinuclear complex – $\text{Au}_3(\text{imidazolate})_3$ was investigated for its attractive photophysical behavior.

In the investigation to expand the pillarplex SOC family, three macrocyclic ligands $\text{H}_6\text{L}^{\text{b}}(\text{OTf})_2$, $\text{H}_6\text{L}^{\text{t}}(\text{OTf})_4$, and $\text{H}_6\text{L}^{\text{DM}}(\text{OTf})_4$ were prepared to perform macrocycle-templating SOC formation. Based on the original ligand for macrocycle-templated SOC formation, new ligands were modified from three aspects, namely charge modification, backbone modification, and steric/electronic modification. Out of the three ligand systems, steric/electronic modified $\text{H}_6\text{L}^{\text{t}}(\text{OTf})_4$, featuring triazolate moieties in the macrocyclic NHC ligands, was found to afford one new subclass of pillarplex SOC. The solid-state structure of the gold(I) hexafluorophosphate complex $[\text{Au}_8\text{L}^{\text{t}}_2](\text{PF}_6)_4$ revealed unprecedented structural flexibility of the new pillarplexes, possibly caused by the lower steric demand of the introduced nitrogen atom at the rim. This is supported by DFT calculations, showing a significantly higher energy penalty for an attempted similar deformation modeled for the previously reported pyrazolate-based $[\text{Au}_8\text{L}^{\text{Me}_2}_2](\text{PF}_6)_4$ pillarplexes. Additionally, the triazolate nitrogen atom at the rim has been shown to be a hydrogen bond acceptor, enabling a self-recognition between the cationic complexes. The backbone modified ligand $\text{H}_6\text{L}^{\text{DM}}(\text{OTf})_4$, featuring dimethylimidazolium moieties in the macrocyclic NHC ligands, was found to form a $[\text{Ag}_{11}\text{L}_3]\text{X}_5$ ($\text{X} = \text{OTf}$ and PF_6) complex instead of envisioned SOC assembly. Despite the different methods used, charged modified borate-bridged NHC proligand $\text{H}_6\text{L}^{\text{b}}(\text{OTf})_2$ had difficulty forming complexes.

From a generalized perspective, the new pillarplex SOC prove that the

macrocyclic templation strategy is a valid tool to generally tune structural properties of pillarplexes such as flexibility, also to introduce additional functionality to the rim regions. However, the ligand system's criteria required for a successful SOC formation is still ambiguous, which request further investigation.

Pyrazolate based pillarplexes $[M_8L^{Me_2}](X)_4$ ($M = Ag, Au; X = OAc, PF_6$) were studied for their stability and bioactivities. $[Ag_8L^{Me_2}](PF_6)_4$ and $[Ag_8L^{Me_2}](OAc)_4$ behaved like silver nitrate in that they showed antimicrobial and antifungal activity as well as moderate toxicity towards human HepG2 cells, but $[Ag_8L^{Me_2}](OAc)_4$ exhibit low stability in acidic condition or in the presence of chloride. The corresponding gold complexes $[Au_8L^{Me_2}](PF_6)_4$ and $[Au_8L^{Me_2}](OAc)_4$ were inactive against most bacterial strains and fungi, as well as had lower HepG2 toxicity. Water-soluble $[Au_8L^{Me_2}](OAc)_4$ is more resistant to acidic conditions and less affected by chloride addition when compared to the silver congener. The observed differences in bioactivities are concluded to the increased stability of the gold pillarplexes compared to the silver pillarplexes. $Au_3(1\text{-Methylimidazolate})_3$ – the simplest congener of imidazolate-based Au(I) cyclic trinuclear complexes (CTCs) – was investigated for its potential in supermolecular assembly and photophysical properties. A new solvatomorph β was identified and structurally characterized. The new structure featuring a dimeric Au_3 core through strong Au-Au intermolecular interactions, which can be serendipitously obtained from an unconventional cryogenic crystallization condition. The intermolecular metallophilic interactions were then assessed with DFT method, showing stronger interactions between monomer complexes in the dimer than rather small metallophilic interaction within the Au_3^{3+} core. Solvent-free crystal structure α was investigated, a thermochromism behavior was observed, with surprisingly high quantum yield under cryogenic temperature. Studies aiming to further manipulate the intermolecular interactions and utilize the interactions for supramolecular application are

expected in the future.

6 Experimental Method

6.1 General Remarks

Chemicals were purchased from commercial suppliers and used without further purification if not stated otherwise. NMR spectra in solution were recorded on a Bruker Avance DPX 400 and a Bruker DRX 400 spectrometer at room temperature if not stated otherwise. Chemical shifts are given in parts per million (ppm) and scalar coupling constants nJ are given in Hertz (Hz). The spectra were referenced to the residual solvent shift of the deuterated solvent as an internal standard (D_2O : 1H NMR δ 4.79; $MeCN-d_3$: 1H NMR δ 1.94, ${}^{13}C$ NMR δ 118.26; $DMSO-d_6$: 1H NMR δ 2.50, ${}^{13}C$ NMR δ 39.52). ${}^{13}C$ NMR spectra in D_2O were referenced by addition of methanol as a standard. ESI-MS analyses were performed on a Thermo Scientific LCQ/Fleet spectrometer by Thermo Fisher Scientific. Elemental analyses were measured by the microanalytical laboratory at the Technical University of Munich using a HEKAtech Euro EA – CHNS combustion analyzer. Line fitting and determination of the dissociation constant K_d (reciprocal of K_a) of the NMR titration data was performed using DynaFit (nonlinear least-squares regression analysis) with the host concentration, the guest concentration, and K_d as the variable parameters. Emission spectra were measured on a Hamamatsu Absolute PL Quantum Yield C11347 spectrometer. UV-Vis spectra were recorded on an Agilent Cary 60 UV-Vis.

6.2 Single-Crystal X-Ray Diffraction

Data were collected on a Bruker D8 Venture single crystal X-ray diffractometer equipped with a CMOS detector (Bruker Photon-100), a TXS rotating anode with MoK_{α} radiation ($\lambda = 0.71073 \text{ \AA}$) and a Helios optic using the APEX3

software package.¹ Measurements were performed on single crystals coated with perfluorinated ether. The crystals were fixed on top of a Kapton micro sampler and frozen under a stream of cold nitrogen. A matrix scan was used to determine the initial lattice parameters. Reflections were corrected for Lorentz and polarization effects, scan speed, and background using SAINT.² Absorption corrections, including odd and even ordered spherical harmonics were performed using SADABS.² Space group assignments were based upon systematic absences, E statistics, and successful refinement of the structures. The structures were solved using SHELXT with the aid of successive difference Fourier maps, and were refined against all data using SHELXL in conjunction with SHELXLE.³⁻⁵ Hydrogen atoms were calculated in ideal positions as follows: Methyl H atoms were refined as part of rigid rotating groups, with a C–H distance of 0.98 Å and $U_{\text{iso}}(\text{H}) = 1.5 \cdot U_{\text{eq}}(\text{C})$. Non-methyl H atoms were placed in calculated positions and refined using a riding model, with methylene, aromatic, and other C–H distances of 0.99 Å, 0.95 Å and 1.00 Å, respectively, and $U_{\text{iso}}(\text{H}) = 1.2 \cdot U_{\text{eq}}(\text{C})$. Non-hydrogen atoms were refined with anisotropic displacement parameters. Full-matrix least-squares refinements were carried out by minimizing $\sum w(F_o^2 - F_c^2)^2$ with the SHELXL weighting scheme.³ Neutral atom scattering factors for all atoms and anomalous dispersion corrections for the non-hydrogen atoms were taken from *International Tables for Crystallography*.⁶ The unit cell of **[Ag₈L^t₂](OTf)₄** contains 4 molecules of diethyl ether and 8 molecules of acetonitrile and the unit cell of **[Au₈L^t₂](PF₆)₄** contains 8 molecules of diethyl ether which were all treated as a diffuse contribution to the overall scattering without specific atom positions using the PLATON/SQUEEZE procedure.⁷ Images of the crystal structures were generated with Mercury and PLATON.^{8,9} Structure files of **[Ag₈L^t₂](OTf)₄** **[Au₈L^t₂](PF₆)₄** can be downloaded with reference number CCDC 2077680 and 2077681. Relevant files and crystallographic data of other structures mentioned in this thesis could be requested from SC-XRD laboratory of Catalysis

Research Center in Technical University of Munich.

6.3 Experimental Details of Section 4.1

UV-Vis Experiment Details

Stability tests of pillarplexes against chloride

The titrations of the silver pillarplex **4** and gold pillarplex **6** against chloride ions were carried out by stepwise addition of an increasing volume of a 3.072M sodium chloride solution to 2 mL of a $1.38 \cdot 10^{-5}$ M aqueous pillarplex solution followed by thorough mixing in a quartz cuvette. The UV-Vis absorption spectra were recorded immediately after the addition. The measured absorbance was corrected for the increase of the sample volume.

Stability tests of pillarplexes against pH

The stability of silver pillarplex **4** and gold pillarplexes **6** in different concentrations of trifluoromethanesulfonic acid (HOTf) was monitored by UV-Vis spectroscopy. 1 mL of a $2.76 \cdot 10^{-5}$ M aqueous pillarplex solution were injected into an equal volume of HOTf solution with pH values 2, 4, 5 and 6 in the quartz cuvette. The absorption spectra were recorded after 1 min, 1 hour, 7 hours, 24 hours, 48 hours and 72 hours.

6.4 Experimental Details of Section 4.2

Synthetic Procedures of Section 4.2

Calix[4]dimethylimidazolium[2]pyrazolium tetrakis(trifluoromethanesulfonate), $H_6L^{DM}(OTf)_4$

The following synthesis procedures were adapted from the Master's Thesis of David. Mayer. 1 L Schlenk flask was charged with 3,5-Bis(4,5-dimethylimidazol-1-ylmethyl)-1-(tetrahydropyran-2-yl)-1H-pyrazole (500 mg, 1.38 mmol, 1.0 equiv.) in 400 mL dry acetonitrile. The clear solution was cooled to -40 °C and subsequently a solution of methylene-bis(trifluoromethanesulfonate) (430 mg,

1.38 mmol, 1.00 equiv.) in 20 mL acetonitrile was added over a period of 40 minutes under vigorous stirring. The resulting mixture was allowed to warm to room temperature overnight and the solvent concentrated to 20 mL. Subsequently, trifluoromethanesulfonic anhydride (0.950 mL, 6.00 equiv.) and water (0.950 mL) were added, and the reaction solution stirred for 2 h at room temperature. After addition of diethyl ether (200 mL) a white solid precipitated, which was filtered and washed with diethyl ether (2 x 10 mL) and acetone (2 x 10 mL). After drying *in vacuo*, the product was obtained as a white powder in a yield of 452 mg (55 %, 0.379 mmol). ^1H NMR (400 MHz, DMSO- d_6 , 298 K): δ (ppm) = 13.09 (s, 1H, H_{NH}), 12.95 (s, 1H, H_{NH}), 9.92 (m, 4H, H_{NCHN}), 6.59 (m, 6H, $H_{\text{NCH}_2}, H_{\text{CCHC}}$), 5.42 (m, 8H, $H_{\text{CCH}_2\text{N}}$), 2.30 (m, 24H, H_{CH_3}). $^{13}\text{C}\{^1\text{H}\}$ NMR (100.62 MHz, DMSO- d_6 , 298 K): δ (ppm) = 136.6, 128.1, 127.9, 122.7, 119.5, 116.2, 54.9, 8.73, 8.57.

Calix[4]imidazolium[2]triazolium[2]borate bis(trifluoromethanesulfonate), $\text{H}_6\text{L}^{\text{b}}(\text{OTf})_2$

In a 100 mL Schlenk tube, 3,5-bis(imidazol-1-ylmethyl)-1-(tetrahydropyran-2-yl)-1H-pyrazole (200 mg, 640.1 μmol , 1.0 eq) was dissolved in acetonitrile (50mL). 1M solution of dibutylboron triflate in DCM (0.64 mL, 640.1 μmol , 1.0 eq) was added dropwise over a period of 20 mins and the clear solution was stirred for 0.5 h at room temperature. Then the solution was contracted to 20mL under reduced pressure. After addition of diethyl ether (200 mL) a yellow gel precipitated, which was washed with diethyl ether (2 x 10 mL). 30 mL EtOH was added to dissolve the residual gel. 2 mL HOTf was added dropwise under vigorous stirring at 0 °C. The resulting mixture was allowed to warm to room temperature overnight. After addition of diethyl ether (100 mL) a dark yellow gel precipitated, which was recrystallized in acetone with 1% MeOH to afford product as a transparent crystal with 11% yield. ^1H NMR (400.13 MHz, MeCN- d_3 , 298 K): δ (ppm) = 11.60 (s, 2H, H_{CCH}), 8.22 (s, 4H, H_{NCHN}), 7.18 (s,

4H, H_{NCHC}), 7.07 (d, $^2J = 10.7$ Hz, 4H, H_{NCHC}), 6.37 (s, 2H, H_{CCH}), 5.24 (s, 8H, H_{CCH_2}), 1.20–1.40 (m, 8 H, H_{butyl}), 0.75–1.02 (m, 28H, H_{butyl}).

3,5-bis((1*H*-imidazol-1-yl)methyl)-1-(tetrahydro-2*H*-pyran-2-yl)-1*H*-1,2,4-triazole

A Schlenk flask was charged with 3,5-bis(chloromethyl)-1-(tetrahydropyran-2-yl)-1*H*-1,2,4-triazole (10.2 g, 40.7 mmol, 1.0 equiv.) and sodium imidazolidide (8.06 g, 89.6 mmol, 2.2 equiv.) under inert atmosphere and cooled to 0 °C. Dry MeCN (300 mL) was added under vigorous stirring. The resulting suspension was stirred for one hour at 0 °C and allowed to reach room temperature overnight. After filtration, all volatiles were removed under reduced pressure. The crude product was dissolved in DCM (100 mL) and washed with brine (2x100 mL). After separation of the organic phase, the aqueous phase was extracted with DCM (2x100 mL). The combined organic phases were dried over $MgSO_4$, filtrated and concentrated to dryness. After drying *in vacuo*, the product was obtained as a highly viscous brown oil in 80% yield (10.2 g, 32.56 mmol). 1H NMR (400.13 MHz, $CDCl_3$, 298 K): δ (ppm) = 7.51 (d, $^4J = 5.7$ Hz, 2H, H_{NCHN}), 6.94 (s, 1H, H_{NCHC}), 6.93 (s, 2H, H_{NCHC}), 6.91 (s, 1H, H_{NCHC}), 6.87 (s, 1H, H_{NCHC}), 5.24 (d, $^2J = 3.3$ Hz, 2H, H_{CH_2}), 5.19-5.21 (m, 1H, $H_{NCHO,thp}$), 4.99 (s, 2H, H_{CH_2}), 3.80 (dt, $^2J = 11.6$ Hz, $^3J = 4.1$ Hz, 1H, $H_{OCH_2,thp}$), 3.49-3.54 (m, 1H, $H_{CHCH_2,thp}$), 1.83-1.98 (m, 3H, $H_{CH_2,thp}$), 1.48-1.54 (m, 3H, $H_{CH_2,thp}$). $^{13}C\{^1H\}$ NMR (100.62 MHz, $CDCl_3$, 298 K): δ (ppm) = 157.8, 151.5, 137.2, 137.1, 129.6, 129.1, 119.2, 119.0, 85.1, 67.0, 43.8, 41.7, 29.1, 24.3, 21.1.

Calix[4]imidazolium[2]triazolium tetrakis(trifluoromethanesulfonate),

$H_6L^t(OTf)_4$

A Schlenk flask was charged with 3,5-bis((1*H*-imidazol-1-yl)methyl)-1-(tetrahydro-2*H*-pyran-2-yl)-1*H*-1,2,4-triazole (2.00 g, 63.8 mmol, 1.0 equiv.) and dry MeCN (500 mL) was added. The solution was cooled to –35 °C before

the addition of methylene bis(triflate) (1.99 g, 63.88 mmol, 1.0 equiv.). The resulting solution was allowed to reach room temperature overnight under vigorous stirring. After removal of the solvent under reduced pressure, 30 mL EtOH was added to dissolve the residual solid. 2 mL TfO₂ and 2 mL of water were added dropwise under vigorous stirring. The mixture was stirred at room temperature for 16 hours before 200 mL of Et₂O were added to precipitate a white solid which was washed twice with 10 mL of acetone. After drying *in vacuo*, **H₆L^t(OTf)₄** was obtained as an off-white solid in 50% yield (1.73 g, 16.00 mmol). ¹H NMR (400.13 MHz, DMSO-*d*₆, 298 K): δ (ppm) = 14.63 (s, 2H, *H_{NH}*), 9.51 (s, 4H, *H_{NCHN}*), 7.98 (s, 4H, *H_{NCHC}*), 7.87 (d, ²J = 10.7 Hz, 4H, *H_{NCHC}*), 6.64 (s, 4H, *H_{NCH₂}*), 5.74 (s, 4H, *H_{CCH₂}*), 5.62 (s, 4H, *H_{CCH₂}*). ¹³C{¹H} NMR (100.62 MHz, DMSO-*d*₆, 298 K): δ (ppm) = 138.2, 124.0, 122.4, 58.3, 46.0, 44.1. ESI-MS (*m/z*): 121.86 (H₆L^t)⁴⁺, 242.48 (H₄L^t)²⁺, 392.53 (L^tOTf₂)²⁺, 483.30 (H₃L^t)⁺, 633.11 (H₄L^tOTf)⁺, 783.05 (H₅L^tOTf₂)⁺, 933.18 (H₆L^tOTf₃)⁺. Elemental analysis (%) calcd. for H₆L^t(OTf)₄: C 28.84; H 2.42; N 18.11; S 11.84; found: C 28.70; H 2.53; N 17.11; S 11.57.

Bis(calix[4]imidazolylidene[2]triazolato)octakisilver(I) tetrakis(trifluoroethanesulfonate), [Ag₈L^t](OTf)₄

H₆L^t(OTf)₄ (500 mg, 0.452 mmol, 1.0 equiv.) and Ag₂O (524 mg, 2.260 mmol, 5 equiv.) were suspended in 50 mL acetonitrile and stirred under exclusion of light at room temperature for 16 h. The mixture was filtered through a pad of Celite® and to the resulting clear brown solution diethyl ether was added until a brown precipitate formed and a colourless supernatant was obtained. The suspension was filtered through a pad of Celite® and 200 mL diethyl ether were added to the stirred filtrate. The resulting white solid was isolated by filtration and washed with diethyl ether three times. After drying *in vacuo* at 150 °C for several days, **[Ag₈L^t](OTf)₄** was obtained as a white powder in a yield of 160 mg (0.0659 mmol, 28%). ¹H NMR (400.13 MHz, MeCN-*d*₃, 298 K): δ (ppm)

= 7.62 (d, $^3J = 1.9$ Hz, 8H, H_{NCHC}), 7.55 (d, $^3J = 1.9$ Hz, 8H, H_{NCHC}), 6.64 (d, $^2J = 14.5$ Hz, 4H, H_{CH2}), 6.10 (d, $^2J = 14.5$ Hz, 4H, H_{CH2}), 5.79 (d, $^2J = 14.7$ Hz, 8H, H_{CH2}), 5.26 (d, $^2J = 14.7$ Hz, 8H, H_{CH2}). 1H NMR (400.13 MHz, DMSO- d_6 , 298 K): δ (ppm) = 7.99 (d, $^3J = 1.9$ Hz, 8H, H_{NCHC}), 7.66 (d, $^3J = 1.9$ Hz, 8H, H_{NCHC}), 6.87 (d, $^2J = 14.5$ Hz, 4H, H_{CH2}), 6.19 (d, $^2J = 14.5$ Hz, 4H, H_{CH2}), 6.10 (d, $^2J = 14.7$ Hz, 8H, H_{CH2}), 5.27 (d, $^2J = 14.7$ Hz, 8H, H_{CH2}). $^{13}C\{^1H\}$ NMR (100.62 MHz, DMSO- d_6 , 298 K): δ (ppm) = 124.0, 122.4, 63.5, 46.3. ESI-MS (m/z): 456.38 [$Ag_8L^t_2$] $^{4+}$ (calcd. 455.41), 658.75 [$Ag_8L^t_2$](OTf) $^{3+}$ (calcd. 656.87), 1061.15 [$Ag_8L^t_2$](OTf) $^{2+}$ (calcd. 1059,78). Elemental analysis (%) calcd. for [$Ag_8L^t_2$](OTf) $_4$: C 18.58; H 1.43; N 10.74; S 7.46; found: C 18.32; H 1.78; N 10.68; S 7.08.

Bis(calix[4]imidazolylidene[2]triazolato)octakisilver(I) tetrakis(hexafluorophosphate), [$Ag_8L^t_2$](PF $_6$) $_4$

A solution of [$Ag_8L^t_2$](OTf) $_4$ (150 mg, 61.7 mmol, 1.0 equiv.) in 10 mL NH $_3$ (aq) (25%) was added to a stirring solution of NH $_4$ PF $_6$ (60 mg, 370 mmol, 6.0 equiv.) in 1 mL H $_2$ O. After stirring for one hour, the suspension was centrifuged and the precipitate was washed with cold H $_2$ O (2x10mL) and Et $_2$ O (10mL), then dried *in vacuo*. [$Ag_8L^t_2$](PF $_6$) $_4$ was obtained as an off-white solid in 40% yield (55 mg, 24.7 mmol). 1H NMR (400.13 MHz, MeCN- d_3 , 298 K): δ (ppm) = 7.61 (d, $^3J = 1.9$ Hz, 8H, H_{NCHC}), 7.53 (d, $^3J = 1.9$ Hz, 8H, H_{NCHC}), 6.64 (d, $^2J = 14.5$ Hz, 4H, H_{CH2}), 6.09 (d, $^2J = 14.5$ Hz, 4H, H_{CH2}), 5.79 (d, $^2J = 14.7$ Hz, 8H, H_{CH2}), 5.26 (d, $^2J = 14.7$ Hz, 8H, H_{CH2}). 1H NMR (400.13 MHz, DMSO- d_6 , 298 K): δ (ppm) = 8.00 (d, $^3J = 1.9$ Hz, 8H, H_{NCHC}), 7.66 (d, $^3J = 1.9$ Hz, 8H, H_{NCHC}), 6.87 (d, $^2J = 14.5$ Hz, 4H, H_{CH2}), 6.19 (d, $^2J = 14.5$ Hz, 4H, H_{CH2}), 6.10 (d, $^2J = 14.7$ Hz, 8H, H_{CH2}), 5.27 (d, $^2J = 14.7$ Hz, 8H, H_{CH2}). $^{13}C\{^1H\}$ NMR (100.62 MHz, DMSO- d_6 , 298 K): δ (ppm) = 160.0, 124.3, 122.6, 63.8, 46.8. ^{31}P NMR (161.97 MHz, DMSO- d_6 , 298 K): δ (ppm) = -144.2. ESI-MS (m/z): 457.97 [$Ag_8L^t_2$] $^{4+}$ (calcd. 455.41). Elemental analysis (%) calcd.

for $[\text{Ag}_8\text{L}^{\text{t}_2}](\text{PF}_6)_4$: C 21.97; H 1.76; N 16.30; S 0.00; found: C 20.39; H 1.99; N 14.83; S 1.08.

Bis(calix[4]imidazolylidene[2]triazolato)octakisgold(I) tetrakis(hexafluoro phosphate), $[\text{Au}_8\text{L}^{\text{t}_2}](\text{PF}_6)_4$

A solution of $[\text{Ag}_8\text{L}^{\text{t}_2}](\text{PF}_6)_4$ (40 mg, 17.9 mmol, 1.0 equiv.) in 4 mL MeCN was added to a stirring suspension of chloro(tetra-hydrothiophene)gold(I) (50 mg, 145 mmol, 8.1 equiv.) in 4 mL MeCN. After stirring at 60 °C for 16 hours, the solid by-product was filtered off by passing the suspension through a Celite® pad. The product was precipitated by addition excess Et_2O (20 mL), then dried *in vacuo*. $[\text{Au}_8\text{L}^{\text{t}_2}](\text{PF}_6)_4$ was obtained as an off-white solid in 48% yield (30 mg, 8.7 mmol). ^1H NMR (400.13 MHz, $\text{MeCN-}d_3$, 298 K): δ (ppm) = 7.7 (d, $^3\text{J} = 2.1$ Hz, 8H, H_{NCHC}), 7.56 (d, $^3\text{J} = 2.1$ Hz, 8H, H_{NCHC}), 6.92 (d, $^2\text{J} = 14.7$ Hz, 4H, H_{CH_2}), 6.00 (d, $^2\text{J} = 14.7$ Hz, 4H, H_{CH_2}), 5.87 (d, $^2\text{J} = 14.8$ Hz, 8H, H_{CH_2}), 5.30 (d, $^2\text{J} = 14.8$ Hz, 8H, H_{CH_2}). ^1H NMR (400.13 MHz, $\text{DMSO-}d_6$, 298 K): δ (ppm) = 8.07 (d, $^3\text{J} = 2.1$ Hz, 8H, H_{NCHC}), 7.78 (d, $^3\text{J} = 2.1$ Hz, 8H, H_{NCHC}), 6.99 (d, $^2\text{J} = 14.7$ Hz, 4H, H_{CH_2}), 6.18 (d, $^2\text{J} = 14.7$ Hz, 4H, H_{CH_2}), 5.96 (d, $^2\text{J} = 14.9$ Hz, 8H, H_{CH_2}), 5.47 (d, $^2\text{J} = 14.9$ Hz, 8H, H_{CH_2}). $^{13}\text{C}\{^1\text{H}\}$ NMR (100.62 MHz, $\text{DMSO-}d_6$, 298 K): δ (ppm) = 167.78, 158.85, 124.02, 123.37, 63.09, 45.52. ^{31}P NMR (161.97 MHz, $\text{DMSO-}d_6$, 298 K): δ (ppm) = -144.2. ESI-MS (m/z): 634.67 $[\text{Au}_8\text{L}^{\text{t}_2}]^{4+}$ (calcd. 633.53), 846.15 $[\text{Au}_8\text{L}^{\text{t}_2}]^{3+}$ (calcd. 844.71), 894.25 $[\text{Au}_8\text{L}^{\text{t}_2}](\text{PF}_6)^{3+}$ (calcd. 893.03). Elemental analysis (%) calcd. for $[\text{Au}_8\text{L}^{\text{t}_2}](\text{PF}_6)_4$: C 16.95; H 1.36; N 12.58; found: C 16.8; H 1.4; N 12.7.

6.5 Experimental Details of Section 4.3

Synthetic Procedures of Section 4.3

The 1-methylimidazole was freshly distilled and degassed before use. Hexane and THF were dried using an MBraun MBSPS 5 apparatus and stored over 4 Å molecular sieves. All other reagents were used as supplied. NMR spectra

were recorded on a Bruker AV400 spectrometer at room temperature. ^1H NMR spectra were referenced to the signals of CDCl_3 . 2 mg of 1-methylimidazole was dissolved in tetrahydrofuran, then cooled to -30°C . To the stirred solution of methylimidazole in tetrahydrofuran, one equivalent of n-butyllithium in hexane was added drop-wisely under argon. The pale-yellow mixture was kept stirring for 1.5 hours at -30°C , before the addition of equal equivalent amount of chloro(tetrahydrothiophene)gold(I) in 5 ml tetrahydrofuran. The reaction was kept at -30°C for another hour, then 0.5 mL of dry methanol was added to quench the reaction. Afterward, the mixture was evaporated to dryness at 0°C . The precise temperature control and anaerobic condition are obligatory for the deprotonation and metalation to happen. The remaining solid was dissolved in dichloromethane then filtered with Celite. Recrystallization in dichloromethane offered the analytical product. Elemental analysis: Calculated for $\text{C}_{12}\text{H}_{15}\text{Au}_3\text{N}_6$: C, 17.28; H, 1.81; Au, 70.83; N, 10.07. Found: C, 17.36; H, 1.87; N, 9.77. UV-Vis (solid state, nm): 222, 259, 276.

6.6 References of Chapter 6

1. Bruker, A., 3, v2016. 1-0. Bruker AXS Inc.: Madison, WI, USA, 2015.
2. Saint, V., 7.56 a and SADABS Version 2008/1. Bruker AXS Inc., Madison, Wisconsin, USA, 2008, 16, 435-436.
3. C. B. Hübschle, G. M. Sheldrick and B. Dittrich, *J. Appl. Crystallogr.*, 2011, **44**, 1281-1284.
4. G. Sheldrick Shelxl-2014/7: Program for the Solution of Crystal Structures, 2014.
5. G. Sheldrick *Shelxl-97 (Release 97-2) University of Göttingen, Germany*: 1998.
6. A. Wilson, ed. E. Prince, Kluwer, Dordrecht, The Netherlands, 1992, vol. C, ch. Mathematical, Physical and Chemical Tables, pp. 500-502, 219-222, 193-199.

7. A. L. Spek, *Acta Crystallogr. C Struct. Chem.*, 2015, **71**, 9-18.
8. A. L. Spek, *Acta Crystallogr. Sect. D. Biol. Crystallogr.*, 2009, **65**, 148-155.
9. C. B. I. Macrae and J. Chisholm, *A J. Appl. Cryst*, 2008, **41**, 466.

7 Appendix

7.1 NMR Spectroscopy

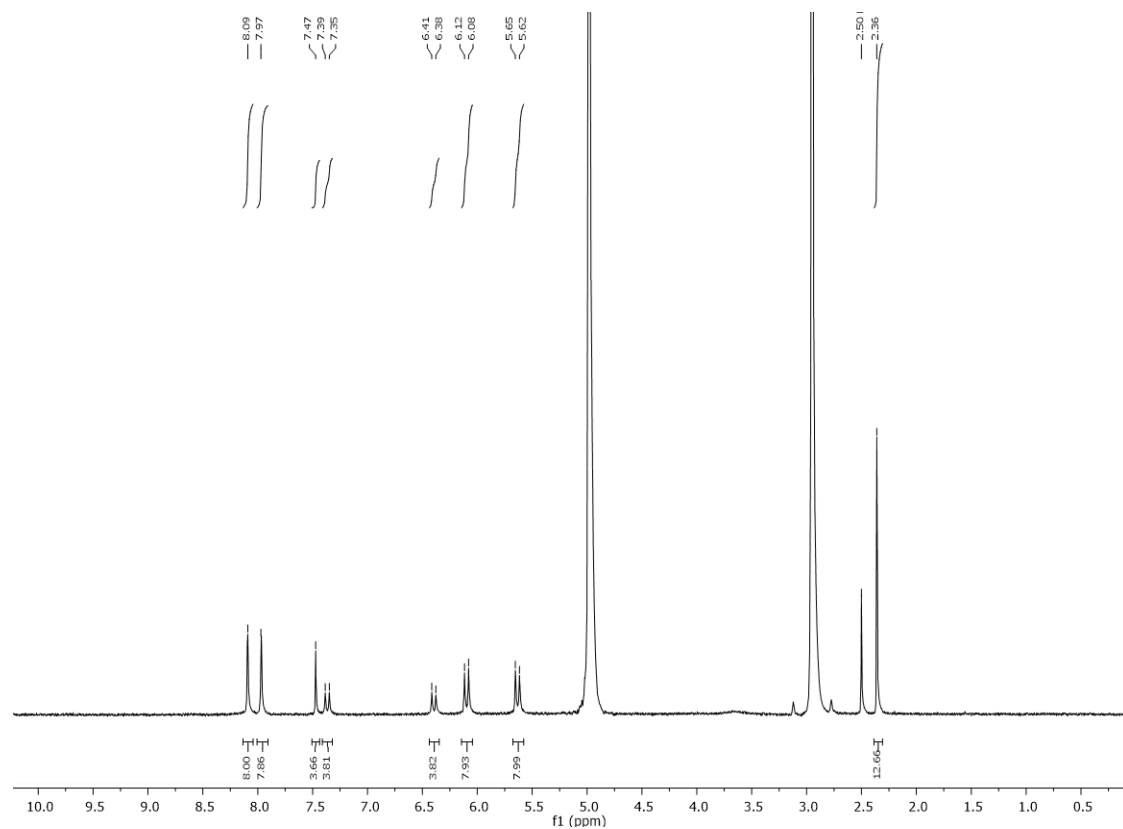
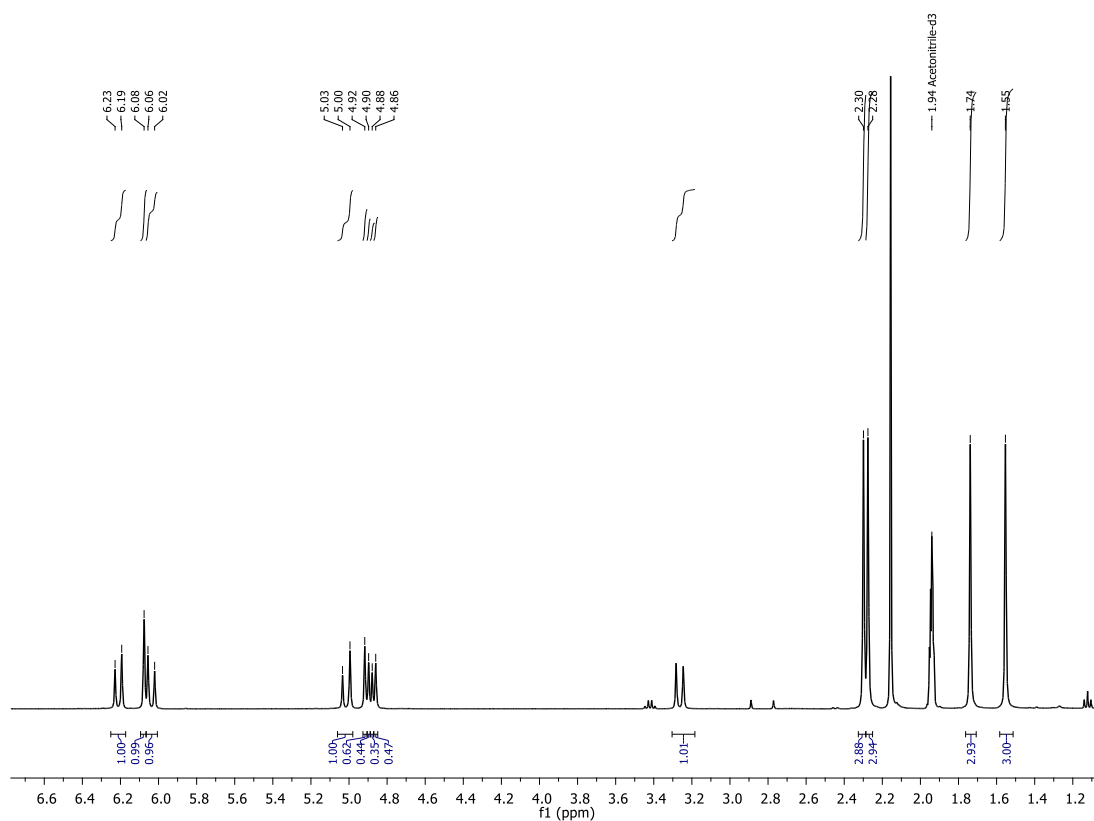
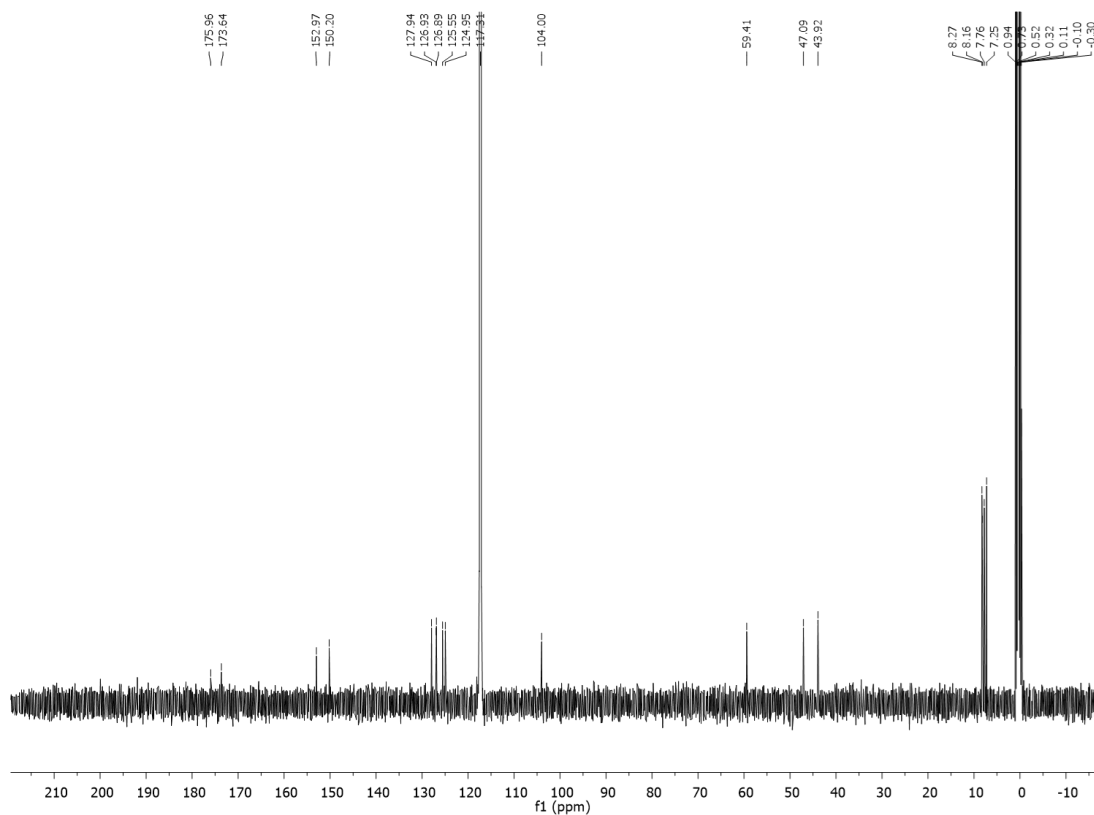


Figure S1. ^1H NMR spectrum (400 MHz, 298 K) of 1.7 mg $[\text{Au}_8\text{L}^{\text{Me}_2}](\text{OAc})_4$ in 0.3 ml D_2O into a 20 mM solution of HOTf in equal volume of D_2O . The proton concentration of resulting solution is 10 mM, corresponding to pH 2.

Figure S2. ^1H NMR spectra of $[\text{Ag}_{11}\text{L}^{\text{DM}}_3](\text{PF}_6)_{2.32}(\text{OTf})_{2.68}$ in MeCN-d_3 at 400.13 MHz.Figure S3. ^{13}C NMR spectrum of $[\text{Ag}_{11}\text{L}^{\text{DM}}_3](\text{PF}_6)_{2.32}(\text{OTf})_{2.68}$ in MeCN-d_3 at 100.62 MHz.

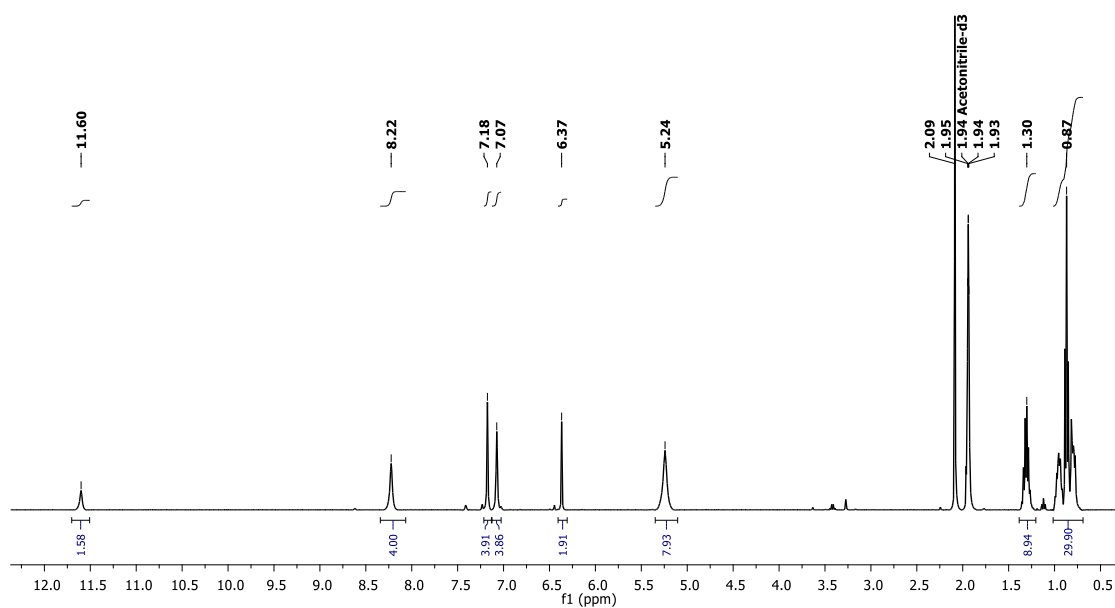


Figure S4. ^1H NMR spectra of $\text{H}_6\text{L}^{\text{b}}(\text{OTf})_2$ in $\text{MeCN-}d_3$ at 400.13 MHz.

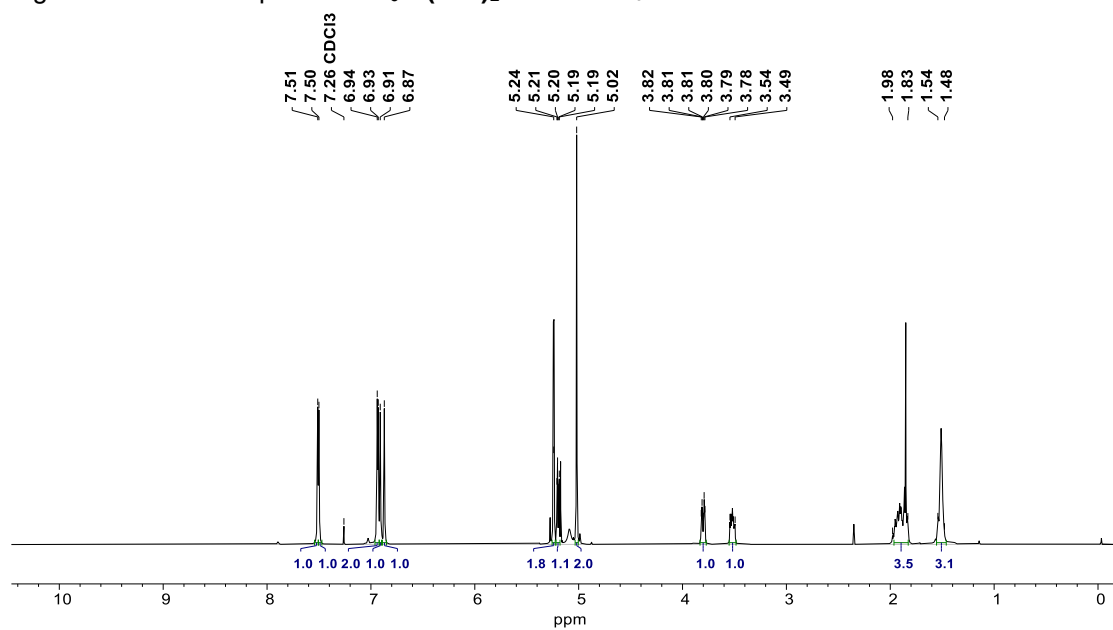


Figure S5. ^1H NMR spectrum of 3,5-bis((1*H*-imidazol-1-yl)methyl)-1-(tetrahydro-2*H*-pyran-2-yl)-1*H*-1,2,4-triazole in CDCl_3 at 400.13 MHz.

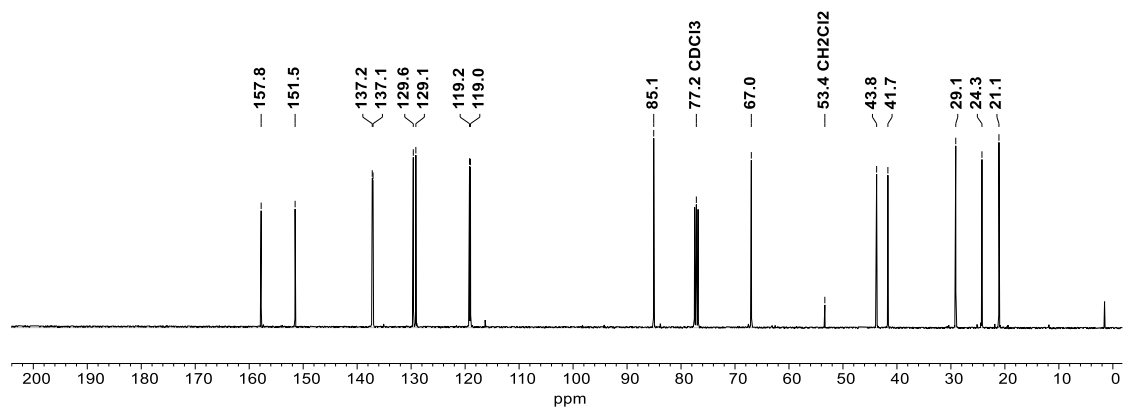
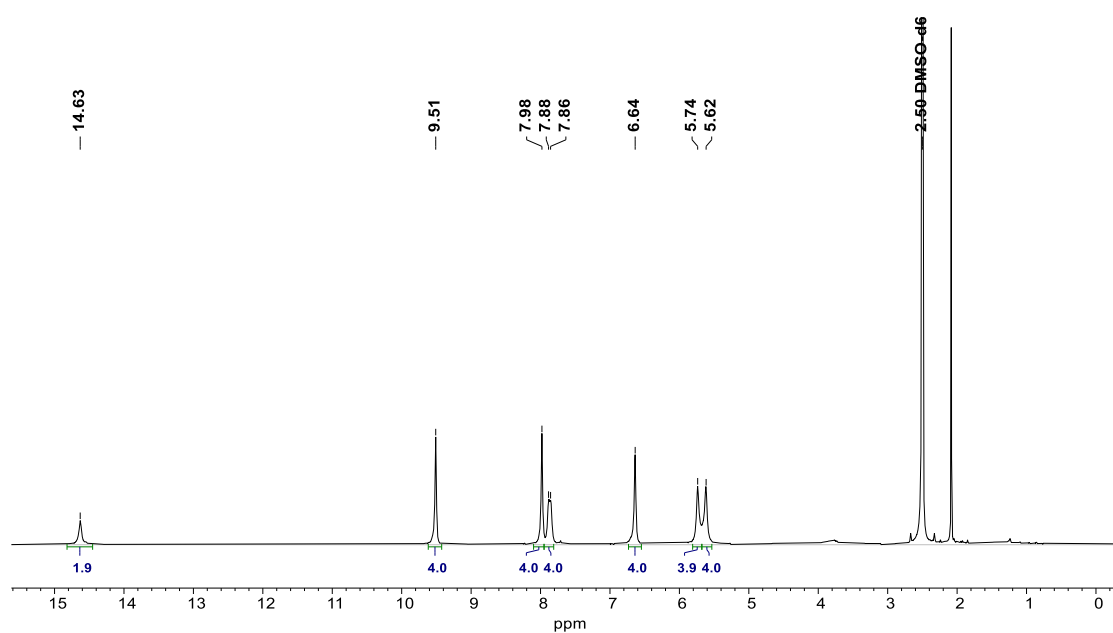
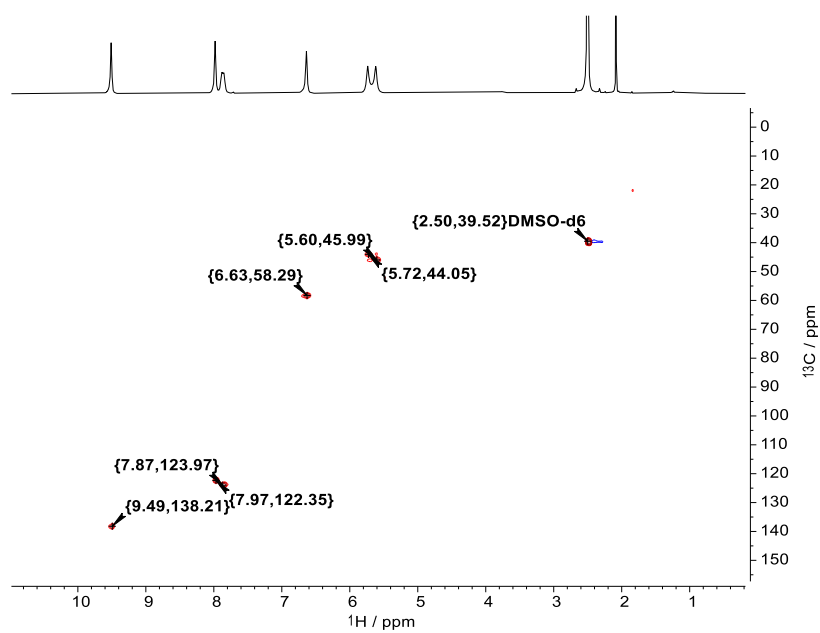


Figure S6. ^{13}C NMR spectrum of 3,5-bis((1*H*-imidazol-1-yl)methyl)-1-(tetrahydro-2*H*-pyran-2-yl)-1*H*-1,2,4-triazole in CDCl_3 at 100.62 MHz.

Figure S7. ^1H NMR spectrum of $\text{H}_6\text{L}^+(\text{OTf})_4$ in $\text{DMSO}-d_6$ at 400.13 MHz.Figure S8. ^1H , ^{13}C HSQC NMR spectrum of $\text{H}_6\text{L}^+(\text{OTf})_4$ in $\text{DMSO}-d_6$ at 400.13 MHz.

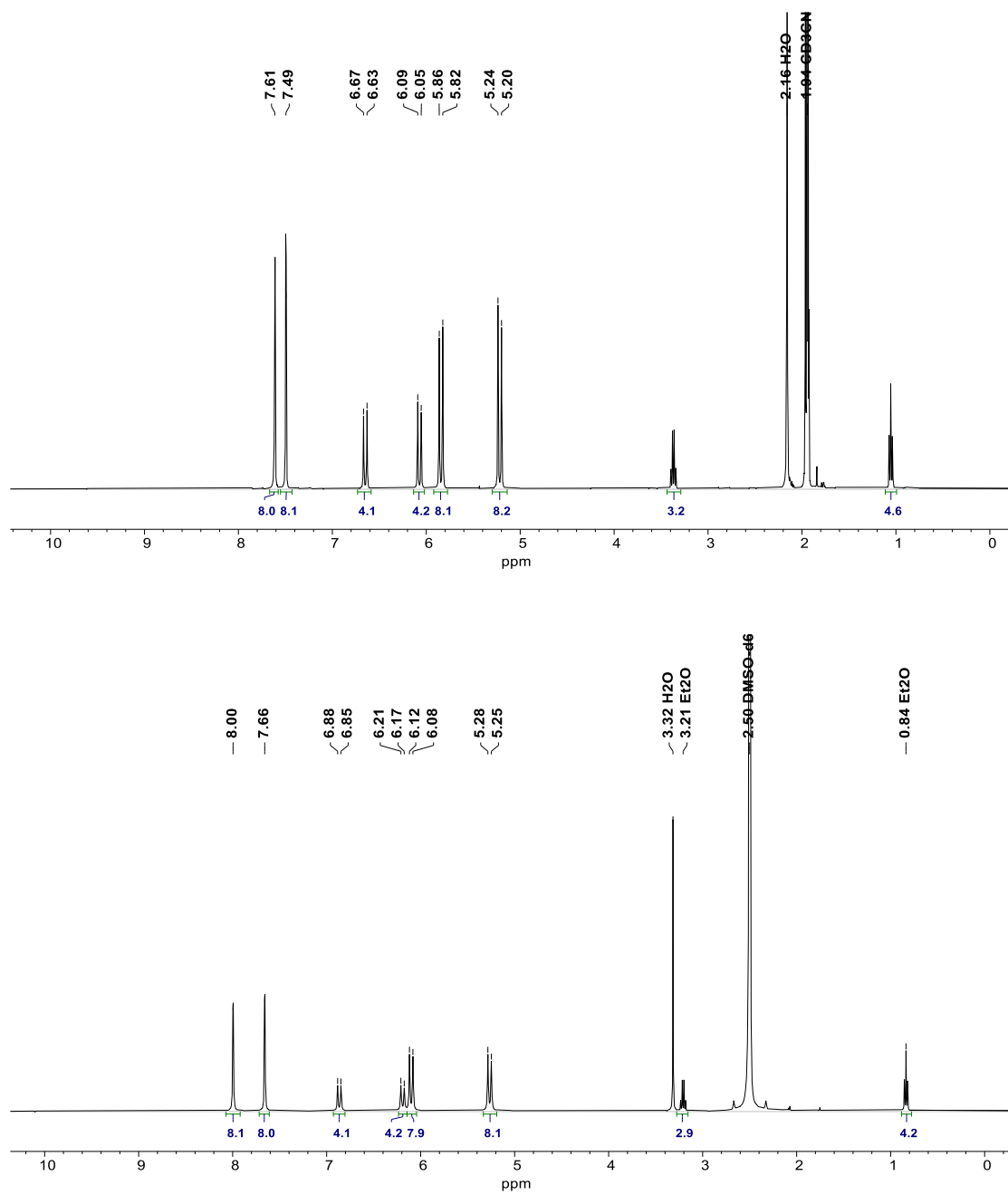


Figure S9. ^1H NMR spectra of $[\text{Ag}_8\text{L}_2](\text{OTf})_4$ in $\text{MeCN-}d_3$ (top) and $\text{DMSO-}d_6$ (bottom) at 400.13 MHz. One molecule of diethyl ether remains in the pore of the pillared complex.

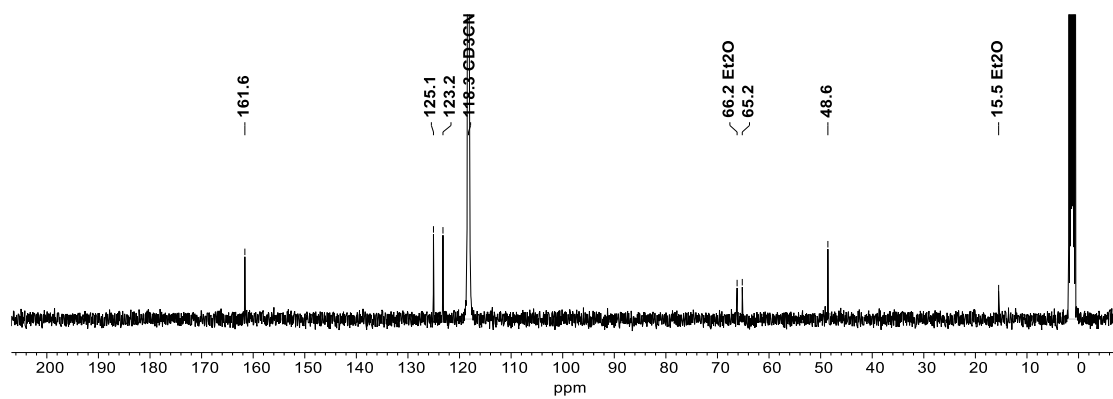


Figure S10. ^{13}C NMR spectrum of $[\text{Ag}_8\text{L}_2](\text{OTf})_4$ in $\text{MeCN-}d_3$ at 100.62 MHz.

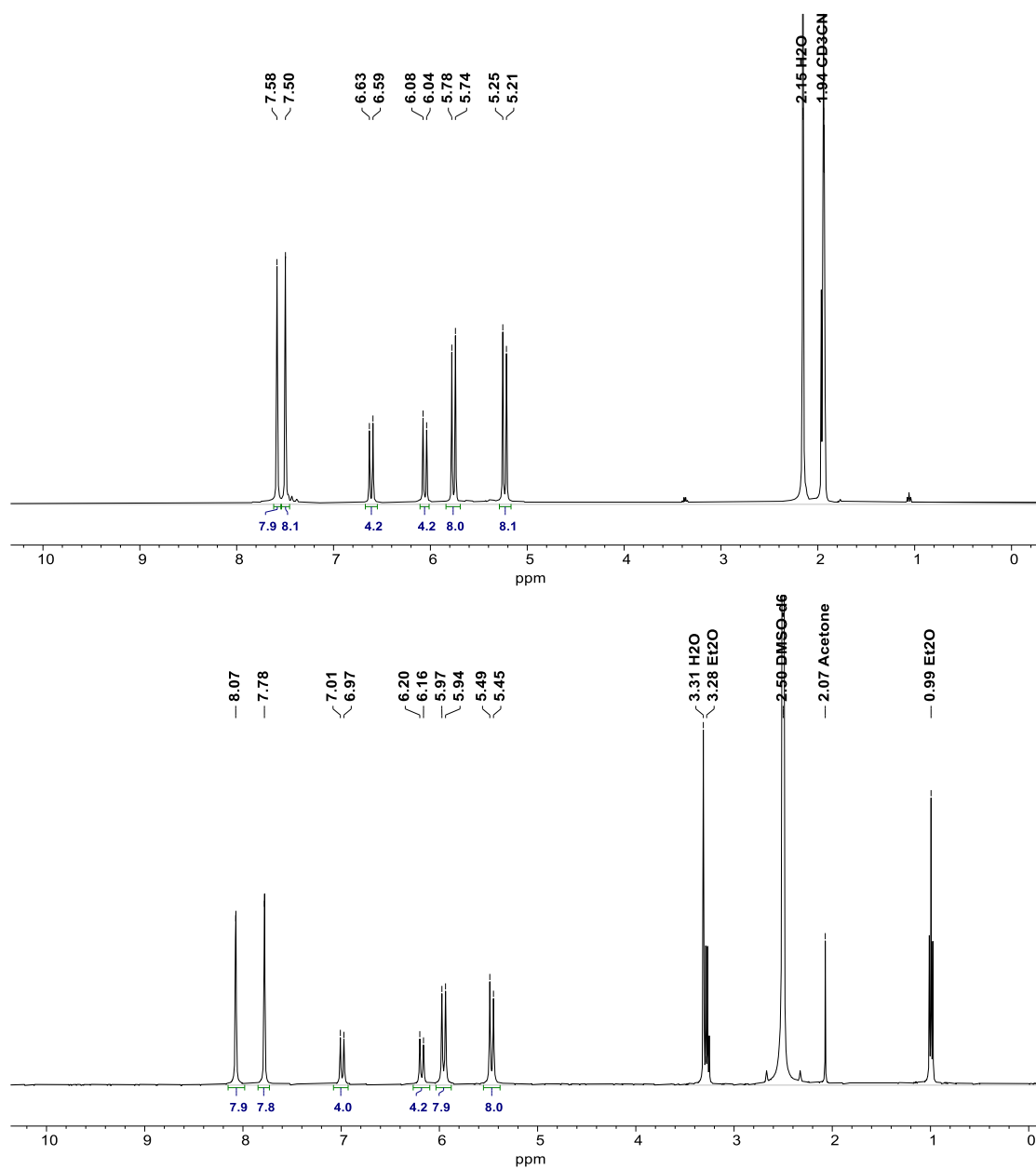


Figure S11. ^1H NMR spectra of $[\text{Ag}_8\text{L}_2](\text{PF}_6)_4$ in $\text{MeCN-}d_3$ (top) and $\text{DMSO-}d_6$ (bottom) at 400.13 MHz.

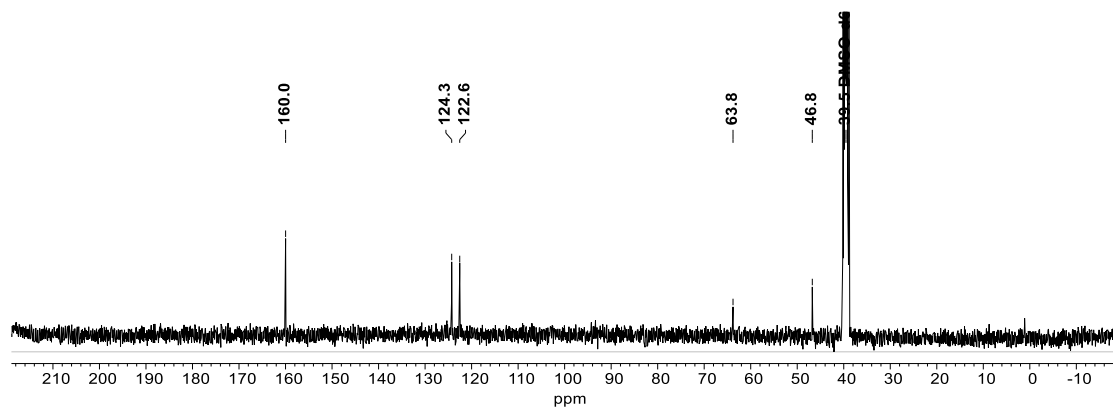


Figure S12. ^{13}C NMR spectrum of $[\text{Ag}_8\text{L}_2](\text{PF}_6)_4$ in $\text{DMSO-}d_6$ at 100.62 MHz.

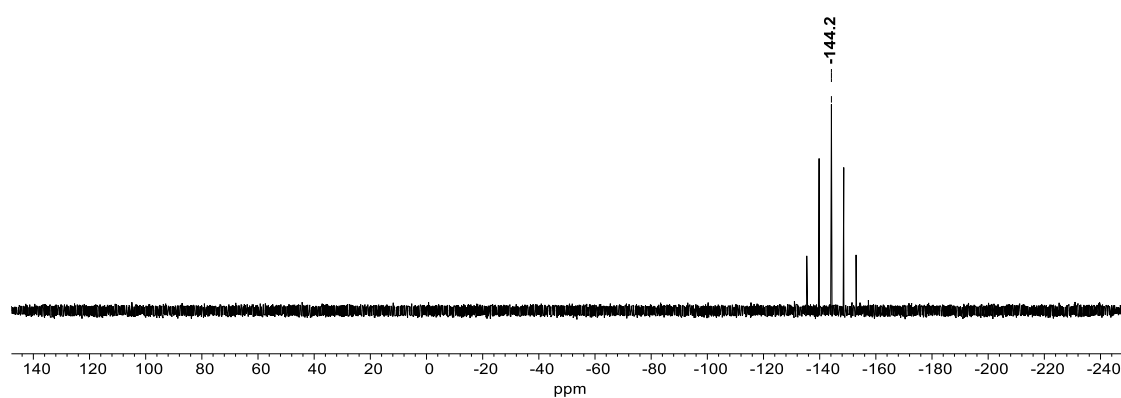


Figure S13. ^{31}P NMR spectrum of $[\text{Ag}_8\text{L}_2](\text{PF}_6)_4$ in $\text{DMSO-}d_6$ at 161.97 MHz.

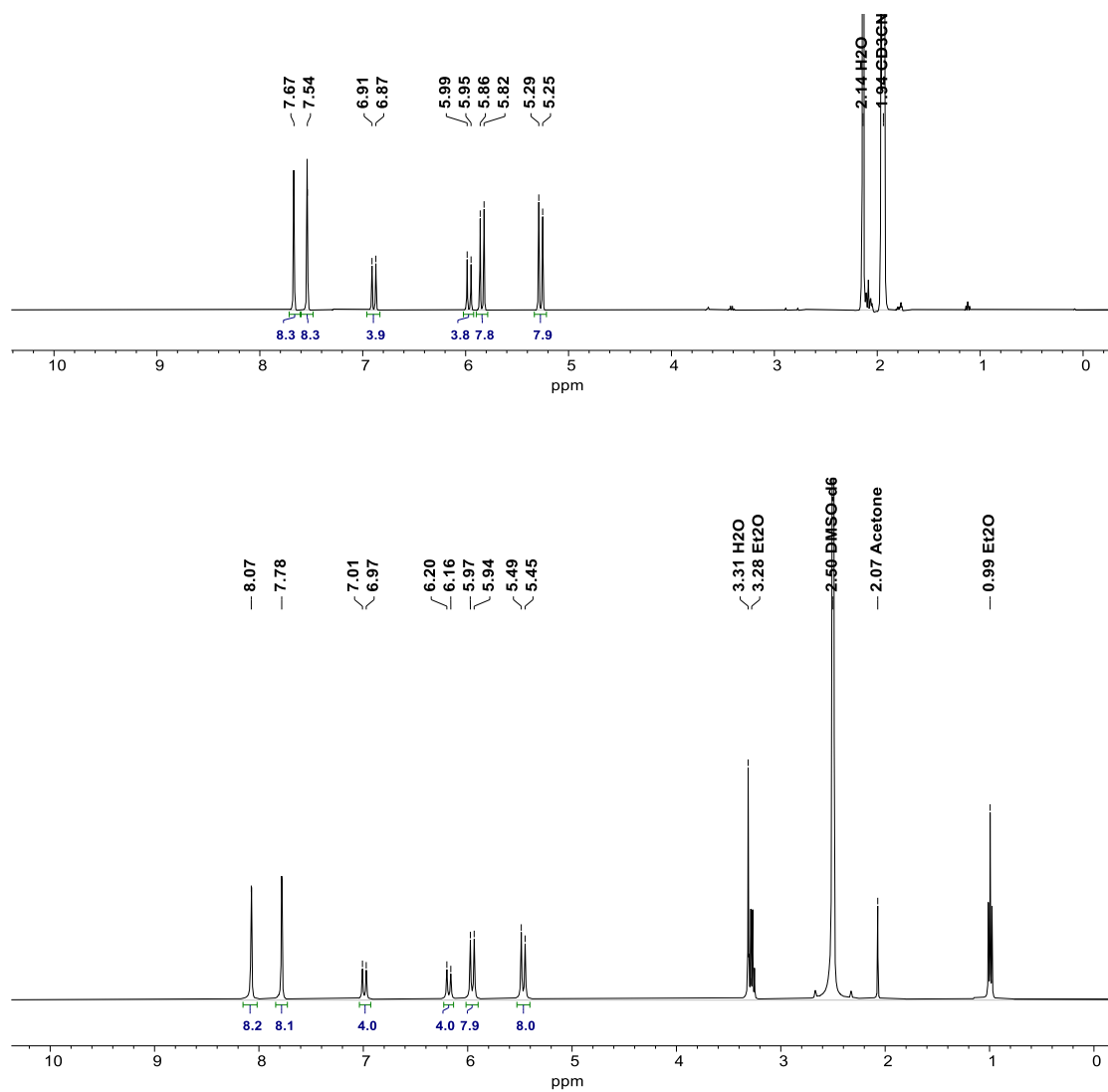


Figure S14. ^1H NMR spectra of $[\text{Au}_8\text{L}_2](\text{PF}_6)_4$ in MeCN- d_3 (top) and DMSO- d_6 (bottom) at 400.13 MHz.

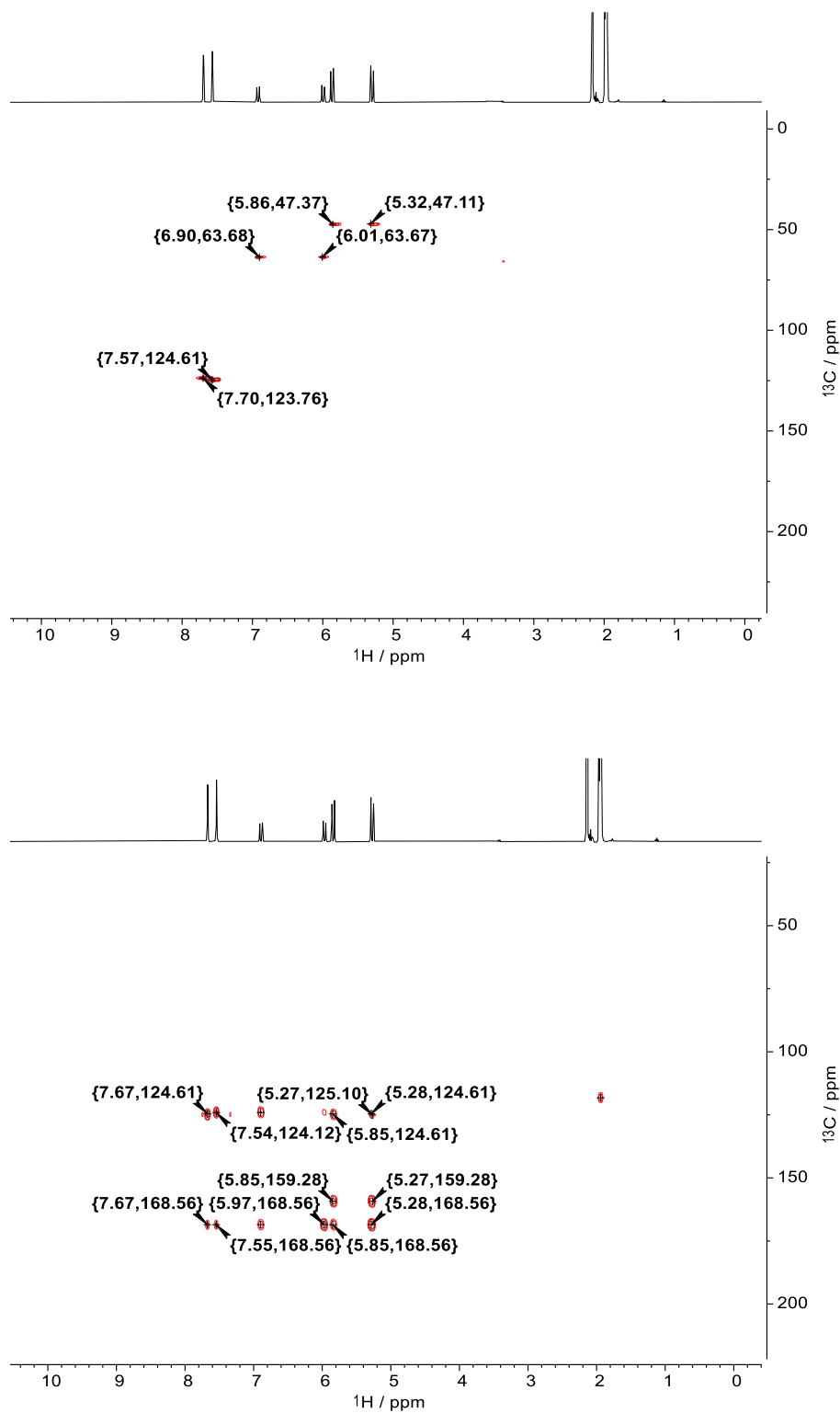


Figure S15. $^1\text{H},^{13}\text{C}$ HSQC (top) and HMBC spectra (bottom) of $[\text{Au}_8\text{L}_2](\text{PF}_6)_4$ in $\text{MeCN-}d_3$ at 400.13 MHz.

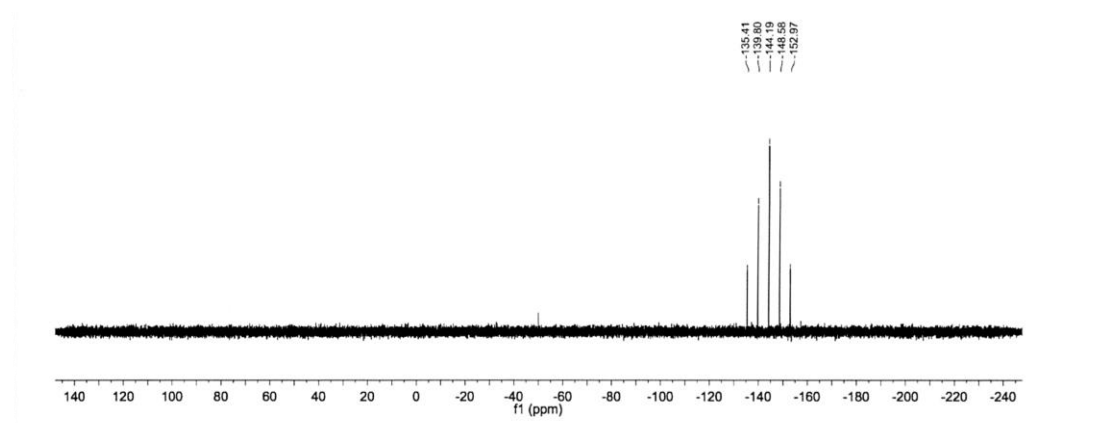


Figure S16. ^{31}P NMR spectrum of $[\text{Au}_8\text{L}'_2](\text{PF}_6)_4$ in $\text{DMSO-}d_6$ at 161.97 MHz.

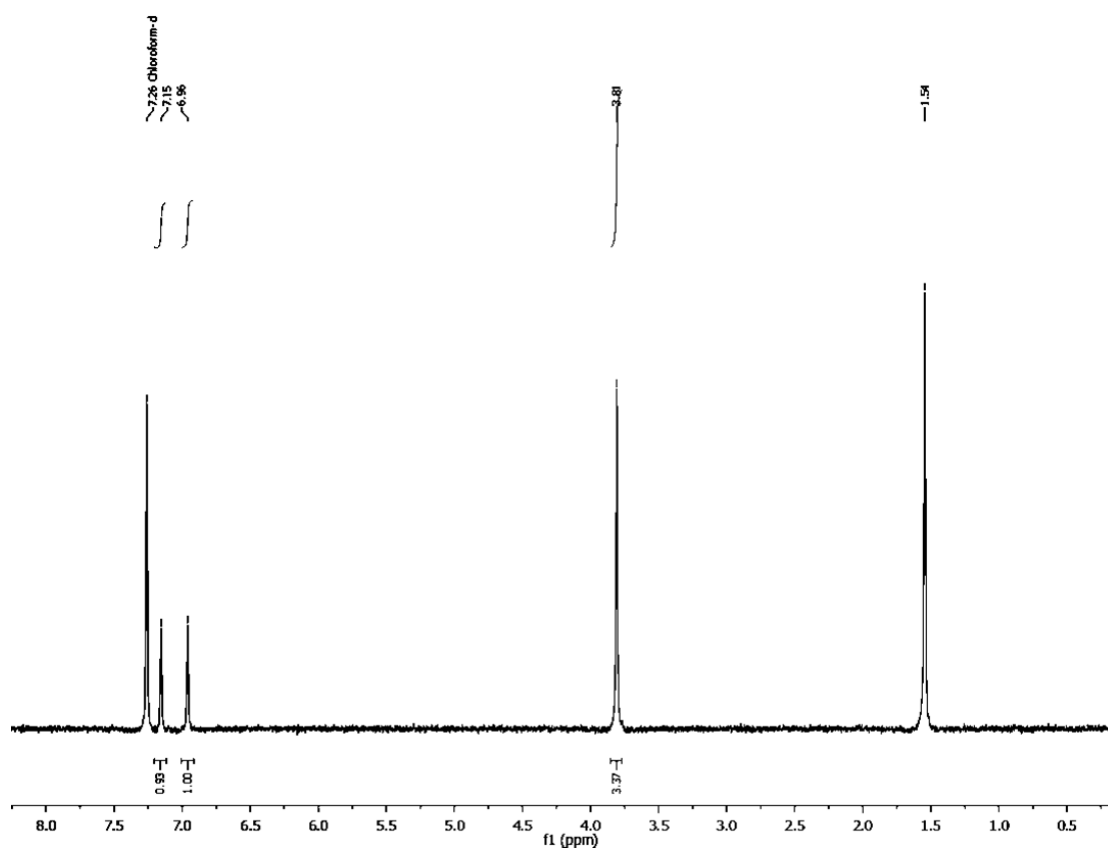


Figure S17. ^1H NMR spectra of $\text{Au}_3(\text{Melm})_3$ in polymorph β in CDCl_3-d_1 (top) at 400.13 MHz.

7.2 ESI-MS Spectra

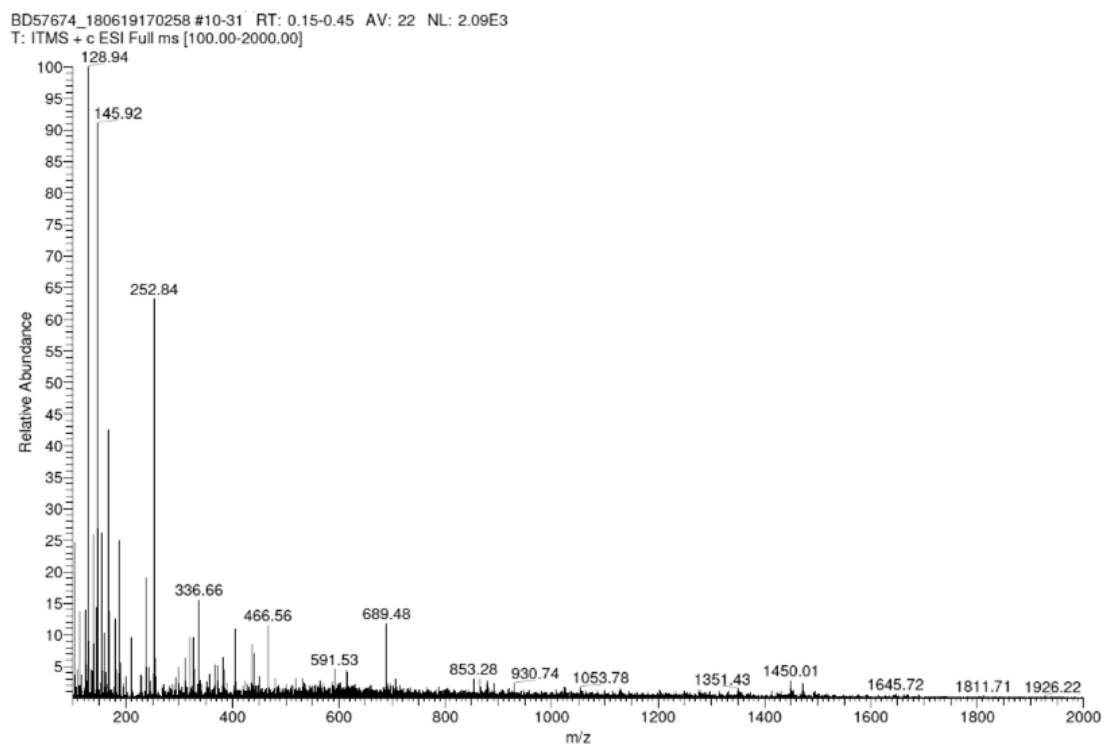


Figure S18. ESI-MS spectrum of deprotonation and metalation product of proligand $\text{H}_6\text{L}^{\text{DM}}(\text{OTf})_4$, with possible composition $[\text{Au}_8\text{L}^{\text{DM}}_2](\text{OTf})_4$ Signal assignment (m/z): 689.48 $[\text{Au}_8\text{L}^{\text{DM}}_2]^{4+}$ (calcd. 689.10).

PF49751 #6-23 RT: 0.09-0.33 AV: 18 NL: 2.48E3
T: ITMS + c ESI Full ms [100.00-2000.00]

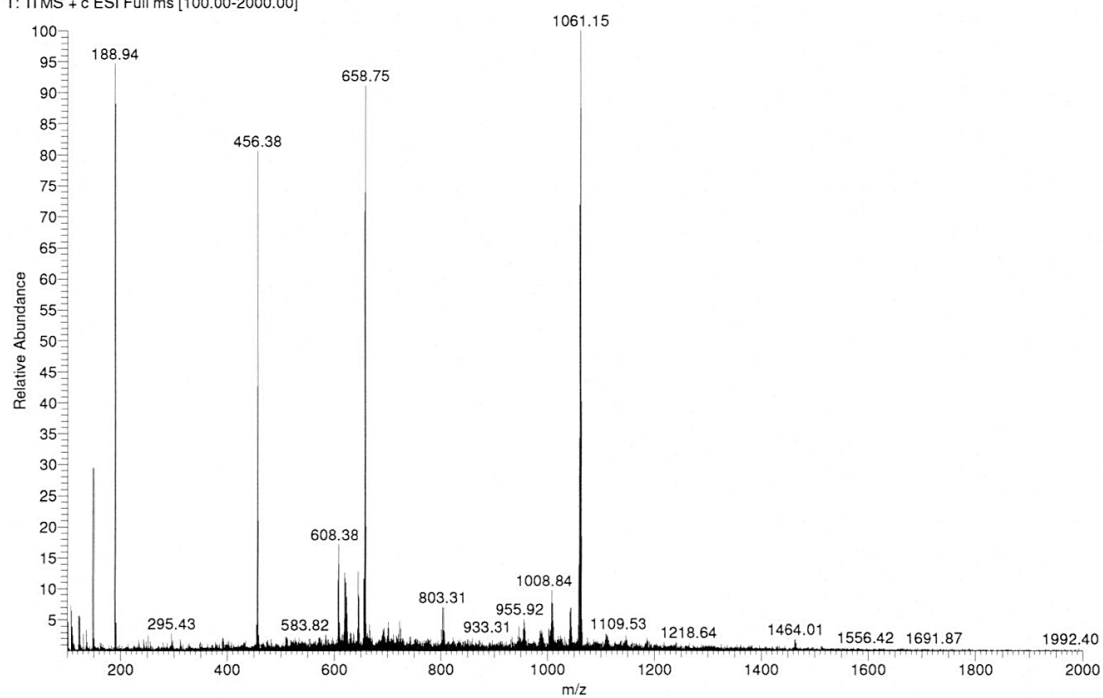


Figure S19. ESI-MS spectrum of compound $[\text{Ag}_8\text{L}_2](\text{OTf})_4$. Signal assignment (m/z): 456.38 $[\text{Ag}_8\text{L}_2]^{4+}$ (calcd. 455.41), 658.75 $[\text{Ag}_8\text{L}_2](\text{OTf})^{3+}$ (calcd. 656.87), 1061.15 $[\text{Ag}_8\text{L}_2](\text{OTf})_2^{2+}$ (calcd. 1059.78).

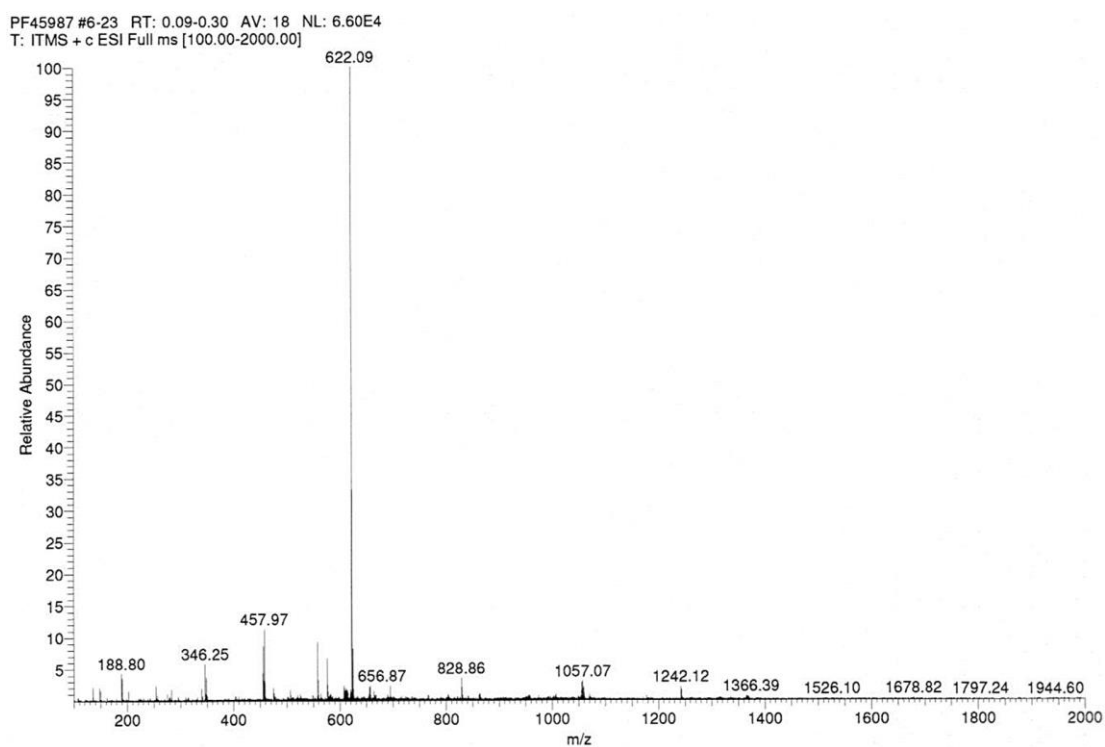


Figure S20. ESI-MS spectrum of compound $[\text{Ag}_8\text{L}_2](\text{PF}_6)_4$. Signal assignment (m/z): 457.97 $[\text{Ag}_8\text{L}_2]^{4+}$ (calcd. 455.41).

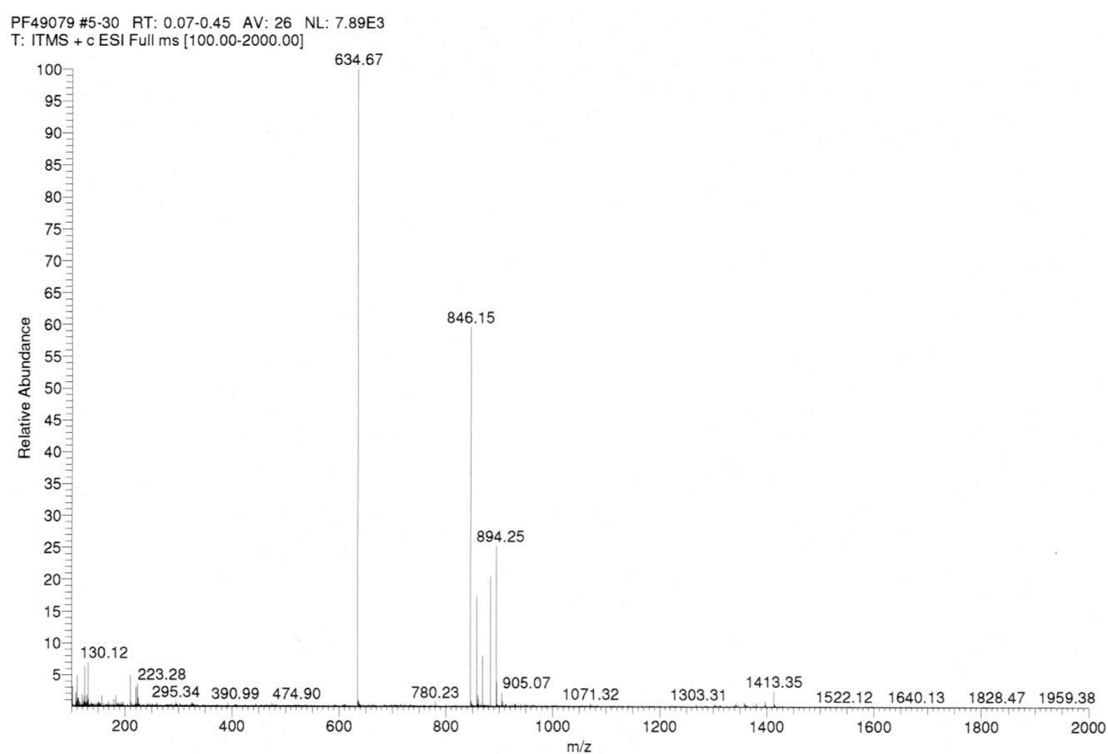


Figure S21. ESI-MS spectrum of compound $[\text{Au}_8\text{L}_2](\text{PF}_6)_4$. Signal assignment (m/z): 634.67 $[\text{Au}_8\text{L}_2]^{4+}$ (calcd. 633.53), 846.15 $[\text{Au}_8\text{L}_2]^{3+}$ (calcd. 844.71), 894.25 $[\text{Au}_8\text{L}_2](\text{PF}_6)^{3+}$ (calcd. 893.03).

7.3 Job-Plot Titrations

To determine the binding stoichiometry of 1,8-diaminooctane and $[\text{Au}_8\text{L}^{\text{t}_2}](\text{PF}_6)_4$, Job Plot titrations were performed in $\text{MeCN-}d_3$, followed by ^1H NMR spectroscopy.^{511,512} Stock solutions (2.4 mM) of the gold complex $[\text{Au}_8\text{L}^{\text{t}_2}](\text{PF}_6)_4$ (host) and 1,8-diaminooctane (guest) were prepared. For each experiment, eleven samples were prepared with a different host–guest ratio so that the overall concentration ($[\text{host}] + [\text{guest}]$) for each sample was 1.2 mM.

Table S1. Data for the Job plot titration of $[\text{Au}_8\text{L}^{\text{t}_2}](\text{PF}_6)_4$ and 1,8-diaminooctane in $\text{MeCN-}d_3$.

No.	V host (μL)	V guest (μL)	[host] (mM)	[guest] (mM)	[guest]/([host]+[guest])	δ (ppm)	$\Delta\delta$ (ppm)	$(\Delta\delta)[\text{guest}]/([\text{host}]+[\text{guest}])$
1	0	500	0	1.200	1	1.292	0	0
2	50	450	0.12	1.080	0.9	1.238	0.054	0.0486
3	100	400	0.24	0.960	0.8	1.179	0.113	0.0904
4	150	350	0.36	0.840	0.7	1.093	0.199	0.1393
5	200	300	0.48	0.720	0.6	0.975	0.317	0.1902
6	250	250	0.6	0.600	0.5	0.847	0.445	0.2225
7	300	200	0.72	0.480	0.4	0.782	0.51	0.204
8	350	150	0.84	0.360	0.3	0.858	0.434	0.1302
9	400	100	0.96	0.240	0.2	0.957	0.335	0.067
10	450	50	1.08	0.120	0.1	0.957	0.335	0.0335
11	500	0	1.2	0.000	0	0	1.292	0

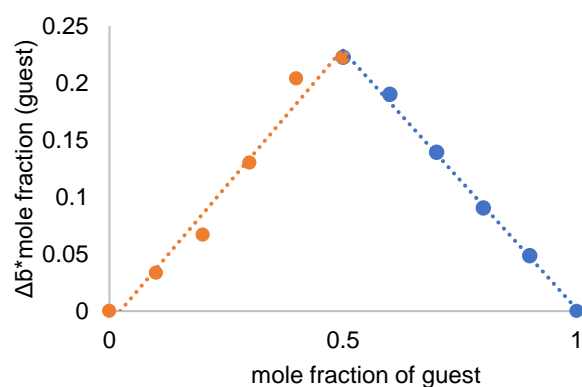


Figure S22. Job-plot of titration of $[\text{Au}_8\text{L}^{\text{t}_2}](\text{PF}_6)_4$ against 1,8-diaminooctane in $\text{MeCN-}d_3$. The maximum was found at a mole fraction of the guest of 0.5, indicating a 1:1 stoichiometry of the interaction.

7.4 Solid-State Emission Spectra

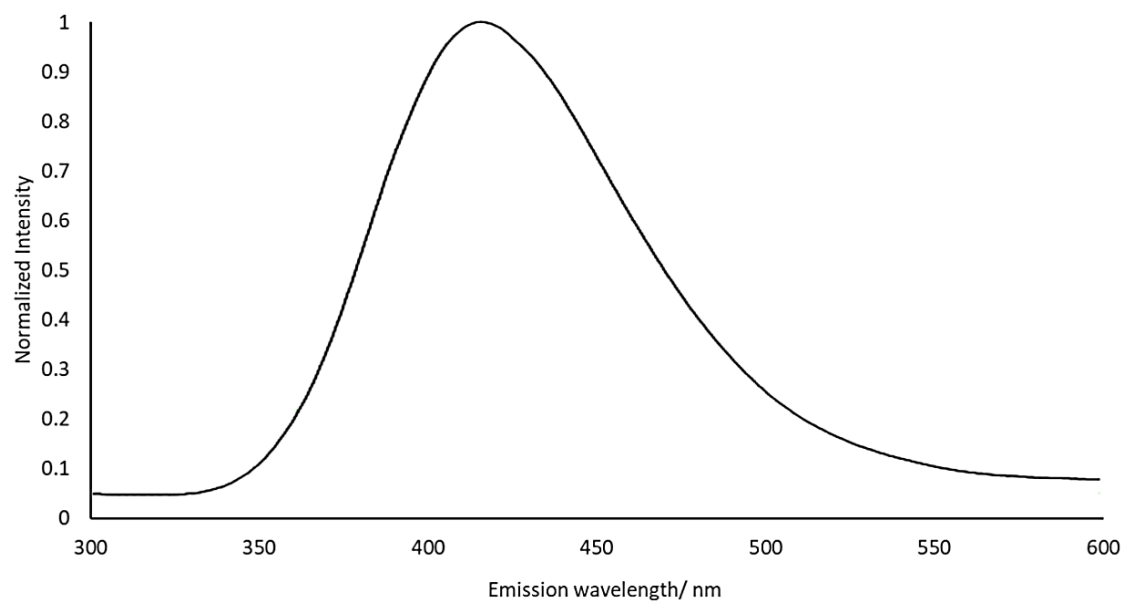


Figure S23. Emission spectrum of $[\text{Au}_8\text{L}_2](\text{PF}_6)_4$ (solid state, $\lambda_{\text{ex}} = 270$ nm), peak maximum found at 400 nm. I screened excitation wavelengths from 250 nm to 400 nm to find the highest emission intensity. Quantum yield 31%.

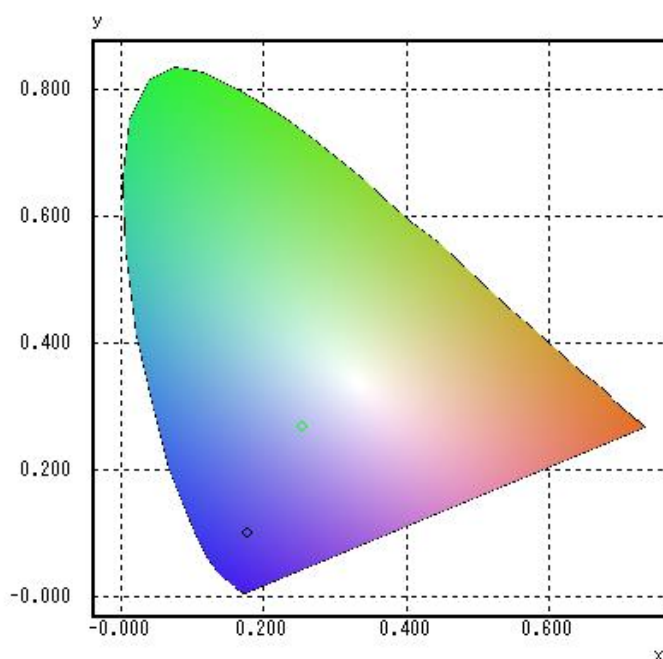


Figure S24. CIE color space chromaticity diagram with the emission of $[\text{Au}_8\text{L}_2](\text{PF}_6)_4$ circled in green, excitation circled in black. Excitation wavelength 270 nm, emission wavelength 400 nm.

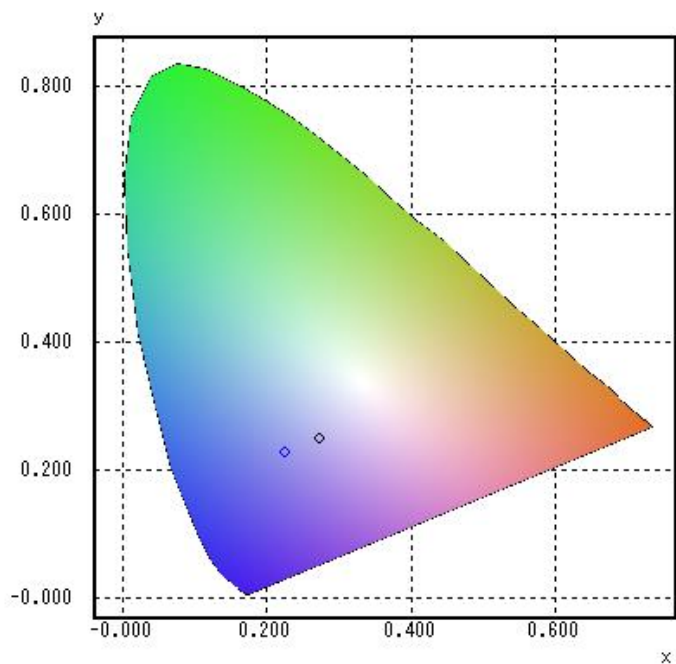


Figure S25. CIE colour space chromaticity diagram of $\text{Au}_3(\text{Melm})_3$ in polymorph **a** at room temperature with the emission circled in black, excitation circled in blue. Excitation wavelength 256 nm, emission wavelength 710 nm.

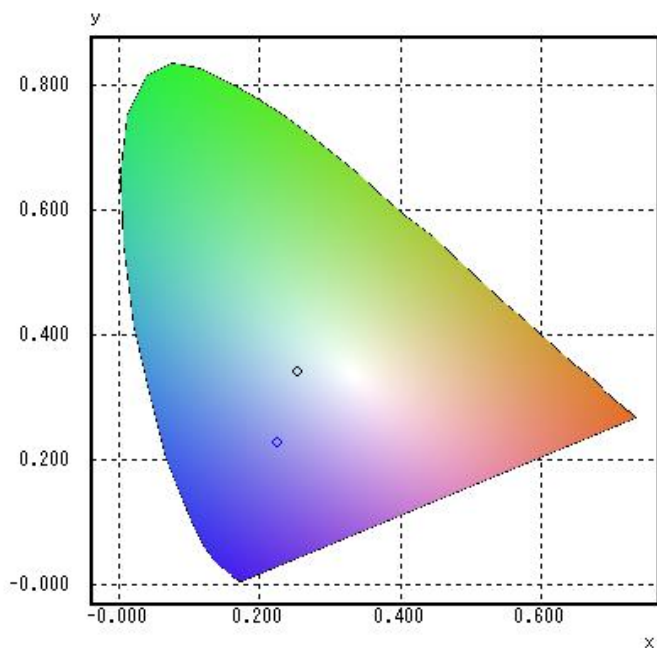


Figure S26. CIE colour space chromaticity diagram of $\text{Au}_3(\text{Melm})_3$ in polymorph **a** at cryogenic temperature with the emission circled in black, excitation circled in blue. Excitation wavelength 256 nm, emission wavelength 510 nm.

7.5 Crystallographic Data

Compound $\text{H}_6\text{L}^{\text{b}}\text{OTf}_2$

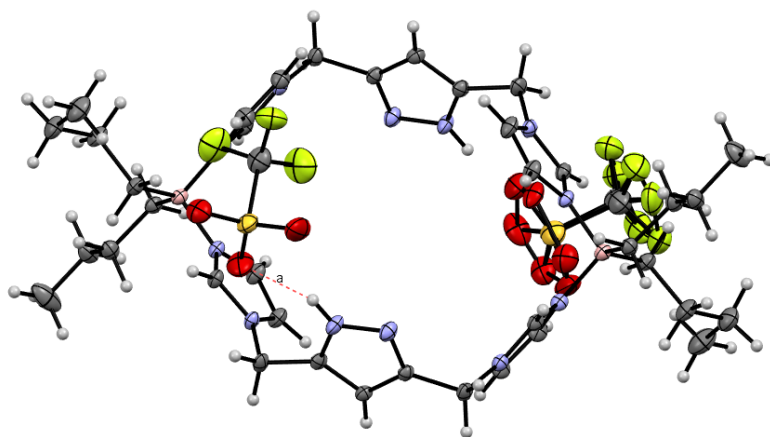


Figure S27. Crystal structure of $\text{H}_6\text{L}^{\text{b}}\text{OTf}_2$, ADPs are given at 50% probability level.

Identification code	GuaSh16
Diffractometer operator	C. Jandl
scan speed	1-10 s per frame
2740 frames measured	
phi-scans with $\Delta\phi = 0.5$	
omega-scans with $\Delta\omega = 0.5$	
Mode	shutterless mode
<i>Crystal data</i>	
$\text{C}_{40}\text{H}_{60}\text{B}_2\text{F}_6\text{N}_{12}\text{O}_6\text{S}_2$	Mo $K\alpha$ radiation, $\lambda = 0.71073 \text{ \AA}$
$M_r = 1004.74$	$D_x = 1.172 \text{ Mg m}^{-3}$
Triclinic, $P-1$	Melting point: ? K
$a = 10.360(2) \text{ \AA}$	
$b = 15.188(3) \text{ \AA}$	$\alpha = 88.924(6)^\circ$
$c = 19.135(4) \text{ \AA}$	$\beta = 76.802(6)^\circ$

$V = 2846.8(1) \text{ \AA}^3$	$T = 100 \text{ K}$
$Z = 2$	<u>Fragment, colourless</u>
$F(000) = 1056$	<u>0.104</u> × <u>0.121</u> × <u>0.277</u> mm
<i>Data collection</i>	
<u>Bruker D8 Venture</u> diffractometer	<u>10820</u> independent reflections
Radiation source: <u>TXS rotating anode</u>	
<u>Helios optic</u> monochromator	$R_{\text{int}} = 0.0396$
Detector resolution: <u>16</u> pixels mm^{-1}	$\theta_{\text{max}} = 25.68^\circ$, $\theta_{\text{min}} = 2.19^\circ$
<u>phi-</u> and <u>omega-</u> rotation scans	$h = -12 \ 12$
Absorption correction: <u>multi-scan</u> <u>SADABS 2016/2, Bruker</u>	$k = -18 \ 18$
$T_{\text{min}} = 0.654$, $T_{\text{max}} = 0.745$	$l = -23 \ 23$
<u>121067</u> measured reflections	
<i>Refinement</i>	
Refinement method	
Refinement program	SHELXL-2014/7(Sheldrick,2014)
	$\sum_w(F_o^2 - F_c^2)^2$
Data/restraints/parameters	
Goodness-of-fit on F^2	1.038
Final R indices	9301 data $i > 2\sigma(I)$; $R1 = 0.0506$, $wR2 = 0.1418$ all data $R1 = 0.0582$, $wR2 = 0.1488$
Weighting scheme	$W = 1/[\sum^2(FO^2) + 148.9416P]$ WHERE $P = (FO^2 + 2FC^2)/3$
Largest diff.peak and hold	1.036 and -6.50 e\AA^{-3}

R.M.S. deviation from mean	0.060 eÅ ⁻³
----------------------------	------------------------

Compound [Ag₁₁L^{DM}₃] (OTf)₄

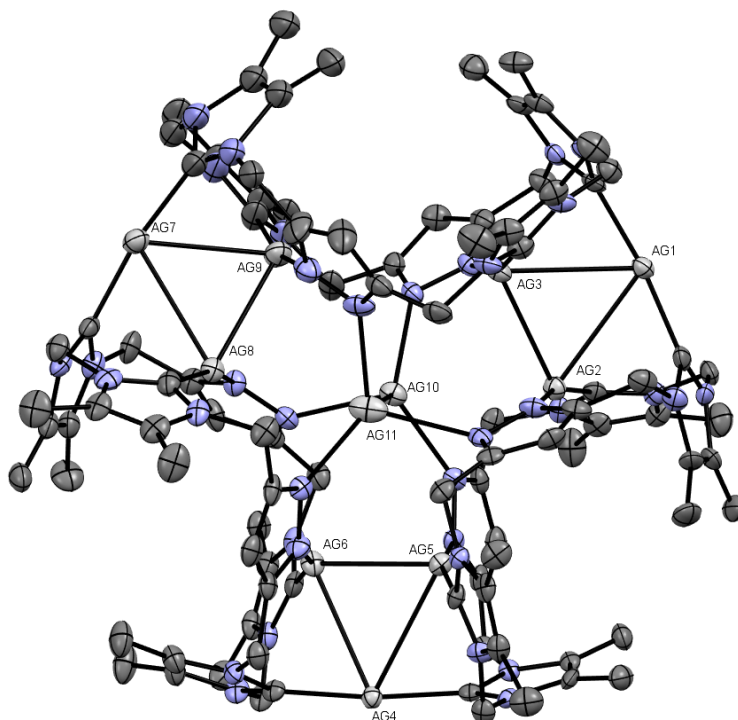


Figure S28. Crystal structure of [Ag₁₁L^{DM}₃] cation, ADPs are given at 50% probability level.

Identification code	GuaSh4
Diffractometer operator	C. Jandl
scan speed	1-10 s per frame
2705 frames measured	
phi-scans with delta_phi = 0.5	
omega-scans with delta_omega = 0.5	
Mode	shutterless mode
<i>Crystal data</i>	
<i>C</i> _{55.65} <i>H</i> _{68.45} <i>Ag</i> _{5.50} <i>F</i> _{10.99} <i>N</i> _{20.15} <i>O</i> _{4.52} <i>P</i> _{1.16} <i>S</i> _{1.34}	Mo K α radiation, $\lambda = 0.71073$ Å
<i>M</i> _r = 1972.82	<i>D</i> _x = 1.902 Mg m ⁻³
Triclinic, <i>P</i> -1	Melting point: ? K

$a = 15.5666 (12) \text{ \AA}$	
$b = 18.1361 (16) \text{ \AA}$	$\alpha = 88.387(3)^\circ$
$c = 26.084 (2) \text{ \AA}$	$\beta = 89.846(2)^\circ$
$V = 6890.5 (10) \text{ \AA}^3$	$T = 100 \text{ K}$
$Z = 4$	<u>Fragment, colourless</u>
$F(000) = 3903$	<u>0.015</u> × <u>0.050</u> × <u>0.163</u> mm
<i>Data collection</i>	
<u>Bruker D8 Venture</u> diffractometer	<u>25243</u> independent reflections
Radiation source: <u>TXS rotating anode</u>	
<u>Helios optic monochromator</u>	$R_{\text{int}} = \underline{0.051}$
Detector resolution: <u>16 pixels mm⁻¹</u>	$\theta_{\text{max}} = \underline{25.35}^\circ$, $\theta_{\text{min}} = \underline{2.17}^\circ$
<u>phi- and omega-rotation scans</u>	$h = \underline{-18}$ <u>18</u>
Absorption correction: <u>multi-scan</u> <u>SADABS 2016/2, Bruker</u>	$k = \underline{-21}$ <u>21</u>
$T_{\text{min}} = \underline{0.654}$, $T_{\text{max}} = \underline{0.745}$	$l = \underline{-31}$ <u>31</u>
<u>217316</u> measured reflections	
<i>Refinement</i>	
Refinement method	
Refinement program	SHELXL-2014/7(Sheldrick,2014)
	$\sum w(F_o^2 - F_c^2)^2$
Data/restraints/parameters	25243/3555/2612
Goodness-of-fit on F^2	1.113

Δ/σ_{\max}	0.001
Final R indices	17903 data $i > 2\sigma(I)$; R1 = 0.0658, wR2 = 0.1313 all data R1 = 0.1057, wR2 = 0.1452
Weighting scheme	$W = 1/[\Sigma^2(FO^2) + 148.9416P]$ WHERE $P = (FO^2 + 2FC^2)/3$
Largest diff. peak and hole	3.055 and -2.520 $e\text{\AA}^{-3}$
R.M.S. deviation from mean	0.163 $e\text{\AA}^{-3}$

Compound $[\text{Ag}_8\text{L}^t_2](\text{OTf})_4$

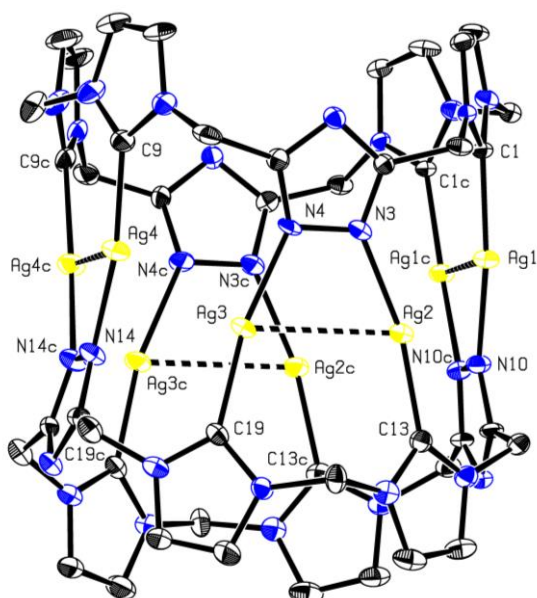


Figure S29. Crystal structure of $[\text{Ag}_8\text{L}^t_2](\text{OTf})_4$ cation, ADPs are given at 50% probability level. (CCDC 2077680)

Identification code	GuaSh17
Diffractometer operator	C. Jandl
scan speed	1-10 s per frame
2805 frames measured in 9 data sets	
phi-scans with $\Delta\phi = 0.5$	
omega-scans with $\Delta\omega = 0.5$	
Mode	shutterless mode
<i>Crystal data</i>	

$C_{22}H_{20}Ag_4N_{14} \cdot 2(CF_3O_3S)$	
$M_r = 1210.14$	$D_x = 2.029 \text{ Mg m}^{-3}$
Orthorhombic, <i>Pnma</i>	Melting point: ? K
Hall symbol: $-P\ 2ac\ 2n$	Mo $K\alpha$ radiation, $\lambda = 0.71073 \text{ \AA}$
$a = 19.357 (7) \text{ \AA}$	Cell parameters from 6188 reflections
$b = 21.269 (8) \text{ \AA}$	$\theta = 2.4\text{--}26.3^\circ$
$c = 19.244 (7) \text{ \AA}$	$\mu = 2.14 \text{ mm}^{-1}$
$V = 7923 (5) \text{ \AA}^3$	$T = 100 \text{ K}$
$Z = 8$	Fragment, colourless
$F(000) = 4672$	$0.31 \times 0.24 \times 0.13 \text{ mm}$
<i>Data collection</i>	
Bruker D8 Venture diffractometer	7736 independent reflections
Radiation source: TXS rotating anode	7276 reflections with $I > 2\sigma(I)$
Helios optic monochromator	$R_{\text{int}} = 0.051$
Detector resolution: 16 pixels mm^{-1}	$\theta_{\text{max}} = 25.7^\circ$, $\theta_{\text{min}} = 2.3^\circ$
phi- and ω -rotation scans	$h = -23\ 23$
Absorption correction: multi-scan SADABS 2016/2, Bruker	$k = -25\ 25$
$T_{\text{min}} = 0.654$, $T_{\text{max}} = 0.745$	$l = -23\ 23$
82118 measured reflections	
<i>Refinement</i>	
Refinement on F^2	Secondary atom site location: difference Fourier map

Least-squares matrix: <u>full</u>	Hydrogen site location: <u>inferred from neighbouring sites</u>
$R[F^2 > 2\sigma(F^2)] = \underline{0.055}$	<u>H-atom parameters constrained</u>
$wR(F^2) = \underline{0.132}$	$W = 1/[\Sigma^2(FO^2) + 148.9416P]$ WHERE $P = (FO^2 + 2FC^2)/3$
$S = \underline{1.26}$	$(\Delta\sigma)_{\max} < \underline{0.001}$
<u>7736</u> reflections	$\Delta\rho_{\max} = \underline{1.22} \text{ e } \text{\AA}^{-3}$
<u>657</u> parameters	$\Delta\rho_{\min} = \underline{-1.41} \text{ e } \text{\AA}^{-3}$
<u>792</u> restraints	Extinction correction: <u>none</u>
<u>0</u> constraints	Extinction coefficient: <u>-</u>
Primary atom site location: <u>iterative</u>	

Compound $[\text{Au}_8\text{L}^t_2](\text{PF}_6)_4$ (CCDC 2077681)

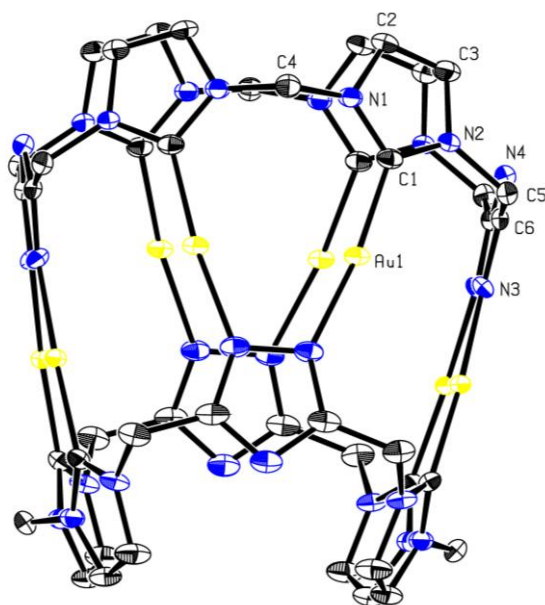


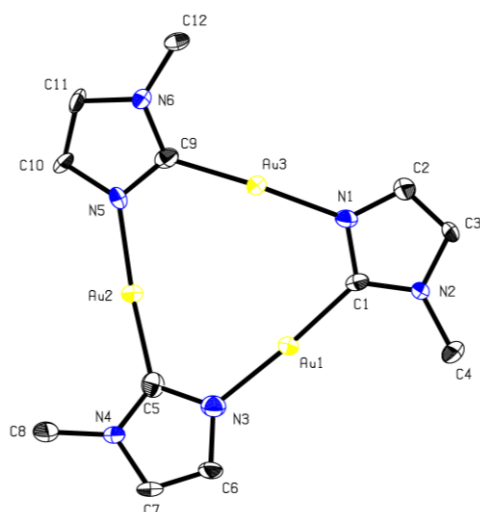
Figure S30. Crystal structure of $[\text{Au}_8\text{L}^t_2](\text{PF}_6)_4$ cation, ADPs are given at 50% probability level.

Identification code	GuaSh11
Diffractometer operator	C. Jandl
scan speed	2-20 s per frame
1205 frames measured in 9 data sets	
phi-scans with $\Delta\phi = 0.5$	

omega-scans with delta_omega = 0.5	
Mode	shutterless mode
<i>Crystal data</i>	
<u>C₄₄H₄₀Au₈N₂₈·4(F₆P)</u>	$D_x = \underline{2.590} \text{ Mg m}^{-3}$
$M_r = \underline{3116.68}$	Melting point: ? K
<u>Tetragonal, <i>I4/mcm</i></u>	<u>Mo Kα radiation, $\lambda = \underline{0.71073} \text{ \AA}$</u>
Hall symbol: <u>-I 4 2c</u>	Cell parameters from <u>9902</u> reflections
$a = \underline{16.222} \text{ (4) \AA}$	$\theta = \underline{2.5-26.7}^\circ$
$c = \underline{30.371} \text{ (8) \AA}$	$\mu = \underline{14.81} \text{ mm}^{-1}$
$V = \underline{7992} \text{ (4) \AA}^3$	$T = \underline{103} \text{ K}$
$Z = \underline{4}$	<u>Cube, colourless</u>
$F(000) = \underline{5632}$	<u>0.08 × 0.06 × 0.03 mm</u>

<i>Data collection</i>	
<u>Bruker D8 Venture</u> diffractometer	<u>2199</u> independent reflections
Radiation source: <u>TXS rotating anode</u>	<u>1932</u> reflections with $I > 2\sigma(I)$
<u>Helios optic monochromator</u>	$R_{\text{int}} = \underline{0.031}$
Detector resolution: <u>16 pixels mm⁻¹</u>	$\theta_{\text{max}} = \underline{26.4}^\circ$, $\theta_{\text{min}} = \underline{2.5}^\circ$
<u>phi- and ω-rotation scans</u>	$h = \underline{-20} \ \underline{20}$
Absorption correction: <u>multi-scan</u> <u>SADABS 2016/2, Bruker</u>	$k = \underline{-19} \ \underline{20}$
$T_{\text{min}} = \underline{0.643}$, $T_{\text{max}} = \underline{0.745}$	$l = \underline{-37} \ \underline{37}$
<u>35016</u> measured reflections	
<i>Refinement</i>	
Refinement on <u>F^2</u>	Secondary atom site location: <u>difference</u> <u>Fourier map</u>
Least-squares matrix: <u>full</u>	Hydrogen site location: <u>inferred from</u>

	neighbouring sites
$R[F^2 > 2\sigma(F^2)] = \underline{0.020}$	H-atom parameters constrained
$wR(F^2) = \underline{0.044}$	$W = 1/[\Sigma^2(FO^2) + (0.0052P)^2 + 115.086P]$ WHERE $P = (FO^2 + 2FC^2)/3$
$S = \underline{1.15}$	$(\Delta/\sigma)_{\max} = \underline{0.003}$
<u>2199</u> reflections	$\Delta\rho_{\max} = \underline{0.95} \text{ e } \text{\AA}^{-3}$
<u>150</u> parameters	$\Delta\rho_{\min} = \underline{-0.75} \text{ e } \text{\AA}^{-3}$
<u>0</u> restraints	Extinction correction: <u>none</u>
<u>0</u> constraints	Extinction coefficient: <u>-</u>
Primary atom site location: <u>iterative</u>	

Figure S31. β - $\text{Au}_3(\text{Melm})_3$ measured at 100K, ADPs are given at 50% probability level.

Identification code	GuaSh18
Diffractometer operator	C. Jandl
scan speed	2-20 s per frame
1918 frames measured in 10 data sets	
phi-scans with $\Delta\phi = 0.5$	
omega-scans with $\Delta\omega = 0.5$	
Mode	shutterless mode

<i>Crystal data</i>	
<u>C₁₂H₁₅Au₃N₆·CH₂Cl₂</u>	$F(000) = 816$
$M_r = 919.14$	
<u>Triclinic, $P\bar{1}$</u>	$D_x = 3.246 \text{ Mg m}^{-3}$
Hall symbol: <u>-P 1</u>	Melting point: ? K
$a = 9.9981 (18) \text{ \AA}$	<u>Mo Kα radiation, $\lambda = 0.71073 \text{ \AA}$</u>
$b = 10.0717 (17) \text{ \AA}$	Cell parameters from <u>7084</u> reflections
$c = 10.981 (2) \text{ \AA}$	$\theta = 2.3\text{--}26.3^\circ$
$\alpha = 75.885 (5)^\circ$	$\mu = 23.63 \text{ mm}^{-1}$
$\beta = 80.441 (6)^\circ$	$T = 100 \text{ K}$
$\gamma = 61.468 (5)^\circ$	<u>Needle, colourless</u>
$V = 940.5 (3) \text{ \AA}^3$	<u>0.11 × 0.04 × 0.02 mm</u>
$Z = 2$	

<i>Data collection</i>	
<u>Bruker Photon CMOS</u> diffractometer	<u>3709</u> independent reflections
Radiation source: <u>TXS rotating anode</u>	<u>2880</u> reflections with $I > 2\sigma(I)$
<u>Helios optic monochromator</u>	$R_{\text{int}} = 0.087$
Detector resolution: <u>16 pixels mm⁻¹</u>	$\theta_{\text{max}} = 26.0^\circ$, $\theta_{\text{min}} = 2.3^\circ$
<u>phi- and ω-rotation scans</u>	$h = -12 \ 12$
Absorption correction: <u>multi-scan</u> <u>SADABS 2016/2, Bruker</u>	$k = -12 \ 12$
$T_{\text{min}} = 0.567$, $T_{\text{max}} = 0.745$	$l = -13 \ 13$
<u>21842</u> measured reflections	
<i>Refinement</i>	
Refinement on <u>F^2</u>	Secondary atom site location: <u>difference</u> <u>Fourier map</u>

Least-squares matrix: <u>full</u>	Hydrogen site location: <u>inferred from neighbouring sites</u>
$R[F^2 > 2\sigma(F^2)] = \underline{0.034}$	H-atom parameters <u>constrained</u>
$wR(F^2) = \underline{0.066}$	$W = 1/[\Sigma^2(FO^2) + (0.0129P)^2 + 7.7003P]$ WHERE $P = (FO^2 + 2FC^2)/3$
$S = \underline{1.03}$	$(\Delta/\sigma)_{\max} \leq \underline{0.001}$
<u>3709</u> reflections	$\Delta\rho_{\max} = \underline{1.83} \text{ e \AA}^{-3}$
<u>220</u> parameters	$\Delta\rho_{\min} = \underline{-1.47} \text{ e \AA}^{-3}$
<u>0</u> restraints	Extinction correction: <u>none</u>
<u>0</u> constraints	Extinction coefficient: <u>-</u>
Primary atom site location: <u>iterative</u>	

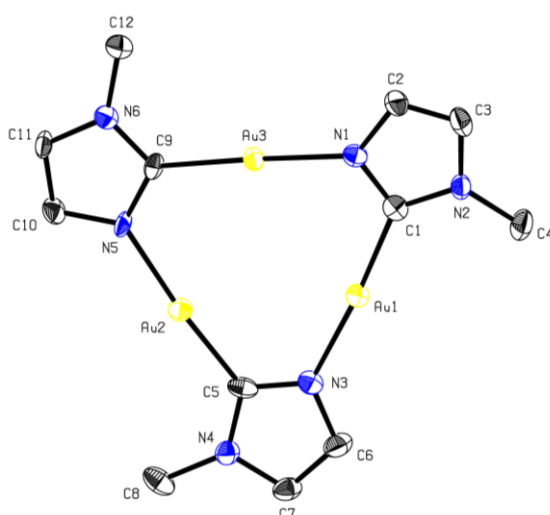


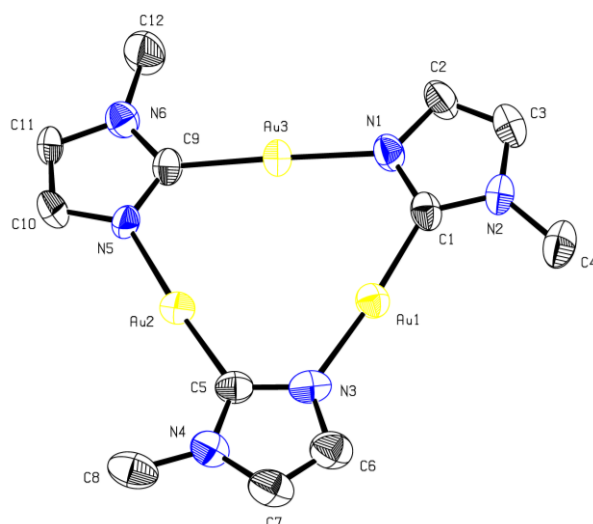
Figure S32. $\alpha\text{-Au}_3(\text{Melm})_3$ at 100K, previously published by Ruiz *et al.* (CCDC 1955200).

Identification code	GuaSh23
Diffractometer operator	C. Jandl
scan speed	2-20 s per frame
5670 frames measured in 18 data sets	
phi-scans with $\Delta\phi = 0.5$	
omega-scans with $\Delta\omega = 0.5$	
Mode	shutterless mode

<i>Crystal data</i>	
<u>2(C₁₂H₁₅Au₃N₆)</u>	
$M_r = \underline{834.21}$	$D_x = \underline{3.547} \text{ Mg m}^{-3}$
Monoclinic, <u>P2₁/c</u>	Melting point: ? K
Hall symbol: <u>-P 2ybc</u>	<u>Mo Kα</u> radiation, $\lambda = \underline{0.71073} \text{ \AA}$
$a = \underline{19.925} (4) \text{ \AA}$	Cell parameters from <u>9666</u> reflections
$b = \underline{7.8253} (17) \text{ \AA}$	$\theta = \underline{2.3-26.6}^\circ$
$c = \underline{20.088} (4) \text{ \AA}$	$\mu = \underline{28.11} \text{ mm}^{-1}$
$\beta = \underline{94.030} (6)^\circ$	$T = \underline{100} \text{ K}$
$V = \underline{3124.4} (11) \text{ \AA}^3$	<u>Plate, colourless</u>
$Z = \underline{8}$	<u>0.28 × 0.07 × 0.02</u> mm
$F(000) = \underline{2928}$	

<i>Data collection</i>	
<u>Bruker D8 Venture</u> diffractometer	<u>6382</u> independent reflections
Radiation source: <u>TXS rotating anode</u>	<u>5884</u> reflections with $I > 2\sigma(I)$
<u>Helios optic monochromator</u>	$R_{\text{int}} = \underline{0.068}$
Detector resolution: <u>16 pixels mm⁻¹</u>	$\theta_{\text{max}} = \underline{26.4}^\circ$, $\theta_{\text{min}} = \underline{2.3}^\circ$
<u>phi- and ω-rotation scans</u>	$h = \underline{-24} \quad \underline{24}$
Absorption correction: <u>multi-scan</u> <u>SADABS 2016/2, Bruker</u>	$k = \underline{-9} \quad \underline{9}$
$T_{\text{min}} = \underline{0.433}$, $T_{\text{max}} = \underline{0.745}$	$l = \underline{-25} \quad \underline{25}$
<u>115875</u> measured reflections	
<i>Refinement</i>	
Refinement on <u>F^2</u>	Secondary atom site location: <u>difference Fourier map</u>
Least-squares matrix: <u>full</u>	Hydrogen site location: <u>inferred from neighbouring sites</u>
$R[F^2 > 2\sigma(F^2)] = \underline{0.027}$	<u>H-atom parameters constrained</u>

$wR(F^2) = 0.088$	$W = 1/[\Sigma^2(FO^2) + (0.0649P)^2 + 15.6336P]$ WHERE $P = (FO^2 + 2FC^2)/3$
$S = 1.03$	$(\Delta/\sigma)_{\max} = 0.002$
6382 reflections	$\Delta\rho_{\max} = 1.83 \text{ e } \text{Å}^{-3}$
385 parameters	$\Delta\rho_{\min} = -1.98 \text{ e } \text{Å}^{-3}$
0 restraints	Extinction correction: <u>none</u>
0 constraints	Extinction coefficient: <u>_</u>
Primary atom site location: <u>iterative</u>	

Figure S33. $\alpha\text{-Au}_3(\text{Melm})_3$ at 100K, ADPs are given at 50% probability level.

Identification code	GuaSh18
Diffractometer operator	C. Jandl
scan speed	2-20 s per frame
1290 frames measured in 6 data sets	
phi-scans with delta_phi = 0.5	
omega-scans with delta_omega = 0.5	
Mode	shutterless mode
<i>Crystal data</i>	
$\text{C}_{12}\text{H}_{15}\text{Au}_3\text{N}_6 \cdot \text{CH}_2\text{Cl}_2$	
$M_r = 834.21$	$D_x = 3.452 \text{ Mg m}^{-3}$

Monoclinic, $P2_1/c$	Melting point: ? K
Hall symbol: $-P 2_1bc$	Mo K α radiation, $\lambda = 0.71073 \text{ \AA}$
$a = 19.994 (5) \text{ \AA}$	Cell parameters from 9446 reflections
$b = 7.927 (2) \text{ \AA}$	$\theta = 2.8\text{--}26.4^\circ$
$c = 20.298 (5) \text{ \AA}$	$\mu = 27.36 \text{ mm}^{-1}$
$\beta = 93.814 (9)^\circ$	$T = 293 \text{ K}$
$V = 3210.0 (14) \text{ \AA}^3$	Plate, colourless
$Z = 8$	$0.28 \times 0.08 \times 0.03 \text{ mm}$
$F(000) = 2928$	

<i>Data collection</i>	
Bruker D8 Venture diffractometer	6319 independent reflections
Radiation source: TXS rotating anode	5631 reflections with $I > 2\sigma(I)$
Helios optic monochromator	$R_{\text{int}} = 0.049$
Detector resolution: 16 pixels mm^{-1}	$\theta_{\text{max}} = 26.0^\circ$, $\theta_{\text{min}} = 2.8^\circ$
phi- and ω -rotation scans	$h = -24 \text{ } 24$
Absorption correction: multi-scan SADABS 2016/2, Bruker	$k = -9 \text{ } 9$
$T_{\text{min}} = 0.389$, $T_{\text{max}} = 0.745$	$l = -22 \text{ } 25$
49266 measured reflections	
<i>Refinement</i>	
Refinement on F^2	Secondary atom site location: <u>difference Fourier map</u>
Least-squares matrix: <u>full</u>	Hydrogen site location: <u>inferred from neighbouring sites</u>
$R[F^2 > 2\sigma(F^2)] = 0.029$	H-atom parameters constrained
$wR(F^2) = 0.083$	$W = 1/[\Sigma^2(FO^2) + (0.0556P)^2 + 4.056P]$

	WHERE $P = (FO^2 + 2FC^2)/3$
$S = 1.07$	$(\Delta/\sigma)_{\max} = 0.002$
6319 reflections	$\Delta\rho_{\max} = 1.76 \text{ e } \text{\AA}^{-3}$
386 parameters	$\Delta\rho_{\min} = -1.83 \text{ e } \text{\AA}^{-3}$
0 restraints	Extinction correction: <u>SHELXL2018</u> , $FC^* = KFC[1 + 0.001XFC^2\Lambda^3/\text{SIN}(2\Theta)]^{-1/4}$
0 constraints	Extinction coefficient: <u>0.00087 (5)</u>
Primary atom site location: <u>iterative</u>	

7.6 Hirshfeld Surface Analysis Fingerprint Plots

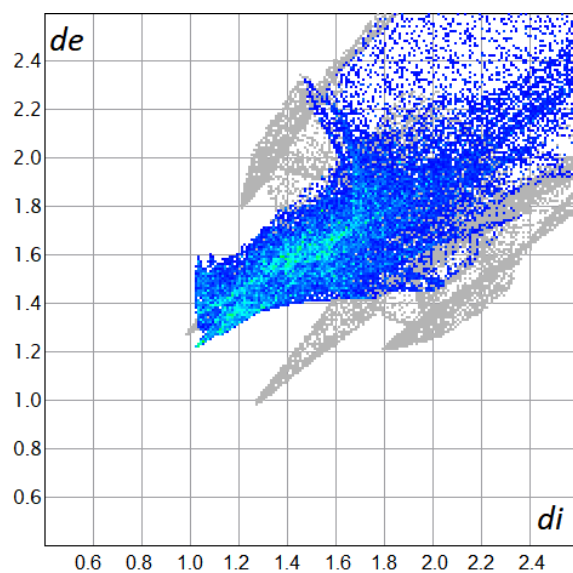


Figure S34. Hirshfeld surface analysis fingerprint plots of P-F \cdots H interactions in $[\text{Au}_8\text{L}_2](\text{PF}_6)_4$

(54.8% of the total interactions).

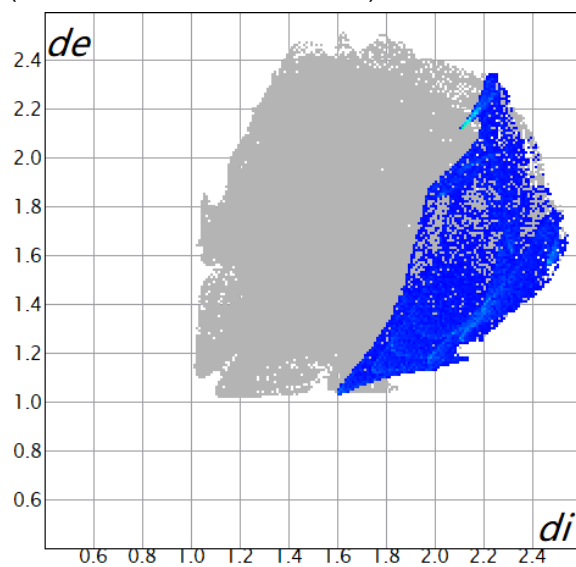


Figure S35. 2D fingerprint plot of $\text{Au}_3(\text{Melm})_3$ single trimer within β structure in Hirshfeld surface analysis. Close contacts of Au atoms to all outside atoms are highlighted, surface area included is 10.1%.

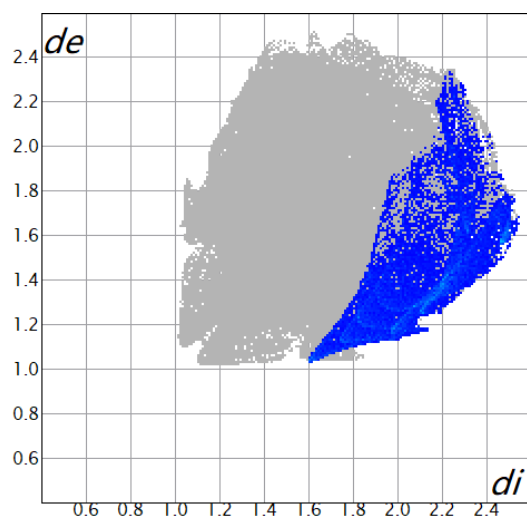


Figure S36. 2D fingerprint plot of $\text{Au}_3(\text{Melm})_3$ single trimer within β structure in Hirshfeld surface analysis. Close contacts of Au atoms to surrounding H atoms are highlighted, surface area included is 8.7%.